2013

Damage Detection in RC Earthquake Systems Using Dense Sensor Networks

Kristen Ann Peterson
Lehigh University

DAMAGE DETECTION IN RC EARTHQUAKE SYSTEMS USING DENSE SENSOR NETWORKS

by

Kristen A. Peterson

A Thesis

Presented to the Graduate and Research Committee

of Lehigh University

in Candidacy for the Degree of

Master of Science

in

Structural Engineering

Lehigh University

(September 2013)

This thesis is accepted and approved in partial fulfillment of the requirements for the Master of Science in Structural Engineering.

_____

Date

_____

Dr. Shamim N. Pakzad
Thesis Advisor

_____

Dr. Sibel Pamukcu
Department of Civil and Environmental Engineering

Acknowledgments

This research was conducted at Lehigh University's Advanced Technology for Large Structural Systems (ATLSS) Research Center in Bethlehem, PA, USA.

First I would like to thank my thesis advisor Dr. Shamim N. Pakzad. I truly appreciate all of the support, advice, and guidance you have provided me with throughout my time at Lehigh especially during my master's studies. I am also grateful for the support provided by Dr. Yahya Kurama, Dr. Michael McGinnis, and Steven Barbachyn from the NEES Coupled Shear Wall project. Additionally, the assistance provided by the ATLSS laboratory staff and Darrick Fritchman was greatly appreciated.

Finally thank you to my family, especially my mother, for their encouragement and love. And last but definitely not least, thank you to Mallory Nigro for not getting sick of spending all day, every day with me.

Table of Contents

List of Tables

Table of Figures

Abstract

In this thesis, a data-driven damage detection method is developed to detect and localize the yielding of the steel reinforcement, spalling of the concrete cover, and crushing of the concrete core in reinforced concrete earthquake-resistant structures. The proposed method utilizes pairwise damage indices to establish an instantaneous relationship between the structural responses of two sensor locations on the structure. When damage occurs, the physical properties of the structure change, which cause a change in the structural response. These changes are reflected by the damage indices; thus indicating damage. The indices are verified with two simulation models of earthquake-resistant structures and are found to correctly identify and localize all three damage modes. Considerations for extending this technique into large-scale experiments and structural health monitoring are examined by developing an instrumentation plan for large-scale testing and performing a series of small–scale experiments using digital image correlation (DIC).

1. INTRODUCTION

1.1. Overview

The incorporation of Structural Health Monitoring (SHM) systems into civil structures increases safety, improves performance, and reduces maintenance time and costs. SHM can also minimize the uncertainty associated with post-earthquake damage assessments; thus allowing for safer and quicker reoccupation after such a disaster. Therefore, integrating SHM systems into earthquake resistant structures can significantly mitigate structural damage and other losses associated with major seismic events (Balageas 2006). Several earthquake resistant structures are constructed out of reinforced concrete (RC) because previous earthquakes have revealed that RC structures perform satisfactorily under the large lateral displacements resulting from earthquakes. Consequently, the monitoring of RC earthquake-resistant structures has the potential to save lives and protect potential economic losses due to structural failures.

Structural Health Monitoring (SHM) is defined as the process of identifying structural damage through the use of novel sensing technologies and analytical methods (Lynch and Loh 2006). Damage is characterized as any changes introduced into a system that adversely affects the performance of that system (Farrar and Worden 2007). The changes can be caused by wear from continuous usage or by extreme events like earthquakes or severe wind. SHM offers an automated method for continuous monitoring, inspection, and damage detection in order to identify and evaluate these changes and track the health

of the structure (Chang 1999). As a result, if the structure becomes damaged, the damage can be localized and repaired before catastrophic failure.

The most valuable SHM system can detect the extent, type, and location of damage, but most SHM methods are only capable of detecting damage (Huston 2011). For example, vibration-based techniques have been used to characterize damage based on the concept that local damage causes a reduction of local stiffness, which influences the global behavior of a structure (Fritzen 2006). However, it has been found that they are not effective damage detection or localization methods since modal properties only reflect the global state of the structure. As a result, a large amount of damage must be present for the modal properties to be affected; therefore local damage is often overlooked (Doebling *et al* 1998). In an effort to localize and evaluate damage, it is common to locally conduct Non-Destructive Evaluation (NDE) after the damage has been identified (Chang and Liu 2003; Farrar and Worden 2007). Although NDE techniques are useful in several applications, they each have their own limitations. For example, some require *a priori* knowledge of the damage location and material properties (Shull 2002; Farrar and Worden 2007).

Therefore, there is a need to establish a SHM method that detects damage both globally and locally and does not require any prior knowledge about the damage or the structure. However, a dense network of sensors must be implemented in order to obtain rich enough data for damage detection and localization. With more sensors, there will be more data from several locations which can be used to evaluate structural damage extent,

type, and location. Establishing damage sensitive features from the data are a means for condensing the data from densely clustered sensor networks into manageable and informative quantities (Labuz 2011; Labuz *et al* 2011; Dorvash *et al* 2012).

Overall, this thesis develops an effective damage detection method in reinforced concrete (RC) earthquake-resistant structures using strains measured from densely clustered sensors to develop damage sensitive features. The proposed method relies on two pair-wise influence coefficients obtained from a linear regression between two sensor responses in order to condense the data. The foundation for these damage sensitive features is the concept that the responses of any two sensors located near each other on the structure are highly correlated. When damage occurs, the structural responses are affected; thus changing the relationship between the two locations. As a result, each pairwise coefficient is sensitive to damage in the structure.

The validity of these proposed damage indices is verified through simulation data. Future work will include extending these methods to large-scale testing of RC earthquake-resistant structures instrumented with dense sensor networks for further validation.

1.2.Research Objectives

The purpose of this research is to develop an effective method for detecting damage in earthquake-resistant RC structures using data collected from dense sensor networks. This is accomplished by the following objectives:

1. Identify possible damage modes of RC and how damage affects the structural response.
2. Develop data-driven damage features and validate them using simulation data and future experimental data from RC earthquake-resistant structures.
3. Prepare for experimental validation by developing an effective instrumentation plan for a large-scale testing and damage detection and determining how damage features will differ from those established by simulation data.
4. Establish an effective method for data collection and evaluation of the spatially dense data produced by Digital Image Correlation (DIC) for damage detection and confirm the reliability of DIC measurements.

1.3.Scope of Research

The scope of this thesis includes the following work in order to accomplish the research objectives stated in the previous section. First, two damage features were established to detect rebar yielding, the concrete cover spalling, and the concrete core crushing in reinforced concrete structures. A DRAIN-2DX fiber element model of a post-tensioned coupled shear wall was studied to develop an effective instrumentation plan for future large-scale testing and to validate the damage features. Additionally, an ABAQUS finite element model of a two-bay, two-story RC frame was developed and used to numerically validate the damage features. Lastly, small scale experiments were performed using DIC to establish effective methods for data collection and evaluation in

order to employ damage detection methods to the dense data that will be produced in future large-scale testing.

1.4.Organization of Thesis

This thesis is organized into the following chapters:

Chapter 1 presents an overview and the motivation for the research, objectives, and the organization of the thesis.

Chapter 2 presents a literature review of SHM, modal-based methods for damage detection, and NDE techniques. Also, the use of damage feature extraction and change point analysis for damage detection is explored and innovations in damage detection in RC are highlighted.

Chapter 3 first defines damage in reinforced concrete and how damage affects the structural response of a RC structure. Then it introduces two damage indices for damage detection, explains how the damage indices are affected by damage, and presents the methodology for the validation of damage detection techniques.

Chapter 4 introduces the NEES Coupled Shear Wall and the expected behavior of the structure. Next, it reviews the DRAIN-2DX fiber element of the structure and the observed behavior under large lateral displacements. Then, expected damage modes and how damage influences the elements in the model are determined. The results from the application of the damage indices for the detection of the yielding of the energy dissipating rebar, spalling of the unconfined concrete cover spalling, and crushing of the

confined concrete core are presented. Finally, preparations for extending the damage detection techniques to experimental testing are introduced. This includes establishing the instrumentation plan for the 40% scale experiment of the shear wall structure and explaining how expected experimental data will differ from the simulation data.

Chapter 5 begins by explaining the premise of digital image correlation (DIC) amd the application of DIC in SHM. Then a series of small scale experiments using 3D DIC is discussed in order to develop an effective procedure for data collection and to evaluate the dense data produced by DIC. This is important for extending the proposed damage detection methods to spatially dense data produced by DIC in upcoming large-scale experiments.

Chapter 6 discusses an ABAQUS finite element model of a two-bay, two-story RC special moment-resisting frame that was created to further validate the damage indices by applying them to a more commonly used earthquake-resistant structure. The performance of the damage indices to detect and localize yielding of the rebar and spalling of the concrete cover in the model is assessed. Lastly, a future project for damage detection in a ductile moment resisting RC frame is introduced. The project includes simulation models, component testing, and ultimately large-scale testing at Lehigh University's Advanced Technology for Large Structural Systems (ATLSS) Center.

Chapter 7 presents a summary of the thesis, conclusions, and future work.

2. LITERATURE REVIEW

This chapter presents a literature review of Structural Health Monitoring (SHM), modal-based damage detection methods, and Non-Destructive Evaluation (NDE) techniques in Section 2.1, Section 2.2, and Section 2.3, respectively. Then, the use of damage feature extraction for data condensation and change point detection methods to categorize damage is explored in Section 2.4 and Section 2.5, respectively. Lastly, innovations in damage detection in reinforced concrete will be highlighted in Section 2.6.

2.1.Structural Health Monitoring (SHM)

According to Huston (2011), SHM can be separated into five levels of classification: Level 1: Detection, Level 2: Localization, Level 3: Assessment, Level 4: Prognosis, and Level 5: Remediation. Most SHM methods are capable of accomplishing Level 1 on a global level, but the most valuable SHM system can detect the extent, type, and location of the damage.

A typical SHM system is composed of a sensor system, a data processing system, and a health evaluation system (Li *et al* 2004). First, the sensor system periodically gathers sampled response measurements. Various methods of data collection are available for the damage detection and monitoring of structures and each method depends on the physical quantities to be monitored. Kinematic quantities that are typically measured for SHM are acceleration, strain, and displacement. Next, the data processing system performs the data acquisition, transmission, and storage. Data processing is primarily

used to condense large data sets into less voluminous forms with more useful information and ultimately identify the condition of the structure (Chang 1999; Huston 2011). During this phase, data is compressed and damage-sensitive properties are identified from measurements in order to distinguish between the undamaged and damaged state of the structure (Sohn *et al* 2004). Finally, the health evaluation system uses algorithms and pattern recognition techniques to diagnose the health of the structure and detect damage.

2.2.Modal-Parameter Based Damage Detection Methods

A majority of previously developed SHM techniques use modal parameter estimations to condense data based on measured vibration signals (Chintalapudi *et al* 2006; Chang *et al* 2003). Vibrations are often ambient vibrations experienced by the structure under normal operating conditions or forced vibrations imparted on the structure by actuators, shakers, and other forms of measured impact. After the physical measurements are collected from the sensors due to these vibrations, the modal properties are used as damage-sensitive parameters to determine damage (Lynch and Loh 2006). Vibration-based techniques are based on the concept that local damage causes a reduction of local stiffness, which influences the global behavior of a structure (Fritzen 2006). Local shifts of resonant frequencies, increases in damping, and changes of vibration modes are often changes in global behavior that are used to detect damage (Sohn *et al* 2004). Some successful modal-parameter based techniques include the use of: the frequency response function to identify changes in structural properties like mass,

stiffness, and damping (Lee and Shin 2002), changes in frequency and mode shapes to identify changes in the stiffness or flexibility matrices (Pandey and Biswas 1994; Bernal 2006), and changes in the curvature of the mode shapes to locate damage (Chang *et al* 2003; Maek and DeRoeck 2000).

Modal-parameter-based techniques have previously dominated SHM, but it has been found that they are not effective damage detection or localization methods since natural frequencies and mode shapes are not sensitive enough to accurately characterize a complex system (Banks *et al* 1996; Doebling *et al* 1998). Since modal properties only reflect the global state of the structure, a large amount of damage must be present for the modal properties to be affected. As a result, local damage is often overlooked.

2.3.Non-Destructive Evaluation (NDE)

In order to locate and evaluate damage, NDE techniques are commonly conducted locally after the damage location has been identified by other methods (Chang and Liu 2003; Farrar and Worden 2007). Although NDE techniques are useful in several applications, they each have their own limitations. For example, more primitive techniques like visual inspection and tap tests rely on a trained professional. Also, visual inspection cannot detect subsurface damage or damage in hard to reach areas of a structure and a tap test can only find voids near the surface and significant cracks (Balageas 2006).

More sophisticated methods like acoustic emission, ultrasound, thermal, and magnetic methods have been used for damage detection in various materials and civil structures. Acoustic emissions can locate flaws like cracks in concrete, but must be actively monitoring at the time when the cracks develop (Carpinteri *et al* 2011). As a result, it may miss critical changes that occur in the structure of interest. Ultrasonic, thermal, and magnetic techniques like pulse-echo, thermography, and x-rays are difficult to employ globally to a structure due to equipment limitations, so they are often only used locally once damage is already located (Rens *et al* 1997; Farrar and Worden 2007). Furthermore, thermal and magnetic methods are best for steel structures and ultrasonic methods have been found to be unreliable for concrete structures (Yehia *et al* 2007).

Additionally, the proper implementation of these NDE methods often requires an *a priori* knowledge of the damage location and material properties (Shull 2002; Farrar and Worden 2007). Overall, most NDE techniques are best for local damage identification and must be used in conjunction with other techniques for global identification (Chang and Liu 2003; Rens *et al* 1997).

2.4.Damage Feature Extraction

In order to obtain rich enough data for damage detection and localization, a dense network of sensors must be implemented. A dense network produces an abundance of spatially rich data which can be used to evaluate structural damage extent, type, and location. As an alternative to installing a large network of traditional sensors like strain

gauges, advanced sensing technologies such as Digital Image Correlation (DIC) can also provide dense data. However, dense networks lead to vast amounts of extremely dense data to process. This can cause difficulties in data transmission, storage, and analysis because transmitting data from the sensors to be processed consumes power (Lynch and Loh 2006). As a result, methods must be utilized in order to condense and translate the data into information regarding the health of the structure. Damage feature extraction identifies damage sensitive properties from measured responses of the structure to condense data and distinguish between the damaged and undamaged states of a structure (Fugate *et al* 2001).

Examples of different damage features previously developed for damage detection include damage influence coefficients (Labuz *et al* 2011; Dorvash *et al* 2012), improved influence coefficients (Yao *et al* 2012), and auto-regressive coefficients (Sohn *et al* 2001; Lu and Gao 2005; Yao and Pakzad 2012).

2.4.1. Damage Influence Coefficients (IC)

Labuz *et al* (2011) developed a damage detection algorithm which uses damage influence coefficients as an index for detecting changes in the properties of the structure. The structural model this method is based upon assumes linear damage, which is when the initially linear-elastic structure remains linear-elastic after damage (Dorvash *et al* 2012). Influence coefficients (IC) are obtained from linear regression between two nodal responses. The relationship between any two near locations *i* and *j* can be defined by:

$$u_j(t_k) = \beta_{ij} + \alpha_{ij}[u_i(t_k)] + \varepsilon_{ij}(t_k) \quad (2.1)$$

Where u_j and u_i are the structural responses measured by the sensor network at time t_k, β_{ij} is the intercept value of regression, α_{ij} is the influence coefficient, and ε_{ij} is the residual of the regression model.

A damaging event causes the structural properties of the element to change, which changes the correlation between the structural responses. Therefore when damage occurs between the two compared nodes, the linear relationship changes and is reflected in the IC, thus indicating damage (Dorvash *et al* 2012). This regression-based method is capable of finding localized damage with no prior knowledge of the structure through vibration responses measured by a dense sensor network pre- and post-damage (Labuz *et al* 2011; Dorvash *et al* 2012). Labuz (2011) successfully used the acceleration responses from simulations and experiments of a beam-column connection and two-bay plane frame to detect and localize damage.

2.4.2. Improved Damage Influence Coefficients

Damage indices suggested by Yao *et al* (2012) include improved influence coefficients (IIC) and influence coefficients using hybrid vibration responses (ICHVR). The IIC approach accounts for structural geometry and sensor network layout by regressing one node's acceleration response on all adjacent nodes as shown below. The IIC damage index is α_{ij}.

$$u_j(t_k) = \sum_{i=1}^{n} \alpha_{ij}[u_i(t_k)] + \varepsilon(t_k) \quad (2.2)$$

ICHVR uses the following regression model as a damage detection algorithm by incorporating the acceleration responses at neighbor nodes as well as the strain data from near-by nodes. Here, $\varphi_l(t_k)$ are the strain measurements from adjacent nodes of j and α_{ij} and β_{jl} are the corresponding regression coefficients used as damage indices.

$$u_j(t_k) = \sum_{i=1}^{n} \alpha_{ij}[u_i(t_k)] + \sum_{l=1}^{m} \beta_{jl}[\varphi_l(t_k)] + \varepsilon(t_k) \quad (2.3)$$

2.4.3. Damage Indices from Time Series Analysis

Small scale time series analyses like Auto-Regressive (AR), Auto-Regressive with exogenous input (ARX), and Auto-Regressive-Moving-Average (ARMA) models are commonly used for feature extraction in SHM. Regression based algorithms are good for damage evaluation because they are computationally efficient and easy to implement (Lynch 2007). Even though AR/ARX features do not directly correspond to well-defined structural properties, they still reflect possible changes in certain aspects of the model (Yao and Pakzad 2012).

An AR model with *p* terms can be written as:

$$x(t) = \sum_{j=1}^{p} \varphi_{xj} x(t-j) + \epsilon_x(t) \quad (2.4)$$

Here *x(t)* is the measurement at discrete time index *t* and $\epsilon_x(t)$ and φ_{xj} are the AR coefficients. An AR model is fit to all of the reference data available and a new dataset *y(t)* is collected from an unknown structural state of the system.

The error $\epsilon_x(t)$ between the measurement and prediction obtained by the AR model is mainly caused by the unknown external input. Therefore an ARX model adds

an additional regression term for an external input *e(t)*. It establishes a relationship between different locations *i* and *j* on the structure at any time step *t* based on the past inputs and outputs and the current input as follows:

$$x(t) = \sum_{i=1}^{a} \alpha_i x(t-i) + \sum_{j=1}^{b} \beta_j e_x(t-j) + \epsilon_x(t) \quad (2.5)$$

Commonly used damage-sensitive features in AR/ARX modeling are model residuals, model coefficients, and model spectra (Lu and Gao 2005). Model residuals are the one-step prediction of error of an AR or ARX model over a dataset obtained by fitting a model from a baseline *x(t)* to a dataset collected from an unknown state *y(t)*. Several auto-regressive models use residuals and characteristics of residuals as damage sensitive features.

Yao and Pakzad (2012) and Sohn *et al* (2001) define the ratio of standard deviations of the residuals, $\sigma(\varepsilon_y)/\sigma(\varepsilon_x)$, as another damage sensitive feature. This ratio increases in the presence of damage. Therefore damage localization is possible assuming that the increase in residual errors would be at a maximum at the sensor located near the actual damage. Sohn *et al* (2001) successfully applied this approach to detect damage in an eight DOF mass-spring system using acceleration time histories.

2.5.Change Point Detection

A change in model coefficients can represent structural damage (Sohn *et al* 2001; Dorvash *et al* 2012). The change can be observed and quantified using change point

detection, which is an outlier analysis. An outlier is defined as an observation in a dataset that is surprisingly different from the rest of the data which most likely indicates that it is generated by an alternative mechanism such as damage (Worden *et al* 2000). Therefore damage can be defined as when the damage indices from the damaged state yields a significant change from the undamaged state (Fugate *et al* 2001). However, statistical methods must be used in order to define what a "significant change" is. Damage thresholds determine if the variation in the influence coefficients/damage sensitive features is significant enough to be considered damaged.

Dorvash *et al* 2012 proposes the Influence-based Damage Detection Algorithm (IDDA) which implements a Bayesian statistic to test the hypothesis that the mean of the IC for each successive test is equal to the mean of the IC from the undamaged state.

Yao *et al* (2012) uses a combination of Cumulative Sum with bootstrapping to detect changes in the IC, IIC, and ICHVR. They found that the IC did not always identify the existence of damage but IIC and ICHVR did. They also discovered that the more accurate damage localization occurred using the more complex damage detection algorithm. Since ICHVR had multiple regression parameters, it was better at reporting the damage location with a smaller likelihood of false positives.

Yao and Pakzad (2012) suggest the use of the Mahalanobis distance of AR coefficients as a discordance test in order to evaluate if an observation is an outlier. When a structure is damaged, the Mahalanobis distance value for the AR coefficients should increase substantially. Additionally, they use the Cosh spectral distance from AR

spectrum estimates because the AR spectrums were found to be more stable for damage detection than the Mahalanobis distance of AR coefficients. After performing numerical simulations, they confirmed that the Cosh spectral distance value increases when the system is damaged and it is more sensitive to change than the AR coefficients.

Nigro *et al* 2013 introduces several univariate and multivariate change point analysis techniques for influence coefficients with thresholds established from bootstrapping. Univariate techniques include Cumulative Sum, Exponentially Weighted Moving Average, and Mean Square Error. Multivariate statistics include Mahalanobis Distances and the Fisher Criterion. Each method was tested using vibration data collected from a two-bay steel tube frame. All methods effectively identified that damage occurred as well as the location of damage on the steel frame.

2.6.Damage Detection in Reinforced Concrete

Damage detection in reinforced concrete is often more complex than damage detection in homogenous materials such as steel because RC has a combination of concrete and steel properties. In this section, there is an overview of some techniques previously used for damage detection in RC.

Villemure (1995) assesses damage in reinforced concrete based on structural properties and modal properties. For each type of assessment, three indices are used to characterize damage of 45% scale RC bridge bents subjected to slow lateral cyclic loading until failure. The structural property based indices use data from load-

displacement relationships or hysteresis curves to evaluate the extent of excessive displacements, local stiffness degradation, and energy absorption. Indices based on modal properties use vibration measurements to evaluate changes in dynamic responses of the structure reflected by fundamental frequencies, mode shapes, and damping ratios. Overall, the structural based indices provided a good indication of the failure mode of the specimen. However, the only failure modes this study distinguished between were shear and flexure. The indices did not distinguish between local damages like spalling or yielding occurring in the specimens.

Acoustic-wave based techniques are commonly used in the evaluation of reinforced concrete structures. Acoustic waves are formed when energy is released as transitory waves within a material undergoing a dynamic deformation process. As a result, short-duration, high frequency sound waves are produced when the material undergoes an internal change such as stress or damage due to an external force (Huston 2011). Acoustic emission (AE) detectors are passive sensors that use this phenomenon to identify the existence of cracks and fractures as well as the location of the damage. Carpinteri *et al* 2011 use AE techniques for long-term monitoring of cracks on a load-bearing wall of an RC structure in Italy. Also, in the past five years the development and implementation of special embedded AE sensors called smart aggregates has become a topic of interest in the field of damage detection in RC.

Smart aggregates (SA) are low cost piezoelectric devices created by Song *et al* (2008) which are capable of performing comprehensive monitoring of concrete

structures. Each smart aggregate is a piezoelectric patch coated with insulation and embedded in a small concrete block, which gets embedded into the host structure for monitoring. They are low cost, light weight, quick responding, highly reliable, and can be used as both a sensor and an actuator. When the aggregate is used as an actuator, it generates an electrical charge when subjected to stress/strain. As a sensor, a stress/strain response is produced when an electrical charge is applied (Song *et al* 2008). A combination of actuator and sensor smart aggregates can easily formulate a sensor network for monitoring RC structures.

The proposed smart aggregates can monitor early-age concrete strength, detect and evaluate impacts, and monitor the health of the structure (Song *et al* 2008). Gu *et al* (2006) devised a technique for early-age strength monitoring of concrete using the smart aggregates embedded in concrete cylinders to observe the high frequency harmonic wave responses. They found that the harmonic amplitude was correlated with Young's modulus in that when it decreased, Young's modulus increased. Since concrete strength increases when Young's modulus increases, the harmonic amplitude and concrete strength could be related. This was accomplished by using a fuzzy correlation system (i.e. if harmonic amplitude is small, concrete strength is large, etc.). The correlation system was trained using the amplitude-strength data recorded and was used to predict future strength data. The estimated compressive strength determined by the cylinders embedded with smart aggregates paired with the fuzzy correlation system matched the

compressive strength from experimental compressive tests. Therefore, this technique proved to have potential in monitoring strength of concrete structures.

Song *et al* (2007) used smart aggregates for impact detection and evaluation by monitoring the peak voltages of the SA. Experimental results on a concrete beam and a two-story concrete frame showed that when the structure was impacted, the impulse response was captured by the smart aggregates, and the amplitude of the sensor signal, sensor energy, and energy distribution related to the location of the impact (Song *et al* 2008). The highest signal amplitude and sensor energy came from the smart aggregate closest to impact. As a result, this method is proven to be affective in determining damage extent and location.

Song *et al* (2008) also introduced a method for structural health monitoring using a smart aggregate as an actuator that generates a sine sweep signal and the others used as sensors that detect the sine sweep response. The amplitude of the wave and transmission energy decreased when damage existed. Furthermore, the degree of damage or severity, correlated with the degree of the drop of transmission energy. Signals were processed using wavelet packet analysis and a damage index determined the structure's health. A damage index of one meant complete failure and zero meant the structure was undamaged. They found that the damage index increased as seismic excitement level increased and harmonic amplitude and transmission energy decreased. They were able to monitor the evolution of damage and extract the damage location by the index between

sensor pairs in an experimental model of a concrete beam and two-story RC frame (Song *et al* 2008).

After the introduction of smart aggregates from these preliminary experiments, SA were implemented for a variety of studies. For example, Yan *et al* (2009), Gu *et al* (2010), and Laio *et al* (2011) used SA to determine the dynamic structural response and white noise response, and to monitor the health of reinforced concrete structures. Meng and Yan (2012) improved the use of smart aggregates for SHM by extracting damage features from collected data by wave packet analysis. The feature they found to be sensitive to damage was the energy index or signal amplitude of the SA. The feature was found for a damaged and undamaged state and evaluated by a statistical analysis that compared the probability density functions before and after damage. Their method successfully identified damage degree and location on a simply supported RC beam subjected to bending.

Overall, there has been a lot of progress in the development of damage feature extraction and SHM techniques for reinforced concrete structures. However, there is still need for the improvement of existing techniques and the development of new techniques in order to find a method that successfully identifies several damage modes, such as rebar yielding and concrete spalling and crushing, and the location at which damage occurs.

3. DEVELOPMENT OF DATA-DRIVEN DAMAGE FEATURES

Damage can be caused by typical wear and tear of every day operations or by extreme events such as earthquakes and severe winds. No matter what the cause, damage adversely affects the performance of the structure. In reinforced concrete structures, damage to the overall structure results from damage to individual components of the structure such as beams, columns, and shear walls. Each component is composed of a concrete cover, concrete core, and steel reinforcement. When damage occurs, it alters the structure's physical properties, such as the stiffness. Then, the changes in the physical properties are reflected in the changes in the structural response. Damage features that are sensitive to these structural responses can detect and localize damage in a structure. Therefore, the damages can be located and repaired before catastrophic failure.

This chapter first defines damage in reinforced concrete structures based on theory, research experiments, and design codes. Then, it reviews how these damages affect the components of an RC structure based on the concepts from a RC section analysis. Additionally, two damage indices are introduced which are developed from the assumption that damage is nonlinear. Finally, the effect that the damage modes have on the damage indices is explained as well as the methodology for the validation of these damage indices for damage detection.

3.1. Definition of Damage

Damage is apparent through changes in the physical properties of a structure such as the stiffness. The stiffness of a beam or column is affected by the material's modulus as well as the cross sectional area. For example, the flexural stiffness is dependent on *EI* and axial stiffness is dependent on *EA* where *E* is the modulus of the material, *I* is the moment of inertia of the cross section, and *A* is the cross sectional area.

In reality, there is a loss in the cross sectional area when damage such as the concrete cover spalling occurs, which causes a majority of the reduction in stiffness. However, the simulation models used in this research do not experience loss of cross sectional area because the geometric properties remain the same regardless of damage. Consequently, the stiffness is only influenced by the changes in the moduli of the materials caused by damage. Therefore, the damage modes considered are limited to material failures apparent from the stress-strain curves of the concrete cover and concrete core in compression, and the longitudinal steel reinforcement in tension. Knowledge of the stress-strain relationship of each material is essential for the development of all analysis procedures and the understanding of damages incurred in a reinforced concrete structure. In the following sections, the stress-strain curves and corresponding damage modes in steel and concrete are summarized from theory, research experiments, and ACI-318.

3.1.1. Damage in Steel Reinforcement

The stress strain curve of typical grade 60 steel has a linear portion leading to a well-defined yield point, or proportionality limit, at 60 ksi. Before yield, the material is perfectly elastic; therefore if it is loaded and unloaded there will be no permanent deformation (Salmon 2009). The yield strength in tension is used in specifications to define the behavior of steel reinforcement in reinforced concrete, but the same behavior occurs in compression as long as it precludes buckling. The slope of the elastic portion of the stress-strain curve is the modulus of elasticity or Young's Modulus and it is generally taken to be 29,000 ksi for steel.

After the yield point, there is a long plateau known as the plastic range at which the stress is constant (Salmon 2009). In higher strength steels, the stresses in the plastic range are not constant, but are increasing at a much slower rate. Therefore, the modulus of the steel is lower than the elastic modulus because the steel has softened. Then, strain hardening begins at strains 15 to 20 times larger than the yield strain and lasts until the ultimate strength of the steel (Salmon 2009). During strain hardening the stress continues to increase, but since the steel is softer, the strain is increasing at a faster rate as well. As a result, slope of the stress-strain curve becomes flatter. Finally, when the ultimate strength is reached, the steel fractures and no longer contributes any strength.

In design, ACI318-08 Section 10.2.4 assumes that the stress in reinforcement below its yield strength is proportional to the strain. Therefore the stress in reinforcement below the yield strength is the modulus of elasticity of steel reinforcement (29,000 ksi) E_s

multiplied by the strain in the steel. After the yield strength is reached, the stress in the reinforcement is assumed to be equal to the yield strength, even after the strain exceeds the yield strain. This neglects the increase in strength due to strain hardening. The calculation for determining the strain in the reinforcement by ACI318-08 is summarized in the equation from Section R10.2.4 shown below.

$$A_s f_s = \begin{cases} A_s E_s \varepsilon_s \; when \; \varepsilon_s < \varepsilon_y \\ A_s f_y \; when \; \varepsilon_s \geq \varepsilon_y \end{cases} \quad \text{(R10.2.4)}$$

Based on the changes in the stress-strain curve, the damage modes for steel reinforcement include yielding at the elastic limit and fracture at the ultimate strength of the steel.

3.1.2. Damage in Concrete

Since concrete is a non-homogeneous material, it is difficult to obtain an exact model that is a perfect representation of the response of concrete. As a result, the response of concrete is defined by stress-strain curves and material properties derived from experimental investigation. Standardized tests like uniaxial compression tests can be used to determine material properties such as the maximum compressive strength and elastic modulus. Other experiments use observations paired with the measured load-responses to associate modes of damage to certain points on the stress-strain curve.

3.1.2.1. Typical Stress-Strain Curve and Material Properties

The material response of concrete can be described by the stress-strain curve, which is defined by the compressive strength and moduli. A typical stress-strain curve provides a basis for understanding how the properties of the concrete material change under axial compression. Certain points on the stress-strain curve of the material correspond to different types of damage that directly affect the physical properties of the material.

According to Nawy (2000), a typical stress strain curve of concrete under uniaxial compression has the following properties. The first portion of the curve up to about 40% of the compressive strength is essentially linear. Then, after about 70% of the compressive strength, the stiffness of the material is reduced which causes the curve to become nonlinear. At the maximum compressive strength, cracks parallel to the direction of the loading form. Lastly, the strength of the concrete will drop shortly after an ultimate strain is reached until failure.

Kosmatka *et al* 2002 defines the compressive strength in the *Design and Control of Concrete Mixtures* handbook from the Portland Cement Association (PCA) as the measured maximum resistance of a concrete specimen to axial loading, generally at the age of 28 days. It is important to note that the maximum compressive strength depends on the type of cement, water-cement ratio, extent of hydration, curing and environmental conditions, and age of the concrete (Kosmatka *et al* 2002); therefore each mixture of

concrete has different material properties. Ordinary concrete strength often ranges from 3,000 psi to 9,000 psi (Nawy 2000).

Changes in the material's physical properties are exhibited by the modulus of the material at various levels of stress and strain. A modulus expresses the ratio between a stress that acts to change the length of a body and the fractional change in length caused by this force. The tangent modulus is the slope of the tangent to any point on the non-linear curve portion of the stress-strain diagram (Nawy 2000). Young's modulus, or the elastic modulus, is the initial tangent modulus. These moduli are used to characterize the stiffness of the concrete at various levels of stress and strain on the stress-strain curve.

Section 8.5 of ACI-318 defines the modulus of elasticity as the slope of the line from zero stress to $0.45f'_c$. However, this value may vary depending on the modulus of the aggregate. For normal weight concrete the elastic modulus, E_c is given by the equation from 8.5.1 shown below. The design code uses this modulus to estimate the strength of the concrete in an RC section at any point during loading, regardless of strain levels.

$$E_c = 57000\sqrt{f'_c} \tag{8.5.1}$$

According to ACI 318-08 Chapter 10.2, the strain in the reinforcement and concrete can be assumed to be linear across the cross section. Hence the strain is directly proportional to the distance from the neutral axis. The commentary states that the maximum concrete compressive strain at the extreme compression fiber at which crushing of the concrete is observed can vary from 0.003 to higher than 0.008. Since the strain at which ultimate moments are developed is usually between 0.003 and 0.004, the

code uses a maximum strain at the extreme compression fiber to be 0.003. The commentary of 10.6 describes the general shape of a stress-strain curve as a "rising curve from zero to a maximum at a compressive strain between 0.0015 and 0.002 followed by a descending curve to an ultimate strain (crushing of the concrete) from 0.003 to higher than 0.008". Therefore, ACI considers crushing to occur at a strain after the ultimate strength is reached.

3.1.2.2. Observed Experimental Behavior

The observed behavior of concrete under various loadings makes it possible to identify modes of damage that correspond to certain material properties and portions of the stress-strain curve. Figure 3.1 shows a plot of the stress-strain curve of a typical concrete mix subjected to compressive monotonic and cyclic loading generated from several tests performed by Bahn and Hsu (1998). Important characteristics of the stress-strain relationship and response of the material were summarized by Mehta and Monteiro (1993) as follows (Lowes 1999):

1. Zone A begins when loading commences until about 30% of the peak compressive strength. Inside this zone, the concrete remains linear elastic and there is minimal stable crack growth in the transition zone surrounding the aggregate. A stable crack does not grow under a constant load.
2. Zone B ranges from 30% to 50% of the peak compressive strength. During this phase, there is some reduced material stiffness resulting from the

significant increase in crack initiation and growth. However the crack growth is still stable.

3. Zone C ranges from 50% to 75% of the concrete strength. There is a further reduction in material stiffness partially due to crack initiation and partially due to the development of unstable cracks that continue to grow even under a constant load.
4. Zone D begins at about 75% of the concrete's strength and ends at the peak compressive strength. Spontaneous cracks grow in the transition zone around the aggregates and in the hydrated cement paste (hcp) during this time. Additionally, the micro cracks begin to consolidate into a continuous crack system. Once a crack system traverses the transition zone and hcp, there is a resulting loss of load capacity (Lowes 1999).
5. Finally Zone E is beyond the maximum compressive strength and results in reduced strength from the development of multiple continuous crack systems.

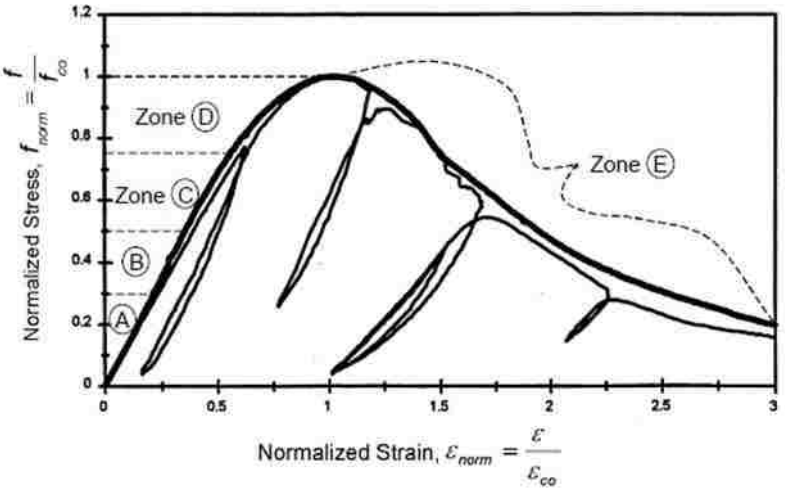

Figure 3.1: Concrete response to monotonic and cyclic compression load. Data from Bahn and Hsu, 1998 (Lowes 1999)

Overall, the general behavior of concrete is controlled by changes in the stiffness that cause a different stress-strain path (Bah and Hsu 1998). The most significant change in stiffness occurs after the maximum compressive strength. This is due to the development of several unstable cracks that consolidate into multiple growing crack systems. Therefore, the maximum compressive strength initiates a damage mode in plain concrete.

3.1.3. Damage in Reinforced Concrete

Although concrete is strong in compression, the use of confining reinforcement in a compression member significantly increases the strength and ductility. Additionally, confinement enhances ductility in plastic regions, prevents buckling of longitudinal bars, and prevents shear failure (Mander *et al* 1988a). However calculations to determine the strength and behavior of a reinforced concrete component considering the effects of the

confinement can be computational intensive. In an effort to simplify predictive calculations, Mander *et al* (1988) devised a theoretical model for the stress-strain curve of reinforced concrete that utilizes two material types: unconfined and confined concrete. Unconfined concrete is the concrete cover and confined concrete is the concrete core that would be encompassed by spirals or ties. Generally, confined concrete generally is modeled with a higher compressive strength and ductility in order to consider the effects of the confinement reinforcement.

The *Mander Model* is shown in Figure 3.2. The concrete in tension is modeled linearly up to the tensile strength f'_t. When the tensile strength is exceeded, cracks open and the tensile strength for all subsequent loading is assumed to be zero. The compressive behavior is governed by the unconfined and confined concrete.

The behavior of the unconfined concrete cover is similar to the behavior of unreinforced concrete which was described in Section 3.1.2. The compressive stress in the unconfined concrete cover increases linearly until it reaches the unconfined concrete maximum compressive strength f'_{co} at ε_{co}. After the cover reaches f'_{co}, the stress is assumed to decrease linearly until it reaches zero stress at the spalling strain ε_{sp}. At this point, the cover will crack longitudinally and separate from the concrete core at strains around 0.004 (Scott *et al* 1982).

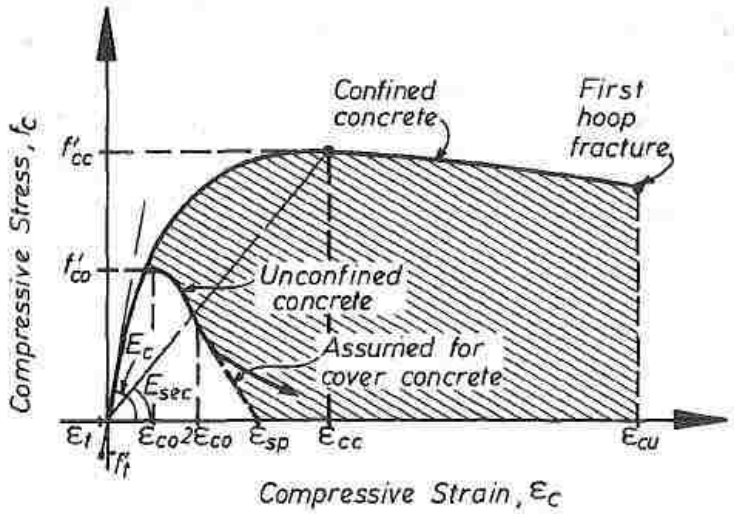

Figure 3.2: Stress-strain model proposed for monotonic loading of unconfined and confined concrete (Mander et al 1988a)

After the ultimate compressive strength of the concrete cover is reached, transverse strains in the reinforced concrete become higher from the concrete core pushing against the reinforcement (Scott *et al* 1982). Therefore, Mander *et al* 1988a estimates the confining pressures to determine a stress-strain relationship for the confined concrete. The pressure can be calculated based on the confinement effectiveness coefficient which is dependent on the geometry of the section, the amount of transverse reinforcement, and the spacing of ties or pitch of spirals. Assuming that the lateral confining pressures from the transverse reinforcement are uniformly distributed over the surface area of the core concrete, it is possible to estimate the maximum compressive strength of the confined concrete $f'_{cc.}$

Lastly, the ultimate strain of the confined concrete, ε_{cu}, is defined by Scott *et al* (1982) as the longitudinal strain at which the first hoop fracture occurs. It can be

regarded as the end of the useful region of the stress-strain curve for the confined concrete core. After the ultimate strain, there is a sudden drop in the compressive load capacity of the core because of the reduction in confinement and loss of buckling restraint for the longitudinal reinforcement in compression. Mander *et al* (1988a) predicts the ultimate strain by using the energy balance approach. This is based on the concept that the additional ductility available when the concrete is confined is due to energy stored in the transverse reinforcement. The total strain energy per unit volume required to fail the concrete is the area under the stress-strain curve as shown by Equation 3.1 (Mander *et al* 1988a). The ultimate strain energy capacity of the confinement reinforcement over the volume of the confined concrete is U_{sh}, the area under the confined concrete stress-strain curve is U_{cc}, the area under the unconfined concrete stress-strain curve is U_{co}, and the additional energy needed to maintain yield in longitudinal reinforcement is U_{sc}.

$$U_{sh} = U_{cc} + U_{sc} - U_{co} \tag{3.1}$$

This relationship relates the increase in strain energy absorbed by the concrete core to the strain energy available in yielding hoop sets. Therefore it is possible to estimate the ultimate strain at the first hoop fracture from knowledge of the compressive strength of the unconfined concrete and the stress in the longitudinal reinforcement (Mander *et al* 1988a).

In order to validate the theoretical stress-strain curve, Mander *et al (*1988b) conducted several experiments on concentrically loaded columns with various cross sectional geometry and reinforcement layouts. The stress-strain of the total column, the

spiral, the vertical reinforcement, and an unreinforced specimen of the same size were recorded as shown in the top plot in Figure 3.3a. Then, these measurements were manipulated to obtain stress-strain curves for the unconfined and confined concrete shown in the bottom plot of Figure 3.3a. They found that the theoretical curves gave good predictions of the actual stress-strain curves and the theoretical and observed confined concrete compressive strength were in close agreement. Also, they confirmed that the estimates of the axial strain corresponding to the 1st hoop fracture, or ultimate strain, by the energy approach were compatible with experimental results. Furthermore, Mander *et al* (1988b) conducted similar experiments on rectangular wall sections. Once again they found that their theoretical model matched the observed behavior as shown in Figure 3.3b.

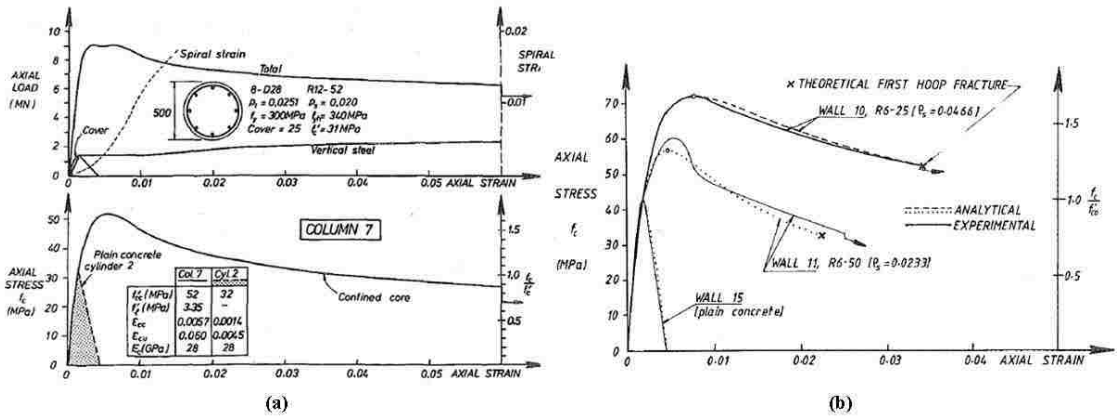

Figure 3.3: Typical experimental stress-strain curves for: (a) spirally reinforced circular columns and (b) rectangular wall sections with various reinforcement ratios (Mander et al 1988b)

For spiral columns, the strain associated with the maximum compressive strength typically ranged from 0.0014 to 0.0015 for the unconfined concrete cover and 0.003 to

0.008 for the confined concrete core. Additionally, the ultimate compressive strain corresponding to the 1st hoop fracture ranged from 0.035 to 0.06 (Mander *et al* 1988b). For rectangular columns and wall sections, the strain associated with the maximum compressive strength typically ranged from 0.0018 to 0.0022 for the unconfined concrete cover and 0.0046 to 0.021for the confined concrete core. The ultimate compressive strain typically ranged from 0.025 to 0.055 (Mander *et al* 1988b).

Overall, the damage mode for the concrete cover include spalling at the maximum compressive strength of the unconfined concrete and ultimate when the cover no longer contributes any strength to the section. The damage modes for the concrete core include crushing at the maximum compressive strength of the confined concrete, which was determined by the confining pressures, and ultimate which corresponds to the first hoop fracture.

3.2. Effects of Damage on Reinforced Concrete Section

The effectiveness of reinforced concrete relies on the tensile strength of the reinforcement combined with the compressive strength of the concrete. Consequently, both are affected when one is damaged. Based on the discussion in Section 3.1, the possible damage modes of RC that will be studied include: (1) yielding of rebar in tension, (2) initiation of spalling of the concrete cover at the maximum compressive strength of the unconfined concrete at the extreme compression fibers, (3) the ultimate

strength of the entire concrete cover, and (4) the crushing of the concrete core at the maximum compressive strength of the confined concrete.

In order to analyze how damage affects the section of a reinforced concrete beam or column, a section analysis can be performed. As an example, the coupling beam on the first story of the NEES shear wall structure will be studied. Figure 3.4 shows the geometry of the cross section. The complete details of the structure and the fiber element model used to extract the data for this analysis are in Chapter 4.

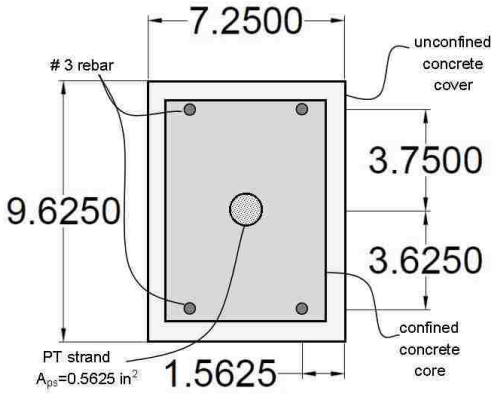

Figure 3.4: Cross section of first story coupling beam

All material properties were modeled by multi-linear stress-strain curves and the concrete was modeled using the Mander Model. Therefore, given the strain output ε from the model, it is possible to determine the stress σ in the component of the section by Equation 3.2. The slope of the stress-strain curve for the given level of strain is *E*.

$$\sigma = E \cdot \varepsilon \tag{3.2}$$

The axial force in the PT strand and the strain in the reinforcement in tension, reinforcement in compression, and concrete were output from a fiber element model

(described in Chapter 4). The strains were used to calculate the force contribution from each component by Equation 3.2. The unconfined concrete, confined concrete, and rebar in compression contributed to the compressive strength of the section while the rebar in tension contributed to the tensile strength. In order for the section to maintain equilibrium, the sum of the tensile and compressive forces must be equal to the axial force in the PT strand. This analysis was performed at the occurrence of damage, the step before damage, and the step after damage for each possible damage mode. Differences in stresses, strains, forces, and neutral axis depth of the entire reinforced concrete cross section were influenced the onset of damage.

The behavior of the reinforcement's strain responses between steps were considered to characterize how damage affects the section. Because strain gauges are commonly affixed to the reinforcement embedded in the structure during experimental testing, a majority of the structural responses will be measured from the reinforcement. Consequently, the changes in the response of the reinforcement must reflect the changes in the entire section due to damage. Details on the effects of damage in the cross section are summarized in the following sections and the complete section analysis can be found in Appendix A.

3.2.1. Yielding of Steel Reinforcement

Yielding occurs when the stress in the rebar exceeds the maximum tensile strength of the steel material. For the section being analyzed, the top reinforcement is in

tension. Upon yield, the rebar softens. As a result, the change in strain in the rebar in tension will be larger for the same increase in applied load.

Since the rebar contributes less tensile strength to the section, the neutral axis of the section moves away from the rebar in order to balance the tensile and compressive forces. Therefore, there is a larger change in the neutral axis depth upon yielding than when no damage occurs. When the neutral axis moves away from the rebar, it reduces the area of the concrete in compression. However, since there are smaller tensile forces in the section from softening, there is no great increase in strains in the concrete or reinforcement in compression between steps. Consequently, there is a decrease in the change in strain in the concrete in the section. Overall, the yielding of rebar in tension can be categorized by the increase in the change in strain in the yielded bar and decrease in the change in strain in the rebar in compression.

3.2.2. Spalling of Concrete Cover

Spalling is initiated when the extreme compression fibers of the concrete cover reach the maximum compressive strength of the unconfined concrete. Spalling of the cover in a section causes the change in strain to decrease in the reinforcement in tension and increase in the reinforcement in compression. This behavior is exhibited due to the following changes in the section when spalling occurs.

After the maximum compressive strength, there is a reduction in strength of the cover that causes the neutral axis to move toward the tensile reinforcement to balance the

forces. This engages more concrete in compression to match the tensile forces in the rebar. Therefore, the concrete core and reinforcement in compression will have to take on more loads in order to balance the section and the rebar in tension will have relatively constant strains. As a result, the change in strain in the concrete and reinforcement in compression increases as the change in strain in the rebar in tension decreases.

However, these changes are not especially drastic in the model used in the section analysis because spalling only leads to a 2% reduction in the strength of the cover. The effects of spalling will be greater in reality because the reduction in the modulus of the concrete material due to the consolidation of unstable cracks will be accompanied by a reduction in the cross sectional area. As a result, the strength of the cover will drop significantly, which would induce greater changes in the strains measured in the rebar between pre- and post- spalling.

3.2.3. Ultimate Strength of Concrete Cover

The ultimate strength is when the entire concrete cover has reached the ultimate strain of the unconfined concrete. Hence, the cover is completely failed and it contributes no compressive strength to the section. This induces a decrease in the change in strain in the rebar in tension and an increase in the change in strain in the rebar in compression due to the following behavior.

In reality, complete failure of the concrete cover will cause a drastic drop in the neutral axis away from the failed concrete to engage more concrete in compression. For

this reason, the concrete core that is still intact and rebar in compression must carry more loads, which will cause higher compressive strains in these regions. This corresponds to an increase in the change in strain in the concrete and reinforcement in compression. However, the strain in the tensile reinforcement will remain relatively constant because the total compressive forces in the section have not greatly increased due to the failure. As a result, there will be a decrease in the change in strain in reinforcement in tension.

3.2.4. Crushing of Concrete Core

Crushing of the concrete core is initiated when the extreme compression fibers of the core reach the maximum compressive strength of the confined concrete. Crushing causes the change in strain to decrease in the reinforcement in tension and increase in the reinforcement in compression. This behavior is caused by the redistribution of forces in the section once the concrete cover has spalled and the concrete core begins to crush.

When crushing initiates, the strength of the core decreases. For example, the strength of the concrete core decreases by 20% in the model used in this analysis. Consequently, the remaining section of the core and rebar in compression must take on higher loads and the neutral axis moves towards the tensile reinforcement in order to maintain equilibrium. The compressive strains increase while the tensile strains remain relatively constant. This induces an increase in the change in strain of the undamaged concrete and a decrease in the change in strain in the tensile reinforcement.

Overall, the spalling and ultimate of the concrete cover and the crushing of the concrete core can be categorized by the decrease in the change in strain in the rebar in tension and increase in the change in strain in the rebar in compression.

3.3. Damage Indices

When a structure is instrumented with a dense network of sensors, there is an abundance data that must be analyzed. It is possible to condense the data into more meaningful information regarding the health of the structure by establishing damage sensitive features from the measured structural responses. Damage indices are coefficients used to detect changes in the properties of the structure. This section explains the development of the damage sensitive features from the structural model in Section 3.3.1 and the structural response in Section 3.3.2. Then, the proposed damage indices are introduced in Section 3.3.3 and Section 3.3.4.

3.3.1. Structural Model

The proposed method of damage detection uses damage indices to determine a relationship between sensor locations *i* and *j* on a structure. The structural model used to establish the damage indices is based on an instantaneous linear relationship between the structural responses of any neighbor nodes on a structure. Assuming that the structural responses of two neighbor sensors are highly correlated and that damage changes the structural response, the relationship between the two locations will change if damage

occurs. Data can be collected pre- and post- damage or during a damaging event because the indices establish an instantaneous linear relationship between two sensors.

The theoretical instantaneous linear relationship upon which the damage indices are established does not account for measurement noise. In reality measurement noise contaminates measured signals such that information from some damages may be covered by noise (Yan *et* al 2007). The effects of noise can be managed through data processing and by collecting several sets of measurements. During data collection, an abundance of measurements will be captured by the sensors; therefore the theoretical linear relationship without noise will be the limit of the relationships established with noisy data. Noise is not an issue in simulations because measurement noise is not present.

Overall, the damage indices are based on the premise that changes in the physical properties are reflected in the structural responses which are directly translated into changes in the damage indices. Therefore discontinuities or peaks in the damage indices signify a change in the relationship, i.e. possible damage, between the sensors compared by the damage index.

3.3.2. Structural Response

The structural response chosen for this thesis is the change in strain between load steps because the strain at any point on a structure is easily obtainable directly from the measurements output by strain gauges. Also, strain directly corresponds to different

material limits at which damage occurs, which was described in the Sections 3.1 and 3.2. Consequently, strain is a variable that is directly affected by damage.

The change in strain at any step *t* can be calculated using Equation 3.3. Overall, the change in strain is determined based on how much the base shear has varied between the steps. In the application to the DRAIN-2DX model in Chapter 4, Equation 3.4a shows how the value between base shears is chosen throughout the loading. These values were chosen because in the beginning load steps, there is a larger change in base shear between steps while there is a smaller change in strain. Equation 3.4b shows how the value of base shear is chosen for the change in strain of the ABAQUS model in Chapter 6. Most importantly, the calculation of the change in strain can be modified according to the loading of the structure being monitored and the data available.

$$\Delta\varepsilon(t) = \varepsilon(V_b(t)) - \varepsilon(V_b(t) - s) \tag{3.3}$$

$$s = \begin{cases} 5\ kips\ if\ V_b \leq 150\ kips \\ 1\ kip\ if\ 150 < V_b < 275\ kips \\ 0.5\ kip\ if\ V_b \geq 275\ kips \end{cases} \tag{3.4a}$$

$$s = \begin{cases} 20\ kips\ if\ V_b < 250\ kips \\ 12\ kip\ if\ 250 \leq V_b < 500\ kips \\ 6\ kip\ if\ V_b \geq 500\ kips \end{cases} \tag{3.4b}$$

3.3.3. Regression Coefficient, α

The first damage index proposed is α which is a regression coefficient between two nodes *i* and *j*. It is calculated for all steps by Equation 3.5 where the change in strain at load step t in location j is $\Delta\varepsilon_j(t)$.

$$\alpha_{ij}(t) = \frac{\Delta\varepsilon_j(t)}{\Delta\varepsilon_i(t)} \tag{3.5}$$

3.3.4. Slope of Regression Coefficient, β

β is the slope or first derivative of α. It is the slope between two load steps on a plot of α_{ij} versus base shear as shown in Equation 3.6. This damage index is based on the observation of when α_{ij} is plotted against the base shear V_b at any given load step *t* the slope between the damage index and base shear *s* steps before will change during the onset of damage. A step size of one proved to be affective in this application.

$$\beta_{ij}(t) = \frac{|\alpha_{ij}(t) - \alpha_{ij}(t-s)|}{|V_b(t) - V_b(t-s)|} \tag{3.6}$$

3.4.Effects of Damage on Damage Indices

In general, when the material strain limits are reached in an element, it is inferred that the element will exhibit the corresponding damage mode at a certain value of base shear; thus inducing a change or peak in the damage index. Furthermore, each change or peak in the damage index can be associated with a corresponding level of base shear or load step. An effective damage index exhibits these peaks at the step associated with a material damage mode.

The behavior of the damage index is dependent on the type of damage, which sensors are compared, and on how the damage index is calculated. Generally, damage in an element causes an increase in the rate of change of the strain. The stress in an element at any time can be directly calculated by the basic stress-strain relationship described in Equation 3.2 where E is the modulus or slope of the stress-strain curve at any strain ε. The initial elastic modulus of steel or concrete is the steepest. After yielding, spalling, or crushing, the modulus decreases and slope of the stress-strain curve becomes flatter; thus there is a larger change in strain for the same change in stress.

Consequently, α will increase if the damaged element is used as sensor j and will decrease if it is used as sensor i in Equation 3.5. On a plot of α against the base shear during loading, damage will be recognized as a change in slope of α. Therefore, if α decreases, β will show a negative peak and if α increases, β will show a positive peak when the element becomes damaged. Figure 3.5 summarizes the effects each damage mode has on the components of the RC cross section that were discussed in Section 3.2. Then, the effect that damage mode has on the change in strain in a sensor can be used to determine how the damage indices will be influenced by using Figure 3.6. Understanding the behavior of the damage indices is crucial for numerical validation.

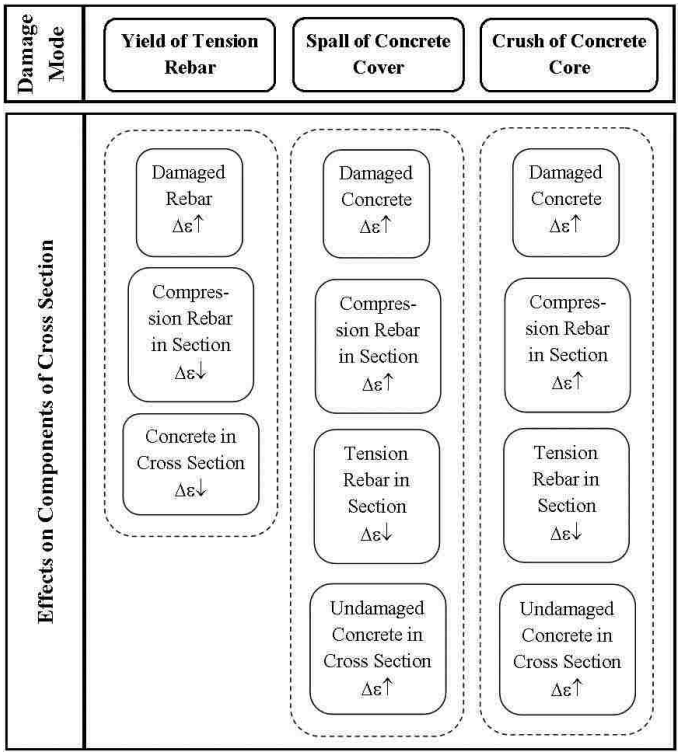

Figure 3.5: Effects of damage modes on strain in components of beam cross section

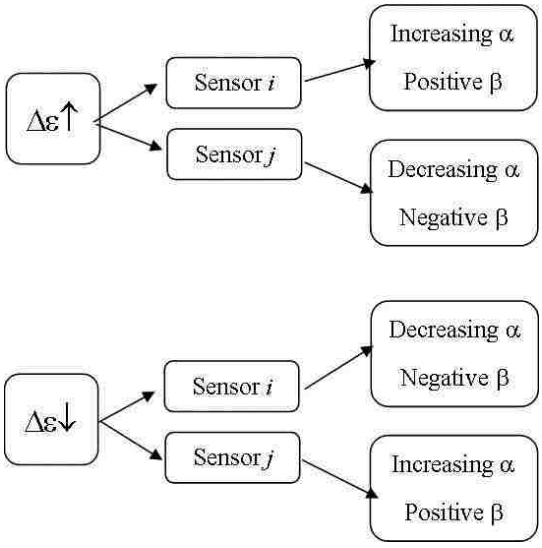

Figure 3.6: Flowchart of how changes in strain affect damage indices α and β

3.5.Methodology for Validation of Damage Indices

Validation of the damage indices through simulation models and experiments is necessary to confirm that the proposed damage detection methods are effective. Simulation data produced from a fiber or finite element model is an easy and inexpensive means for generating data for damage detection. Models are especially valuable because the structural geometry and all of the material properties are known. Consequently, the behavior of the structure and expected damages are simple to predict. Additionally, large amounts of data can be extracted from the model in order to simulate a dense sensor network. Two simulation models were used in the development and verification of the damage indices: a DRAIN-2DX fiber element model and an ABAQUS finite element model.

A DRAIN-2DX fiber element model was previously developed by The University of Notre Dame for a new type of earthquake resistant structure that utilizes post-tensioned coupling beams to transfer the loads to reinforced concrete shear walls. The geometry, material properties, modeling assumptions, and observed behavior of the structure are analyzed in the beginning of Chapter 4. Then, the damage modes of the model as well as when and where damage occurs in the structure are defined. Finally, both damage indices are calculated using the strains output from select elements at each story level of the structure. Since changes in slope of α and peaks of β categorize damage, each sensor pair combination is examined to verify that these changes in damage indices correspond to a particular damaging event and location.

An ABAQUS finite element model of a two-bay, two-story reinforced concrete special moment-resisting frame (SMRF) subjected to large lateral loads was formulated in order to evaluate the performance of the damage indices on a more widely used earthquake-resistant structure. The development of the model is detailed in the beginning of Chapter 6. The strain data from select elements that experience damage are used to calculate the damage indices. Since the material properties are known, the load step at which damage occurs in each element is known. Therefore, known damages are compared to changes of slope in α and peaks in β to verify the damage indices.

Experimental testing differs from simulation models in that exact material properties are unknown, structural geometry may be different than expected due to construction errors, and there is measurement noise. Most importantly, experiments display how a structure will behave in reality; whereas simulation models often have several simplifications and assumptions that are not necessarily true in real life. As a result, it is extremely important to validate the damage indices with experimental data. A 40% scaled version of the post-tensioned coupled shear wall is scheduled to be tested using hybrid simulation in September 2013. The structure is instrumented with hundreds of strain gauges and ten digital image correlation (DIC) camera set-ups in order to create a dense sensor network of data. Data extracted from the experiment will be utilized to calculate the damage indices. Observations will be used to determine if changes of slope in α and peaks in β correspond to certain damages in the structure. Details about the large scale testing and how damage indices may differ from the simulation data can be

found in Section 4.1.2 and Section 4.6 respectively. Additionally, a future project of an RC ductile moment frame will validate the damage indices experimentally through a series of component testing, scaled testing, and hybrid simulation. Further details on the RC frame project are in Section 6.6.

3.6.Considerations for Validation

Two error types are possible in identifying damage: false positives and false negatives (Fugate *et al* 2001). A false positive detects a possible damage when no damage has occurred and a false negative does not detect a possible damage when damage is present. Although false positives can lower the confidence in the damage detection method, false negatives are more detrimental (Farrar *et al* 2001). False negatives can result in serious life-safety hazards if damage is not recognized before catastrophic failure of the structure.

The focus of this analysis is to ensure that the proposed damage indices show a change in behavior when damage occurs such that there are no false negatives. Any false positives will be ignored in this current research, but will be examined in future work. Therefore the performance of the damage indices during the simulation and experimental validation studies will be evaluated only on their ability to detect the known damages.

4. NEES POST-TENSIONED COUPLED SHEAR WALL

4.1. Introduction

Coupled shear wall systems are lateral load resisting systems that are frequently used to effectively transfer the loads between the wall piers and dissipate energy during an earthquake. A common way of achieving the desired ductile behavior is by using diagonal reinforcement, which is difficult to construct. The NEES Coupled Shear Wall being studied at Lehigh University's ATLSS in conjunction with The University of Notre Dame and The University of Texas at Tyler proposes a new system as a superior alternative to diagonally reinforced coupling beams.

Overall, the project has two main purposes. The first is to study the behavior of this new system to prove that it provides significant performance, construction, and economic benefits and sustains little damage during a severe earthquake. The second purpose is the focus of this research, which is to develop data-driven damage detection methods to detect the existence and location of damage in reinforced concrete structures. Data from a simulation model and experimental testing with dense instrumentation are used to develop and validate these methods.

The proposed specimen is a shear wall core of a hypothetical 8-story building in a high-seismic region shown in Figure 4.1. It is composed of 2 C-shaped shear walls linked at each floor level by post-tensioned coupling beams with debonded reinforcement that extends into the wall pier for energy dissipation.

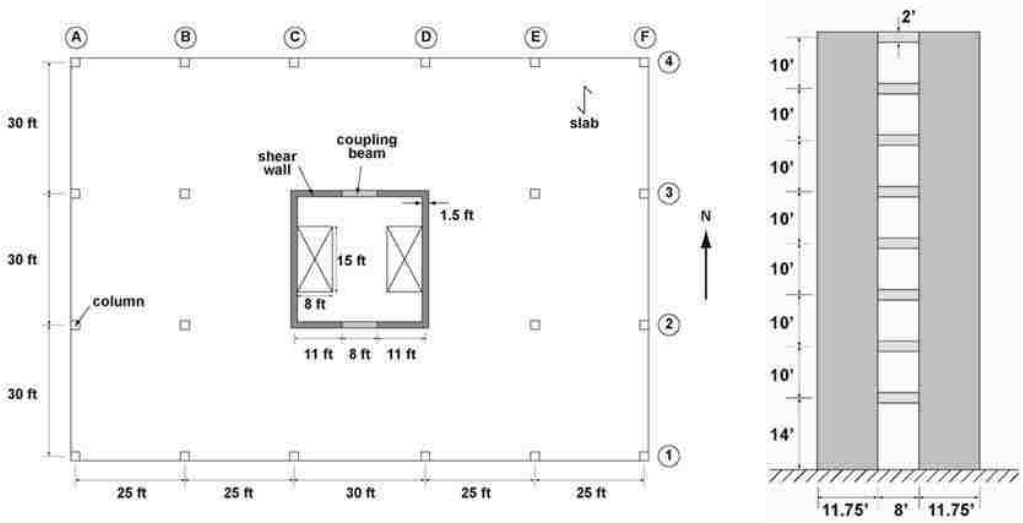

Figure 4.1: 8-story specimen: (a) prototype plan (b) prototype elevation (courtesy of Steven Barbachyn)

This type of system has several advantages over traditional lateral resisting systems under large lateral displacements because of key unique components such as reinforcement that extends into the beam-wall interface and post-tensioning strands in the coupling beams. The debonded reinforcement, or energy dissipating (ED) steel bars, are not bonded to the coupling beam; therefore they will yield to provide energy dissipation. Post-tensioning (PT) tendons provide additional strength and stiffness to the beam as well as a "self-centering" force. This "self-centering" force brings the structure back to its original position after large lateral displacements, thus greatly reducing the residual lateral displacement at the end of an earthquake. Lastly, the coupling beams are much simpler to construct than a diagonally reinforced beam and are easy to replace if severe damage occurs.

Additionally, the PT strands and ED reinforcement induce behaviors in the system, like gap opening and concentrated cracking, which further dissipate energy and reduce damage. Previous experiments and fiber element models of coupled shear wall systems (Kurama *et al* 2004, 2006, 2007, 2010) provide a basis for predicting these behaviors in the structure and the transfer of loads in the coupling beams, which is depicted in Figure 4.2a. As the lateral displacement of the wall structure increases, the beam begins to elongate and develop an axial force N_b opposing the PT force. The upper shear force F_{wts} will be less than the lower shear force at a story F_{wbs} causing the axial force in the beam to become larger than the PT force. This should be visible by gap opening at the beam ends. Also, diagonal compressive struts form in the coupling beams opposite to the gap opening. At the ends of the compressive strut, cracking occurs at the beam ends in compression as shown in Figure 4.2b on the left. This cracking is controlled to the corners only as opposed to the extensive cracking that would develop in a typical monolithic RC beam shown in Figure 4.2b on the right. Overall, the gap opening can be viewed as "lumped cracking" at controlled locations which reduces damage to the end of the coupling beam (Kurama and McGinnis 2011).

Lastly, under large lateral displacements, the forces in the first story coupling beam should be higher than those in the upper story beams. As a result, the most critical forces are near the wall causing cracking at the feet of the wall piers as shown in Figure 4.2a (Kurama *et al* 2004).

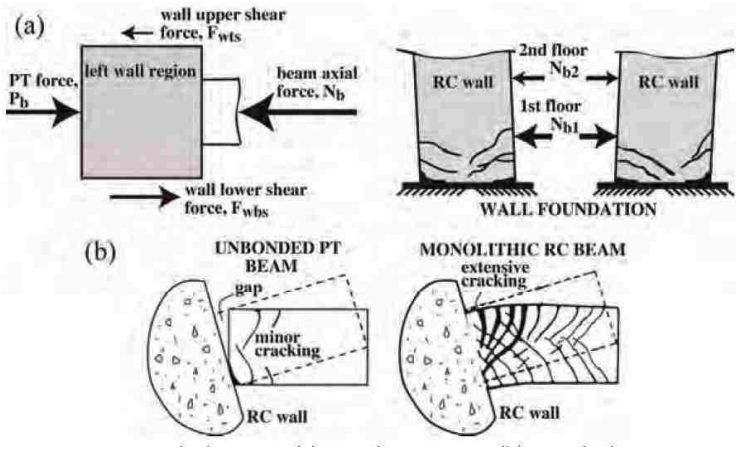

Figure 4.2: Predicted behavior: (a) axial restraint; (b) axial elongation, gap opening, and controlled cracking (Kurama and McGinnis 2011)

The performance of the proposed PT coupled shear wall system will be evaluated through simulation data and large-scale testing. Furthermore the simulation model will be examined to study the behavior of the structure, possible modes of damage, and create an instrumentation plan for experimental testing. Data generated from the simulation model and future large-scale experiments will be extracted to generate the damage indices in order to validate the damage detection methods established in Chapter 3.

4.2. Large-Scale Testing

A 3-story 40% scale structure under static reversed cyclic loading up to 3% roof drift will be used to model the 8-story structure under earthquake loading using ASCE7-10 Equivalent Lateral Forces (ELF) and hybrid simulation. The hybrid simulation implemented in this project involves the technique of substructuring, which divides the reference structure into a physical substructure and a numerical or computational substructure (NEES 2013). The two substructures are linked by using actuators to enforce

equilibrium and compatibility at the interface. The process for determining the forces that will be applied to the physical substructure in large-scale testing is summarized in Figure 4.3.

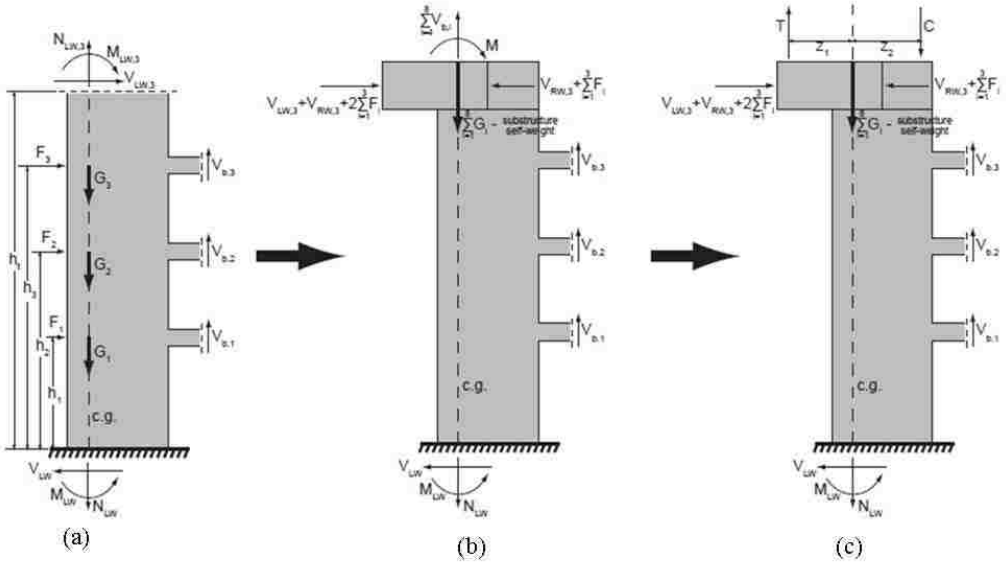

Figure 4.3: Laboratory test hybrid simulation: (a) ELF's by ASCE 7-10 on 8-story structure, (b) lateral forces converted to lab substructure, (c) forces applied on 3-story lab substructure for hybrid simulation (courtesy of Steven Barbachyn).

First, in order to simulate the earthquake forces on the structure, the equivalent lateral forces acting on all eight stories are calculated by the equivalent lateral force procedure of ASCE7-10 (Figure 4.3a). The ASCE7-10 ELF procedure places static forces on a structure with magnitudes and directions that closely approximate the dynamic effects of an earthquake. Then, the forces are converted to the 40% scale three-story substructure while still obtaining the same global reaction forces at the base of the wall piers and inside the coupling beams (Figure 4.3b). Lastly, the moment and axial forces at the level

of the 3rd story determined from a DRAIN-2DX model are used to simulate the top five stories of the building with hybrid simulation (Figure 4.3c).

The schematic of the proposed setup in the laboratory at ATLSS is depicted in Figure 4.4. During testing, one horizontal actuator will apply the static reverse-cyclic lateral force at the third story level to develop the desired base shear. Two additional horizontal actuators will distribute the lateral force between the two walls. This is necessary because the lateral loads are not evenly carried by the two shear walls by design. Lastly, four vertical actuators will apply forces to the third story for hybrid simulation. The instrumentation plan for the laboratory specimen is presented in Section 4.5.

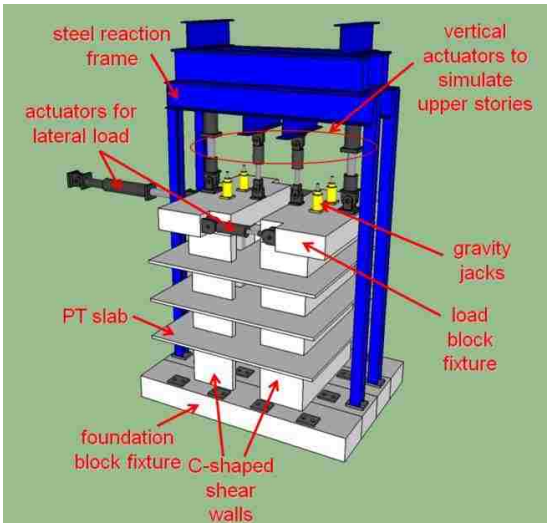

Figure 4.4: Proposed laboratory setup at ATLSS (courtesy of Steven Barbachyn)

4.3. DRAIN-2DX Model

4.3.1. Description of Model

A fiber element model in DRAIN-2DX was previously developed to study the behavior of the structure under large lateral displacements. The initial purpose of this model is to determine the expected behavior of the structure before constructing the laboratory specimen and to examine strain and stress concentrations to develop an effective instrumentation plan. For the focus of this research, the DRAIN model is used to extract data, such as strains in components of the structure, to develop and validate data-driven damage detection techniques.

In order to determine expected damage modes and the effect of damage on the structure, it is necessary to completely understand the components, the assumptions of the model, and the behavior observed in each of the components. This information is crucial to the development of damage detection methods and to the verification of their capabilities on the simulation data. Therefore this section reviews the formulation of the model through the element groups, material properties, loading, important outputs, slaving, and the distribution of displacement and strains.

4.3.1.1.Element Groups and Material Properties

In the DRAIN input, element groups specify the material properties, cross sections, and behaviors. An element connects two nodes in the structure and the structure is divided into different element groups depending on the location of the nodes. The

element groups include the: (1) left and right C-shaped wall piers, (2) coupling beams, (3) and (4) PT tendons, and (5) ED steel as shown in Figure 4.5.

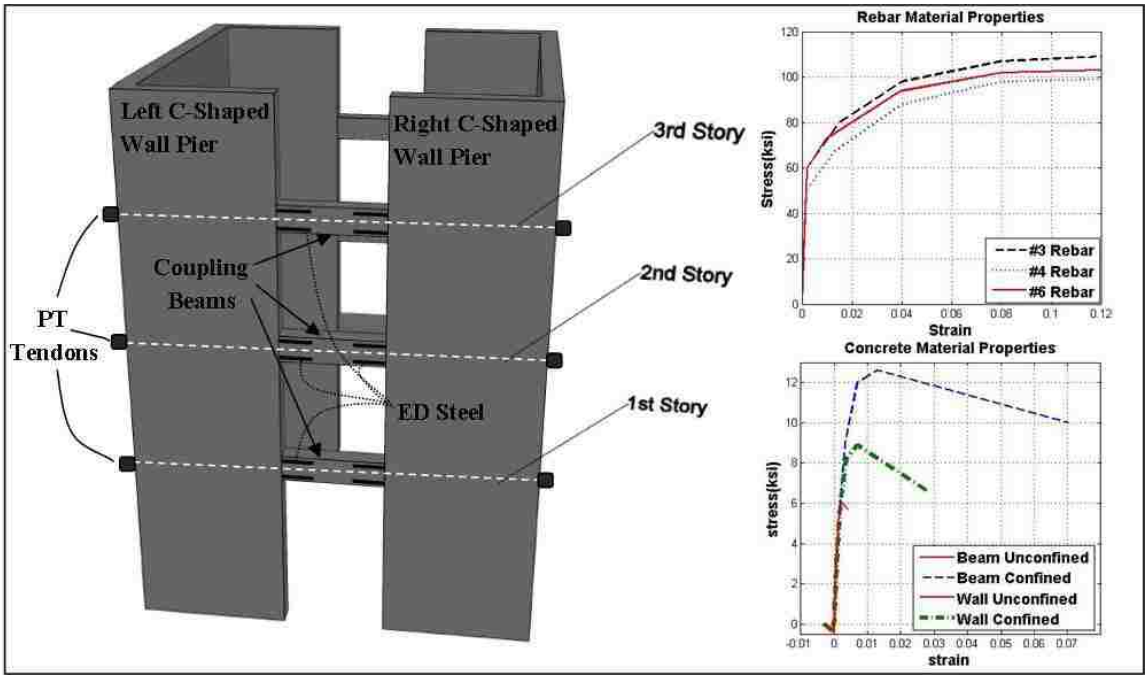

Figure 4.5: DRAIN element groups and material properties.

DRAIN defines material properties by a stress-strain curve specified by the user. This stress-strain relationship uses a multi-linear idealization to consider nonlinear properties of the materials. Concrete has a multi-linear relation in tension and compression (compression positive) as shown in Figure 4.6a. The concrete begins to lose strength after E2C, S2C. The behavior of steel is governed by the stress-strain relationship shown in Figure 4.6b. These properties are consistent in tension and compression. Yield occurs at E1, S1.

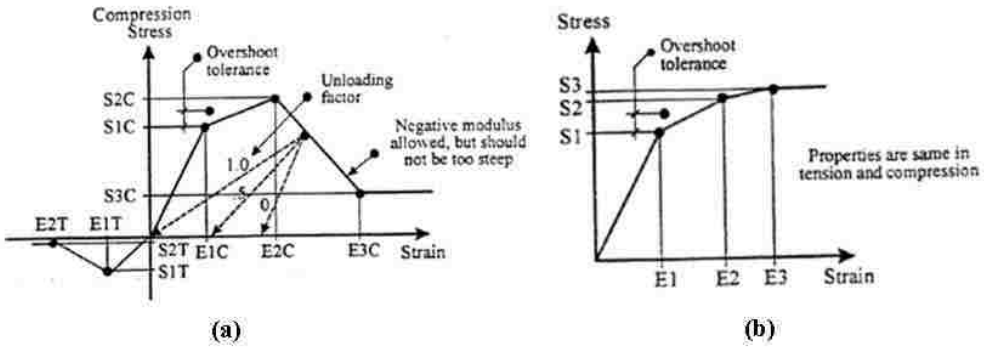

Figure 4.6: DRAIN 2DX material properties for: (a) concrete and (b) steel (Prakash 1993)

The DRAIN model of the shear wall structure is comprised of 9 different materials: unconfined concrete and confined concrete in wall piers, zero-tension unconfined and confined concrete at coupling beam ends, linear-tension unconfined and confined concrete in the remainder of the coupling beams, #3 mild rebar for the ED steel, and #4 and #6 rebar for the vertical reinforcement in the wall piers. Each uses a multi-linear idealization to consider nonlinear properties of the materials as shown in Figure 4.5. Since the transverse reinforcement is not physically modeled, the concrete elements' cross sections are composed of two concrete materials—unconfined and confined concrete using the Mander Model. Unconfined concrete is the strength of the concrete cover and confined concrete is the core of the beam encompassed by the transverse reinforcement. It has a higher compressive strength than the unconfined concrete in order to simulate the added strength from the confinement

Wall Piers

The wall piers consist of an unconfined concrete cover and a confined concrete core. They are longitudinally reinforced by #6 mild steel rebar with a yield strength of 60 ksi and by #4 mild steel rebar with a yield strength of 50 ksi. The stress-strain relationships for the wall pier element materials are shown in Table 4.1 and Table 4.2 Highlighted values indicate values of stress and strain at which possible damage or failure modes of the material occur.

Table 4.1: Stress-strain input for wall pier concrete material properties

Unconfined Concrete			**Confined Concrete**		
Stress	*Strain*	*Damage Modes*	*Stress*	*Strain*	*Damage Modes*
-0.01	-3.09E-03		-0.01	-3.09E-03	
-0.4	-9.06E-05		-0.4	-9.06E-05	
3.3113	0.00075		3	0.0007	
5.58	0.0015		6	0.0019	
6	0.002	*Max Comp. Strength-Spall*	8.2	0.0036	
5.9	0.003		8.88	0.0068	*Max Comp. Strength-Crush*
5.7	0.004	*Ultimate*	6.6	0.028	*Ultimate*

Table 4.2: Stress-strain input for wall pier steel material properties

Mild Steel (#6- 0.75" dia.)			**Mild Steel (#4-0.5" dia.)**		
Stress	*Strain*	*Damage Modes*	*Stress*	*Strain*	*Damage Modes*
0	0		0	0	
60	0.00207	*yield*	50	0.00172	*yield*
73	0.01		67	0.013	
94	0.04		88	0.04	
102	0.08		98	0.08	
103	0.12	*ultimate*	99	0.12	*ultimate*

Coupling Beam Concrete

The coupling beams consist of #3 mild reinforcement for the ED steel, zero-tension unconfined and confined concrete at the ends, and linear-tension unconfined and

confined concrete in the remainder of the beam. The concrete material properties are summarized in Table 4.3. Highlighted values indicate values of stress and strain at which possible damage or failure modes of the material occur.

Table 4.3: Stress-strain input for beam zero-tension unconfined and confined concrete material properties

Zero Tension Unconfined			**Zero Tension Confined**		
Stress	*Strain*	*Damage Modes*	*Stress*	*Strain*	*Damage Modes*
0	0	*Tension Failure*	0	0	*Tension Failure*
3.3113	0.00075		4	0.00091	
5.58	0.0015		9	0.0033	
6	0.002	*Max Comp. Strength-Spall*	12	0.007	
5.9	0.003		12.6	0.013	*Max Comp. Strength-Crush*
5.7	0.004	*Ultimate*	10	0.0702	*Ultimate*
Linear Tension Unconfined			**Linear Tension Confined**		
Stress	*Strain*	*Damage Modes*	*Stress*	*Strain*	*Damage Modes*
-40	-0.009	*Tension Failure*	-40	-0.009	*Tension Failure*
0	0		0	0	
3.3113	0.00075		4	0.00091	
5.58	0.0015		9	0.0033	
6	0.002	*Max Comp. Strength-Spall*	12	0.007	
5.9	0.003		12.6	0.013	*Max Comp. Strength-Crush*
5.7	0.004	*Ultimate*	10	0.0702	*Ultimate*

Since a majority of the damages will occur at the beam ends, the zero-tension unconfined and confined concrete material models are examined further for complete understanding of the behavior. The stress-strain curve for the zero-tension unconfined concrete is shown in Figure 4.7a. The stress-strain curve can be compared to the typical curve and corresponding zones described by Mehta and Monteiro (1993) in Section 3.1.2 in order to determine when damage occurs.

In the concrete cover, the elastic modulus is initially 4415 ksi until $0.55f'_c$. According to the observed behavior by Mehta and Montiero (1993), the concrete will then be in *Zone C* and will begin to develop unstable cracks; thus causing a reduction in stiffness. As a result, the modulus becomes 3720 ksi until $0.93f'_c$. Then, spontaneous cracks form and grow causing the concrete to lose stiffness again (*Zone D*). Subsequently, the slope decreases to a modulus of 840 ksi until the maximum compressive stress is reached. After the maximum compressive strength (*Zone E*), the modulus becomes negative as the strength of the unconfined concrete diminishes.

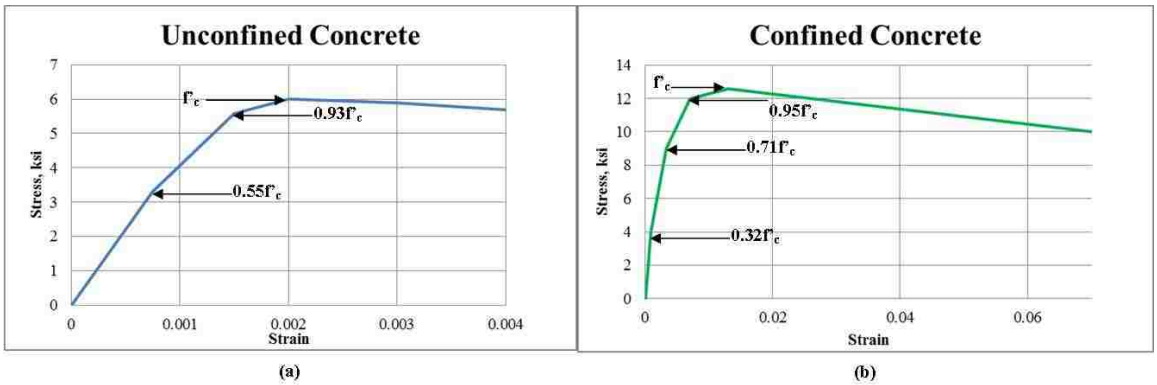

Figure 4.7: Stress-strain curve for: (a) zero-tension unconfined concrete and (b) zero-tension confined concrete in DRAIN model

The confined concrete has a higher compressive strength, can withstand higher strains, and has a more ductile reduction in strength than the unconfined concrete. The stress-strain curve for the zero-tension confined concrete is shown in Figure 4.7b. Initially, the elastic modulus is 4395 ksi until $0.32f'_c$ which is considered *Zone A*. Here the concrete remains linear elastic. Then in *Zone B*, the modulus decreases to 2727 ksi due to some reduction in material stiffness from stable crack growth until $0.71f'_c$. After

$0.71f'_c$ in *Zone C*, unstable cracks lower the stiffness to 810 ksi until $0.95f'_c$. Finally in *Zone D*, the stiffness drops significantly to 100 ksi as unstable micro cracks consolidate into a continuous crack system until the maximum compressive strength is reached. Afterwards, the modulus becomes negative in *Zone E* and the strength of the confined concrete diminishes until an ultimate strain.

In the DRAIN model, the compressive strength of the unconfined concrete is 6 ksi at 0.002 strain and the compressive strength of the confined concrete is 12.6 ksi at 0.013 strain. After f'_c is reached, the strength and stiffness of the concrete is greatly reduced and damage will be initiated at the maximum compressive strain associated with f'_c. Therefore in the analysis presented, the maximum compressive strength of the unconfined and confined concrete will be considered a damage mode and will be referred to as spalling and crushing respectively.

By the definition of crushing defined by ACI318-08, the unconfined concrete cover and confined concrete core crush at the ultimate strains of the concrete and lose all of their strength. This corresponds to 0.004 strain for unconfined concrete and 0.0702 strain for confined concrete. However, the concrete never completely loses all strength in the model. Instead, DRAIN assumes that the strength of the unconfined concrete and confined concrete remain at 5.7 ksi and 10 ksi respectively after ultimate. In this thesis the ultimate strength of the concrete will be referred to as ultimate instead of crushing. It is not realistic to assume that the unconfined concrete cover still contributes to the strength of the section once it fails, but for the purposes of this research the significance

of this error will not be considered. Instead, the detection of ultimate will be disregarded as a possible damage mode from the simulation data. However, it should be considered in experimental testing since it will greatly affect the strength of the section.

Coupling Beam ED Steel

The debonded rebar at the ends of the coupling beams are modeled by the ED Steel Elements in DRAIN. The lengths of the ED Elements, L_{cr}, were chosen based on desired demand. The stress-strain curve for the mild steel reinforcement used for the energy dissipating steel in the DRAIN model is shown in Figure 4.8 and in Table 4.4 in tabular form.

Figure 4.8: Stress-strain curve for ED steel in DRAIN model

It is important to note that the steel behaves the same in tension and compression. ED steel will behave linear elastically until yield at 60 ksi and 0.00207 strain. Then, two linear portions of the curve represent the plastic range until strain hardening begins at 0.04 strain. Lastly, the steel will fracture at an ultimate strain of 0.12.

Table 4.4: Stress-strain input for material properties of ED steel

ED Mild Steel(#3-0.375" dia.)		
Stress	*Strain*	*Damage Modes*
0	0	
60	0.00207	*yield*
80	0.015	
98	0.04	
107	0.08	
109	0.12	*ultimate*

4.3.1.2.Loading

The DRAIN Model is loaded in 5 different load segments. Segment 1 applies the pre-stress force. Segment 2 applies the gravity dead and live loads. Segments 3-5 consist of static displacement controlled monotonic loading to about 3% roof drift. Roof drift is measured as the relative displacement between the top floor and the base of the structure. Each segment is composed of 425 steps with 0.01 inches of displacement applied per step for an overall segment length of 4.25 inches. Since loading of the DRAIN model is displacement controlled, the displacement increases linearly each step. The roof drift versus load step can be seen in the top plot of Figure 4.9.

4.3.1.3.Important Output

Base Shear

The shears at the wall pier bases are output to use as a reference throughout loading. The shear at the base of the structure, V_b, can be calculated by Equation 4.1 where V_{101} is the shear force in Element 101 at the base of the left wall pier and V_{201} is the shear force in Element 201 at the base of the right wall pier.

$$V_b = V_{101} + V_{201} \tag{4.1}$$

The base shear is calculated for every step during every load segment and it does not increase linearly from step to step as shown in the bottom plot of Figure 4.9. It is important to understand the behavior of base shear because it directly corresponds to the loading and behavior of the structure. Also, it will be used as a scale to which strains in certain elements and other behaviors will be plotted against.

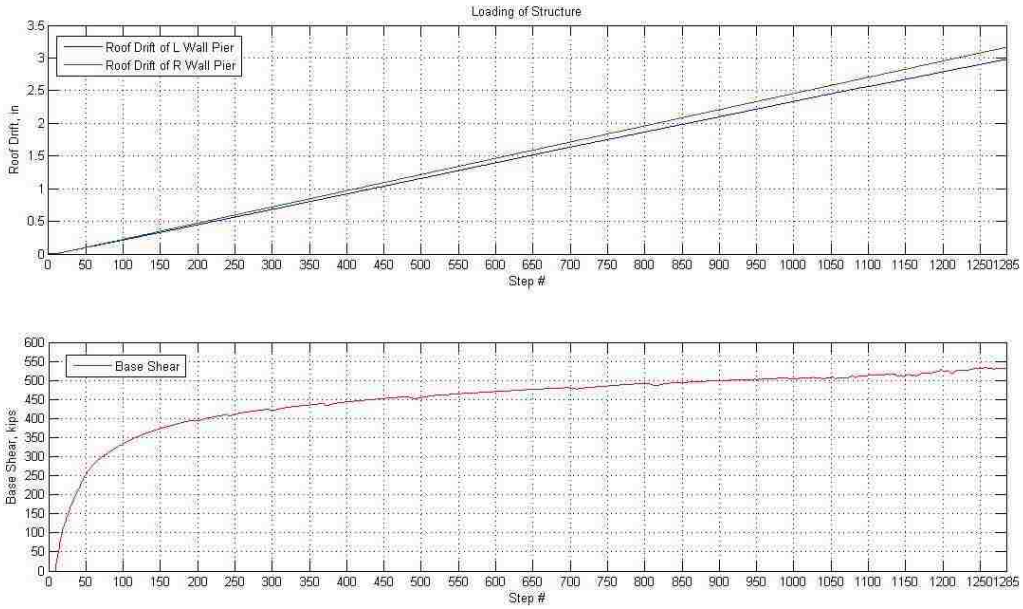

Figure 4.9: Loading of model: roof drift (top) and base shear (bottom)

Strain

Since the damage indices are sensitive to the change in strain, it is necessary to extract the strain in each sensor location from the model output. The elements used in the model are type 15, which assume that plane sections remain plane. Using this

assumption, the strain distribution over the cross section of the beam or wall pier can be computed by Equation 4.2. The variables are illustrated in Figure 4.10.

$$\varepsilon_1 = \varepsilon_c + \varphi x_1$$

$$\varepsilon_2 = \varepsilon_c + \varphi x_2 \tag{4.2}$$

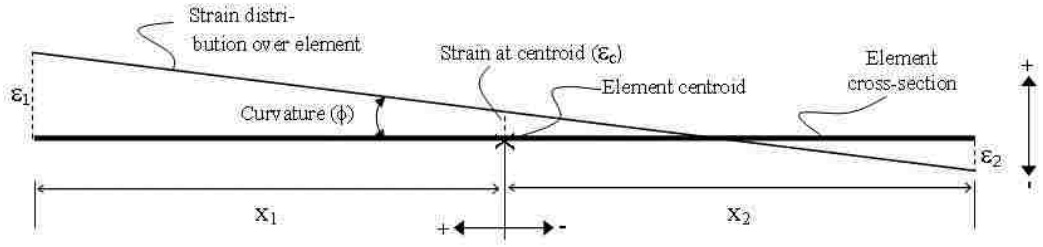

Figure 4.10: Strain distribution over cross section

For each element in the model, the DRAIN output provides the strain at the element centroid ε_c and the curvature φ at each load step. Tensile strains are positive and compressive strains are negative. Therefore the strains on at a particular location of interest, such as the location of a sensor in the large-scale testing or at the extreme compression fiber of the beam cross section, can be estimated using Equation 4.2.

4.3.1.4.Slaving

In order to model the connectivity between different elements in the structure, certain nodes are slaved to each other. It is important to examine how the elements are connected in the model to understand how the different components will react with each other. ED steel elements are only slaved to an interior beam node at one end and a wall pier node at the other. Concrete beam nodes in between these nodes are not slaved to the ED element since the ED bars are not bonded to the concrete that surrounds it. For

example, ED Nodes 14 and 18 are slaved to Wall Node 203 and ED Nodes 13 and 17 are slaved to Beam Node 308 as shown in Figure 4.11. Additionally, the wall pier element is slaved to the end beam element on the same story level (Wall Element 203 and Beam Element 311). Consequently, ED Node 18 is indirectly slaved to Beam Node 311 at the far right end of the coupling beam.

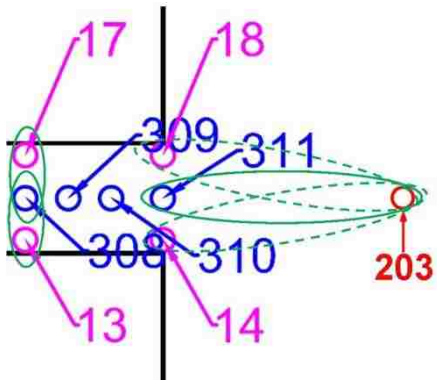

Figure 4.11: Slaving on 1st story of DRAIN model

These constraints are only displacement compatible and they account for the location of the node. For example, Figure 4.12a shows the x-displacement of the slaved nodes on the right side of the 1st story coupling beam (depicted in Figure 4.11). The x-displacement is exactly the same in the wall node and right end beam node (Nodes 203 and 311). However, the x-displacement is less in the bottom ED end node (Node 14) and greater in the top ED end node (Node 18). Additionally, the interior beam node experiences less lateral displacement than the end beam node. The x-displacement is greater in the bottom ED interior node (Node 13) and less in the top ED interior node (Node 17).

Similarly, the y-displacement for the same nodes is shown in Figure 4.12b. The y-displacement is exactly the same for the ED end nodes (Nodes 14 and 18) and beam end node (Node 203). It is also equal for the ED interior nodes (Nodes 13 and 17) and the beam interior node (Node 308). However, the y-displacement is less in the interior beam and interior ED nodes than the end beam and end ED nodes, but more than in the wall node. The differences in the y-displacement are due to the curvature of the elements.

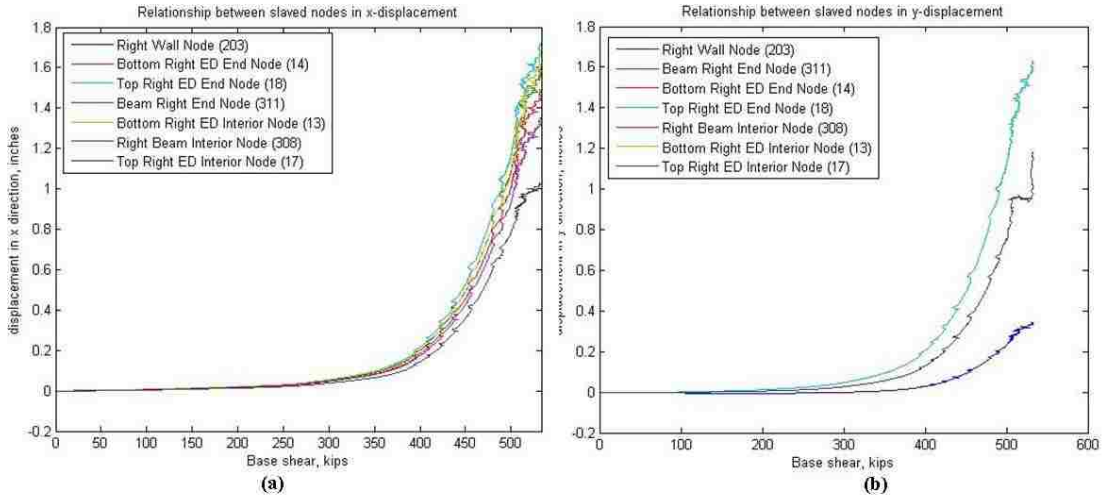

Figure 4.12: Displacement of slaved nodes on right side of 1st story beam in the (a) x-direction and (b) y-direction

Overall, slaving produces a linear x-displacement distribution and constant y-displacement across a plane of a cross section. Therefore, if the displacement along the cross section is examined at any load step in the model, the x-displacement distribution is perfectly linear from the compression ED, to the beam centroid, to the tension ED.

4.3.1.5.Strain Distribution across Cross Section

For design calculations, ACI-318 assumes that the strains in the concrete and reinforcement are linear across the cross section so that the strain at any point in the cross section is directly proportional to the neutral axis. It is known that the strain distribution across the concrete in the model is linear because of the element type used. However, it was uncertain if the ED steel strains also fit this linear distribution. Since x-displacements are linear across the cross section of the coupling beams cross section from the compression ED, to the beam centroid, to the tension ED, the strains should also be linear. Therefore the strain distribution was studied further to verify this by estimating strains from the linear x-displacement distribution and comparing the estimated strains to the strains directly output by DRAIN.

It is possible to estimate the strains in an element from the displacement by Equations 4.3. $x_{Node\,R}$ is the x-displacement of the first node in the element, $x_{Node\,L}$ is the x-displacement of the second node in the element, and L is the length of the element (12 inches for ED steel and 4.5 inches for beam).

$$\varepsilon = \frac{x_{Node\,R} - x_{Node\,L}}{L} \tag{4.3}$$

The estimated and calculated strain distributions for three different load steps were compared to ensure that the distribution remains linear across the cross section from the compression ED, to the beam centroid, to the tension ED throughout loading, even after damage. The first step was before any damage, the second step was after spalling and before yielding, and the third step was before crushing. Figure 4.13 shows the comparison for the right end of the 1st story coupling beam as well as the length of the elements and the formulas for calculating the estimated and actual strains.

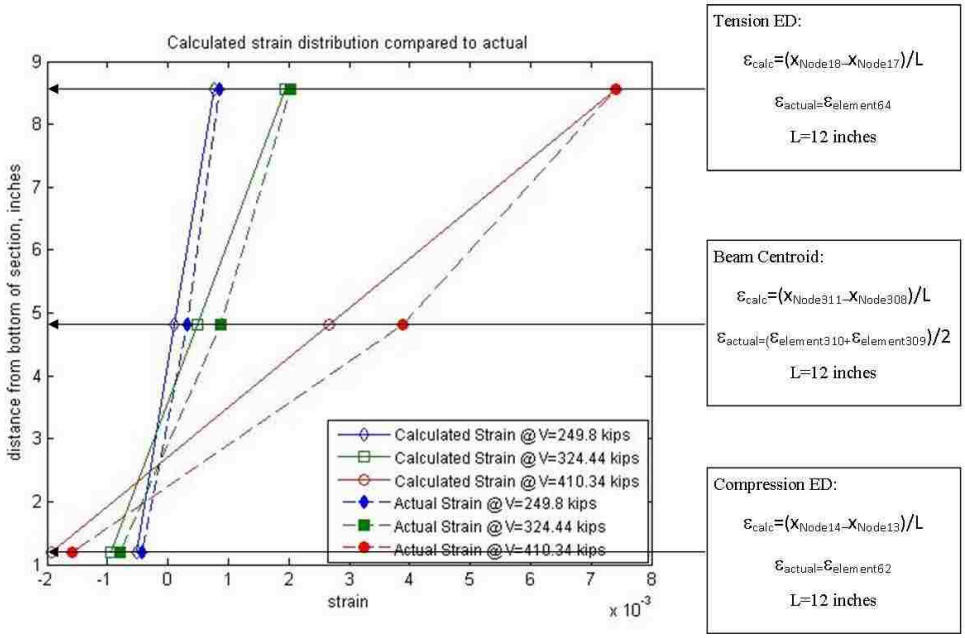

Figure 4.13: Calculated strain distribution compared to actual

The calculated strain distribution is perfectly linear across the cross section and the measured strain is not perfectly linear, but it is very close to the calculated strain. However, the magnitudes of the calculated strains are slightly lower than the measured strains in tension and higher than the measured strains in compression. Also, there is

more of a difference between calculated and measured strains for the beam elements than ED elements. This could be due to the complexity of the beam element compared to the ED element.

In conclusion, since the strain distribution including the ED steel is linear, it confirms that the entire beam cross section, composed of unconfined concrete, confined concrete, tension ED steel, and compression ED steel, acts as a unit.

4.3.2. Additional Model Assumptions

The DRAIN model uses several assumptions in order to model the desired global non-linear behavior of the coupled shear wall system. A majority of the non-linear behavior of the structure occurs at the coupling beams, particularly as gap opening at the beam ends. Therefore all of the tensile properties of the materials are chosen to limit all other forms of tensile deformations in the beam. This is accomplished in the model by using zero-tension concrete at the beam ends and linear-tension concrete in the remainder of the beam.

Zero-tension concrete sets the tensile strength of the concrete at the beam elements ends to zero so that the only non-linear behavior of the beam ends in tension is due to the gap opening. Strain in the end beam elements while in tension measures the gap opening through the percent elongation. Since the length of the end beam element L is 4.5 inches, the gap opening can be calculated throughout the loading by Equation 4.4.

The tensile strain in the concrete at the extreme tension fiber is ε_{cT}. On the 1st story, gap opening does not exceed one inch, even at the highest levels of roof drift.

$$\Delta_{gap} = \varepsilon_{cT} * L \tag{4.4}$$

Linear-tension concrete will induce linear behavior in the interior beam concrete elements in tension until the concrete fails at 40 ksi (0.009 strain). Since the strain in the concrete is not expected to exceed 0.009 until extremely high roof drifts, the tensile strength of the interior beam elements is virtually infinitely linear. Thus the dominant tensile non-linear behavior in the coupling beam will be limited to gap opening. Overall, the tensile behavior of the concrete in the interior sections of the coupling beams is not realistic and should not be used for damage detection.

4.3.3. Model Behavior Observed and Expected Damage

It is important to examine the behavior of the structure and its components in order to determine which elements are valid for damage detection, what type of damage is expected, and where damage will occur. The entire system can be divided into six main components: the base of the wall piers, the beam-wall interface at the left and right wall piers, the coupling beam concrete, the energy-dissipating rebar, and the PT tendons. The DRAIN model outputs are analyzed to determine where high strains are concentrated and where damage will occur.

4.3.3.1.Wall Pier Base

Since the lateral force is being applied from left to right, the left sides of the wall piers are in tension and the right sides are in compression. As a result, the highest compressive strains occur at the right toes of the wall pier bases. Compressive strains are higher in the left wall pier; therefore the unconfined concrete will spall at the right toe of the left wall pier around 410 kips before the right wall pier spalls around 480 kips.

4.3.3.2.Beam-Wall Interface

In order to analyze the behavior of the wall piers at the beam-wall interface there will be strain gauges located on the vertical #6 steel reinforcement during the large scale testing. The locations of these strain gauges on the vertical wall reinforcement correspond to a specific location in the DRAIN model 41.25 inches from the centroid of the wall pier element. Each wall element is divided into segments at which the strain and curvature are measured at. For example, the element from Node 101 to Node 102 is divided into four sections spaced 7.2”-7.2”-9.6”-9.6” as shown in Figure 4.14. Then, the element from Node 102 to Node 103 is divided into two sections spaced 16.8”-16.8”. Lastly, the remaining wall elements in the wall are divided into two equal segments of 24”. The strain in the segment at which each strain gauge is located is used in Equation 4.2 with x=-41.25 inches and x=41.25 inches to find the strain at the location of each gauge on the left and right wall piers respectively.

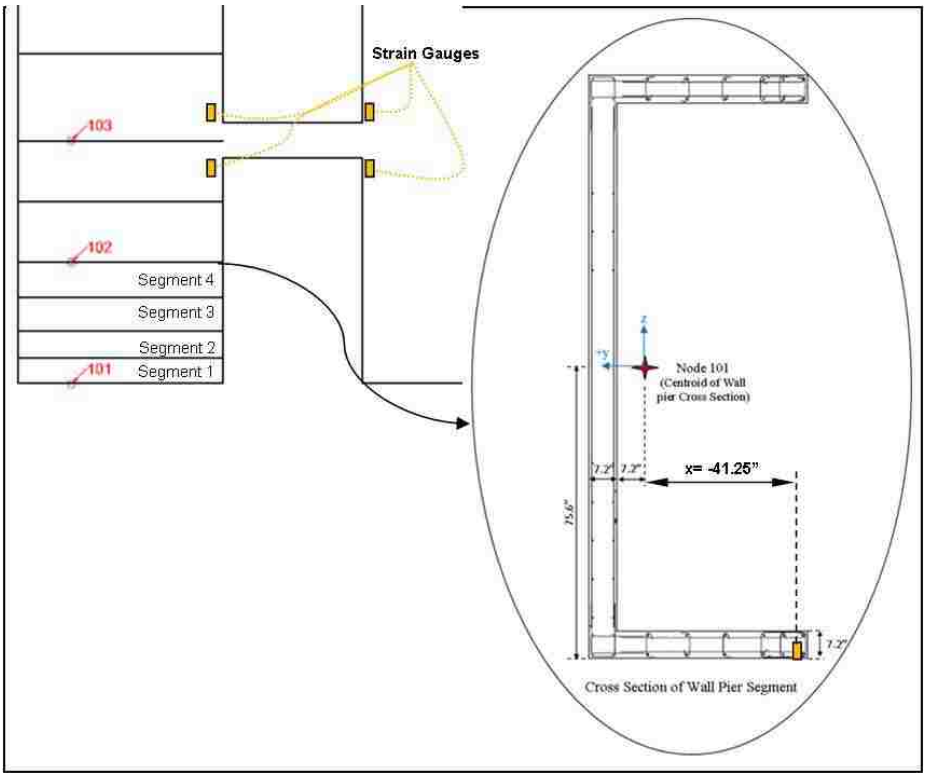

Figure 4.14: Wall pier element segments and cross section (Cross section adapted from drawings courtesy of Steven Barbachyn)

Figure 4.15a shows the strain-base shear relationship of the left wall pier strain gauges. At the location of the strain gauges, the wall is in compression. As the lateral displacement increases, so do the magnitudes of compressive strains at the strain gauges. Additionally it can be seen that there are larger strains closer to the base since the strain at the 1st floor SG's are greater than the strains at the 2nd floor SG's which are greater than the strains at the 3rd floor SG's.

The strain-base shear relationship of the right wall pier at the location of the strain gauges is shown in Figure 4.15b. As the lateral displacement increases, the tensile strains increase. Since the tensile properties for concrete are not realistically modeled, the strain

gauges in the right wall pier will be disregarded for damage detection using the simulation data.

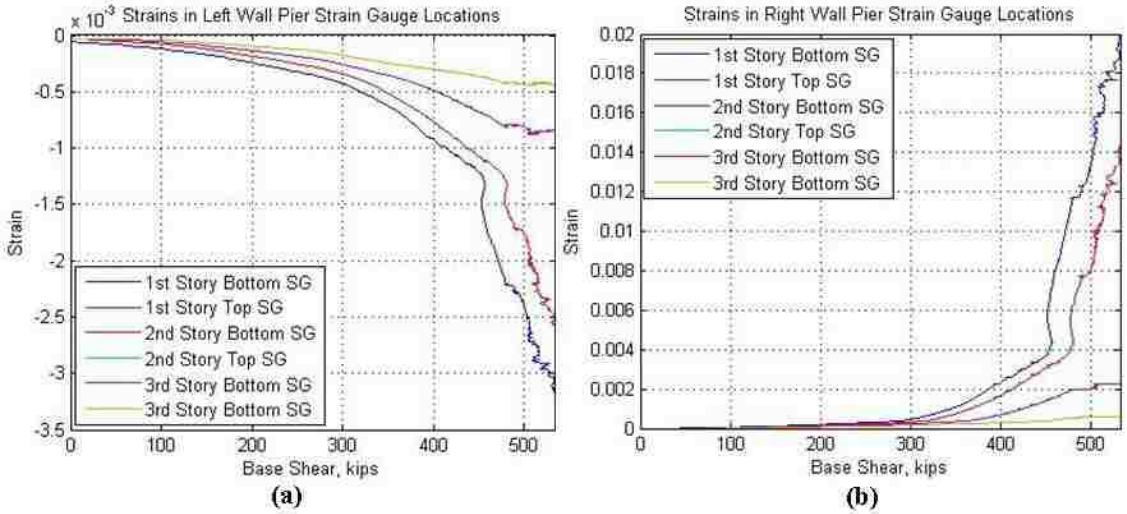

Figure 4.15: Strain in wall pier strain gauge locations: (a) left wall pier and (b) right wall pier

The corresponding base shears at which each of the possible damage modes occurs at each strain gauge is summarized in Table 4.6. Spalling occurs in at the location of the strain gauges below and above the 1st story beam-wall interface and below the 2nd story beam-wall interface.

4.3.3.3.Coupling Beam Concrete

The cross section of a coupling beam in the DRAIN model and large-scale model is shown in Figure 4.16a and Figure 4.16b, respectively. The total depth of the beam is 9.625 inches and the width is 7.25 inches.

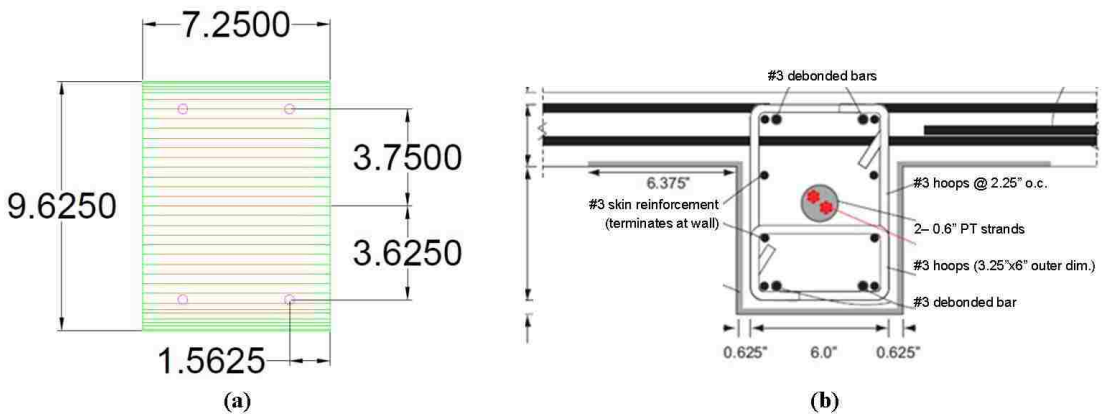

Figure 4.16: Cross section of coupling beam: (a) in DRAIN model and (b) for large scale testing (Courtesy of Steven Barbachyn)

In the large scale model to be tested, the strain gauges will be located along the #3 mild steel reinforcement in the coupling beams. Therefore, the strains at the level of the mild steel reinforcement above and below the centerline of the beam are calculated using Equation 4.2 to use in the damage detection techniques.

In order to examine the behavior of the concrete in the coupling beams where data will be collected in the large-scale test, the strain in each element of the beam at the level of the reinforcement is plotted versus the base shear in Figure 4.17 for the 1st story. The top right corner of the beam (Element 310t) and bottom left corner (Element 301b) have the highest compressive strains which will induce unconfined concrete spalling and confined concrete crushing. Initially, the entire beam is in compression due to the post-tensioning force. After the PT force is overcome, a compressive strut forms in the beam. The strains in each of the interior beam elements in the compressive strut are much lower than the strains in the end beam elements and the ED steel elements. These interior beam

elements do not reach the strain limits for spalling or crushing; therefore they will not experience material failures.

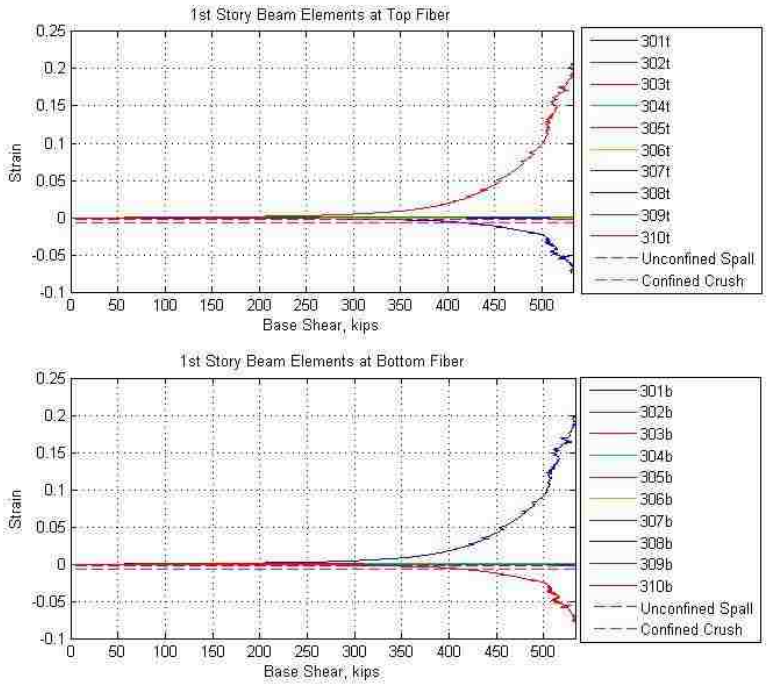

Figure 4.17: Strains in 1st story coupling beam elements

Since the loading is monotonic, once a portion of the beam goes into tension, it remains in tension for the remainder of the loading. However, tensile properties of the concrete are not realistically modeled in order to limit all non-linear tensile behavior in the beams to gap opening at the ends. As a result, only the beam elements in compression can be used for damage detection purposes. In order to examine which elements are valid for damage detection purposes, the strains in all of the linear-tension concrete (interior) beam elements on the 1st story are shown separately in Figure 4.18. The only elements to be in tension are the bottom left (302b) and top right (309t), while

the rest of the beam is entirely in compression. Consequently, these elements are not valid for damage detection.

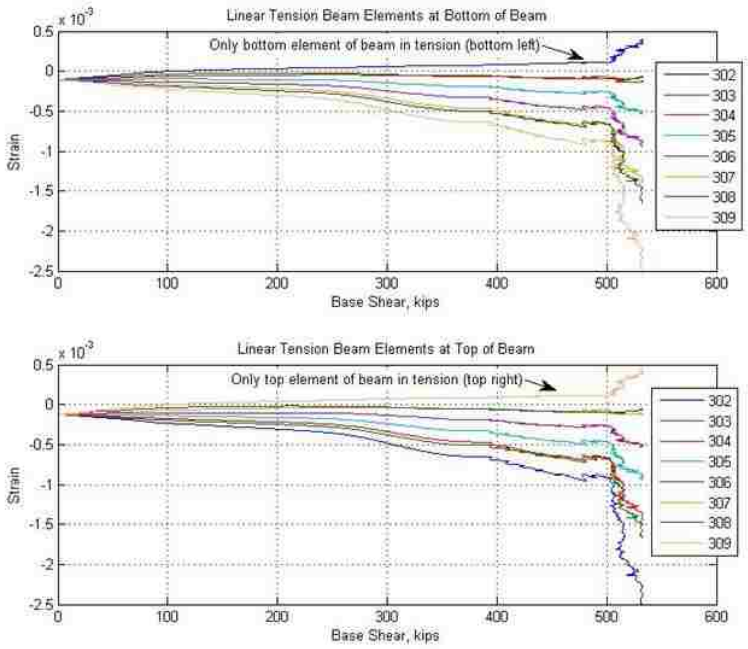

Figure 4.18: Linear tension beam concrete elements on 1st story

Similar behavior is exhibited by the 2nd Story and 3rd Story coupling beams. However, at higher stories compressive strains decrease and tensile strains increase. This behavior is because there will be larger gap openings at higher stories as the beams move with the curvature of the deformed wall piers. As the gap opens, it induces a higher strain in the ED steel in tension and causes the outermost unconfined concrete to spall at the corners in compression. However, gap opening causes less strain to be transferred into the coupling beam concrete in compression from the wall pier; therefore there are lower compressive strains in the concrete at higher stories as the lateral loads increase.

Since the portions of the cross section at which the highest compressive strains occur are at the extreme compression fibers, the strains at the outermost fiber of the unconfined concrete cover and confined concrete core were examined to find the shears at which damage is first initiated. In accordance with the damage modes described in Section 3.1, the spalling of the concrete cover occurs when the extreme compression fiber in the unconfined concrete reaches its maximum compressive strength at 0.002 strain and ultimate of the concrete cover occurs when the extreme compression fiber in the unconfined concrete reaches an ultimate strain of 0.004. Also, the crushing of the concrete core occurs when the extreme compression fiber in the confined concrete reaches its maximum compressive strength at 0.007 strain. The values of base shear at which each of these damage modes occur are summarized in Table 4.6.

4.3.3.4.Energy-Dissipating Steel Reinforcement

The energy-dissipating (ED) steel reinforcement is modeled realistically in tension and compression. Therefore, all ED steel elements are valid for damage detection purposes. The strains in the ED elements on the 1st, 2nd, and 3rd stories are shown in Figure 4.19. All ED bars are expected to yield during the loading of the structure. Bars ED 1 and ED 2 are in tension while bars ED 3 and ED 4 are in compression. The tension bars will yield well before the compression bars yield. Additionally, the bars in tension yield first at higher stories while the bars in compression yield first at the lower stories. The values of base shear at which each of the ED bars yield are summarized in Table 4.6.

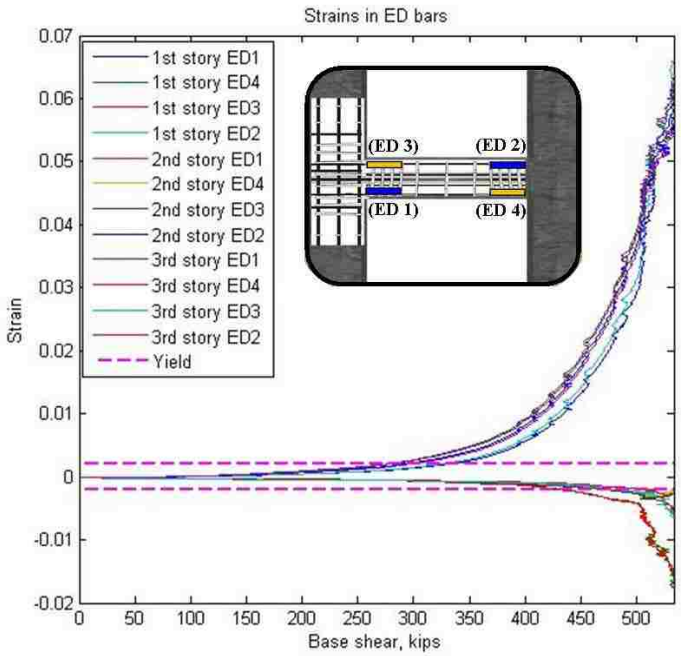

Figure 4.19: Strains in ED steel

4.3.3.5.Post-Tensioning Tendons

The post-tensioning steel tendons are modeled in DRAIN by Element 1 objects which are inelastic truss elements. The PT tendons used on the first story differ from the tendons used in the remainder of the structure. First story PT tendons have a cross sectional area of 0.434 in^2 and the remaining tendons have a cross sectional area of 0.306 in^2. Both tendon types' modulus of elasticity are 28,500 ksi and yield strength are 166 ksi. The tendons will behave elastically and experience strain-hardening. The strain hardening ratio is 0.75 for all tendons, which is the ratio of the post-yield tangent to the initial elastic tangent on the stress-strain curve. Since the elastic modulus is 28,500 ksi, the post yield modulus is 21,375 ksi.

DRAIN output provides the total extension as well as the plastic extension throughout each load step. In this model the plastic extension is zero throughout the loading therefore it can be assumed that the tendons behave linear elastically.

The stress in the PT strands at each story output by DRAIN is plotted against base shear in Figure 4.20. The horizontal dashed line indicates the yield strength of the tendons. First, the PT strands on the 3rd story will yield, followed by the 2nd story and 1st story at higher levels of roof drift. The stresses in the strands continue to increase due to strain hardening. Values of base shear at which the PT tendons yield at each story are summarized in Table 4.6.

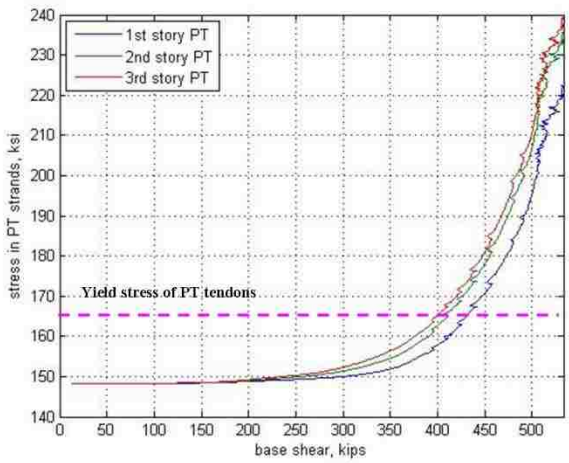

Figure 4.20: Stress in post-tensioning strands

After the strands in the structure yield, they will experience some permanent deformations. As a result, the PT tendons will lose their "self-centering" abilities that restore the structure back to its initial position after large lateral displacements. Additionally, the ED rebar in tension have already yielded and the unconfined concrete cover has completely spalled and reached its ultimate strain when the PT tendons yield.

Therefore, the stiffness of the coupling beams is already greatly reduced and the yielding of the PT reduces the stiffness a significant amount more. Consequently, is not ideal to have the PT strands yield because the structure no longer performs as it should; thus rendering it failed.

4.3.4. Analysis of Stiffness of Structure

The stiffness of the coupling beams directly contributes to the stiffness of the overall structure and changes in stiffness are indicative of damage. Therefore, the changes in stiffness of the coupling beams were further examined by analyzing the moment-rotation relationship of each beam as well as the depth of the gap opening. Also, the global stiffness was evaluated from the behavior of the base shear throughout loading.

4.3.4.1.Moment-Rotation

In a similar study by Weldon and Kurama (2007) on post-tensioned coupled shear wall systems that use angles at the beam ends to dissipate energy rather than the debonded rebar, the subassembly modeled goes through five states: (1) decompression, (2) tension angle yielding, (3) tension angle strength, (4) PT tendon yielding, and (5) confined concrete crushing. The moment-rotation behavior is defined by the five states as shown in Figure 4.21a. Changes in the slope of the moment-rotation indicate that the beam has become less stiff.

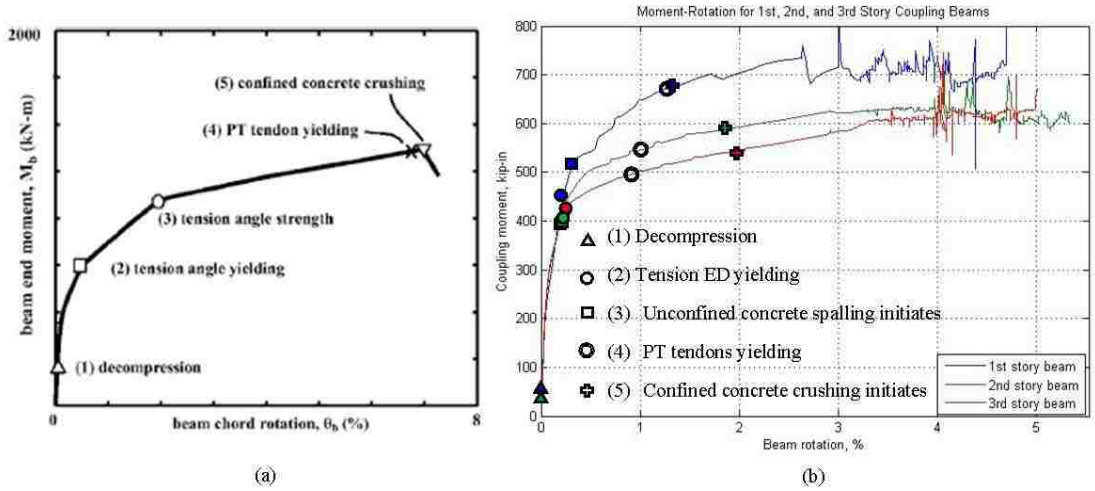

Figure 4.21: Moment vs. chord rotation for: (a) coupling beam in similar PT coupled shear wall assembly (Weldon and Kurama 2007) and (b) 1st, 2nd, and 3rd story coupling beams of proposed coupled shear wall structure

The post-tensioned coupled shear wall system currently being studied exhibits similar changes in stiffness as show in Figure 4.21b. The states for this structure, indicated in the figure, include: (1) decompression, (2) yielding of tension ED steel, (3) initiation of unconfined concrete cover spalling, (4) yielding of PT strands, and (5) initiation of confined concrete crushing. Decompression is when the pre-stress force is overcome and gap opening begins. Unconfined concrete spalling is initiated when the extreme compression fiber of the unconfined concrete reaches its maximum compressive strength. Tension ED steel and PT tendons yield when the steel reaches its maximum tensile strength of 60 ksi and 166 ksi respectively. Lastly, the confined concrete crushing is initiated when the extreme compression fiber of the confined concrete core reaches its maximum compressive strength.

The moment capacity of each beam, M_b, was calculated by Equation 4.7 where V is the vertical shear at the end of the coupling beam output from DRAIN and L is the length of the coupling beam (38.5 inches). The chord rotation θ was calculated by Equation 4.8 where y_L and y_R are the vertical displacement of the left and right end of the beam respectively.

$$M_b = \frac{VL}{2} \tag{4.7}$$

$$\theta = \frac{|y_L - y_R|}{L} \tag{4.8}$$

4.3.4.2.Gap Opening

Additionally, it is important to study the behavior of the gap opening to determine how gap opening affects the stiffness of the beam. According to Weldon and Kurama (2007), before gap opening occurs, the PT strands create initial lateral stiffness in the structure. Then, gap opening results in geometric reduction in lateral stiffness to allow the system to undergo large nonlinear rotations without significant damage. When this occurs, the only damage will be minor which includes the yielding of the ED steel and small amounts of spalling of the concrete cover at beam ends. However, the effect of gap opening on the lateral stiffness is small until the gap extends over a significant portion of the beam's depth. From past experiments, when the gap opening depth was beyond 50% of the total beam depth, there was a significant reduction in stiffness (Weldon and Kurama 2007).

Gap opening in the simulation structure can be calculated in the DRAIN model by the zero-tension concrete elements at the beam ends in tension. The total depth of the gap opening is monitored by the contact depth. The contact depth is the depth of the beam still in contact with the wall pier, which is the distance from the compression face of the beam to the neutral axis. The contact depth versus the beam rotation for the right end of each story's coupling beam is shown in Figure 4.22. After decompression, the gap quickly extends to more than 70% of the cross section. After yielding of the rebar and spalling of the unconfined concrete, the gap extends more gradually to nearly 80% of the cross section before it remains relatively constant for the remainder of loading. Based on this observed behavior, it is apparent that the gap opening most affects the stiffness of the beam around 0.5% beam rotation, which is after decompression and before yielding and spalling. After about 0.5% rotation, the gap opening has reached its maximum depth.

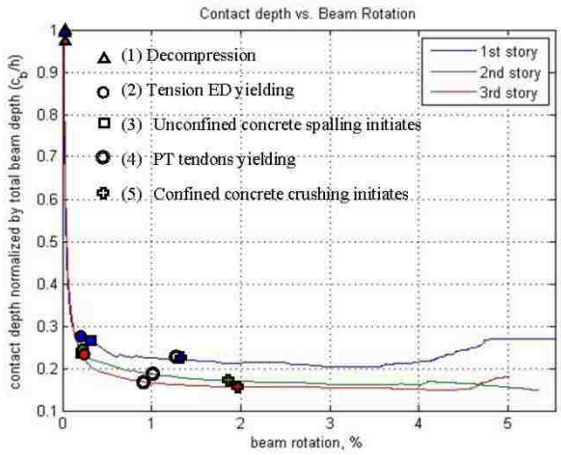

Figure 4.22: Contact depth vs. beam rotation for the right end of the 1st, 2nd, and 3rd story coupling beams

4.3.4.3.Base Shear

Although examining the moment capacity and rotation of the coupling beams is helpful to observe how yielding, spalling, and crushing affect the stiffness of each beam, it does not necessarily show how the damages affect the global stiffness of the entire structure. The overall global stiffness of the structure can be observed by the base shear throughout loading. Figure 4.23a shows the variation of base shear over loading for the portion between 350 kips and 510 kips of base shear. At base shear values of 395, 410, 425, 441, 457, 481, and 490 kips, there is some unloading or decrease in the load before it increases again. At each of these steps, a reduced value of base shear is needed to displace the structure the same amount as previous steps. In order for the force P to decrease while the displacement Δ remains constant, there must be a reduction in stiffness, K, of the overall structure according to the relationship in Equation 4.6. As a result, it can be inferred that the structure experiences some type of failure that has a global impact on the behavior and overall stiffness of the structure.

$$P = K \cdot \Delta \tag{4.6}$$

It is possible to correlate the probable causes of damage by reexamining the moment-rotation of the coupling beams at each of the steps at which a global reduction in stiffness occurs. Figure 4.23b shows the moment-rotation of the coupling beams and the dashed vertical lines indicate the beam rotation at which the global reduction in stiffness occur.

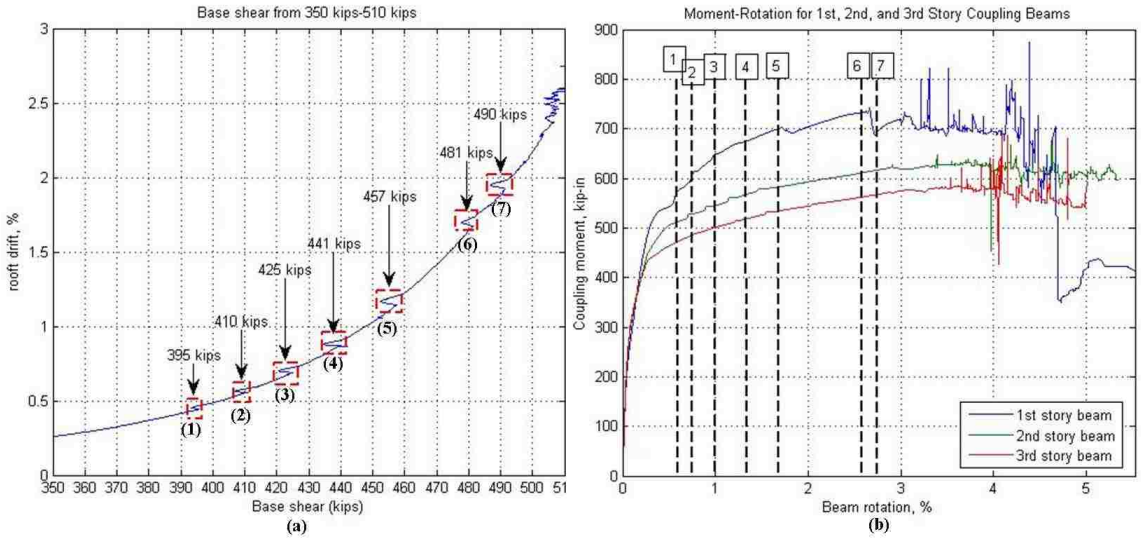

Figure 4.23: Reduction in global stiffness shown by: (a) base shear and (b) moment capacity

Based on known damages in the structure, the most probable damages capable of producing a global reduction in stiffness are summarized in Table 4.5**Error! Reference source not found.**. Damages significant enough to have a global impact include gap opening, spalling at the wall pier toes, concrete crushing or reaching ultimate in the coupling beams, PT tendons yielding in tension, and ED steel yielding in compression. There is no way of verifying that these are indeed the causes of the reduction in global stiffness, but they are the best estimate given in the information available.

In the scope of this thesis, the evaluation of the damage indices for the detection of local damages of yielding, spalling, and crushing will only be considered. Therefore, false negatives in the damage indices at each of these global damages is not a concern in this research, but should be examined in future work.

Table 4.5: Global Damages

#	V_b Range (kip)	Roof Drift Range (in)	Damage Associated
1	395.68-393.34	0.4459-0.4821	Gap opening reaches maximum depth in 1st ,2nd,and 3rd story
2	410.92-406.86	0.5544-0.5810	Left wall pier UC spall at right toe, 2nd & 3rd story PT yield, 1st & 2nd story UC ultimate of entire cover
3	425.2-420.7	0.6873-0.7237	3rd story UC ultimate of entire cover
4	441.98-435.2	0.8668-0.9225	1st story concrete core crush, 1st story ED yield in compression, 1st story PT yield
5	457.58-452.62	1.1432-1.2039	2nd story concrete core crush
6	481.34-477.76	1.6695-1.7318	Right wall pier UC spall at right toe ,top left 2nd story ED yield in compression
7	490.04-486.92	1.9262-1.9790	Bottom right 2nd story & top left 3rd story ED yield in compression

4.4. Application of Damage Indices on Simulation Data

To validate the proposed damage detection methods, strains from the DRAIN-2DX simulation model were extracted and the damage indices were applied to the data. The damage indices α and β were evaluated at six sensor locations on each story, indicated in blue in Figure 4.24, for a total of 15 sensor pair combinations per story. The locations of the elements being analyzed in the DRAIN model are shown superimposed onto the corresponding locations of sensors installed on the large scale test specimen. It is important that the elements analyzed using the simulation data can be related to the actual structure in order to extend these methods to experimental testing for validation.

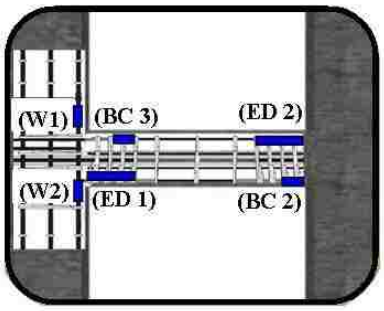

Figure 4.24: Sensor locations

ED 1 and ED 2 are ED steel elements in tension, BC 1 and BC 3 are beam concrete elements in compression at the level of the ED steel, and W1 and W2 are wall pier elements in compression at the location of strain gauges on the beam-wall interface rebar. All sensor pair combinations were evaluated at each story for a total of 45 damage index plots (located in Appendix B); however only representative cases will be presented from the 1st story. Ideally, the sensor pairs at any given story should detect damages in the manner described in Section 3.4 using the flow charts in Figure 3.5 and Figure 3.6. The expected damage modes and corresponding locations in the structure are summarized in Table 4.6.

Table 4.6: Expected Damage Modes and Locations

Story	Damage Mode	Sensor	Base Shear at which damage is initiated (kips)
1st Story	Concrete Cover Spalls	BC1	316
		BC2	312
		W1	504.7
		W2	471.4
	Steel Yields in Tension	ED1	332
		ED2	326.7
	Steel Yields in Compression	ED3	436.5
		ED4	437
	Concrete Cover Ultimate Begins	BC1	380
		BC2	374.7
	Concrete Core Crushes	BC1	445.9
		BC2	434.6
	PT Yields in Tension	PT1	434
2nd Story	Concrete Cover Spalls	BC1	299.6
		BC2	298
		W1	--
		W2	504.7
	Steel Yields in Tension	ED1	299.6
		ED2	295
	Steel Yields in Compression	ED3	475
		ED4	487.6
	Concrete Cover Ultimate Begins	BC1	370.6
		BC2	365.6
	Concrete Core Crushes	BC1	462
		BC2	456.1
	PT Yields in Tension	PT2	411
3rd Story	Concrete Cover Spalls	BC1	290
		BC2	288.4
		W1	--
		W2	--
	Steel Yields in Tension	ED1	283.1
		ED2	279.4
	Steel Yields in Compression	ED3	490
		ED4	515.9
	Concrete Cover Ultimate Begins	BC1	371.2
		BC2	366.9
	Concrete Core Crushes	BC1	466.2
		BC2	460.8
	PT Yields in Tension	PT3	403.4

4.4.1. Yielding of ED Reinforcement

Two sensor pairs from the 1st story will be presented in this section to demonstrate the proposed damage indices' ability to detect and localize the yielding of tension ED reinforcement. Similar behavior is exhibited by the damage indices for all sensor pairs including those on the 2nd and 3rd stories. All of the damage index plots for the detection of ED steel yielding can be found in Appendix B.1 for the 1st story and Appendix B.4 for the 2nd and 3rd stories.

The two ED bars in tension on the 1st story are compared in Figure 4.25 using the damage index specified. It is expected that this sensor pair is capable of detecting yielding in both tensile ED bars because both sensor locations become damaged by yielding. ED 2 yields around 326 kips and ED 1 yields around 332 kips, as indicated by the dashed vertical lines. There is an increase in the change in strain when ED 2 yields as seen in the top plot of Figure 4.25. This increase in strain for the same amount of applied force is due to the steel softening. As a result, the slope of α increases and β forms a positive peak at yielding of ED 2. Similarly, the change in strain in ED 1 increases when ED 1 yields. However this generates a decrease in the slope of α and a negative peak of β.

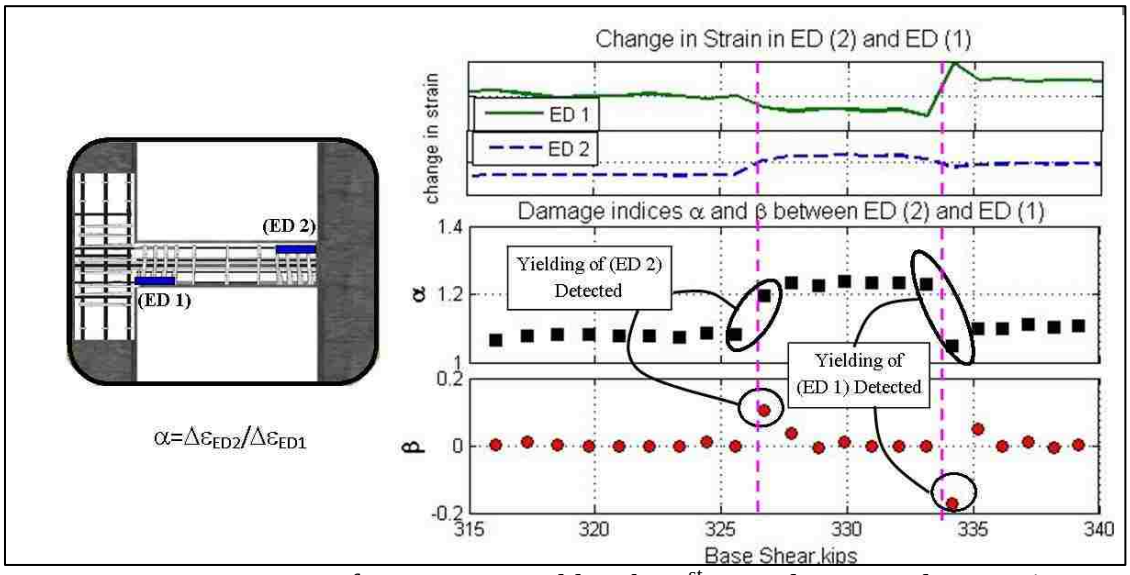

Figure 4.25: Detection of tension ED yielding by 1st story damage index ED2/ED1

Figure 4.26 compares an ED bar sensor (ED 2) and the beam concrete element directly below it in the cross section (BC 2) using the damage index indicated. The vertical dashed lines indicate when yielding occurs in ED 2 and ED1. When ED 2 yields there is an increase in the change in strain in ED 2 due to the softening. Simultaneously, the change in strain in BC 2 decreases due to the movement of the neutral axis. This causes an increase in the slope of α and a positive peak of β. Then, when ED 1 yields, the change in strain decreases in ED 2 and increases in BC 2 since ED 2 is opposite to the damage on the beam. This initiates a decrease in the slope of α and a positive peak of β. It is also significant to note that the magnitude of β is larger in the detection of ED 2 than ED 1 yielding because it shows that the index is capable of damage localization. Similarly, damage index ED1/BC2 has a greater magnitude of β in the detection of yielding of ED 1 (seen in Appendix B.1).

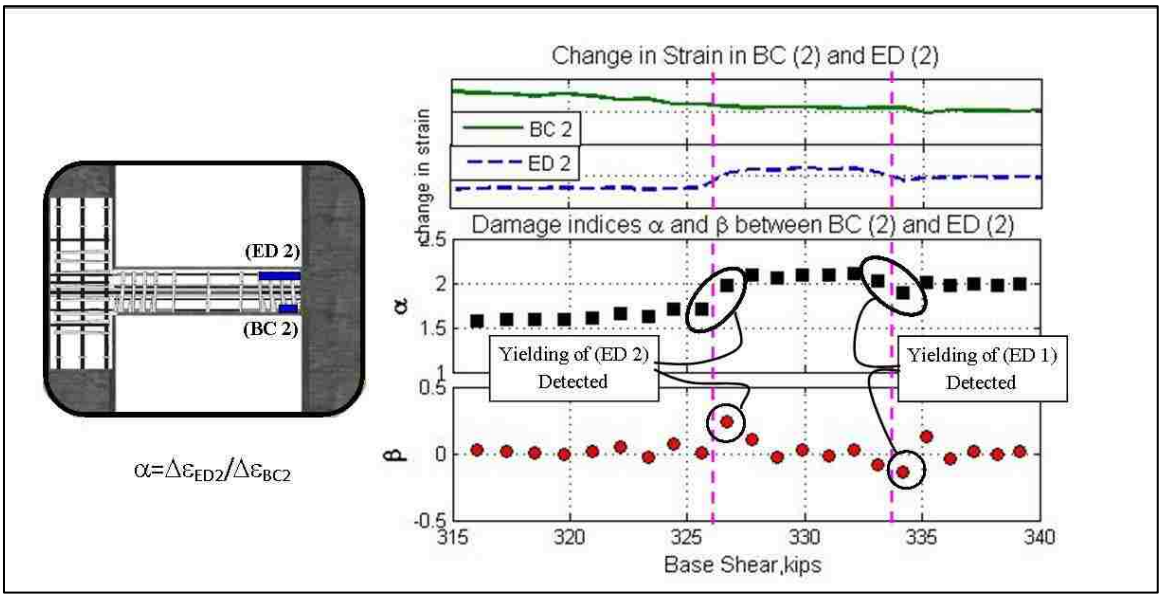

Figure 4.26: Detection of tension ED yielding by 1st story damage index ED2/BC2

Overall, the damage indices at each story level were capable of detecting yielding of the tension reinforcement and localizing it to that story level. For example, the damage indices from the 1st story successfully identified yielding of the 1st story ED rebar; but they did not identify yielding of the 2nd or 3rd story ED rebar. Additionally, some sensor pairs were able to localize yielding to a specific sensor location.

4.4.2. Spalling of Unconfined Concrete Cover

Two sensor pairs from the 1st story are presented in this section to demonstrate the proposed damage indices' ability to detect and localize the spalling of the concrete cover. The remainder of the 1st story damage index plots for spalling can be found in Appendix B.2 and the 2nd and 3rd story plots can be found in Appendix B.4.

The spalling of the unconfined concrete cover was best detected when the damaged beam concrete element was included in the sensor pair. For example, Figure

4.27 shows the detection of spalling in BC 2 with sensor pair BC3/BC2. Both sensors are concrete; therefore they are most affected by this damage mode. When spalling is initiated at the extreme compression fibers of the unconfined concrete cover, there is an increase in the change in strain in BC 2. This is due to the softening of the concrete after it meets its maximum compressive strength. BC 3 is not greatly affected directly by the spalling of BC 2 because of its location in comparison to the minor damage. As a result, spalling is detected by a decrease in the slope of α and a negative peak of β.

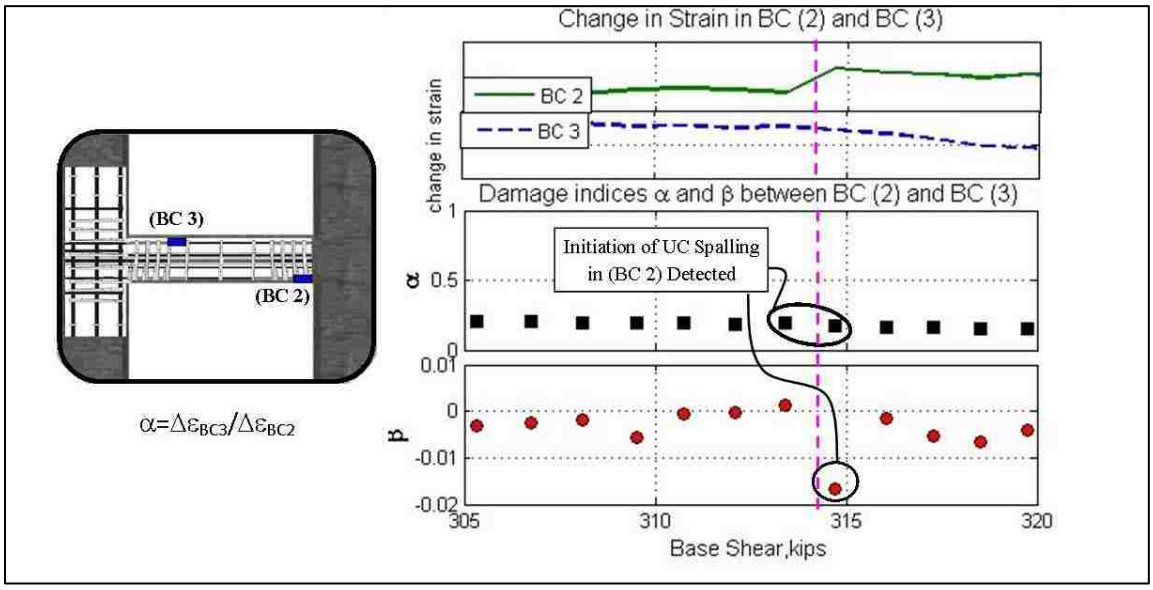

Figure 4.27: Detection of concrete cover spalling by 1st story damage index BC3/BC2

Similarly, the spalling of BC 2 was detected by sensor pair ED2/BC2 as shown in Figure 4.28. There is an increase in the change in strain in BC 2 once it begins spalling, which results in a decrease in the change in strain in ED 2. Therefore, spalling is detected by a decreasing slope of α and a negative peak of β.

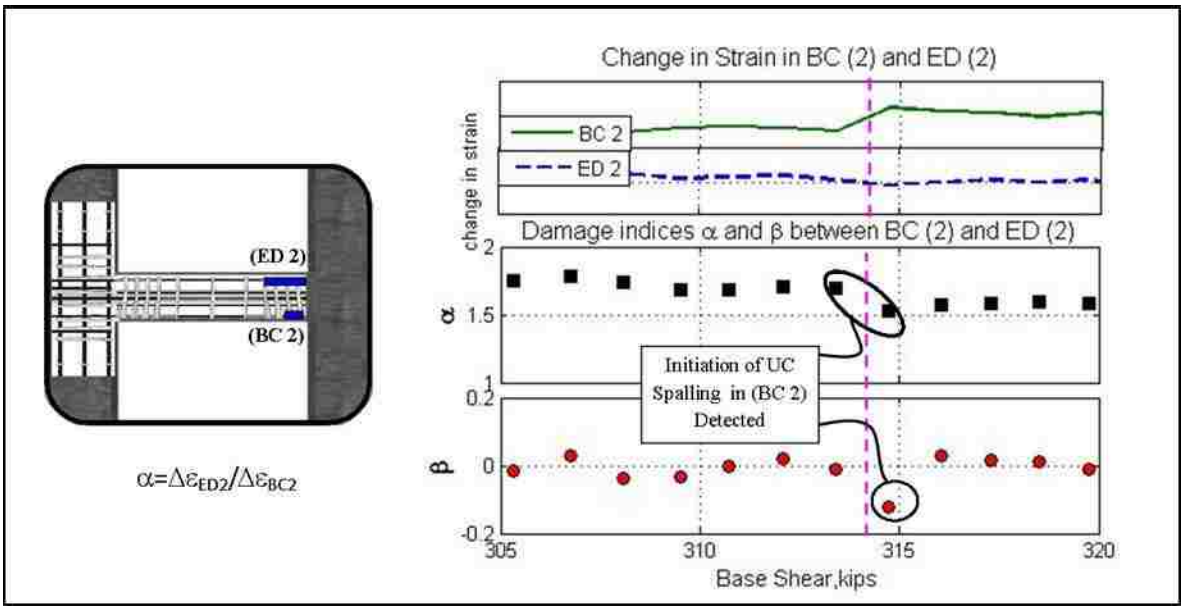

Figure 4.28: Detection of concrete cover spalling by 1st story damage index ED2/BC2

Overall, spalling was detected by sensor pairs that included the damaged beam concrete element. This is another example of the damage localization capabilities of the damage indices. However, spalling was not detected well in the 2nd and 3rd stories. Possible causes for spalling to not be well distinguished from the damage index plots for the 2nd and 3rd stories include that it directly followed the ED steel yielding and that it induced a very small reduction of strength of the concrete cover. Yielding causes an increase in the change in strain in the ED and a decrease in the change in strain in the concrete, but spalling causes an increase in the change in strain in the concrete and a decrease in the change in strain in the ED bars. Therefore when spalling occurs directly after yielding, the effects may cancel each other out, leading to a false negative. Also, in the model spalling only led to less than a 2% reduction in strength of the concrete cover material; therefore it does not affect the beam as strongly as other damages. This is

something that could be examined further in experimental testing and other simulation models.

4.4.3. Crushing of Confined Concrete Core

Two examples of detection of crushing on the 1st story are presented in this section, but all other damage index plots for the 1st story can be found in Appendix B.3 and for the 2nd and 3rd stories in Appendix B.5. Most damage indices detected crushing of the concrete core in the manner described in Section 3.4.

Two concrete beam elements, BC 2 and BC 3, are compared using the damage index indicated in Figure 4.29. BC 3 remains undamaged throughout the entire loading; however the concrete in beam element adjacent to BC 3, BC 1, will crush. The dashed vertical lines indicate when crushing of the confined concrete core initiates in BC 2 after 439 kips and BC 1 after 442 kips. When BC 2 begins to crush the change in strain in the element increases due to the damage, causing a decrease in α. Consequently, this creates a negative peak in β. Then, when BC 1 begins to crush, the change in strain in BC 3 increases to compensate for the loss of strength in the adjacent element. BC 3 is sensitive to the crushing of BC 1 because of its proximity to the large reduction in the strength of the concrete core. As a result, the crushing of BC 1 is detected by the increasing slope of α and positive peak in β.

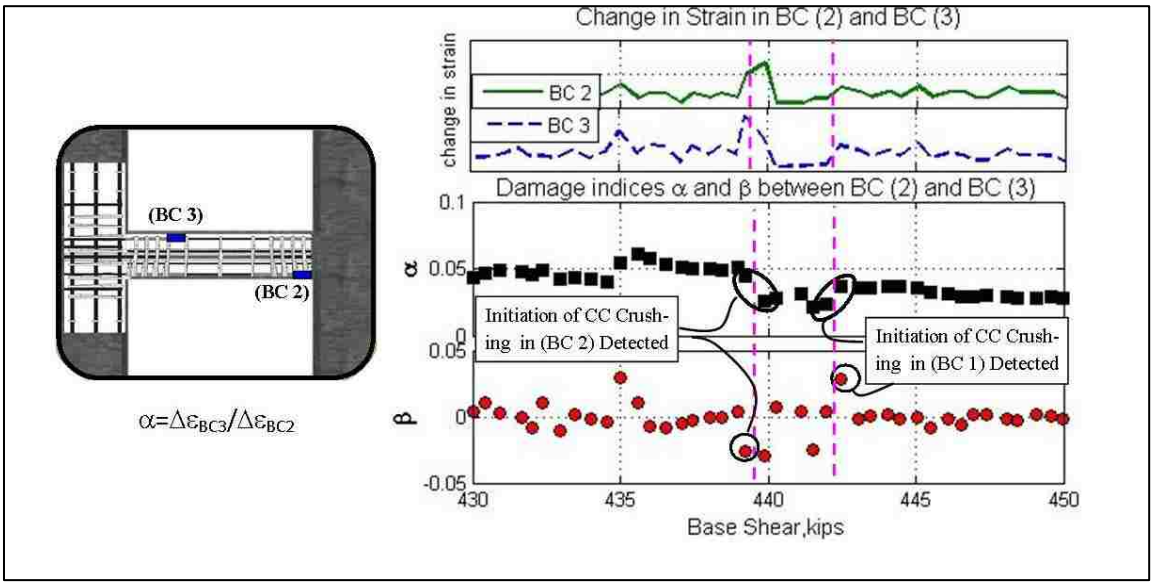

Figure 4.29: Detection of concrete core crushing by 1st story damage index BC3/BC2

Also, damage index ED1/BC3 is capable of detecting the crushing in BC 1 and BC 2 as seen in Figure 4.30. When BC 2 crushes, the reduced strength causes an increase in the change in strain in the element. This causes redistribution within the compression strut in the beam which initiates a decrease in the change in strain in BC 1 and BC 3. Consequently, there is an increase in α and a positive peak of β. Then, when BC 1 crushes, BC 3 is forced to take on the additional loads; therefore BC 3 experiences an increase in the change in strain. This results in a decreasing α and negative peak in β. It is significant to note that the magnitude of β is greater at the detection of BC 1 crushing. Therefore this proves that damage localization was achieved because the sensor pair locations BC 3 and ED 1 are the closest sensors to BC 1.

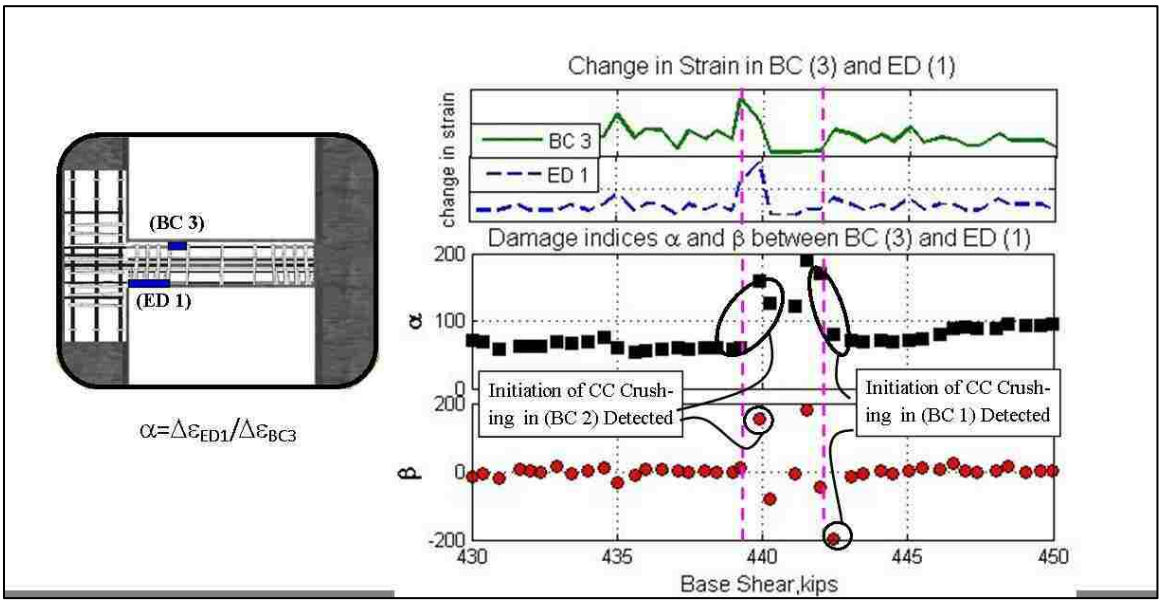

Figure 4.30: Detection of concrete core crushing by 1st story damage index ED1/BC3

In summary, the initiation of crushing of confined concrete core was detected more effectively than spalling of the unconfined concrete cover at all three story levels. This is because the crushing of the core leads to a 20% reduction in the strength of the concrete core material as opposed to the 2% reduction in strength from spalling. Therefore the structural response and damage indices are more greatly affected by crushing than spalling. Crushing of the concrete core was successfully localized to each story level and even to a specific sensor location in some cases.

4.5. Instrumentation Plan for Large- Scale Testing

In order to thoroughly study the behavior of the proposed system and collect enough data for damage detection, it is necessary to have dense instrumentation. However, too much instrumentation leads to excessive amounts of data that can be difficult and time

consuming to process. Therefore, an instrumentation plan utilizing strain gauges and digital image correlation (DIC) systems was developed to optimize sensor placement and data collection to obtain the best data for damage detection from the 40% scale experiment of the post tensioned coupled shear wall structure.

Results from the simulation influenced the placement of strain gauges and DIC in the network of sensors for the instrumentation plan. The locations for the strain gauges were chosen where the largest stresses and most damages were expected to occur. These locations include along the wall pier base, at the beam-wall interface at each story, and along the coupling beams as indicated in Figure 4.31. Each sensor has a corresponding location in the DRAIN model that was examined and used in the damage identification strategies proposed in this paper.

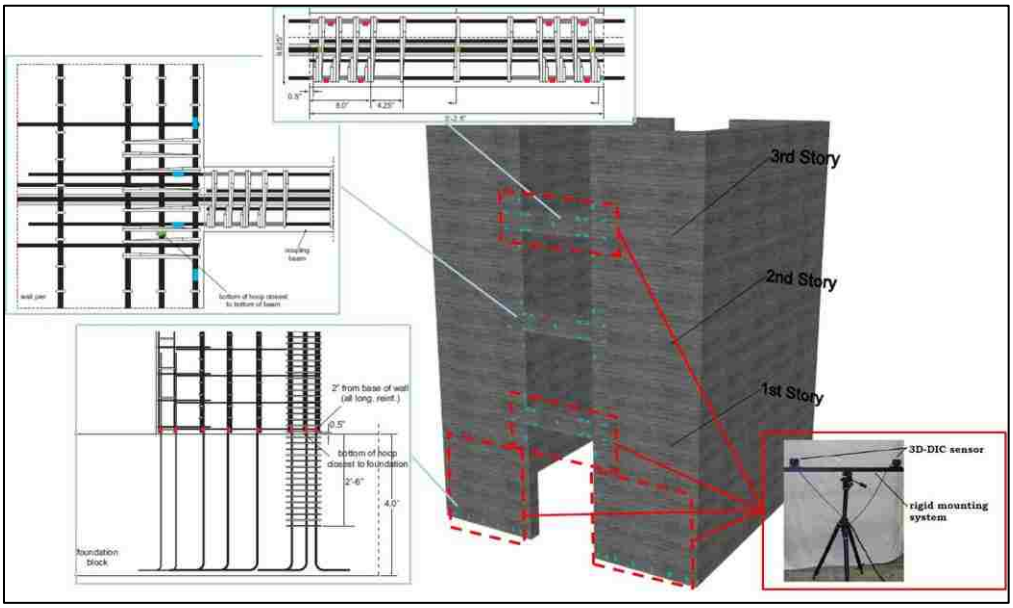

Figure 4.31: Instrumentation plan for large-scale testing

A total of over 240 strain gauges were affixed to longitudinal and transverse reinforcement and embedded in the structure shown in Figure 4.32. Since yielding is expected to occur in the rebar, high elongation gauges were used in the entire structure. High elongation gauges are commonly used on any specimen that is expected to yield. They are capable of measuring +/-20% strain whereas regular gauges will break at strains greater than +/-5%. Gauges on the vertical reinforcement at the beam-wall interface and wall pier base were ¼" with 350 ohms resistance and strain gauges on the coupling beam longitudinal reinforcement were 1/8" with 120 ohm or 350 ohm resistances. Smaller strain gauges were used in the beams because the longitudinal reinforcement in the coupling beams is smaller than the reinforcement in the wall piers. 350 ohm gauges were used for a majority of the strain gauges because they produce larger output signals which lead to better data resolution, but 120 ohms were used when the 350 ohm gauges were no longer available.

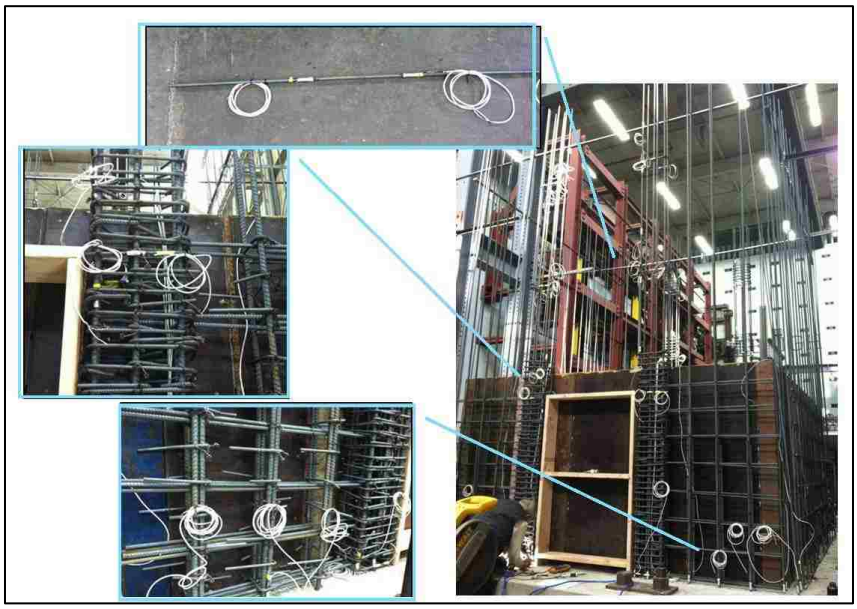

Figure 4.32: Actual instrumentation on large-scale specimen

In addition to the hundreds of embedded strain gauges, DIC cameras will be used to collect surface data from nearly 200 square feet of the structure. Several of the DIC fields of view that will be used are encompassed by the dashed boxes in Figure 4.31. Since cracking and crushing of the concrete is expected to occur at the ends of the coupling beams and bases of the wall piers, DIC systems will collect data at these areas of interest. Additionally, the floor slabs were not modeled in the DRAIN model; therefore DIC systems will monitor the floor slabs to study their behavior under large lateral loads. More details on DIC and its use in SHM will be discussed in Chapter 5.

The cameras were chosen such that all of the desired measuring volumes in the structure could be monitored. Other important factors that were considered in designing the setup included the space constraints surrounding the specimen in the lab and the visual obstructions from test frame obscuring some areas of the structure. Table 4.7

displays the camera types, setup, measuring volume, and measuring distance for the large-scale test.

Table 4.7: DIC camera setup specifications

Camera	Set-up Type	Measuring Volume			Measuring Distance
		Location	length(in)	width(in)	ft
ARAMIS: 1.4/8 Cinegon	3D	1st Story Bottom Beam & Slab	68.90	51.18	6.96
12mm Fastec Hispec 1	2D	Left Wall Pier Base	56.50	56.50	4.93
12mm Fastec Hispec 1	2D	Right Wall Pier Base	56.50	56.50	4.93
Canon Rebel T3-18.3mm	2D	Top of 1st Story Slab	36.00	36.00	2.50
ARAMIS: 1.4/17 Cinegon	3D	3rd Story Bottom Beam & Slab	68.90	51.18	14.11
Hero Go Pro	2D	Top of 3rd Story Slab	36.00	36.00	2.50
PhotronFastCam (20mm)	3D	1st Story Bottom Beam & Slab	68.90	55.12	7.35
Hero Go Pro	2D	Left Wall Pier Base	56.50	56.50	4 or 5
Hero Go Pro	2D	Right Wall Pier Base	56.50	56.50	4 or 5
Hero Go Pro	2D	Top of 1st Story Slab	36.00	36.00	2.50

Two-dimensional setups utilize one camera each and are best at collecting data on an object directly planar to the camera. For this reason, four 2D setups will be used for the wall pier bases, two for the top of the 1st story slab, and two for the top of the 3rd story slab. A schematic for the 2D set-ups for the wall pier bases using the Hero Go Pros are shown are Figure 4.33.

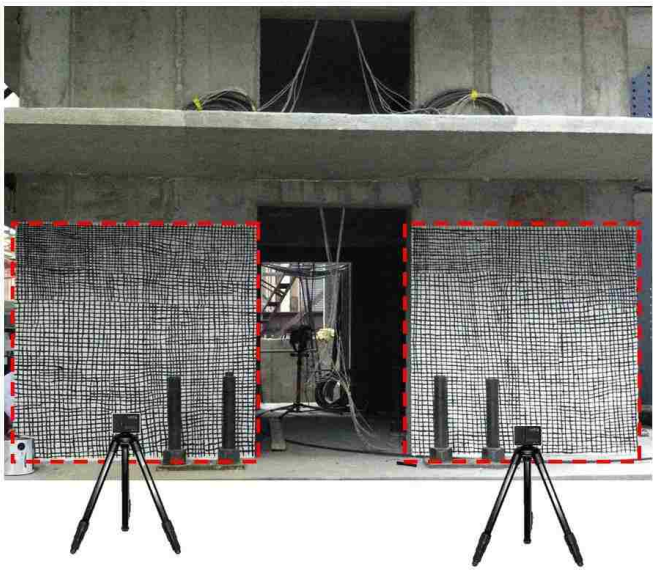

Figure 4.33: Schematic of 2D DIC set-up for monitoring wall pier bases

Three-dimensional setups utilizing two cameras each are necessary to view the bottom of the beam and slab on the 1st and 3rd stories because the field of view involves several surfaces at different angles to the camera. The proposed 3D setup for the 1st story beam and slab using the ARAMIS cameras with Cinegon 8mm lens is shown in Figure 4.34. The expected measuring volume and the distances required to capture this field of view are labeled in the schematic. In summary, a total of 13 cameras—three 3D and seven 2D setups will be used to capture data from over 190 square feet of the structure.

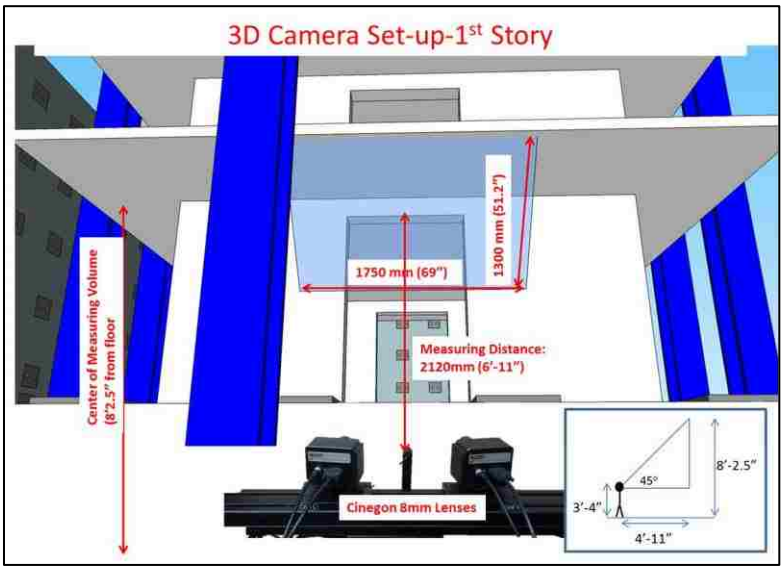

Figure 4.34: Proposed DIC set-up for 1st story coupling beam and slab

4.6. Comparison of Expected Data to Simulation Data

There will be several significant differences between the data collected experimentally from strain gauges and DIC, and the data generated by the DRAIN-2DX simulation model. Some differences may arise from simplifications and assumptions used to establish a working fiber element model. Additionally, the experiment will be performed under different conditions than the simulation model where the data is denser, sensor noise is present, and imperfections and uncertainties may exist.

The simplifications made for modeling will cause the simulation data to vary from reality. For example, only the ED reinforcement was physically modeled in order to simplify the structure. Instead of modeling all of the transverse reinforcement, the concrete cross sections of the beams were composed of unconfined and confined concrete to simulate the added strength and ductility due to the confinement. In the experiment,

longitudinal and transverse steel reinforcement bars are included; therefore there are more possible locations to experience yielding and fracture of the reinforcement.

Also, changes in the cross sectional areas due to damages, such as spalling or crushing, were not accounted for in the model. Changes in the stiffness of the materials were only apparent through changes in the moduli or slopes of the stress-strain curves. As a result, the effects of damage are will be more severe in reality when the loss of cross sectional area is also considered.

Assumptions in the model for the material properties will cause some variation in the data produced and affect the damage detection methods. Therefore the effects of the multi-linear idealization of the stress-strain curves, zero tension and linear tension concrete, and modeling of the concrete cover must be considered.

The multi-linear idealization of the stress-strain curve for the concrete and steel material properties is a reasonable simplification to estimate the nonlinear behavior of the materials, but actual behavior will differ. A real stress-strain plot curves after the elastic limit is reached in the material; therefore there will not be a single point at which the plot transitions from one linear slope to another linear slope. As a result, the damage mode will still be detected, but it may be exhibited by several peaks in β instead of one defined peak. Also, the properties of the concrete and steel will be estimated from standard compression tests of representative concrete cylinders and standard tensile tests of the steel reinforcement. The exact material properties will not be known; therefore

observations are critical for the validation of the damage indices in order to be able to correlate peaks in β to actual damages.

Another assumption made in the model is that the concrete has zero strength in tension at the ends of the coupling beams. In design calculations and modeling, this is a valid assumption since the strength of concrete in tension is very low. However in reality, the concrete does contribute to the tensile strength of the section until it cracks. Also, the interior elements of the coupling beams were modeled with linear tension concrete that essentially acted infinitely linear throughout loading. Actual concrete will not remain linear-elastic in tension past the point at which it begins to crack. Therefore an additional damage mode should be considered in experimental testing at which the concrete cracks and loses stiffness in tension. Since cracking will cause a reduction in the stiffness of the material and cross sectional area loss, it is expected that the damage indices will be capable of detecting this damage mode in the same manner as the unconfined concrete cover spalling in compression.

Another significant difference expected is due to the modeling of the unconfined concrete cover. In the model, the strength of the concrete cover drops by less than 2% when spalling initiates whereas the affects would be more drastic in reality since there will be loss of cross sectional area accompanied by the reduced modulus. Also, the strength of the cover remains at 5.7 ksi after the ultimate strain in the unconfined concrete is reached. However the concrete cover should contribute no strength to the section after ultimate. Therefore the ultimate strength of the concrete cover must be considered as a

possible damage mode in the experimental testing. This extreme drop in strength and stiffness will be easily captured by the damage indices and detection should be in the same manner as the confined concrete crushing.

It is important to acknowledge that real-life conditions are not the same as the model. First, the quantity of data collected experimentally will be much more extensive. In the simulation, the first three stories of the structure were composed of only 53 elements whereas in the experiment there are over 240 strain gauges and 200 square feet of DIC measuring volumes. As a result, there will be much denser data that must be condensed. Furthermore, the DRAIN elements reported strain over the entire length of the element, but strain gauges give strain at a point. This means that there will be several more possible sensor pair combinations to consider for damage detection.

Real-life conditions are also less than the ideal conditions of a simulation model. For instance, construction errors and material imperfections can potentially cause stress concentrations and damage that were not initially expected. Furthermore, any noise from the sensors may affect the effectiveness of the damage indices. Some post-processing may be necessary to eliminate the effects of noise.

Overall, experimental testing poses some new challenges for data collection and processing and introduces additional damage modes to consider like the tensile failure and ultimate failure of concrete. However, experimental testing is necessary in order to extend these damage detection methods into structural health monitoring of civil structures.

5. DIGITAL IMAGE CORRELATION

Digital Image Correlation (DIC) is a novel sensing technology based on digital images that is non-contact and highly accurate. The best application of DIC is to generate a more local view of deformation since it enables a denser field of data points (Lecompte *et al* 2006). In the upcoming large-scale testing of the NEES Coupled Shear Wall, local damages are expected as the structure experiences increasing levels of roof drift. This local behavior is important for evaluating the performance of the structure; therefore DIC will be used to collect spatially dense data in these areas of interest. Since the DIC data will capture the local damage modes, the data will be valuable for damage detection. In order to employ damage detection methods to this type of data in the future, small scale experiments were performed using DIC to establish effective methods for data collection and evaluation.

This chapter explains the premise of digital image correlation (DIC), the general procedure to implement DIC, and the application of DIC in SHM. Then a series of small scale experiments using 3D DIC and conclusions on the reliability of DIC data compared to traditional sensing methods are discussed.

5.1. Introduction to DIC

Imaging techniques such as Digital Image Correlation (DIC) and LED-CCD cameras use data generated from digital images to evaluate a structure. The use of imaging techniques to identify structural damages has progressed because of the

relatively low cost of digital cameras combined with the ease of instantaneous non-contact field measurements (Eberl *et al* 2008).

Digital Image Correlation (DIC) is a promising imaging technology for the field of SHM that has a wide array of benefits that make it superior to traditional sensors like strain gauges, fiber optic sensors, and displacement transducers. For example, collecting a vast amount of data by DIC is much simpler and faster than collecting a comparable amount with traditional sensors. For DIC, all that is needed to collect data from an entire specimen are cameras and a simple calibration object. No sensors must be affixed to the specimen or wired to a data acquisition system; thus making data collection much quicker and easier and eliminating installation costs. Additionally, DIC is beneficial for field monitoring because it requires no contact. Therefore displacements and strain measurements can be accurately measured from a remote distance if a structure is hard to reach (Kim and Kim 2011). Furthermore, although commercial DIC cameras and software may be a large initial cost, there are no additional operational costs and the labor costs are greatly reduced. Also, it is possible to perform DIC with ordinary digital cameras and computer coding software, such as MATLAB, as a low cost alternative (Eberl *et al* 2008).

The most significant difference between DIC and traditional sensors is that DIC can take measurements at thousands of points on the surface of a structure or object at one time (Helfrick *et al* 2011). As a result, the density of data produced by DIC is much greater than the discrete points of strain measured by an instrumentation plan consisting

of traditional strain gauges; even in a network where hundreds of gauges are used (Nonis *et al* 2013). This feature allows DIC to be effective in determining structural changes with high spatial resolution and providing more information than a visual inspection and traditional sensors (Poudel *et al* 2004). This has been proven in previous research by using DIC to detect cracks in concrete that were not visible to the human eye (Lecompte *et al* 2006; Destrebecq *et al* 2011; Helm 2008; Nonis *et al* 2013).

However, the disadvantages of DIC is that the accuracy is dependent on sub-pixel intensity, the quality of the speckle pattern, subset shape and size, image noise, distance to the target, and hardware performance (Pan *et al* 2008; Lee and Shinozuka 2006). Poor texture of the speckle pattern results in more uncertainty in measurements, but this error will not be an issue if a satisfactory pattern is used. It is also possible to quantify noise by recording a picture prior to the motion of the experiment. The displacements should be zero since the specimen has not moved nor experienced any changes; therefore any values recorded can be regarded as noise and eliminated from subsequent data. It is important to note that the use of DIC in the analysis of structures can lead to uncertainty and problems with spatial resolution and accuracy if these certain details are overlooked.

Overall, the use of high-performance cameras and high-contrast patterns will improve accuracy and decrease image noise (Pan *et al* 2008). Careful procedures of data collection and post-processing of the images can mitigate any other problems that may arise. As a result, DIC has proven to be a highly accurate non-contact sensor.

5.2. The Principle of DIC

DIC measures surface displacements by comparing a series of deformed images to a reference image as illustrated in Figure 5.1. First, a reference photo is taken to serve as a baseline to compare the deformed images to. The reference image (Stage 0) is divided into subsets called facets, outlined in green in the figure, which each have unique pixel identities based on the intensity of the light reflected by the surface of the specimen. The system determines the 2D coordinates of the facets from the facets' corner points in each the left and right image as shown in Figure 5.1. The observed 2D coordinates of the same facet in each image lead to a common 3D coordinate (Hild and Roux 2006). Lastly, each image taken after Stage 0, such as Stage 5, is divided into facets and the difference between that image and reference image is measured. Overall, the displacement field is determined from comparing the deformed image to the reference image by matching subsets based on gray-level intensity. Gray value distribution of a subset in the undeformed image should correspond to the gray value distribution of the same area in deformed image (Lecompte *et al* 2006).

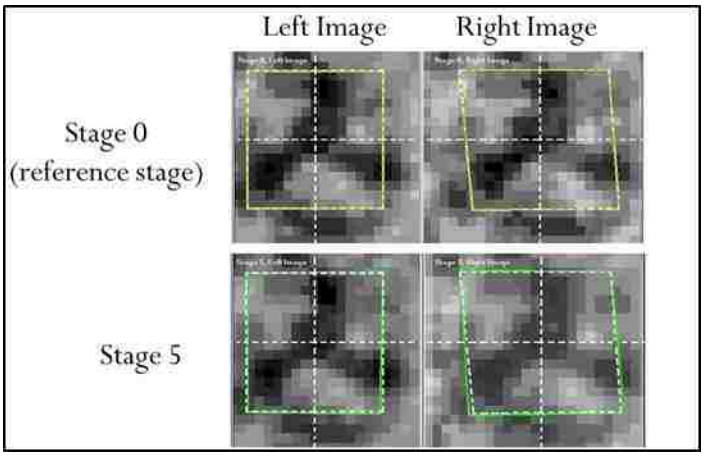

Figure 5.1: Facet computation. Adapted from ARAMIS User's Manual (ARAMIS User's Manual 2007).

5.3.Procedure for DIC

The process of DIC includes (1) specimen preparation, (2) image capture, (3) image processing, and (4) post-processing (Poudel *et al* 2004). All applications require the same general procedure to collect the data of interest.

In order to extract accurate data from the images, the specimen must be properly prepared by creating an appropriately sized pattern. A speckle pattern creates an artificial texture by spray painting black dots or drawing black lines onto the specimen. The pattern is satisfactory if the histogram of the gray-level intensity within a particular region of interest is a Gaussian shaped distribution. This corresponds to a pattern that is about 50% black and 50% white (ARAMIS User's Manual 2007). A high-contrast gray-scale pattern with speckles having a diameter of about 5 pixels when viewed by the camera is best (Helfrick *et al* 2011). Images with bad texture can lead to poor tracking and a large number of potential displacement vectors (Dutton *et al* 2011). Therefore, the

displacement accuracy of DIC is heavily influenced by the size, texture, and quality of the artificial pattern (Dutton *et al* 2011; Kim and Kim 2011). Additionally, the size of the pattern is dependent on the size of the intended measuring volume; therefore the camera set-up must be considered when preparing the specimen.

In the beginning of the image capture phase, the sensors must be calibrated to ensure dimensional consistency in the measuring. One method to calibrate is to take an image of the baseline and scale object. The baseline is the object not in motion. First, the user defines the zones of interest (ZOI) in the image. Then the edge information (location, slope, and curvature) of the scale object is extracted from the images. This is used to determine the scaling factor between lengths and pixels to be used in image processing (Hild and Roux 2006). Most digital image correlation systems, like the ARAMIS 2M at ATLSS, use a calibration object predetermined based on the desired measuring volume. Since the distance between dots on the object are known, the software can determine the position of the cameras relative to each other and the internal distortion parameters of each lens (Helfrick *et al* 2011). At the end of the procedure, a calibration deviation value is given. For the ARAMIS 2M system, calibration deviation may be between 0.01 and 0.04 pixels; anything greater indicates incorrect calibration (ARAMIS User's Manual 2007). Once calibration and scaling is complete, the images of the object of interest can be captured.

Image processing succeeds image capture. During this phase, the subset size is chosen, images are filtered, facets are tracked, and displacements are identified (Poudel *et*

al 2004). First, it is important to select the correct subset size for the data collected. The size of a subset directly determines the area of the image used to track displacements between the reference and the target subsets. The subset must contain enough unique and identifiable features to achieve accurate and reliable displacements (Pan *et al* 2008). A large subset is best to distinguish itself with a distinctive intensity pattern; however a small subset leads to fewer errors (Pan *et al* 2008). Therefore the best size for monitoring is dependent on the specimen and situation. Finally, the reference image and remaining images are compared based on the gray-level distribution of the facets and displacements are calculated.

Post-processing of the data depends on the user's intended application. In ARAMIS, one can view the data as contours of stresses, strains, or displacements. It is also possible to export data of specific sections or points in the measuring volume. An example of the data produced by DIC and some post-processing techniques are presented in Section 5.5.

5.4.Applications in SHM

DIC can be used in a variety of applications including, but not limited to: computing displacements and surface strains, finding material properties, examining the effects of nonlinear behavior, and verifying finite element models (ARAMIS User's Manual 2007). However, the potential of DIC in Structural Health Monitoring is a particular area of interest because it has the capability to compare current surface

geometry, displacement, and strain measurements to baseline measurements made several months or years prior (Nonis *et al* 2013). Some applications of DIC in SHM include: detecting and locating cracks in reinforced concrete beams (Lecompte *et al* 2006; Destrebecq *et al* 2011), reinforced concrete slabs (Helm 2008; Hutchinson and Chen 2006), and even bridge cables (Kim and Kim 2011). Additionally, DIC has even been implemented in vibration studies (Helfrick *et al* 2011) and in field tests of civil structures (Nonis *et al* 2013). This section highlights examples of the use of DIC for Structural Health Monitoring.

Destrebecq *et al* (2011) used displacement fields derived from digital images to analyze cracks and deformation in a full scale reinforced concrete beam. Cracks size and location were determined by analyzing longitudinal displacement measurements in the vicinity of the reinforcement. On a plot of the longitudinal displacement magnitude versus the location along the beam, discontinuities revealed the existence of a crack. The point on the plot at which the discontinuity occurred gave the crack location and the vertical amplitude of the discontinuity corresponded to the width of the crack. These methods proved to be effective in finding early measurements of crack widths, especially starting at an uncracked state. It is especially significant to note that the use of DIC in this application did not require previous visual detection of the crack.

Helm (2008) implemented DIC to analyze specimen with multiple growing cracks. The method correctly identified cracks in a series of experiments on concrete slabs. Hutchinson and Chen (2006) identified cracks in concrete by determining edges in

digital images with strong gray-level contrast. Most importantly, they used an algorithm in conjunction with DIC to automatically detect, localize, and analyze cracks without any human interpretation.

Helfrick *et al* 2011 tested the ability of DIC to measure small displacements of a dryer base subjected to vibrations to extract mode shapes using high speed cameras. DIC was capable of identifying operational mode shapes, which could be useful in the application of monitoring civil structures.

Nonis *et al* (2013) used 3D DIC to monitor the strains and displacements of a reinforced concrete bridge over a period of several months. Crack detection and estimations of crack widths were verified in laboratory tests of several reinforced concrete beams subjected to bending. It was confirmed that DIC could detect cracks before they were visible to the human eye and that the width of a crack could be estimated using the axial strain measurement along a line that intersects the crack. Quantification of spalling was also verified on a small concrete block by monitoring the surface geometry overtime. Finally, these methods were extended into the field to monitor twelve areas of interest on an RC bridge over a period of 4.5 months. This set of experiments proved that DIC can be used for quantitative bridge inspection and SHM applications.

5.5.Small Scale Experiments

A series of small scale experiments on concrete cylinders were performed in order to prepare for the large-scale testing of the NEES Coupled Shear Wall and the future implementation of damage detection methods using DIC. The main purposes of these experiments were to estimate the 28-day stiffness of the concrete from each pour of concrete used in the structure and to develop procedures for collecting and analyzing DIC data. Displacements and strains measured by DIC were also compared to estimated strains and strains measured by strain gauges to confirm that DIC is a viable and superior alternative to strain gauges.

All 28-day stiffness tests were performed on concrete cylinders 4 inches (101.6 mm) in diameter and 8 inches (203.2 mm) high. The SATEC Machine located at Lehigh University's ATLSS Center executed a standard compressive strength test (ASTM C39/C39M − 12a). Throughout the compression test, images were recorded using the ARAMIS-2M 3D digital image correlation system at ATLSS. The procedure developed for these experiments is explained below.

First, the measuring volume was selected based on the size of the cylinder being monitored. To capture the desired measuring volume, the specifications for the set-up of the cameras were selected from the ARAMIS User's Manual for the ARAMIS-2M System with 12 mm lenses and adapted. The cameras needed to be 650mm from the cylinder, 250 mm from each other, and form a 20 degree angle to capture a measuring volume of 350 mm x 275 mm x 275 mm.

The experimental set-up is pictured in Figure 5.2a. The cameras are mounted to a rigid tripod to reduce possible vibrations and unwanted camera movement. Additionally, the back leg of the tripod is stationed on the solid concrete floor and the front two legs are supported by a wooden platform spanning the unstable metal flooring surrounding the SATEC Machine. The wooden platform was necessary because the metal flooring vibrated violently while the SATEC Machine was in use, thus causing the cameras to decalibrate, rendering the data inaccurate. Two lamps provided additional lighting that was distributed evenly across the specimen without causing glare as shown in Figure 5.2b.

Figure 5.2: Experimental setup for stiffness test (a) ARAMIS-2M cameras and (b) additional lighting on specimen

After set-up, the cameras were calibrated using the calibration object shown in Figure 5.3 and the procedure outlined in the ARAMIS software. Calibration was performed before every test to ensure measurement accuracy.

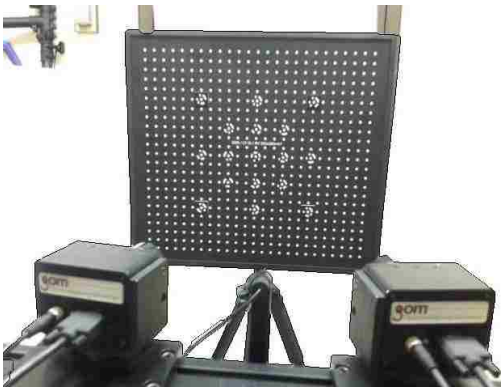

Figure 5.3: Calibration object CP20 350x280

Finally, the compression test was performed and the SATEC Machine's data acquisition system recorded the displacement of the SATEC Machine's head and the corresponding applied load. Photos were taken using the DIC every 5,000 lbf until 60,000 lbf, 2,000 lbf until 70,000 lbf, and then every 1,000 lbf until failure. Whenever a photo was taken with the DIC, the SATEC Machine was paused and the corresponding displacement of the head and load were recorded.

After failure, the images were analyzed in the ARAMIS software v6.0.1.2. The measurement quantity of interest was the displacement in the y-direction in order to calculate the strain in the cylinder. Two sections across the cylinder were chosen in ARAMIS from which to extract the desired information, shown in Figure 5.4 for Pour 2 Cylinder 1. Section 1 (yellow) is located 1.5 inches above the center (black) and Section 2 (red) is located 1.5 inches below the center. The contours in Figure 5.4 display the y-displacement data collected by the DIC. On the left is Stage 0 which is the reference stage; therefore the displacements are zero. The center contour is Stage 14 which is when the cylinder is loaded with about 62,500 lbf and the left is Stage 29 right before failure. It

is important to note that there is data at every point on the contour. As a result, there is a vast amount of extremely dense data.

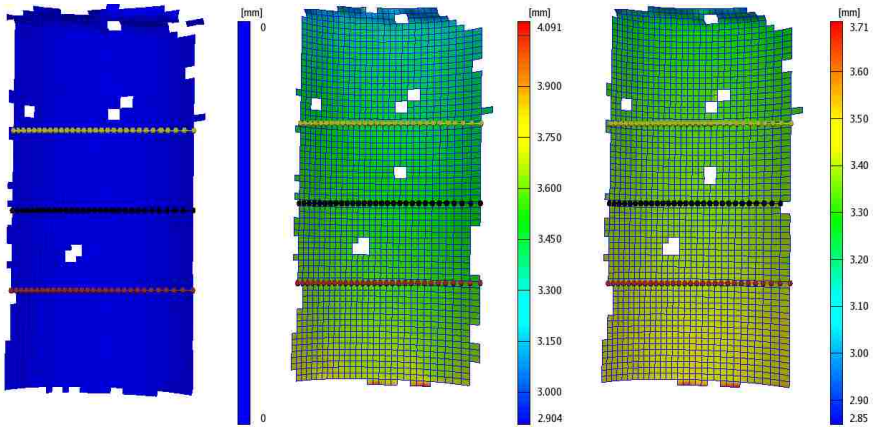

Figure 5.4: Y-displacement for Pour 2 Cylinder 1-Stage 0 (left), Stage 14 (center), and Stage 29 (right)

Figure 5.5 compares the load vs. displacement collected by the SATEC Machine, recorded at each stage, and extracted from the DIC y-displacements of Section 1 and Section 2. Although they have the same slopes, there is an initial offset between the SATEC data and DIC data of about 0.0637 inches. The offset was caused by the movement of the base of the SATEC Machine upon the commencement of the compression test. However, this issue will not affect the calculated strain values because only the difference between the sections is needed for the strain calculations.

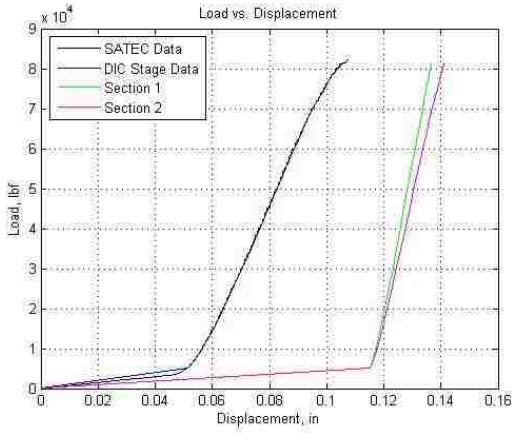

Figure 5.5: Load vs. displacement for Pour 2 Cylinder 1

Next, strains were estimated as the average relative displacement between the two horizontal sections over the average distance between the two sections. To do so, the average y-displacements across each section were calculated at each stage. The difference between the average y-displacement of Section 1 and Section 2 is the average relative displacement. Then, the stress at each stage was calculated by the load applied divided by the cross sectional area of the cylinder and the strain is calculated by the average relative displacement divided by the distance between Section 1 and Section 2.

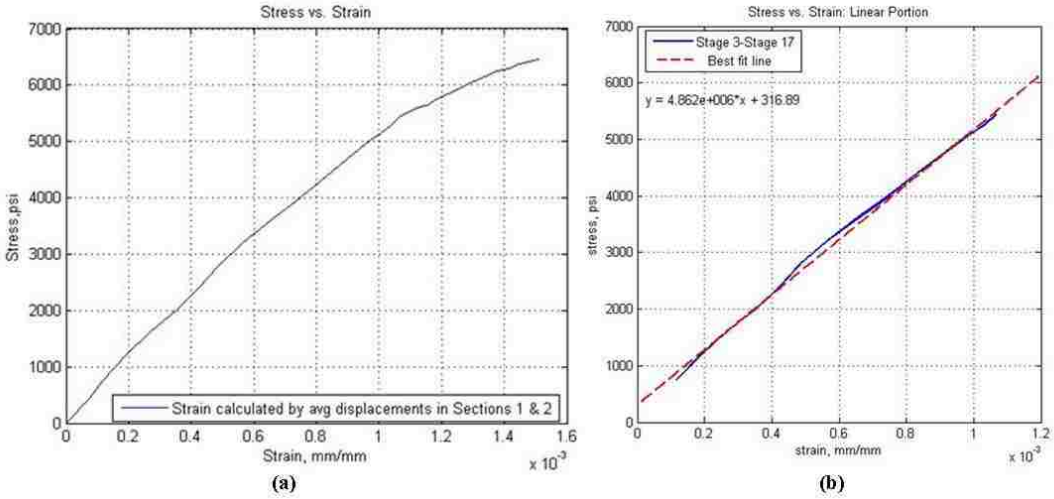

Figure 5.6: Calculated stress-strain curve of Pour 2 Cylinder 1: (a) entire curve and (b) linear-elastic portion

a shows the stress-strain curve Pour 2 Cylinder 1. The cylinder failed at 82,199 lbf, therefore the maximum compressive strength of the cylinder was found to be 6.54 ksi. Since the elastic modulus of the material is the slope of the initial linear portion of the stress-strain curve, the elastic portion was fit with a best-fit line as shown in Figure 5.6b. The linear portion chosen includes Stage 3 to Stage 17 (from 747 psi to 5474 psi). The estimated stiffness for Pour 2 Cylinder 1 is 4861.96 ksi with a correlation coefficient *r* of 0.9987.

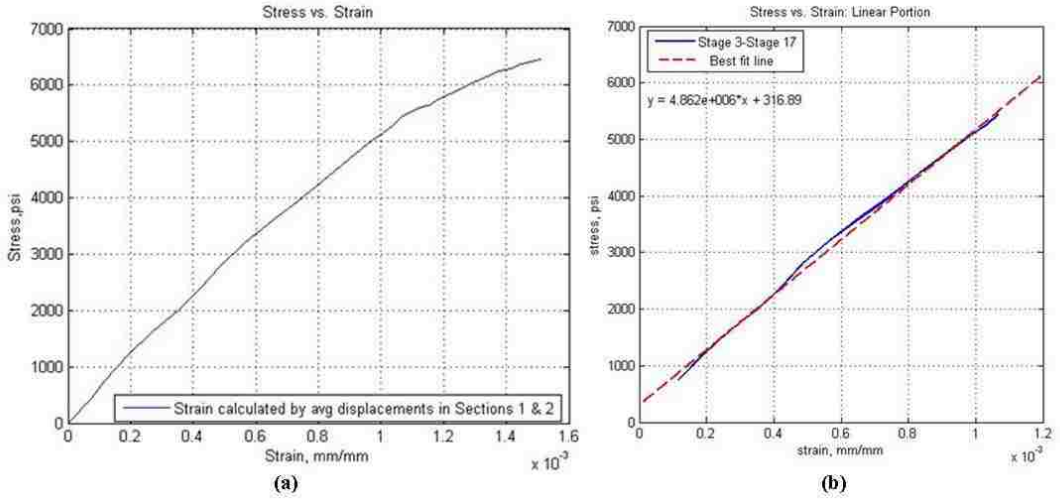

Figure 5.6: Calculated stress-strain curve of Pour 2 Cylinder 1: (a) entire curve and (b) linear-elastic portion

Table 5.1 summarizes the material properties of the concrete cylinders tested from Pour 1 (1st Story walls), Pour 2 (1st Story floor slab), Pour 3 (2nd Story walls), and Pour 4. It can be seen that the calculated stiffnesses are in agreement with each other. If the highest and lowest stiffness values are regarded as outliers, the average stiffness of the concrete used in the large-scale structure is 4,599.70 ksi.

Table 5.1: Summary of material properties from DIC experiments

Specimen ID		Compressive Strength (ksi)	Stiffness (ksi)	Correlation Coefficient (r)
Pour 1	Cylinder 1	6.54	4068.90	0.9960
Pour 1	Cylinder 2	6.43	*N/A*	*N/A*
Pour 1	Cylinder 3	6.12	4439.5	0.9962
Pour 2	Cylinder 1	6.54	4861.96	0.9987
Pour 2	Cylinder 2	5.67	5211.1	0.9982
Pour 2	Cylinder 3	6.69	4856.06	0.9940
Pour 3	Cylinder 1	4.90	6193.03	0.9752
Pour 3	Cylinder 2	5.58	4049.7	0.9607
Pour 3	Cylinder 3	5.74	4225.9	0.9504
Pour 4	Cylinder 1	6.94	2727.2	0.9800
Pour 4	Cylinder 2	7.09	5505.8	0.9894
Pour 4	Cylinder 3	5.92	4178.4	0.9987

5.6.Verification of DIC Measurements

Based on the information and examples described in the previous sections, it is obvious that DIC is fundamentally different than traditional sensing methods. However, the data collected should still provide accurate and acceptable results. In order to confirm that the data produced from DIC is reliable, the DIC data was compared to traditional sensing methods and calculations.

For example, the stress-strain curve for Pour 2 Cylinder 1 was compared to the calculated stress-strain curve from the applied load from SATEC Machine. The strain was estimated from the SATEC load, assuming all deformations were linear elastic. Since the cylinder failed at a maximum compressive load P_{max} of 82,199 lbf, the compressive strength of the concrete f'_c and Young's modulus E could be calculated by Equation 5.1 and Equation 5.2 respectively where A is the cross sectional area of the cylinder (8 inches) and w_c is the density of concrete (150 lb/ft^3 for normal-weight concrete).

$$f'_c = \frac{P_{max}}{A} \tag{5.1}$$

$$E_c = 33 w_c^{1.5} \sqrt{f'_c} \tag{5.2}$$

The resulting Young's Modulus was 4,903.2 ksi, which is less than 1% difference from the 4861.96 ksi calculated using DIC data. Next, the strain from SATEC Load P at each stage was calculated by Equation 5.3.

$$\varepsilon = \frac{P}{AE_c} \tag{5.3}$$

The strains calculated from the SATEC load and the DIC data are compared in Figure 5.7. The estimated strain from the SATEC assumes that the concrete behaves elastically throughout loading, therefore the SATEC stress-strain curve remains linear whereas the DIC stress-strain curve does not. However, the both curves are very similar with a maximum deviation of 8.998 $x10^{-5}$ between the strains at any point. The difference between the curves could be from the inhomogeneity of the concrete material. Since the SATEC strain was calculated only from the force and the cross sectional area, it did not account for how the displacements and strains varied along the cross section of the cylinder; whereas the calculated DIC strain did. Overall, this comparison verifies that the displacements determined by DIC are reliable and accurate.

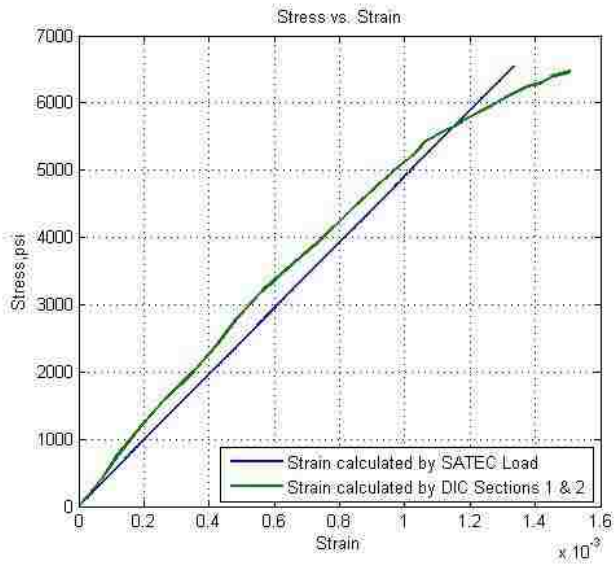

Figure 5.7: Comparison of calculated stress-strain curves from SATEC and DIC data

DIC is also capable of determining strains directly from the images collected. A separate experiment conducted during an independent study at ATLSS compares the

strain output from DIC data to the strain output from strain gauges to determine if strains measured by DIC are accurate. Two 350 ohm strain gauges (SG1 and SG2) were attached on the cylinder located 180 degrees from each other as shown in Figure 5.8a and the same procedure was followed for data collection as for the stiffness tests. Once data was collected, the longitudinal strains in ARAMIS were extracted from the two points indicated in Figure 5.8b which correspond to the same locations as the strain gauges.

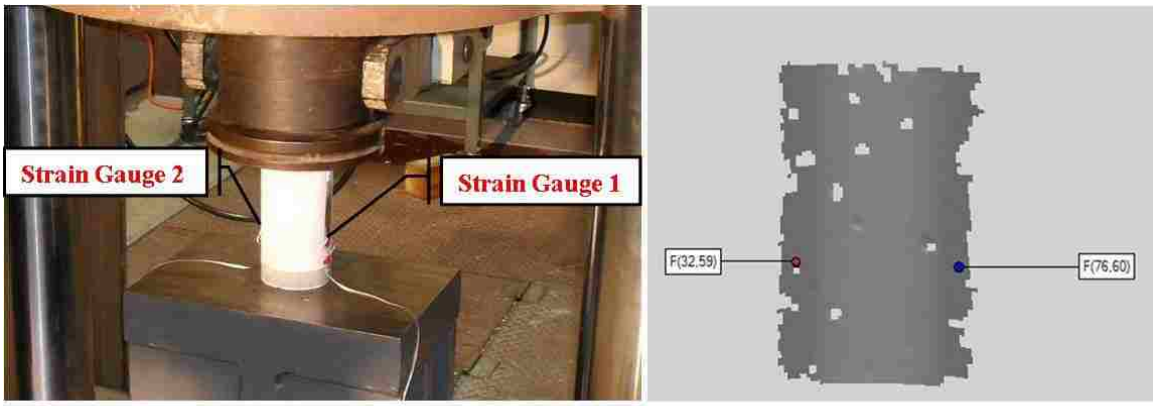

(a) (b)

Figure 5.8: (a) cylinder instrumented with strain gauges and (b) points in DIC corresponding to strain gauge locations

From the stress-strain curve in Figure 5.9, it is apparent that the strains measured by the DIC (dashed curves) correspond to the strains measured by the strain gauges (solid curves). Point F(76,60) and SG1 had a percent difference of only 0.22% in Stage 4 and less than 25% for eight of the nine remaining stages compared. Comparing Point F(32,59) and SG2 resulted in a percent difference of 2.52% in Stage 6 and less than 30% in six of the remaining nine stages.

The deviations between different traditional measuring techniques were used to interpret the accuracy and reliability of the DIC results. For example, the percent difference from comparing the strains measured from SG1 and SG2 to those estimated by the SATEC loads at each stage mostly was between 5% and 30%. Therefore, the deviation between the DIC and strain gauge measurements are not significant, thus proving that DIC is an accurate alternative to traditional measuring devices for measuring strains.

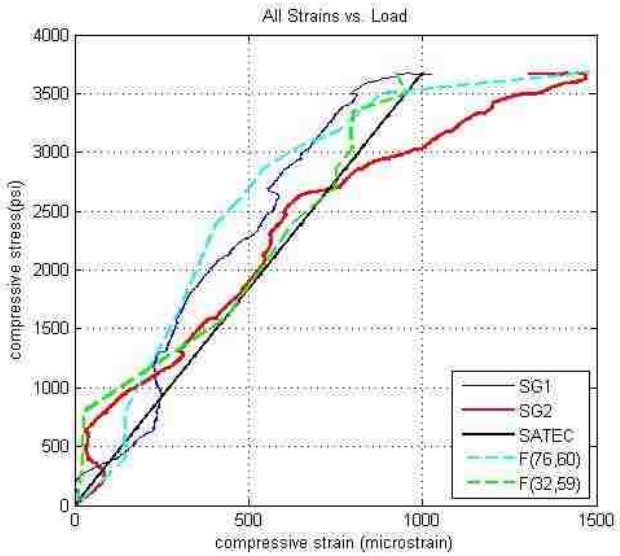

Figure 5.9: Comparison of strains from DIC, strain gauges, and SATEC Machine

5.7.Summary and Conclusions

Digital Image Correlation is a technology that is extremely promising in the field of SHM and damage detection. It is capable of determining high resolution, spatially dense data by comparing an image to a baseline reference image. DIC has been successfully

implemented in SHM to detect, localize, and monitor cracks in reinforced concrete structures in both laboratory and full-field experiments.

Small scale experiments were performed in order to establish effective data collection and analysis techniques for future large-scale testing. Overall, these experiments showed that DIC is an accurate non-contact sensor that requires little equipment, has an easy set-up, and follows a simple, user-friendly procedure. Most significantly, the data produced by DIC is reliable, extremely comprehensive, and rich in valuable information useful for SHM and damage detection.

6. ABAQUS MODEL OF REINFORCED CONCRETE FRAME

The coupled shear wall system introduced by the NEES Shear Wall in Chapter 4 is a novel specialty structure that is not currently approved by design codes for use in high seismic regions. Since the coupled shear wall system is not yet established in practice, a model of a reinforced concrete special moment-resisting frame is constructed and analyzed in this chapter to make more general conclusions about the performance of the proposed damage detection methods for RC earthquake-resistant structures. A RC special moment-resisting frame (SMRF) was chosen because they are one of the most widely used earthquake-resistant systems and they are composed of common beam and column elements.

Chapter 6 discusses the development an ABAQUS finite element model of a two-bay, two-story RC SMRF. The performance of the damage indices to detect the yielding of the reinforcement and spalling of the concrete cover is assessed. Lastly, a project for damage detection in a RC SMRF frame is introduced for future work.

6.1. Introduction

Reinforced concrete moment-resisting frames (MRF) are widely used in high seismic regions as earthquake-resisting systems. The horizontal beams and vertical columns provide gravity and lateral resistance. The strength and stiffness necessary to resist the lateral forces is achieved through the use of rigid connections between beams and columns which prevent any rotations between the beam and column (FEMA P-749

2010). A special moment-resisting frame (SMRF) has additional detailing requirements that improve the seismic resistance of the system compared to an ordinary MRF. The beams, columns, and joints are detailed and proportioned in order to resist flexural, axial, and shearing forces resulting from large displacement cycles present during a seismic event (Moehle *et al* 2008).

It was important to consider minimum code requirements when designing the frame because the proportioning and detailing requirements for SMRF must be satisfied to allow the frame to withstand extensive inelastic deformations that result from earthquakes. Therefore, the *Seismic Design of Reinforced Concrete Special Moment Frames* distributed by the National Earthquake Hazards Reduction Program (NEHRP) was consulted. This guide combines the design requirements from ACI 318-08 and the load requirements from ASCE7 and the International Building Code (IBC).

The frame dimensions, shown in Figure 6.1, were developed from to meet the frame proportioning requirements in ACI 318-08. ACI 318-21.6.1.1 sets the minimum column dimension to 12 inches, but a minimum dimension of 16 inches is suggested. Therefore, no beam or column has a dimension less than 18 inches in the proposed frame. Additionally, the ratio of the cross sectional dimensions for columns are required to be at least 0.4 according to ACI 318-21.6.1.2 so that the section is more compact. Since the frame has square columns, this requirement is met. Lastly, by ACI 318-21.5.1.2 the clear span of the beam must be at least four times its effective depth. In the proposed frame, the beam span is nine times the depth of the beam

The minimum longitudinal reinforcement and spacing were also determined from ACI-318. Other special detailing requirements are not presented in this thesis because the details, such as the layout and spacing of transverse reinforcement, were not physically modeled in ABAQUS.

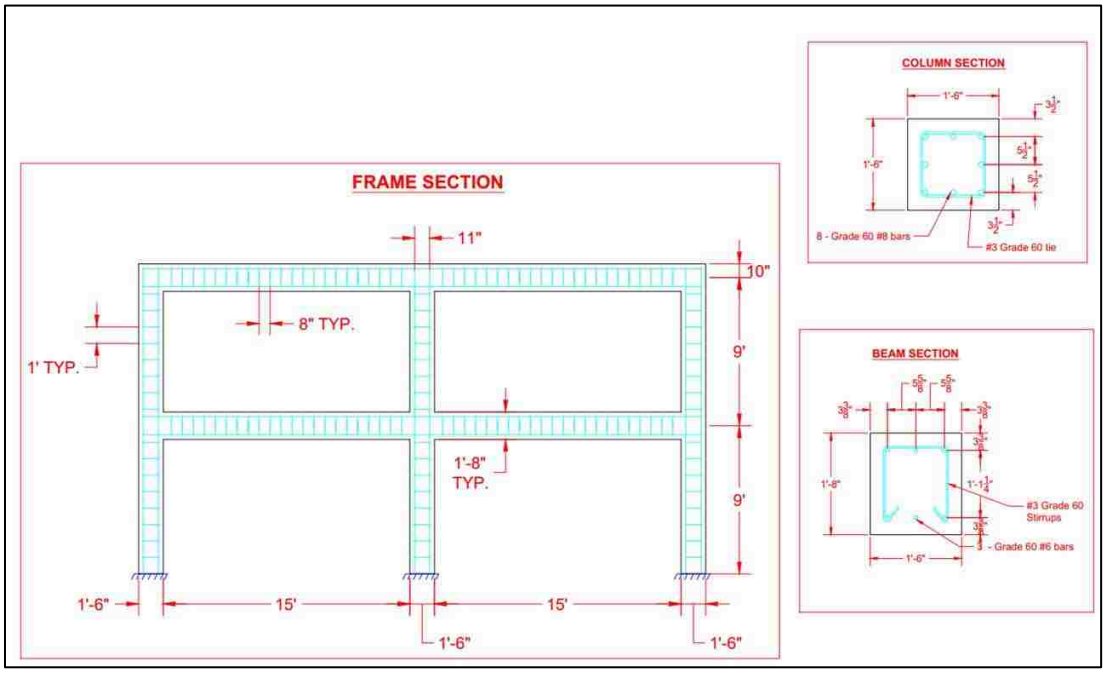

Figure 6.1: Two-story, two-bay reinforced concrete frame dimensions

6.2. Modeling Considerations

6.2.1. Elements and Material Properties

A few assumptions were made in order to simplify the model while maintaining the integrity of the data for future damage identification applications. First, the transverse reinforcement was not physically modeled. Instead, the concrete cover and core in the columns and the beams were modeled by unconfined concrete and confined concrete

tetrahedral solid elements using the Mander Model described in Chapter 3 and Chapter 4. The longitudinal reinforcement was physically modeled with concrete shell elements with rebar embedded inside. Since solid elements were used for the inner confined and outer unconfined concrete, the rotational degrees of freedom were ignored. However, in a SMRF the connections between the beams and columns do not allow for any rotations relative to each other; therefore this simplification is valid. A summary of the elastic material properties and element types for the structure is in Table 6.1.

Table 6.1: Element types and material properties used in ABAQUS model

	Material	Element Type	Young's Modulus (E)	Poisson's Ratio (ν)
Beam	Unconfined Concrete	Tetrahedral Solid Continuum C3D10	4,415 ksi	0.15
	Confined Concrete		4,286 ksi	0.15
	Rebar	Shell S4R with Rebar Layer	29,000 ksi	0.3
Column	Unconfined Concrete	Tetrahedral Solid Continuum C3D10	4,415 ksi	0.15
	Confined Concrete		4,286 ksi	0.15
	Rebar	Shell S4R with Rebar Layer	29,000 ksi	0.3

Material nonlinearities were considered to predict the behavior of the RC frame under large lateral displacements. The material properties for concrete and rebar were idealized by the multi-linear stress-strain curves shown in Figure 6.2a and Figure 6.2b, respectively. Damage modes expected to occur are indicated in the figures and include: the rebar yielding in tension, the unconfined concrete cover spalling, and the confined concrete core crushing.

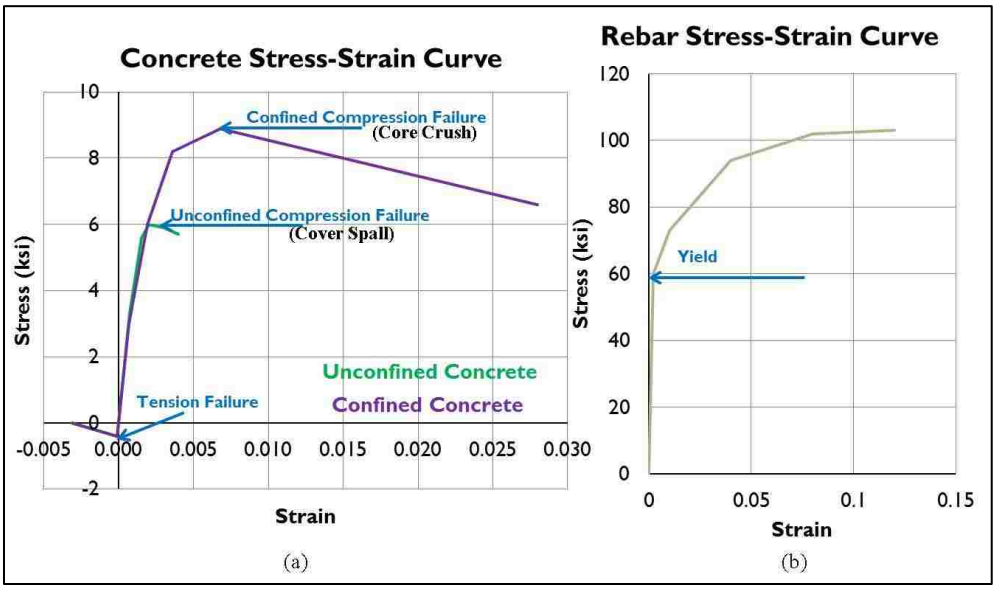

Figure 6.2: Nonlinear material properties in ABAQUS model for: (a) concrete and (b) steel rebar

6.2.2. Assembly of Components

The RC frame is composed of four beams and three columns; each consisting of a confined concrete core, unconfined concrete cover, and two layers of embedded rebar. The assembly of the frame is depicted in Figure 6.3. Select elements are removed in the figure for visualization purposes so the different elements and components of the structure are visible. For example, the unconfined concrete cover was removed from the column on the far right so the confined concrete core is visible. Also, the unconfined and confined concrete elements were removed from top right beam to reveal the embedded rebar elements. To assemble the components, surface ties connected the confined and unconfined concrete, the rebar layers to the confined concrete core, as well as the beam face to the column face. Tie constraints were appropriate because rigid joints were

assumed between the connected surfaces. All nodes on the bottom surface were constrained at the base of the columns to create fixed boundary conditions at the base of the frame.

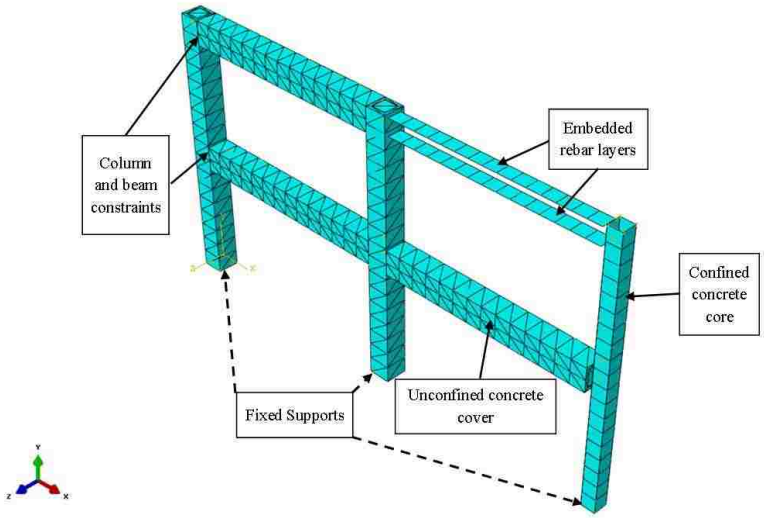

Figure 6.3: Assembly of ABAQUS model

6.2.3. Loading

During an earthquake, a structure experiences large lateral displacements. The performance of an earthquake-resistant structure is often evaluated based on its behavior under various levels of roof drift. Therefore, a static monotonic load was applied to the top left corner of the frame by a displacement controlled boundary condition up to 3% roof drift. This corresponds to a total of 6.66 inches of displacement in the positive x direction.

6.3.Expected Damages

The same multi-linear idealization used in the DRAIN model was used in the ABAQUS model; therefore the possible damage modes are the same. Before any damage occurs, the model behaves linearly. The damage modes that occur include the yielding of the rebar in tension, spalling of the unconfined concrete cover, and crushing of the confined concrete core as described in Chapter 4. The rebar yields at 60 ksi and 0.00207 strain, the concrete cover spalls at 6 ksi and 0.002 strain, and the concrete core crushes at 9 ksi and 0.007 strain. The highest strains occur at the ends of the 1st story beams, as shown by the longitudinal strain contours in Figure 6.4; therefore these are the locations at which damage is expected to occur.

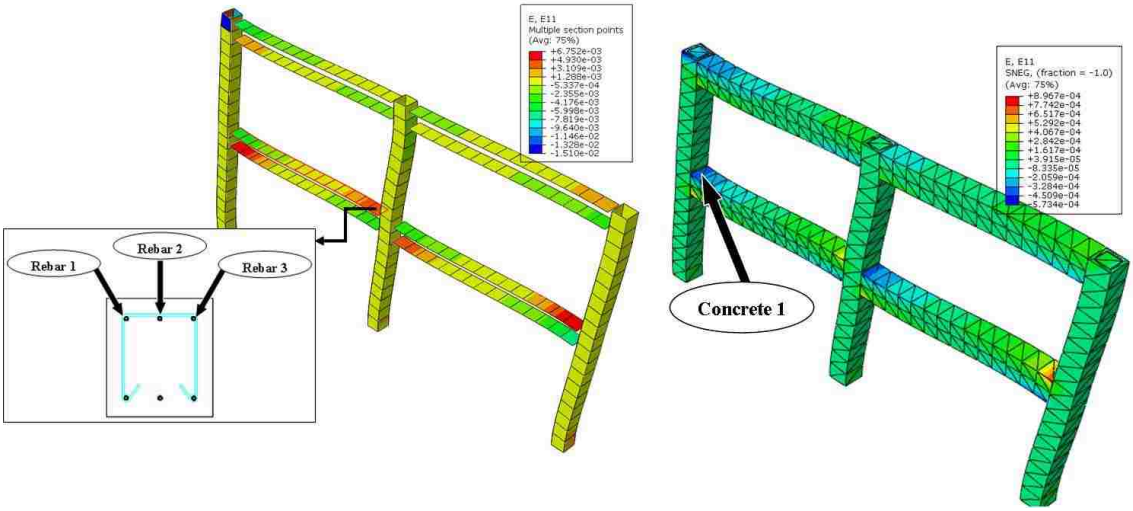

Figure 6.4: Longitudinal strain contours and elements of interest in ABAQUS model

The strain was extracted from the ABAQUS model from four elements of interest along the 1st story left beam of the frame since they experienced the highest levels of strain, as indicated in Figure 6.4. Element Concrete 1 is an unconfined concrete element

in compression that is expected to spall. Elements Rebar 1, 2, and 3 are embedded rebar elements in tension that will yield. The value of base shear at which each of the selected elements will experience damage is summarized in Table 6.2. The damage modes that will be focused on for the remainder of the analysis are the rebar yielding and the unconfined concrete cover spalling.

Table 6.2: Expected damages in RC frame ABAQUS model

Element #	Element Name	Base shear at which damage mode occurs, kips	
		Rebar Yield	Cover Spall
1	Concrete 1		520.3
2	Rebar 1	711.7	
3	Rebar 2	683.1	
4	Rebar 3	698.3	

6.4.Application of Damage Indices

The regression coefficient,α, and its first derivative, β, introduced in Section 3.2 were applied to the strain data extracted model for the concrete and rebar elements shown in Figure 6.4 for a total of six unique sensor pair combinations. Changes in slope of α and peaks of β successfully detected the yielding of the rebar in tension and the spalling of the unconfined concrete cover in the manner described in Chapter 3. First the damage indices were evaluated to confirm the effectiveness of the structural model established in Section 3 for damage detection. Then, the damage indices were further examined to determine their capabilities for damage detection and localization of the concrete cover spalling and rebar yielding.

6.4.1. Detection of Damage

The structural model behind the formulation of the proposed damage indices is based on the concept that the structural responses of two nearby sensors are highly correlated and changes in structural properties due to damage will cause a change in the structural response. This causes a change in the relationship between any two locations on the structure, thus inducing slope changes of α and peaks of β. Therefore before damage occurs, the damage indices will be constant and linear because the materials are elastic. However, once damage occurs, such as the reinforcement yielding, concrete cover spalling, and concrete core crushing, the damage indices will deviate from this line.

The damage index plots for R1/C1 are shown in Figure 6.5 as a representative case of this behavior; however all plots for overall detection of the steel yielding and concrete cover spalling can be found in Appendix C.1.

In Figure 6.5, the damage indices are constant and linear (indicated by the dashed horizontal line) until spalling initiates. Upon spalling, α decreases as the change in strain in Concrete 1 increases due to softening. This causes negative peaks in β values. Then, the damage indices deviate even further from the line when yielding occurs. Similar behavior is exhibited by the other damage indices and can be seen in Appendix C.1. Sensor pairs that included two rebar elements detected yielding more strongly than spalling. Details on the detection and localization of the rebar yielding and concrete cover spalling will be discussed further in the following section.

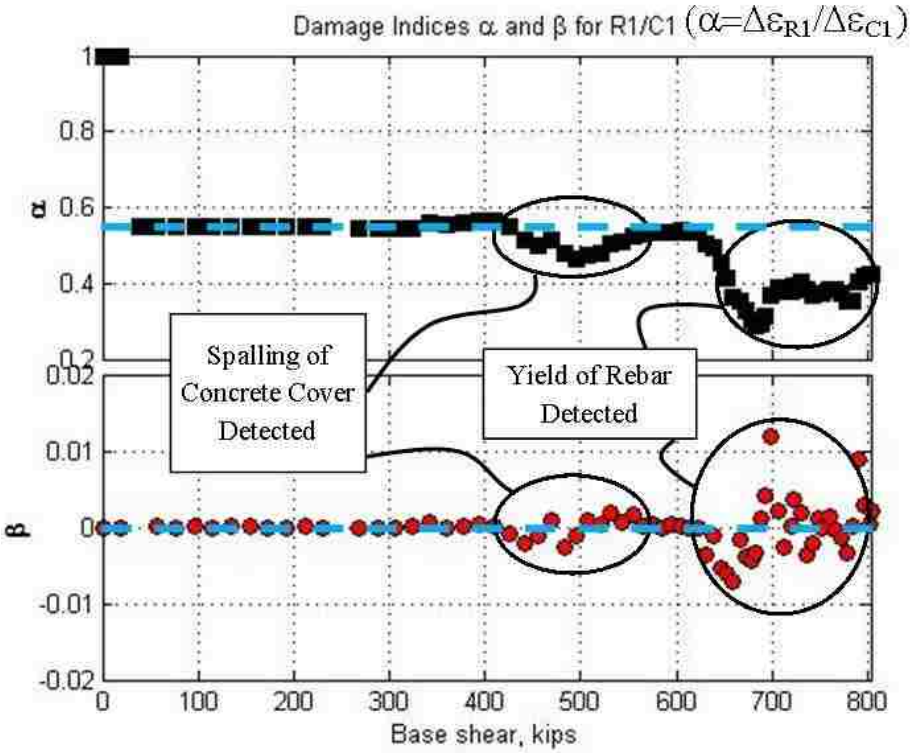

Figure 6.5: Detection of concrete cover spalling and rebar yielding by damage index R1/C1

6.4.2. Damage Detection and Localization

Since damage directly affects the local structural response, the response of a sensor at or near a damaged location will be more affected than a sensor far away. As a result, a damage index including the affected sensor will exhibit stronger changes, such as a larger magnitude of β relative to the other peaks. If this occurs, it is possible to say that the damage was localized by the damage index.

Therefore, the damage indices for all six sensor pair combinations were calculated using the strains output and each damage mode was focused on separately to examine the localization capabilities of the damage indices. Table 6.3 summarizes the performance of

each sensor pair combination to detect the damages from Table 6.2. A check mark indicates that the pair exhibited changes in α and peaks in β when damage occurred; an *X* indicates that it did not. Peaks with the largest magnitude of β were considered the most prominent detections. The highlighted boxes indicate which damage was most prominent for that sensor pair. A few representative examples of the damage index plots will be presented in the text, but all sensor pair combinations are shown in Appendix C.2 for detection of rebar yielding and Appendix C.3 for concrete cover spalling.

Table 6.3: Performance of damage indices

Sensor Pair	Concrete 1 Spall	Rebar 1 Yield	Rebar 2 Yield	Rebar 3 Yield
R1/C1	✓	✓	✓	✓
R2/C1	✓	✓	✓	✓
R3/C1	✓	✓	✓	✓
R2/R1	✓	X	✓	✓
R3/R1	✓	X	✓	✓
R3/R2	✓	X	✓	✓

6.4.2.1.Rebar Yielding

The damage indices were capable of detecting and localizing the yielding of the first story beam reinforcement. Two representative sensor pairs will be presented, but all plots for the detection of the rebar yielding can be found in Appendix C.2.

An example of the detection of the yielding of the rebar using sensor pair R3/R2 is shown in Figure 6.6. The regression coefficient α was calculated as indicated in the figure. When Rebar 2 yields, the change in strain in Rebar 2 and Rebar 3 both increase. The change in strain in Rebar 3 increases because Rebar 2 is located directly adjacent to

Rebar 2; therefore when Rebar 2 yields, Rebar 3 must take on more of the tensile load to keep the section balanced. The increase in the change in strain of Rebar 2 is due to the softening of the material upon yielding and is larger than the change in strain of Rebar 3. Therefore, α is decreasing; thus producing a negative β peak when damage occurs. Similarly, when Rebar 3 yields, both changes in strain are increasing; however the change in strain in Rebar 3 is larger since the material is softening. As a result, α is increasing and there is a positive β peak.

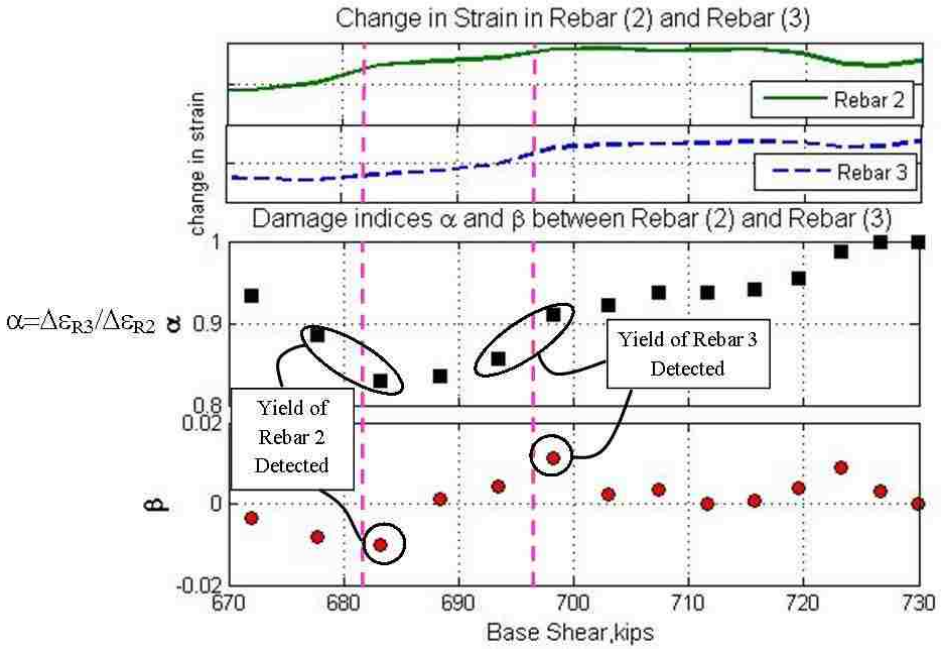

Figure 6.6: Detection of rebar yielding by damage indices R3/R2

Localization is achieved by this sensor pair because the detection of yielding of Rebar 2 and Rebar 3 are detected, but the yielding of Rebar 1 around 711 kips is not. Since the sensor pair includes Rebar 2 and Rebar 3, the yielding of these elements cause a greater change in the structural response and consequently the damage indices, than the yielding

of Rebar 1 does. Therefore, the damage index R3/R2 localizes yielding to Rebar 2 and Rebar 3.

Another example of the successful detection and localization of rebar yielding is shown in Figure 6.7 with sensor pair R3/C1. This damage index correctly identifies the yielding of Rebar 1, 2, and 3, but the peak in β with the greatest magnitude is at the yielding of Rebar 3. Therefore, yielding is localized to Rebar 3 by the damage index R3/C1. Similarly, yielding is localized to Rebar 2 by sensor pair R2/C1 (shown in Appendix C.2.

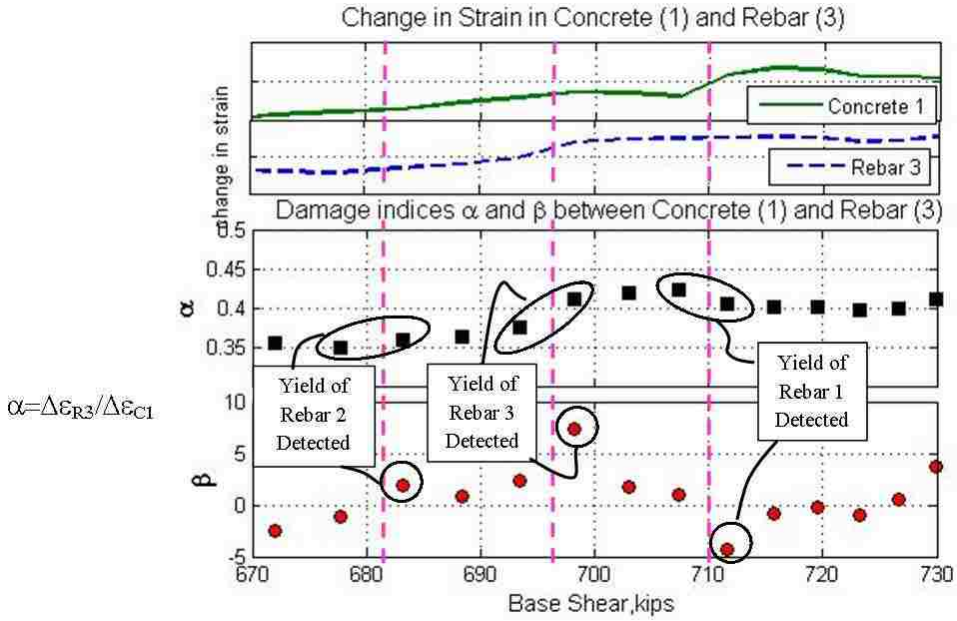

Figure 6.7: Detection of rebar yielding by damage indices R3/C1

Sensor pair R2/R1 and R3/R1 did not identify yielding in Rebar 1. This is particularly alarming because sensor Rebar 1 is one of the sensors used in the calculation of the damage indices; therefore damages that occur in Rebar 1 should be most

prominent. A possible reason for lack of detection may be because by the time Rebar 1 yields, a significant amount of damage has already occurred in the structure; therefore the reduction in stiffness of Rebar 1 does not have as much of an impact on the overall stiffness of the beam section. The cause of this false negative calls for future investigation.

6.4.2.2.Spalling of Unconfined Concrete Cover

The damage indices detected that the spalling of the concrete cover occurred, but the exact point at which spalling was initiated was not as prominent as the detection of the rebar yielding. Instead of one single prominent peak in β, there were multiple peaks after the step where spalling was initiated. The damage index for R1/C1 is presented as an example, but all damage index plots for the detection of spalling of the unconfined concrete cover can be found in Appendix C.3.

The inability to determine one distinct detection point for spalling in the concrete cover may result from the complexity of the concrete solid element as opposed to the simple rebar shell elements. For instance, once spalling begins at the outermost compression fiber, the concrete cover continues to spall at each fiber closer and closer to the core of the beam. Therefore the structural response keeps changing as the physical properties of each fiber change. On the other hand, the entire rebar experiences a change in the structural response at one time when the physical properties change from yielding.

As a result, there is a defined point at which yielding occurs in the rebar; thus making a more prominent detection with the damage indices.

Figure 6.8 shows the damage indices for sensor pair R1/C1. The detection of the cover spalling was clearly visible when the indices deviated from the line in Figure 6.5. However, when the damage index plots are limited to the base shears near the initiation of spalling so that localization can be examined (Figure 6.8), it is more difficult to distinguish a definite point. Instead, spalling is initially flagged at 495 kips as shown in Figure 6.8, but then β afterwards still deviates from zero as spalling continues in the section. When spalling initiates, the change in strain in the concrete element is increasing due to softening of the spalling concrete. As a result, α is decreasing which causes a negative β peak. This same behavior is exhibited by sensor pairs R2/C1 and R3/C1. Additionally, the change in strain in the rebar also increases when the concrete spalls; therefore sensor pairs consisting of only rebar elements (R1/R2, R1/R3, R2/R3) are still capable of correctly identify that spalling occurs. Since every sensor pair detected that spalling occurred and all of the magnitudes of β were generally the same, it is inconclusive whether spalling was localized. In order to determine if this was achieved, a sensor pair far from the damage would need to be investigated; which could be done in future work.

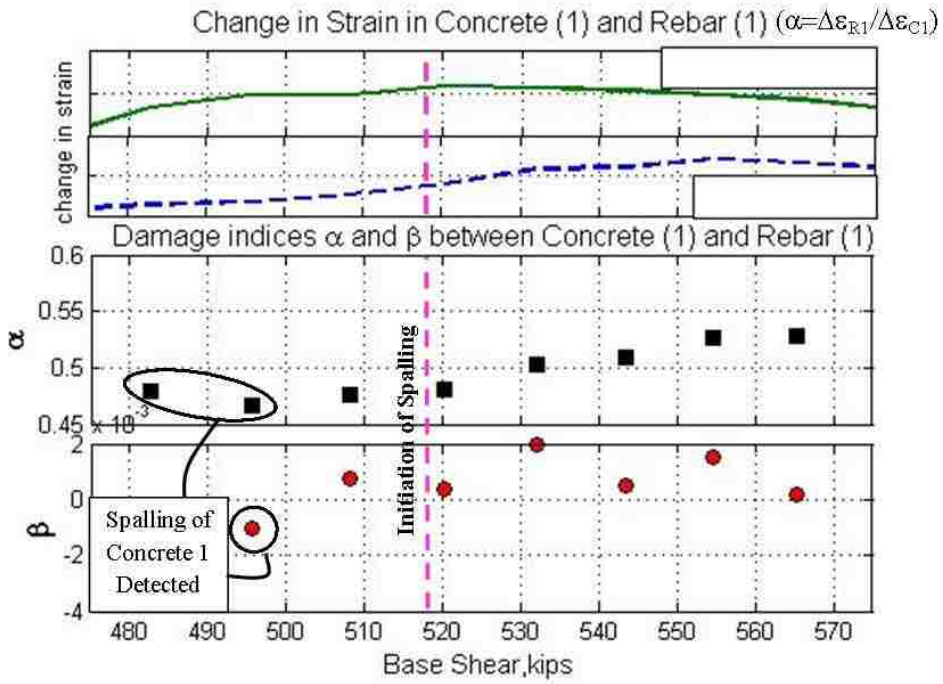

Figure 6.8: Detection of concrete cover spalling by damage indices R1/C1

6.5.Summary and Conclusions

In order to study a more commonly used earthquake-resistant structure, a model of a two-bay, two-story RC special moment frame was created in ABAQUS. The model accounted for nonlinear behavior due to damage by using a multi-linear stress-strain curve for the material properties. It was static monotonically loaded up to 3% roof drift to simulate the large lateral displacements that would be present during an earthquake.

The regression coefficient α and its slope β were applied to four select elements that were expected to become damaged for a total of six unique sensor pair combinations. Each combination was analyzed to make more general conclusions about the performance of the proposed damage indices to detect and localize the steel

reinforcement yielding and the concrete cover spalling. Before any damage occurred, the damage indices remained constant and linear. Once spalling was initiated, the damage indices deviated from the line. Then when the rebar yielded, the indices changed even more. Therefore this behavior proved that the proposed indices were capable of detecting concrete cover spalling and steel yielding.

The damage index plots were examined further to evaluate the damage indices' capabilities to localize damage. Overall, yielding of the reinforcement was localized by the damage indices, but it is not possible to conclude from the given data if spalling of the concrete cover was localized.

Most importantly, the implementation of the damage indices on the RC SMRF in ABAQUS further proved that these features are adequate for damage detection in RC earthquake-resistant structures; not just the specialty structure in Chapter 4.

6.6.Future Work

A future project to further develop and validate damage detection techniques in earthquake-resistant reinforced concrete structures was proposed. The project includes simulation models, component testing, and ultimately large-scale testing at Lehigh University's ATLSS Center. Data from simulation models as well as the performance of the proposed damage indices after large-scale testing of the NEES Coupled Shear Wall will be considered in designing various experiments.

Figure 6.9 illustrates the overall intentions and vision for the project. An 8-story ductile moment resisting frame is the prototype structure shown in Figure 6.9a. In order to investigate failure modes of each of the frame components, full scale component level testing will be performed on a 1st story column (d) and a 1st story beam with connections (c). Then, the results will be considered for 50% scaled testing of the entire 1st story under the effects of an earthquake time history. Finally, a two-story portion of the two-bay frame, similar to the frame in the ABAQUS model will be tested using hybrid simulation.

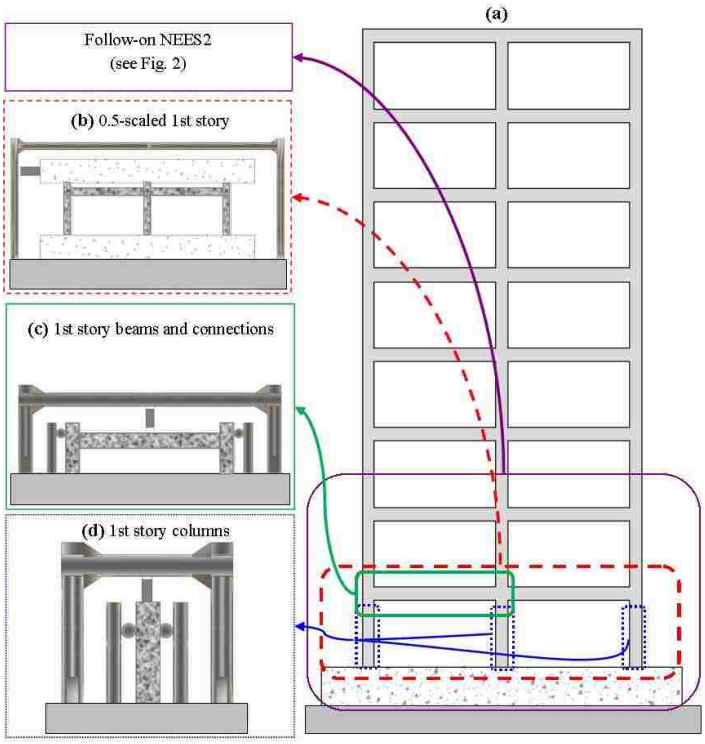

Figure 6.9: Overall plan for future NEES project

Detailed set-ups of the component level testing of the column and beam are illustrated in Figure 6.10a and Figure 6.10b respectively. Each component will be

instrumented with several strain gauges on the longitudinal and transverse reinforcement. Additionally, 3D DIC setups will collect surface data as static loads are applied by actuators until failure.

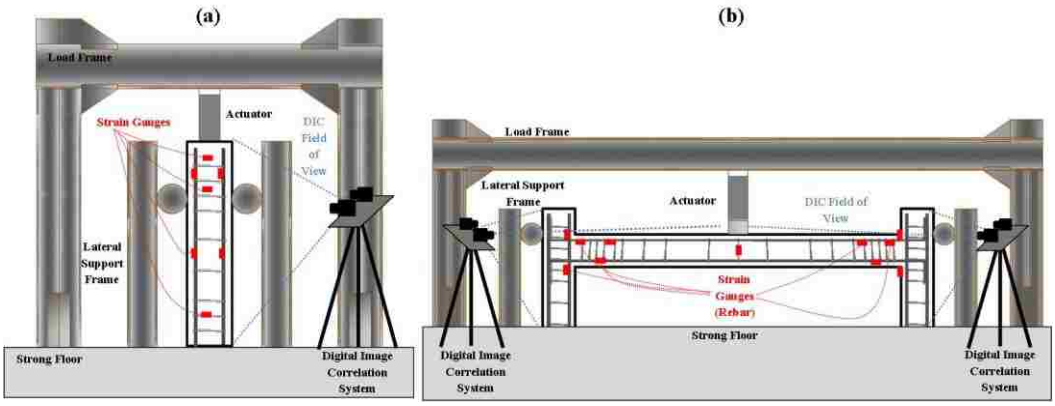

Figure 6.10: Full-scale component level testing of (a) 1st story column and (b) 1st story beam with connections

Since the 50% scaled 1st story of the prototype structure will be tested under an earthquake time history, the structure will be instrumented with accelerometers in addition to the strain gauges and DIC as shown in Figure 6.11. Accelerometers will collect dynamic data while actuators apply lateral loads to simulate an earthquake.

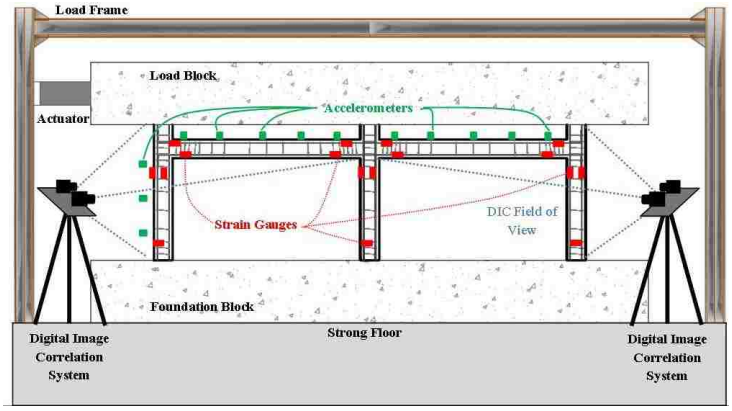

Figure 6.11: 50% Scaled testing of 1st story under earthquake loading

Lastly, Figure 6.12 presents a preliminary plan for testing of the first two stories of the prototype structure using hybrid simulation. Lateral actuators will apply lateral loads similar to those induced by an earthquake while gravity actuators apply forces to the second story to simulate the top six stories of the building. Throughout loading, several strain gauges embedded on the rebar and 3D DIC set-ups will collect data for use in validation of damage detection techniques.

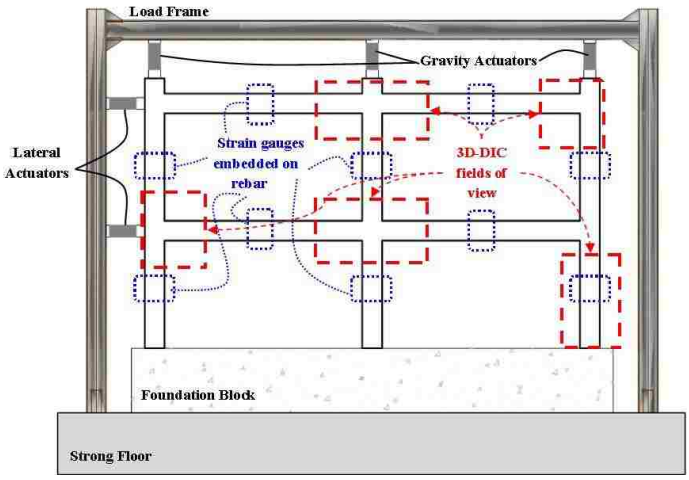

Figure 6.12: Preliminary plan for testing of first two stories of prototype structure

Overall this project will further enhance the damage detection techniques introduced in this thesis by validating them with extensive experimental data. Most importantly, it will create a basis for extending these techniques to real world monitoring of earthquake-resistant structures.

7. SUMMARY, CONCLUSIONS, AND FUTURE WORK

This thesis proposed a technique for detecting and localizing three damage modes in reinforced concrete earthquake-resistant structures. Damage modes considered include the yielding of the steel reinforcement, spalling of the concrete cover, and crushing of the concrete core.

First, a definition of damage in RC was established based on the material properties of steel and concrete from experimental observations and design codes. It was found that when damage was initiated, it induced a change in stiffness in the structure or structural component through a reduction in the moduli of the materials and the cross sectional area of the section. The change in stiffness was apparent from changes in the structural response. The structural response used in this method was the change in strain in an element because strain directly corresponds to material limits at which damage occurs. Therefore it is a variable that is directly affected by damage.

Damage indices were established as damage sensitive features to detect the changes in stiffness due to damage through the structural response. The proposed damage indices created a pairwise relationship between two sensor locations on a structure. Discontinuities or peaks in the damage indices signified a change in the relationship, i.e. possible damage, between the sensors compared by the damage index.

Two simulation models were examined in order to validate these damage detection techniques. First, a DRAIN-2DX fiber element model of a post-tensioned coupled shear wall earthquake-resistant structure was introduced and analyzed to determine the types

and locations of damage. Then, the damage indices were applied to the model to detect the yielding of the energy dissipating (ED) bars, spalling of the concrete cover, and crushing of the concrete core.

Damage modes were successfully identified by the damage indices. Additionally, all detected damages were localized to the story level at which damage occurred. Furthermore, some indices and damage modes were capable of localizing damage to a specific sensor by examining the magnitude of the peak of β. The yielding of the ED bars was the most prominent damage detected and localized. Spalling of the concrete cover was not as easily detected because the model was not sophisticated enough to simulate the detailed behavior of spalling that includes the reduction of the material modulus combined with the loss of cross sectional area. However, spalling was detected in most cases when the spalling sensor location was used to calculate the damage index. Lastly, crushing of the concrete core was effectively detected by most sensor pairs. Overall, the proposed damage indices identified and localized the three intended damage modes using simulation data from DRAIN-2DX model of the NEES Coupled Shear Wall structure.

An ABAQUS finite element model of a two-bay, two-story RC SMRF was produced to further validate the damage indices by applying them to a more general earthquake-resistant structure. The model was examined to determine the types of damage as well as the locations of damage expected. Then, damage indices α and β were applied to the data in order to detect and localize the spalling of the concrete cover and yielding of the

reinforcement. Before any damage occurred, the damage indices remained constant and linear. However, when spalling of the concrete cover initiated and yielding of the reinforcement occurred, the damage indices deviated from the line. Therefore this proved that the indices were capable of damage detection.

Then, the damage index plots for each damage mode were examined further to evaluate the localization capabilities of the damage indices. Overall, several sensor pairs were found to be capable of damage localization, especially for the yielding of the reinforcement.

The next step for validation of the damage detection techniques for RC earthquake-resistant structures includes experimental testing. In preparation for the upcoming large-scale testing of the NEES Coupled Shear Wall, the instrumentation plan was developed and presented. DIC will be used to collect spatially dense data in areas where large amounts of local damages are expected, which will be valuable for damage detection. In order to employ damage detection methods to this type of data in the future, small scale experiments were performed using DIC to establish effective methods for data collection and evaluation. From these experiments, DIC was proved to be reliable for collecting displacement and strain data.

Although the satisfactory performance of the damage indices to detect yielding of the rebar, spalling of the concrete cover, and crushing of the concrete core was verified by two different simulation models, there is much work left to be done to completely develop and validate the proposed damage detection techniques. First, the indices must

be verified through experimental testing. This will be accomplished through testing of the 40% scale coupled shear wall structure at ATLSS in September 2013 and the series of component testing and scaled experiments for a future project described in Chapter 6. Additionally, change point detection methods could be a useful tool for finding when and where damage occurs. The methods introduced in Section 2.3 can potentially be used in conjunction with the damage indices introduced in this thesis to improve the damage detection techniques so that they do not rely on human interpretation. Lastly, the indices can be modified in order to further condense spatially dense data like from DIC.

References

American Concrete Institute (2008). *Building Code Requirements for Structural Concrete (ACI 318–08) and Commentary*.

ARAMIS: User Information-Hardware and Software. (2007) GOM: Optical Measuring Techniques, Germany.

Bahn, B. Y., & Hsu, C. T. T. (1998). "Stress-strain behavior of concrete under cyclic loading." *ACI Materials Journal*, *95*, 178-193.

Balageas, D. (2006). "Introduction to Structural Health Monitoring." *Structural Health Monitoring.* Chapter 1: 13-43. ISTE, California.

Banks, H. T., Inman, D. J., Leo, D. J., & Wang, Y. (1996). "An experimentally validated damage detection theory in smart structures." *Journal of Sound and Vibration*, *191*(5), 859-880.

Bernal, D. (2006). "Flexibility-based damage localization from stochastic realization results." *Journal of engineering mechanics*, *132*(6), 651-658.

Bozorgnia, Yousef and Bertero, Vitelmo V. (2006). *Earthquake Engineering: From Engineering Seismology to Performance-Based Engineering.* International Code Council. Taylor & Francis e-Library.

Carpinteri, A., Lacidogna, G., and Niccolini, J. (2011). "Damage analysis of reinforced concrete buildings by the acoustic emission technique." *Structural Control and Health Monitoring,* 18.6: 660-673.

Chang, F. K. (Ed.). (1999). *Structural Health Monitoring: The Demands and Challenges: Proceedings of the 3rd International Workshop on Structural Health Monitoring: the Demands and Challenges, Stanford University, Stanford, CA, September 12-14, 2001*. CRC Press.

Chang, P. C., & Liu, S. C. (2003). "Recent research in nondestructive evaluation of civil infrastructures." *Journal of materials in civil engineering*, *15*(3), 298-304.

Chintalapudi, K., Fu, T., Paek, J., Kothari, N., Rangwala, S., Caffrey, J., ... & Masri, S. (2006). "Monitoring civil structures with a wireless sensor network." *Internet Computing, IEEE*, *10*(2), 26-34.

Destrebecq, J. F., Toussaint, E., & Ferrier, E. (2011). "Analysis of cracks and deformations in a full scale reinforced concrete beam using a digital image correlation technique." *Experimental Mechanics*, *51*(6), 879-890.

Doebling, S. W., Farrar, C. R., & Prime, M. B. (1998). "A summary review of vibration-based damage identification methods". *Shock and vibration digest*, *30*(2), 91-105.

Dorvash, S., Pakzad, S.N., Labuz, E.L. (2012). *Statistics Based Localized Damage Detection using Vibration Response.* Lehigh University, Bethlehem, PA.

Dutton, M.G, Hoult, N.A., and Take, W.A. (2011). "Towards a Digital Image Correlation Based Strain Sensor." *International Workshop on Structural Health Monitoring*, Stanford, September 2011.

Eberl, C., Gianola, D. S., & Hemker, K. J. (2010). "Mechanical characterization of coatings using microbeam bending and digital image correlation techniques." *Experimental mechanics*, *50*(1), 85-97.

Farrar, C. R., Doebling, S. W., & Nix, D. A. (2001). "Vibration–based structural damage identification." *Philosophical Transactions of the Royal Society of London. Series A: Mathematical, Physical and Engineering Sciences*, *359*(1778), 131-149.

Farrar, C.R. and Worden, K. (2007). "An Introduction to Structural Health Monitoring." *Phil.Trans. R. Soc. A (2007),* 365:303-315.

FEMA P-749. (2010). *Earthquake-Resistant Design Concepts: An Introduction to the NEHRP Recommended Seismic Provisions for New Buildings and Other Structures.* National Institute of Building Sciences Building Seismic Safety Council, Washington, DC.

Fritzen, C. (2006). "Vibration-Based Techniques for Structural Health Monitoring." *Structural Health Monitoring.* Chapter 2: 45-224. ISTE, California.

Fugate, M. L., Sohn, H., & Farrar, C. R. (2001). "Vibration-based damage detection using statistical process control." *Mechanical Systems and Signal Processing*, *15*(4), 707-721.

Gu, H., Moslehy, Y., Sanders, D., Song, G., & Mo, Y. L. (2010). "Multi-functional smart aggregate-based structural health monitoring of circular reinforced concrete columns subjected to seismic excitations." *Smart Materials and Structures*, 19(6), 065026.

Gu, H., Song, G., Dhonde, H., Mo, Y. L., & Yan, S. (2006). "Concrete early-age strength monitoring using embedded piezoelectric transducers." *Smart Materials and Structures*, *15*(6), 1837.

Helfrick, M. N., Niezrecki, C., Avitabile, P., & Schmidt, T. (2011). "3D digital image correlation methods for full-field vibration measurement." *Mechanical Systems and Signal Processing*, *25*(3), 917-927.

Helm, J.D. (2008). "Digital Image Correlation for Specimens with Multiple Growing Cracks." *Experimental Mechanics.* 48: 753-762.

Hild,F. and Roux, S. (2006). "Digital Image Correlation: from Displacement Measurement to Identification of Elastic Properties- a Review." *Strain* (2006) 42:69-80.

Huston, D. (2011). *Structural Sensing, Health Monitoring, and Performance Evaluation.* Taylor & Francis, Boca Raton, Florida.

Hutchinson, T. C., & Chen, Z. (2006). "Improved image analysis for evaluating concrete damage." *Journal of Computing in Civil Engineering*, *20*(3), 210-216.

Kim, S.W. and Kim, N.S. (2011). "Applications of the Vibration-Based Monitoring System Using a Digital Image Correlation Technique to Long-Span Bridge Cables." *Structural Health Monitoring: Condition-Based Maintenance and Intelligent Structures, Proceedings of the Eighth International Workshop on Structural Health Monitoring,* Stanford University, 13-15 September 2011.

Kosmatka, Steven H., Kerkhoff, Beatrix, and Panarese, William C. (2002). *Design and Control of Concrete Mixtures*, EB001, 14th Edition. Portland Cement Association. Skokie, Illinois, USA, 358 pages.

Kurama, Y. C., and McGinnis, M. J. (2011). "NEESR-CR: Post-Tensioned Coupled Shear Wall Systems." *2011 NSF Engineering Research and Innovation Conference*.

Kurama, Y. C., and Shen, Q. (2004). "Posttensioned Hybrid Coupled Walls under Lateral Loads." *Journal of Structural Engineering*, 130(2), 297-309.

Kurama, Y. C., Weldon, B. D., and Shen, Q. (2006). "Experimental Evaluation of Posttensioned Hybrid Coupled Wall Subassemblages." *Journal of Structural Engineering*, 132(7), 1017-1029.

Labuz, E.L. (2011). *A Statistics Based Algorithm Using a Densely Clustered Sensor Network.* Lehigh University, Bethlehem, PA.

Labuz, E.L., Pakzad, S.N., and Cheng, L. (2011). "Damage Detection and Localization in Structures: A Statistics Based Algorithm Using a Densely Clustered Sensor Network." *Proceedings of the ASCE's 43rd Structures Congress*. Las Vegas, NV. pp. 53-64. DOI: 10.1061/41171(401)6.

Lecompte, D., Vantomme, J., and Sol, H. (2006). "Crack Detection in a Concrete Beam using Two Different Camera Techniques." *Structural Health Monitoring* 5(1):59-64.
Lee, U., & Shin, J. (2002). "A frequency response function-based structural damage identification method." *Computers & Structures*, *80*(2), 117-132.

Lee, J. J., & Shinozuka, M. (2006). 'Real-time displacement measurement of a flexible bridge using digital image processing techniques." *Experimental Mechanics*, 46(1), 105-114.

Li, H-N., Li, D-S., Song, G-B. (2004). "Recent applications of fiber optic sensors to health monitoring in civil engineering." *Engineering Structures (2004)***,** 26:1647-1657.

Liao, W. I., Wang, J. X., Song, G., Gu, H., Olmi, C., Mo, Y. L., ... & Loh, C. H. (2011). "Structural health monitoring of concrete columns subjected to seismic excitations using piezoceramic-based sensors." *Smart Materials and Structures*, 20(12), 125015.

Lowes, Laura N. (1999). *Finite Element Modeling of Reinforced Concrete Beam-Column Bridge Connections.* University of California, Berkeley. Chapter 2: Concrete Material Model and Chapter 3: Reinforcing Steel Material Model. 23-126.

Lu, Y., & Gao, F. (2005). "A novel time-domain auto-regressive model for structural damage diagnosis." *Journal of Sound and Vibration*, *283*(3), 1031-1049.

Lynch, J.P. and Loh, K.J. (2006). "A Summary Review of Wireless Sensors and Sensor Networks for Structural Health Monitoring." *The Shock and Vibration Digest* (2006), 38: 91- 128.

Lynch, J. P. (2007). "An overview of wireless structural health monitoring for civil structures."*Philosophical Transactions of the Royal Society A: Mathematical, Physical and Engineering Sciences*, *365*(1851), 345-372.

Maeck, J., Abdel Wahab, M., Peeters, B., De Roeck, G., De Visscher, J., De Wilde, W. P., ... & Vantomme, J. (2000). "Damage identification in reinforced concrete structures by dynamic stiffness determination." *Engineering structures*,*22*(10), 1339-1349.

Mander, J.B., Priestley, M.J.N., and Park, R.(1988a). "Theoretical stress-strain model for confined concrete." *Journal of Structural Engineering* . 114.8:1804-1826.

Mander, J.B., Priestley, M.J.N., and Park, R. (1988b). "Observed stress-strain behavior of confined concrete." *Journal of Structural Engineering.* 114.8: 1827-1849.

Mehta, P. K., & Monteiro, P. J. M. (1993). *Concrete: Structure, Properties, and Materials*. Prentice-Hall, Englewood Cliffs, NJ.

Meng, Yanyu, and Shi Yan. (2012) "Statistical algorithm for damage detection of concrete beams based on piezoelectric smart aggregate." *Transactions of Tianjin University*. 18 432-440.

Moehle, J. P., Hooper, J. D., & Lubke, C. D. (2008). Seismic design of reinforced concrete special moment frames: a guide for practicing engineers. *NEHRP Seismic Design Technical Brief*, (1).

Nawy, Edward G. (2000). *Reinforced Concrete: a Fundamental Approach*, 4th Ed., Prentice Hall, Upper Saddle River, New Jersey. Chapter 3: Concrete and Chapter 4: Reinforced Concrete, 20-88.

NEES (2013). "Hybrid Simulation and Real-time Hybrid Simulation Resources in the NEEShub." *NEEShub*.< https://nees.org/wiki/RTHSwiki> (Aug. 5, 2013).

Nigro, M.B., Pakzad, S.N., and Dorvash, S. (2013). *Localized Structural Damage Detection: A Change Point Analysis.* Lehigh University, Bethlehem, PA.

Nonis, C., Niezrecki, C., Yu, Tzu-Yang, Ahmed, S., Su, Che-Fu, (2013). "Structural Health Monitoring of Bridges using Digital Image Correlation." *Health Monitoring of Structural and Biological Systems 2013*. SPIE Vol. 8695,869507.

Pan, B., Huimin, X., Zhaoyang, W., Qian, K., and Wang, Z. (2008). "Study on subset size selection in digital image correlation for speckle patterns." *Optics Express* (12 May 2008),Vol. 16, No. 10.

Pandey, A. K., & Biswas, M. (1994). "Damage detection in structures using changes in flexibility." *Journal of sound and vibration*, *169*(1), 3-17.

Prakash, V., Powell, G., and Campbell, S. (1993). "DRAIN-2DX Base Program Description and User Guide." 1.10.

Poudel, U.P., Fu, G., and Ye, J. (2004). "Structural damage detection using digital video imaging technique and wavelet transformation." *Journal of Sound and Vibration* (2005) 286:869-895.

Rens, K. L., Wipf, T. J., & Klaiber, F. W. (1997). "Review of nondestructive evaluation techniques of civil infrastructure." *Journal of performance of constructed facilities*, *11*(4), 152-160.

Salmon, C., Johnson, J.E., and Malhas, F.A. (2009). *Steel Structures Design and Behavior: Emphasizing Load and Resistance Factor Design,* 5th Ed. Prentice Hall, Upper Saddle River, New Jersey.

Shen, Q., Kurama, Y. C., and Weldon, B. D. (2006). "Seismic Design and Analytical Modeling of Posttensioned Hybrid Coupled Wall Subassemblages." *Journal of Structural Engineering*, 132(7), 1030-1040.

Sohn, H., Farrar, C.R., Hunter, N.F, and Worden, K. (2001). "Structural Health Monitoring Using Statistical Pattern Recognition Techniques." *Transactions-American Society of Mechanical Engineers Journal of Dynamic Systems Measurement And Control*, 123.4: 706-711.

Sohn, H., Farrar, C.R., Hemez, F., Shunk, D.D., Stinemates, D.W, Nadler, B.R., and Czarnecki, J. (2004). "A Review of Structural Health Monitoring Literature 1996-2001." *Los Alamos National Laboratory Report LA-13976-MS.*

Song, G., Gu, H., and Mo,Y.(2008). "Smart aggregates: multi-functional sensors for concrete structures—a tutorial and a review." *Smart Materials and Structures,* 17.3: 033001.

Villemure, I. (1995). *Damage Indices for Reinforced Concrete Frames: Evaluation and Correlation.* The University of British Columbia. Vancouver, BC, Canada.

Weldon, B. D., and Kurama, Y. C. (2010). "Experimental Evaluation of Posttensioned Precast Concrete Coupling Beams." *Journal of Structural Engineering,* 136(9), 1066-1077.

Weldon, B. D., and Kurama, Y. C. (2007). "Nonlinear Behavior of Precast Concrete Coupling Beams under Lateral Loads." *Journal of Structural Engineering,* 133(11), 1571-1581.

Worden, K., Manson, G., & Fieller, N. R. J. (2000). "Damage detection using outlier analysis." *Journal of Sound and Vibration*, *229*(3), 647-667.

Yan, S., Sun, W., Song, G., Gu, H., Huo, L. S., Liu, B., & Zhang, Y. G. (2009). "Health monitoring of reinforced concrete shear walls using smart aggregates." *Smart Materials and Structures*, 18(4), 047001.

Yan, Y. J., Cheng, L., Wu, Z. Y., & Yam, L. H. (2007). "Development in vibration-based structural damage detection technique." *Mechanical Systems and Signal Processing*, *21*(5), 2198-2211.

Yao, R. and Pakzad, S.N.(2012). "Autoregressive statistical pattern recognition algorithms for damage detection in civil structures." *Mech. Syst. Signal Process.* doi:10.1016/j.ymssp.2012.02.014

Yao, R, Tillotson, M.L., Pakzad, S.N., and Pan, Y. (2012). "Regression-Based Algorithms for Structural Damage Identification and Localization." *Proceedings of the ASCE's 44th Structures Congress.* Chicago, IL. pp. 747-756. DOI:10.1061/9780784412367.067

Yehia, S., Abudayyeh, O., Nabulsi, S., & Abdelqader, I. (2007). "Detection of common defects in concrete bridge decks using nondestructive evaluation techniques." *Journal of Bridge Engineering*, *12*(2), 215-225.

Appendix A: Example Calculations from Section Analysis around Yielding

Strains, Stresses, and Forces in Coupling Beam's Right End (BC2)

Material Properties:

Unconfined Concrete

$$f_{UC} := \begin{pmatrix} 0 \\ 3.3113 \\ 5.58 \\ 6 \\ 5.9 \\ 0 \end{pmatrix} \cdot ksi \qquad \varepsilon_{UC} := \begin{pmatrix} 0 \\ 0.00075 \\ 0.0015 \\ 0.002 \\ 0.003 \\ 0.004 \end{pmatrix}$$

Confined Concrete

$$f_{CC} := \begin{pmatrix} 0 \\ 4 \\ 9 \\ 12 \\ 12.6 \\ 10 \end{pmatrix} \cdot ksi \qquad \varepsilon_{CC} := \begin{pmatrix} 0 \\ 0.00091 \\ 0.0033 \\ 0.007 \\ 0.013 \\ 0.0702 \end{pmatrix}$$

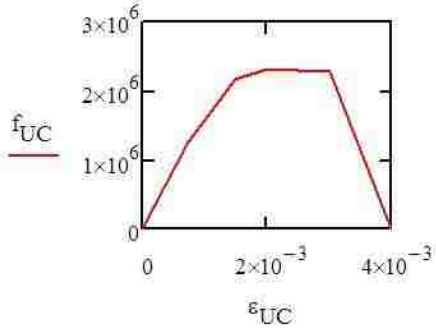

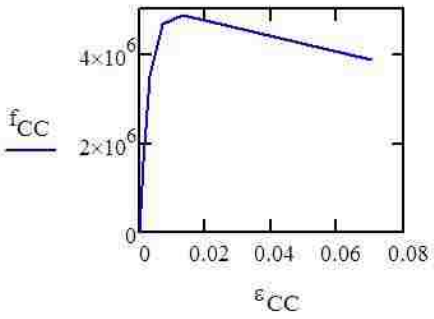

ED Steel

$$f_{steel} := \begin{pmatrix} 0 \\ 60 \\ 80 \\ 98 \\ 107 \\ 109 \end{pmatrix} \cdot ksi \qquad \varepsilon_{steel} := \begin{pmatrix} 0 \\ 0.00207 \\ 0.015 \\ 0.04 \\ 0.08 \\ 0.12 \end{pmatrix}$$

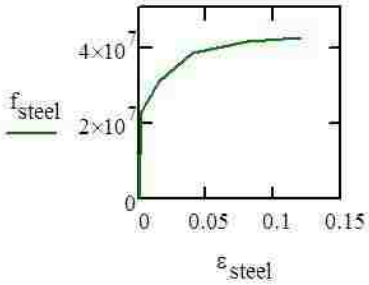

Section Geometry

$b_{total} := 7.25 \cdot in$ bottom cover $d_{cover} := .625 \cdot in$ $A_s := 2 \cdot 0.11 \cdot in^2 = 0.22 \cdot in^2$

$h := 9.625 \cdot in$ $b_{core} := 6 \cdot in$ $E_{ps} := 28500 \, ksi$ $A_{ps} := 0.565 \, in^2$

Yield of ED 2 on 1st Story : Step 92 is just before yield of ED2, Step 93 is at yield of ED2, and Step 94 is just after yield of ED2

Strains output from DRAIN

$$\varepsilon_{92} := \begin{pmatrix} 0.002337531 \\ 0.001772969 \\ 0.001264863 \\ 0.0020344 \\ 0.00078601 \end{pmatrix} \quad \varepsilon_{93} := \begin{pmatrix} 0.002368747 \\ 0.001796403 \\ 0.001281294 \\ 0.0020625 \\ 0.00079374 \end{pmatrix} \quad \varepsilon_{94} := \begin{pmatrix} 0.002399598 \\ 0.001819092 \\ 0.001296636 \\ 0.0020928 \\ 0.00080077 \end{pmatrix}$$

Axial force in beam at each step output from DRAIN: $\text{AxialR} := (-75.070 \ \ -75.380 \ \ -75.670)^{T} \cdot \text{kip}$

Force in PT tendon at each step output from DRAIN: $\text{PTforce} := (65.580 \ \ 65.600 \ \ 65.620)^{T} \cdot \text{kip}$

Section Analysis at Step 92 (just before yielding of ED 2)

$\varepsilon_{\text{section}} := \varepsilon_{92}$ neutral axis depth: $c := 2.5877684\text{in}$

strain and stress in concrete cover at top outer fiber:

$$\varepsilon_{co} := \varepsilon_{\text{section}_{0,0}}$$

$$f_{co} := \text{linterp}(\varepsilon_{UC}, f_{UC}, \varepsilon_{co}) = 5.9662\text{ksi}$$

strain and stress in concrete at UC/CC interface:

$$\varepsilon_{int} := \varepsilon_{\text{section}_{1,0}}$$

$$f_{intUC} := \text{linterp}(\varepsilon_{UC}, f_{UC}, \varepsilon_{int}) = 5.8093\text{ksi}$$

$$f_{intCC} := \text{linterp}(\varepsilon_{CC}, f_{CC}, \varepsilon_{int}) = 5.8054\text{ksi}$$

strain and stress in compression ED:

$$\varepsilon_{sc} := \varepsilon_{\text{section}_{4,0}}$$

$$f_{sc} := \text{linterp}(\varepsilon_{steel}, f_{steel}, |\varepsilon_{sc}|) = 22.7829\text{ksi}$$

strain and stress in tension ED:

$$\varepsilon_{st} := \varepsilon_{\text{section}_{3,0}}$$

$$f_{st} := \text{linterp}(\varepsilon_{steel}, f_{steel}, \varepsilon_{st}) = 58.9681\text{ksi}$$

depth of concrete core in compression: $d_{cc} := c - d_{cover} = 1.9628\text{in}$

depth of UC concrete with slope 1 stiffness: $z_1 := 0.373664619\text{in}$

depth of CC concrete with slope 1 stiffness: $z_2 := 1.580351212\text{in} = 1.5804\text{in}$

depth of CC concrete with slope 1 stiffness: $z_2 := 1.580351212\text{in} = 1.5804\text{in}$

$$x_{UC92} := \begin{pmatrix} d_{cover} \\ d_{cover} \\ z_1 \\ 0 \\ 0 \end{pmatrix} \qquad f_{UC92} := \begin{pmatrix} 0 \\ f_{intUC} \\ 6\cdot\text{ksi} \\ f_{co} \\ 0 \end{pmatrix}$$

stress distribution for UC cover

$$x_{CC92} := \begin{pmatrix} c \\ c \\ z_2 \\ d_{cover} \\ d_{cover} \end{pmatrix} \qquad f_{CC92} := \begin{pmatrix} 0 \\ 0 \\ 4\cdot\text{ksi} \\ f_{intCC} \\ 0 \end{pmatrix}$$

stress distribution for CC core

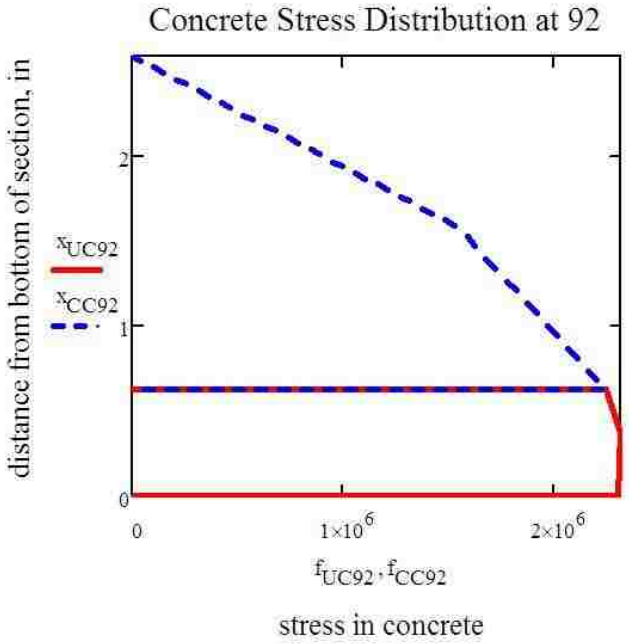

C force from compression ED: $C_s := f_{sc}\cdot A_s = 5.0122\text{kip}$

C force from UC: $C_{uc} := \left[\frac{1}{2}\left(f_{co} + 6\cdot\text{ksi}\right)\cdot z_1 + \frac{1}{2}\cdot\left(6\cdot\text{ksi} + f_{intUC}\right)\cdot\left(d_{cover} - z_1\right)\right]\cdot b_{total} = 26.968\text{kip}$

C force from CC: $C_{cc} := \left[\frac{1}{2}\cdot(4\cdot\text{ksi})\cdot\left(c - z_2\right) + \frac{1}{2}\cdot\left(f_{intCC} + 4\cdot\text{ksi}\right)\cdot\left(z_2 - d_{cover}\right)\right]\cdot b_{total} = 48.565\text{kip}$

C force from concrete: $C_{concrete} := C_{uc} + C_{cc} = 75.533\text{kip}$ compare to $AxialR_{0,0} = -75.07\text{kip}$

Total Compression Force: $C_{total} := C_{concrete} + C_s = 80.5453\text{kip}$

T force from tension ED: $T := f_{st} \cdot A_s = 12.973\text{kip}$

Force from PT: $PT := PTforce_{0,0} = 65.58\text{kip}$

Check Equilibrium: $ForceBalance := T - C_{total} + PT = -1.9923\text{kip}$ OK

Section Analysis at Step 93 (around yielding of ED 2)

$\varepsilon_{section} := \varepsilon_{93}$ $c := 2.586674174\text{in}$

$\varepsilon_{co} := \varepsilon_{section_{0,0}}$

$f_{co} := linterp(\varepsilon_{UC}, f_{UC}, \varepsilon_{co}) = 5.9631\text{ksi}$

$\varepsilon_{int} := \varepsilon_{section_{1,0}}$

$f_{intUC} := linterp(\varepsilon_{UC}, f_{UC}, \varepsilon_{int}) = 5.829\text{ksi}$ $f_{intCC} := linterp(\varepsilon_{CC}, f_{CC}, \varepsilon_{int}) = 5.8544\text{ksi}$

$\varepsilon_{sc} := \varepsilon_{section_{4,0}}$

$f_{sc} := linterp(\varepsilon_{steel}, f_{steel}, |\varepsilon_{sc}|) = 23.007\text{ksi}$

$\varepsilon_{sc} := \varepsilon_{section_{4,0}}$

$f_{st} := linterp(\varepsilon_{steel}, f_{steel}, \varepsilon_{st}) = 58.9681\text{ksi}$

$d_{cc} := c - d_{cover} = 1.9617\cdot\text{in}$ $z_1 := 0.40267199\text{in}$ $z_2 := 1.59295318\text{in}$

$$x_{UC93} := \begin{pmatrix} d_{cover} \\ d_{cover} \\ z_1 \\ 0 \\ 0 \end{pmatrix} \qquad f_{UC93} := \begin{pmatrix} 0 \\ f_{intUC} \\ 6\cdot\text{ksi} \\ f_{co} \\ 0 \end{pmatrix}$$

$$x_{CC93} := \begin{pmatrix} c \\ c \\ z_2 \\ d_{cover} \\ d_{cover} \end{pmatrix} \qquad f_{CC93} := \begin{pmatrix} 0 \\ 0 \\ 4\cdot\text{ksi} \\ f_{intCC} \\ 0 \end{pmatrix}$$

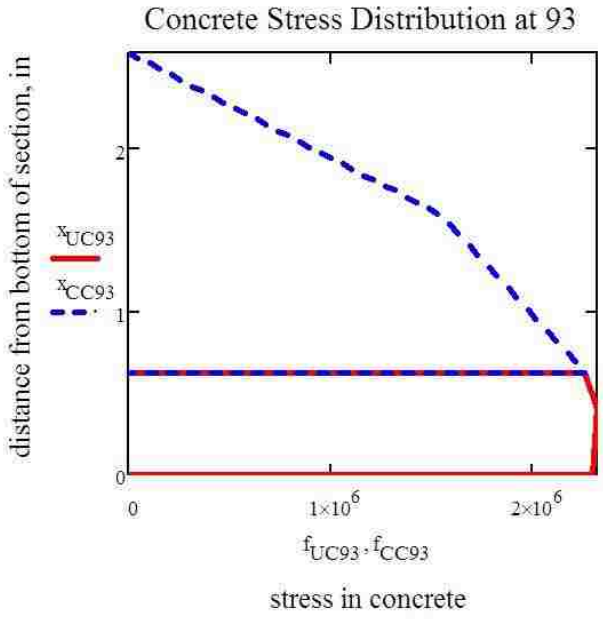

$C_s := f_{sc} \cdot A_s = 5.0615\text{kip}$

$C_{uc} := \left[\frac{1}{2}\left(f_{co} + 6\cdot\text{ksi}\right)\cdot z_1 + \frac{1}{2}\cdot\left(6\cdot\text{ksi} + f_{intUC}\right)\cdot\left(d_{cover} - z_1\right)\right]\cdot 7.25\cdot\text{in} = 26.9958\text{kip}$

$C_{cc} := \left[\frac{1}{2}\cdot(4\cdot\text{ksi})\cdot\left(c - z_2\right) + \frac{1}{2}\cdot\left(f_{intCC} + 4\cdot\text{ksi}\right)\cdot\left(z_2 - d_{cover}\right)\right]\cdot b_{total} = 48.9864\text{kip}$

$C_{concrete} := C_{uc} + C_{cc} = 75.9822\text{kip}$ compared to $\text{AxialR}_{1,0} = -75.38\text{kip}$

$C_{total} := C_{uc} + C_{cc} + C_s = 81.0437\text{kip}$

$T := f_{st} \cdot A_s = 12.973\text{kip}$

$PT := \text{PTforce}_{1,0} = 65.6\text{kip}$

$\text{ForceBalance} := T - C_{total} + PT = -2.4708\text{kip}$ OK

Section Analysis at Step 94 (just after yielding of ED 2)

$\varepsilon_{section} := \varepsilon_{94}$ $c := 2.583518831\text{in}$

$\varepsilon_{co} := \varepsilon_{\text{section}\,0,0}$

$f_{co} := \text{linterp}\left(\varepsilon_{UC}, f_{UC}, \varepsilon_{co}\right) = 5.96\text{ksi}$

$\varepsilon_{int} := \varepsilon_{\text{section}\,1,0}$

$f_{intUC} := \text{linterp}\left(\varepsilon_{UC}, f_{UC}, \varepsilon_{int}\right) = 5.848\text{ksi}$ $f_{intCC} := \text{linterp}\left(\varepsilon_{CC}, f_{CC}, \varepsilon_{int}\right) = 5.9019\text{ksi}$

$f_{intUC} := linterp(\varepsilon_{UC}, f_{UC}, \varepsilon_{int}) = 5.848ksi$ $f_{intCC} := linterp(\varepsilon_{CC}, f_{CC}, \varepsilon_{int}) = 5.9019ksi$

$\varepsilon_{sc} := \varepsilon_{section_{4,0}}$

$f_{sc} := linterp(\varepsilon_{steel}, f_{steel}, |\varepsilon_{sc}|) = 23.2107ksi$

$\varepsilon_{st} := \varepsilon_{section_{3,0}}$

$f_{st} := linterp(\varepsilon_{steel}, f_{steel}, \varepsilon_{st}) = 60.0353ksi$

$d_{cc} := c - d_{cover} = 1.9585in$ $z_1 := 0.430225907in$ $z_2 := 1.60377055in$

$$x_{UC94} := \begin{pmatrix} d_{cover} \\ d_{cover} \\ z_1 \\ 0 \\ 0 \end{pmatrix} \quad f_{UC94} := \begin{pmatrix} 0 \\ f_{intUC} \\ 6 \cdot ksi \\ f_{co} \\ 0 \end{pmatrix}$$

$$x_{CC94} := \begin{pmatrix} c \\ c \\ z_2 \\ d_{cover} \\ d_{cover} \end{pmatrix} \quad f_{CC94} := \begin{pmatrix} 0 \\ 0 \\ 4 \cdot ksi \\ f_{intCC} \\ 0 \end{pmatrix}$$

Concrete Stress Distribution at 94

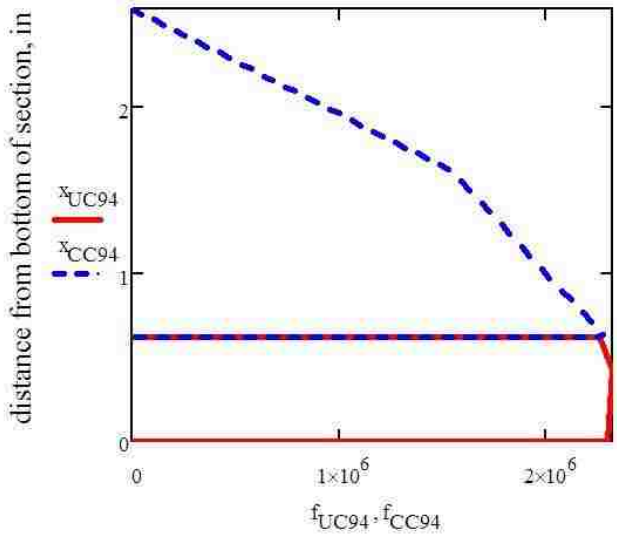

$C_s := f_{sc} \cdot A_s = 5.1064\text{kip}$

$C_{uc} := \left[\frac{1}{2}\left(f_{co} + 6\cdot\text{ksi}\right)\cdot z_1 + \frac{1}{2}\cdot\left(6\cdot\text{ksi} + f_{intUC}\right)\cdot\left(d_{cover} - z_1\right)\right]\cdot b_{total} = 27.0179\text{kip}$

$C_{cc} := \left[\frac{1}{2}\cdot(4\cdot\text{ksi})\cdot\left(c - z_2\right) + \frac{1}{2}\cdot\left(f_{intCC} + 4\cdot\text{ksi}\right)\cdot\left(z_2 - d_{cover}\right)\right]\cdot b_{total} = 49.3386\text{kip}$

$C_{concrete} := C_{uc} + C_{cc} = 76.3565\text{kip}$ compared to $\text{AxialR}_{2,0} = -75.67\text{kip}$

$C_{total} := C_{uc} + C_{cc} + C_s = 81.4628\text{kip}$

$T := f_{st} \cdot A_s = 13.2078\text{kip}$

$PT := \text{PTforce}_{2,0} = 65.62\text{kip}$

$\text{ForceBalance} := T - C_{total} + PT = -2.6351\text{kip}$ OK

Concrete Stress Distribution Around Yield of 1st Story ED2

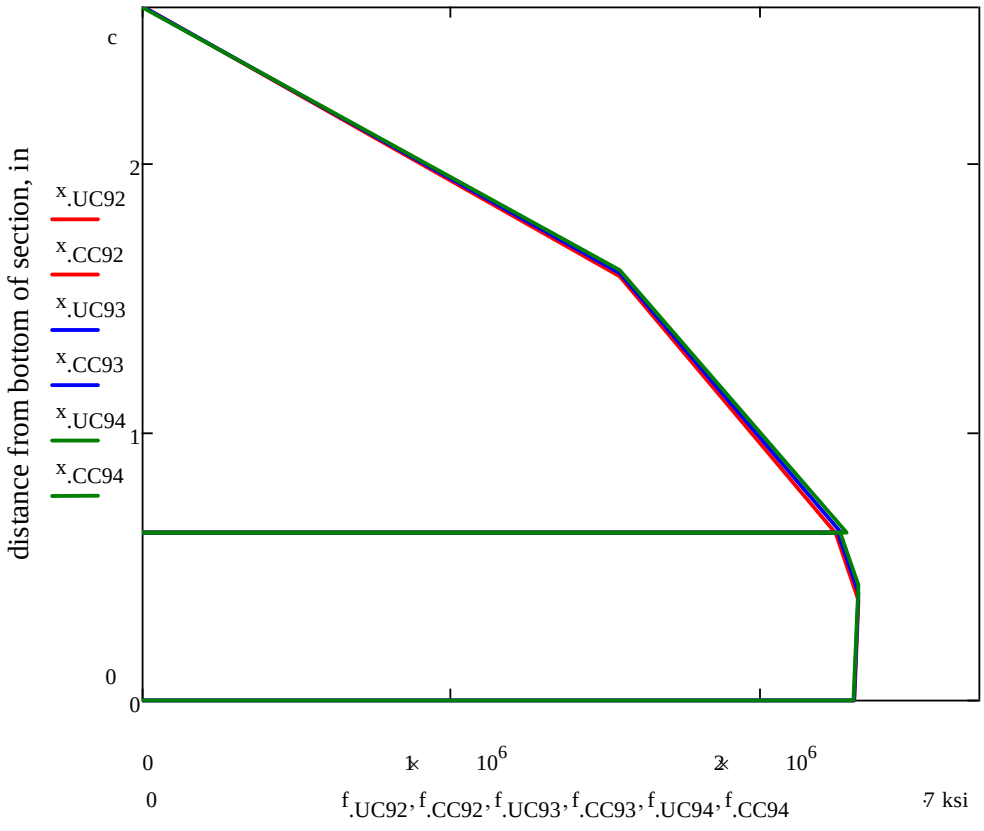

Table A.1: Changes in forces due to damage from section analysis of BC2

			% change per kip of Base Shear						
Description	Index #	ΔNA	ΔC in UC	ΔC in CC	ΔC in Concrete	ΔC in ED	ΔT in ED	ΔForce in PT	ΔAxial in Beam
Yield	93-92	-0.1%	-2.4%	-37.0%	-39.4%	-4.3%	15.7%	1.8%	-27.2%
After Yield	94-93	-0.3%	-2.0%	-32.0%	-34.0%	-4.1%	5.1%	1.8%	-26.4%
Before Spall	100-99	-0.3%	0.3%	-31.7%	-31.4%	-4.1%	1.0%	1.9%	-22.1%
After Spall	101-100	-0.2%	0.6%	-34.8%	-34.2%	-4.4%	1.0%	1.9%	-24.0%
Before Crush	357-356	-0.1%	12.9%	-63.6%	-50.7%	-0.9%	7.0%	16.7%	0.0%
After Crush	358-357	-0.3%	10.7%	-38.5%	-27.8%	-0.8%	6.1%	15.0%	50.0%

Appendix B.1: Additional Damage Index Plots for Steel Yielding using 1st Story Sensors in DRAIN Model

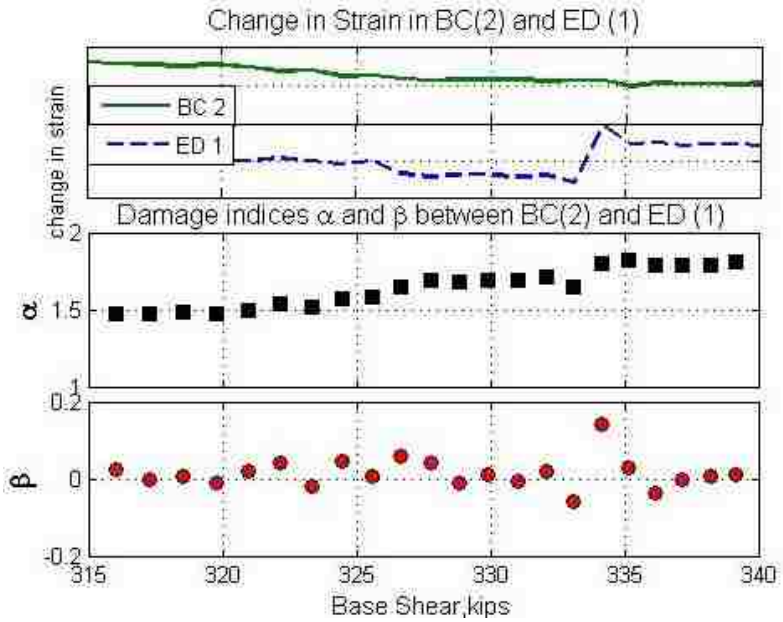

Figure B.1.1: Detection of ED steel yielding by 1st story damage index ED1/BC2

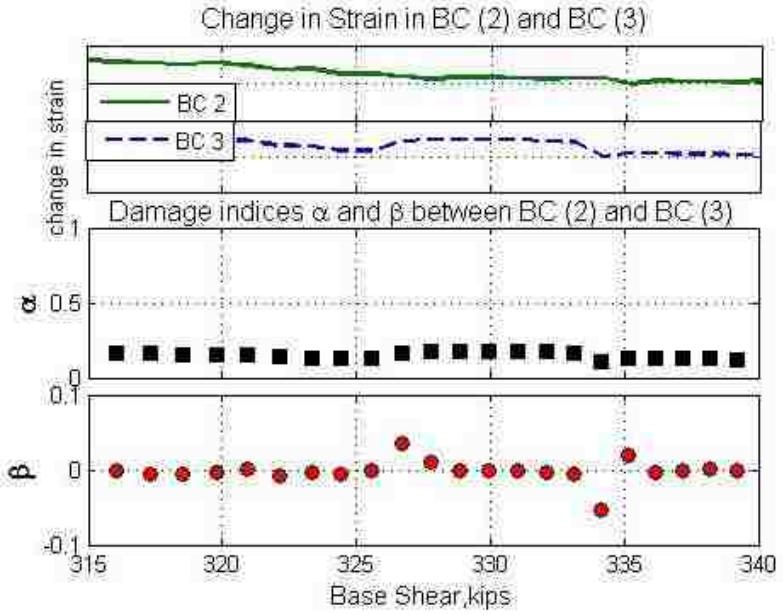

Figure B.1.2: Detection of ED steel yielding by 1st story damage index BC3/BC2

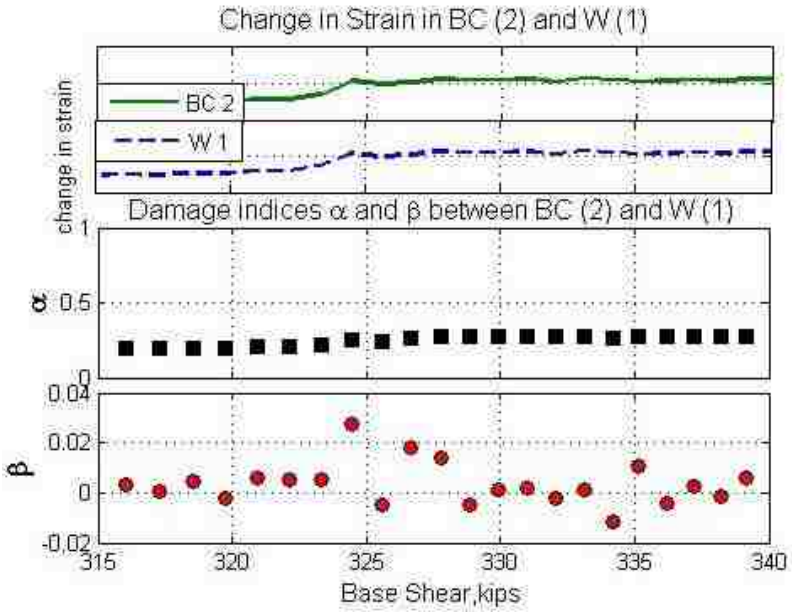

Figure B.1.3: Detection of ED steel yielding by 1st story damage index W1/BC2

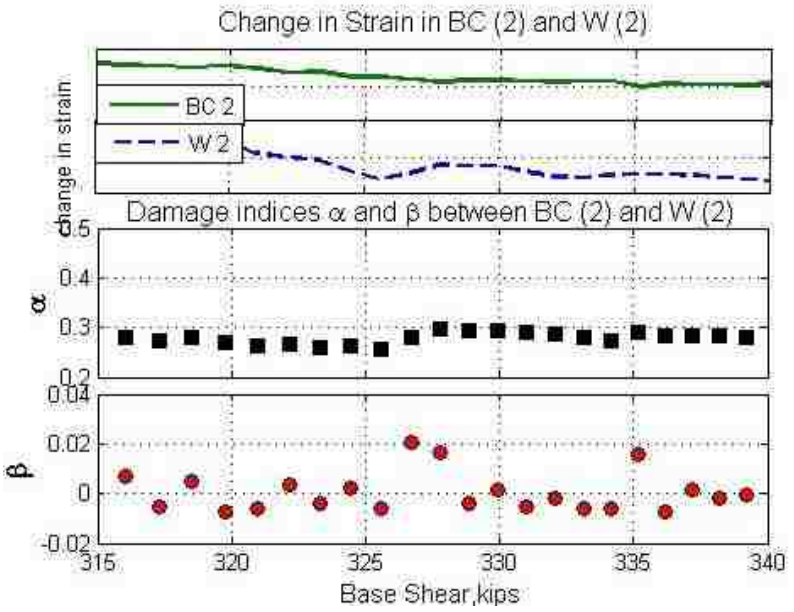

Figure B.1.4: Detection of ED steel yielding by 1st story damage index W2/BC2

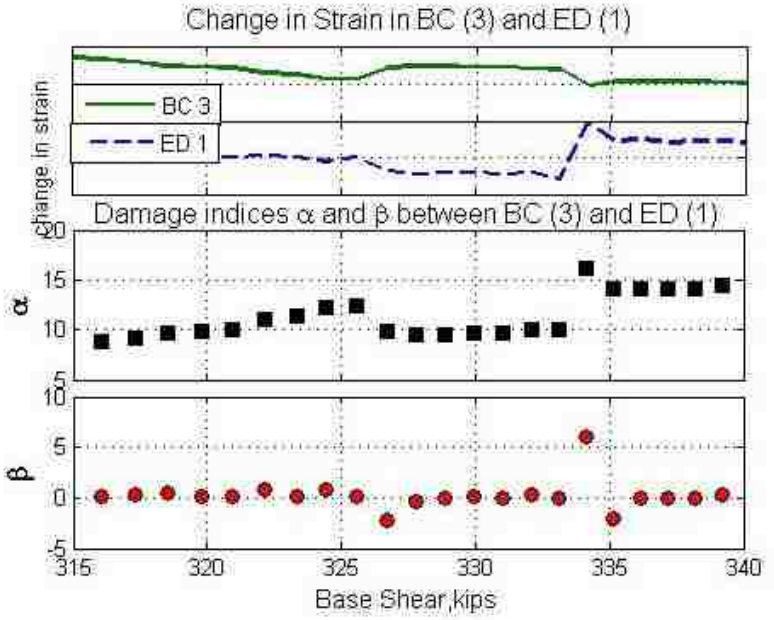

Figure B.1.5: Detection of ED steel yielding by 1st story damage index ED1/BC3

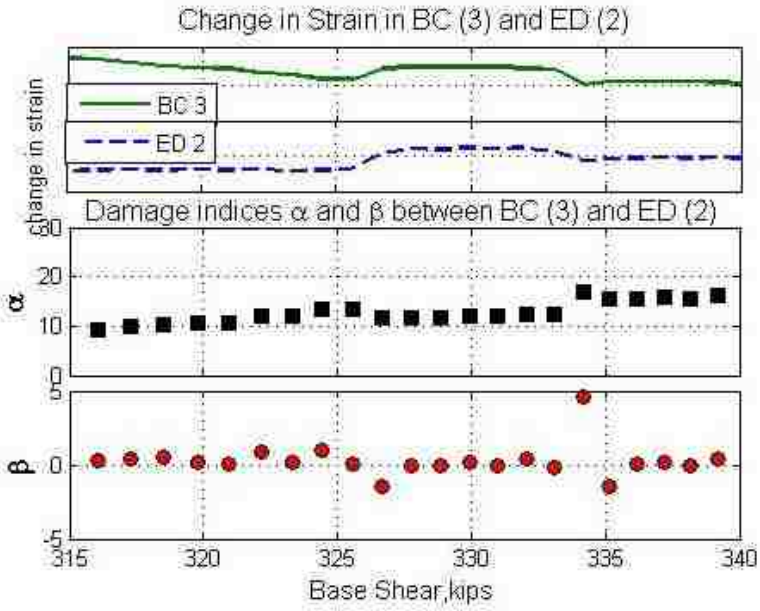

Figure B.1.6: Detection of ED steel yielding by 1st story damage index ED2/BC3

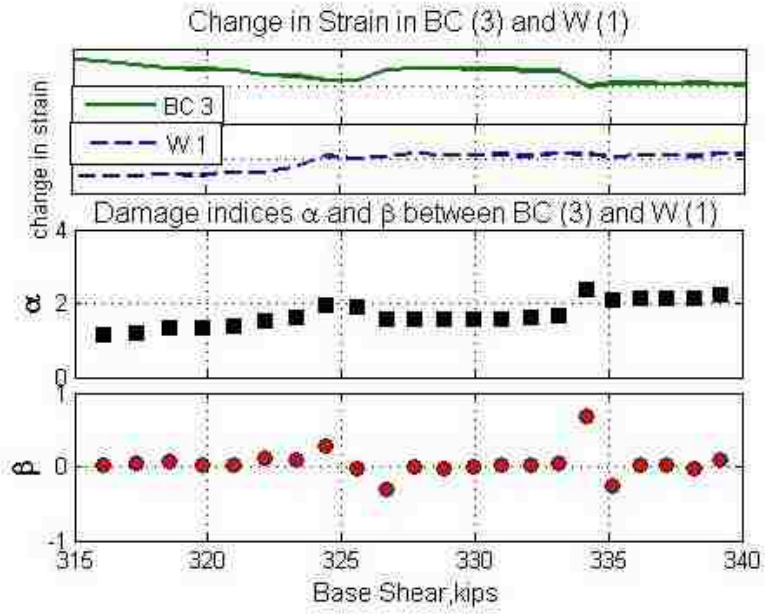

Figure B.1.7: Detection of ED steel yielding by 1st story damage index W1/BC3

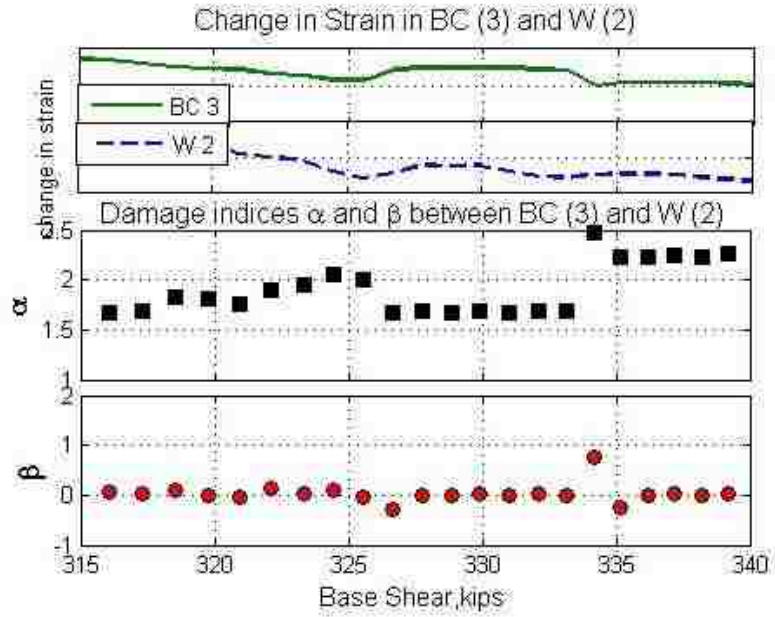

Figure B.1.8: Detection of ED steel yielding by 1st story damage index W2/BC3

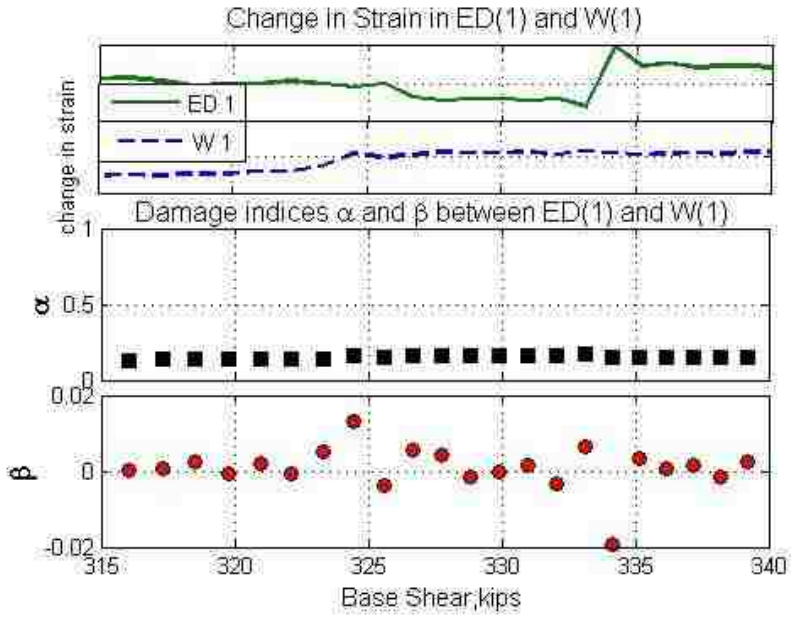

Figure B.1.9: Detection of ED steel yielding by 1st story damage index W1/ED1

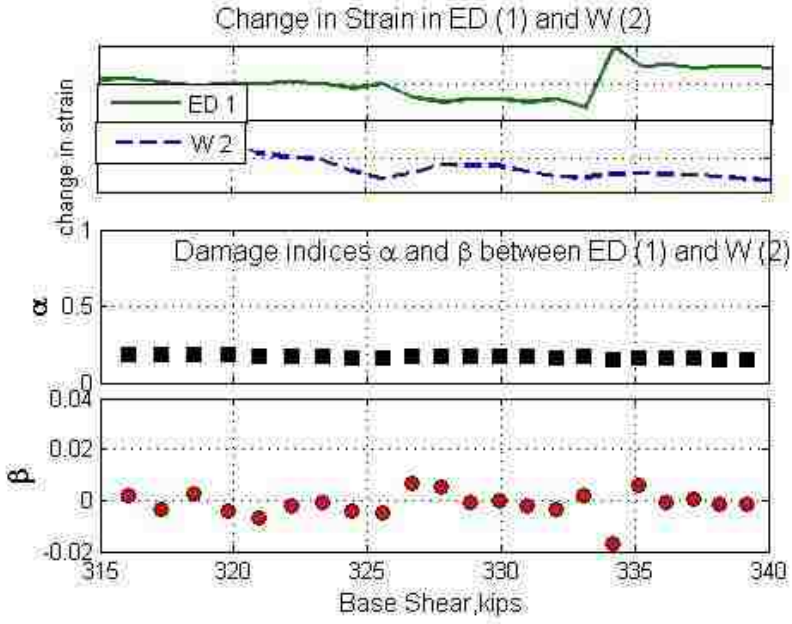

Figure B.1.10: Detection of ED steel yielding by 1st story damage index W2/ED1

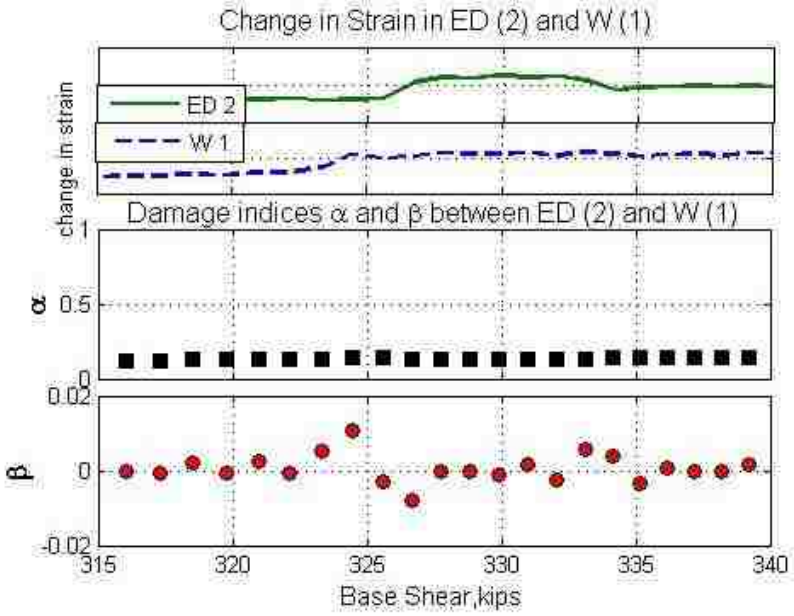

Figure B.1.11: Detection of ED steel yielding by 1st story damage index W1/ED2

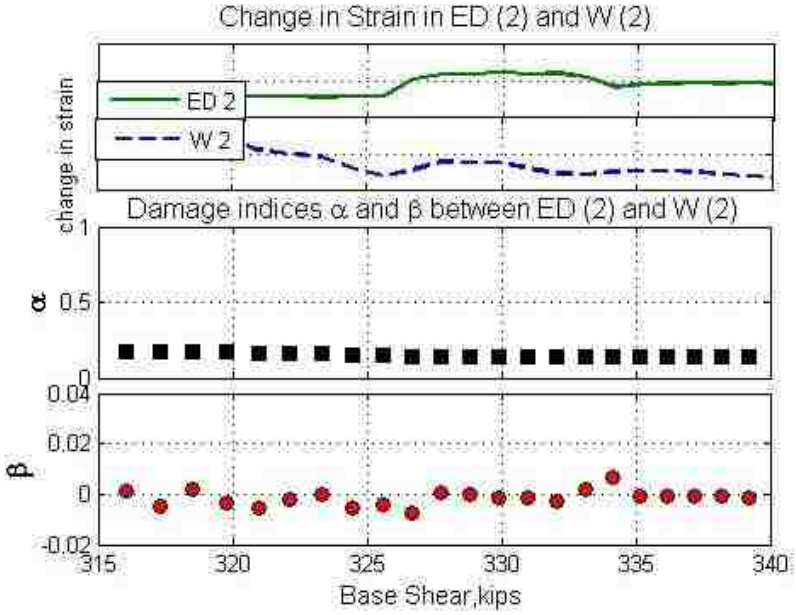

Figure B.1.12: Detection of ED steel yielding by 1st story damage index W2/ED2

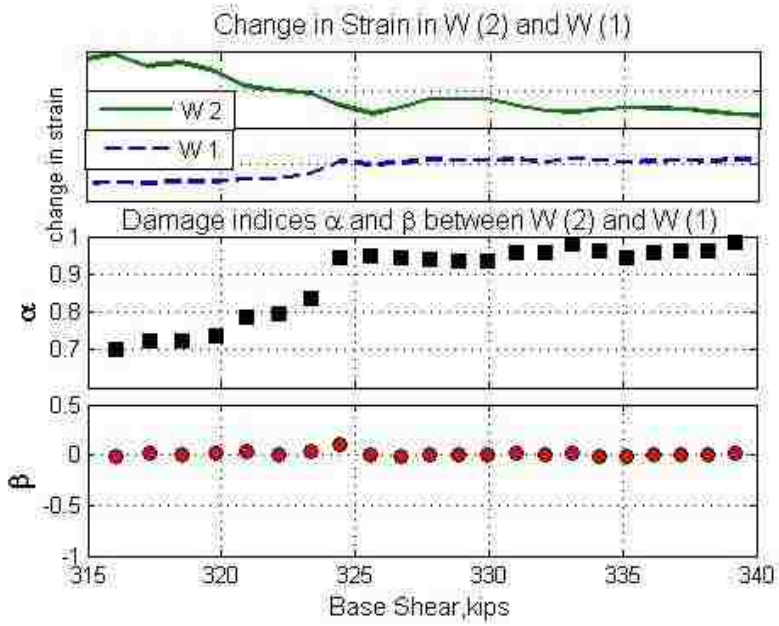

Figure B.1.13: Detection of ED steel yielding by 1st story damage index W1/W2

Appendix B.2: Additional Damage Index Plots for Concrete Cover Spalling using 1st Story Sensors in DRAIN Model

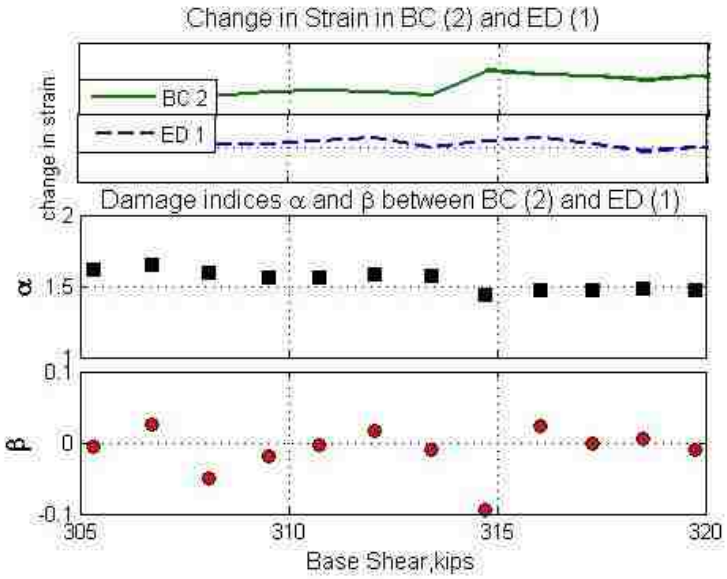

Figure B.2.1: Detection of concrete cover spalling by 1st story damage index ED1/BC2

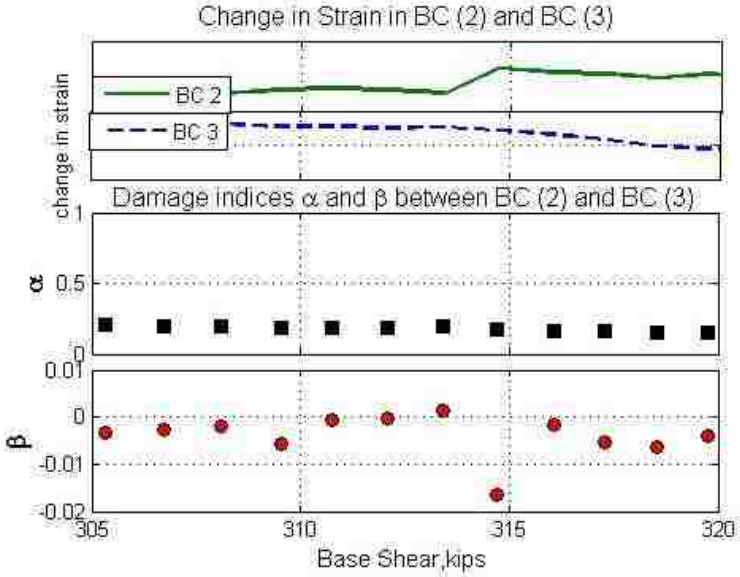

Figure B.2.2: Detection of concrete cover spalling by 1st story damage index BC3/BC2

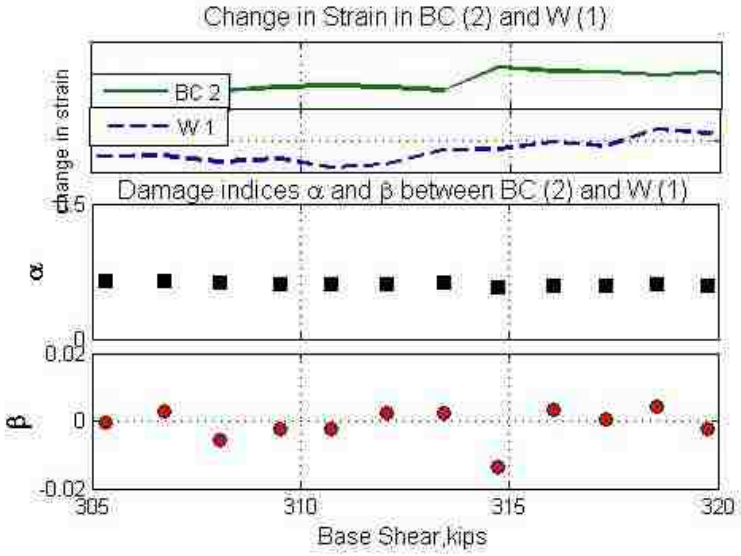

Figure B.2.3: Detection of concrete cover spalling by 1st story damage index W1/BC2

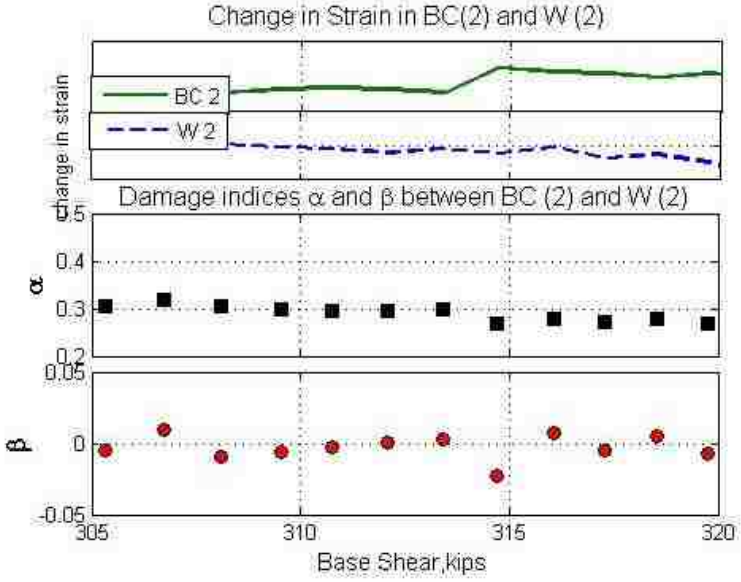

Figure B.2.4: Detection of concrete cover spalling by 1st story damage index W2/BC2

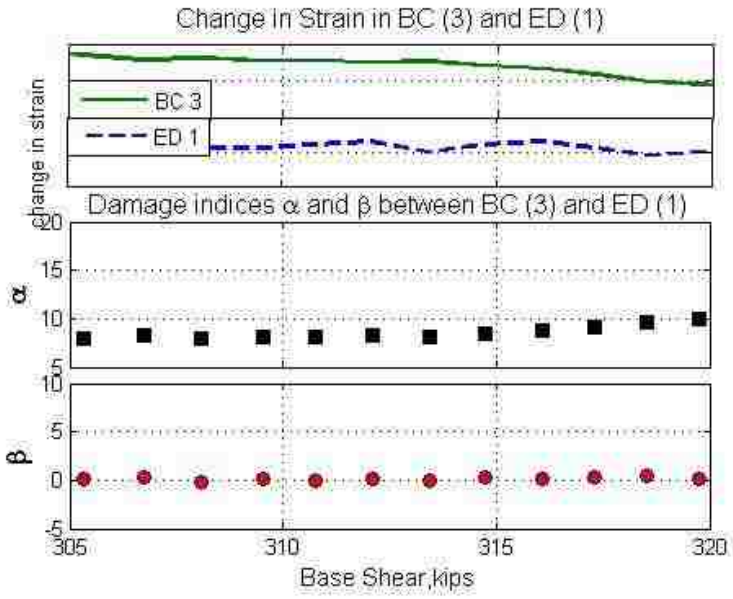

Figure B.2.5: Concrete cover spalling not detected by 1st story damage index ED1/BC3

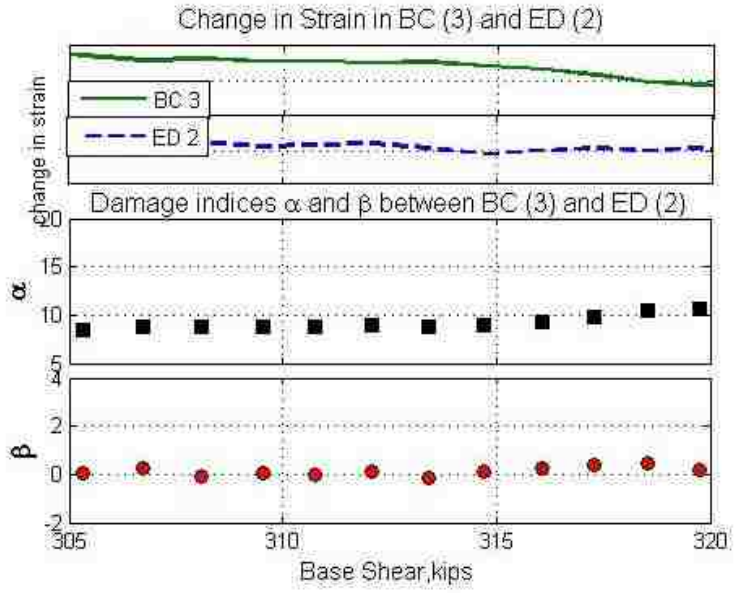

Figure B.2.6: Concrete cover spalling not detected by 1st story damage index ED2/BC3

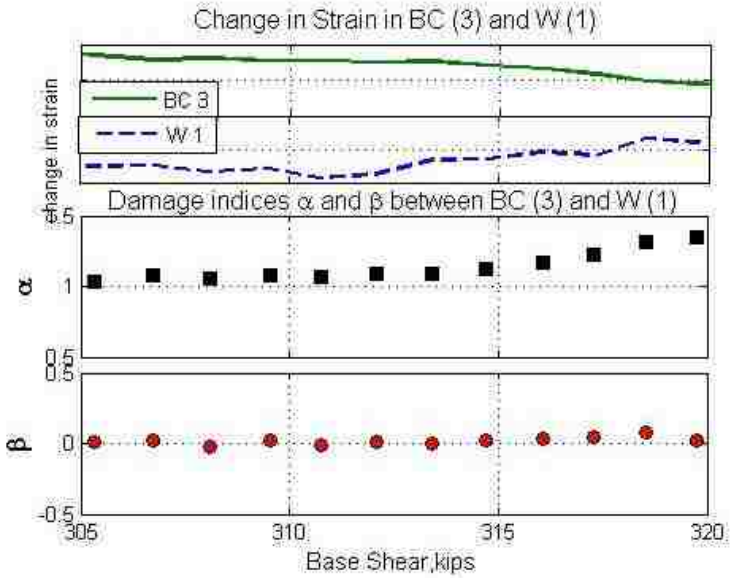

Figure B.2.7: Concrete cover spalling not detected by 1st story damage index W1/BC3

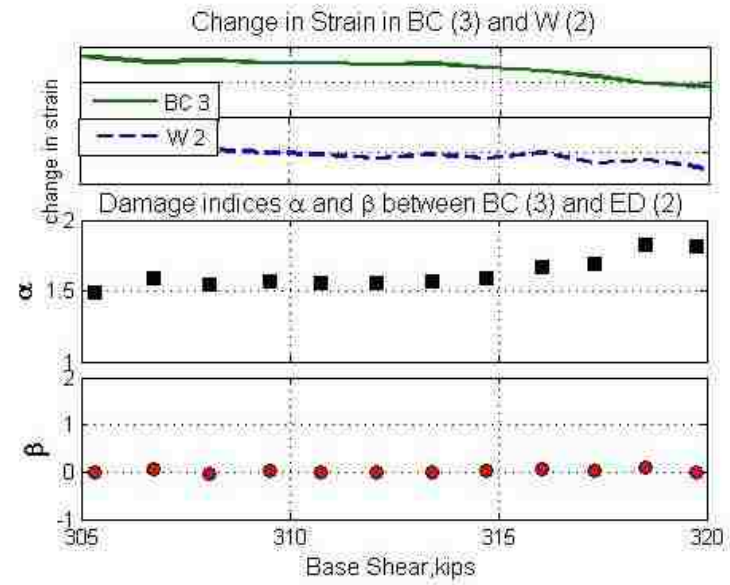

Figure B.2.8: Concrete cover spalling not detected by 1st story damage index W2/BC3

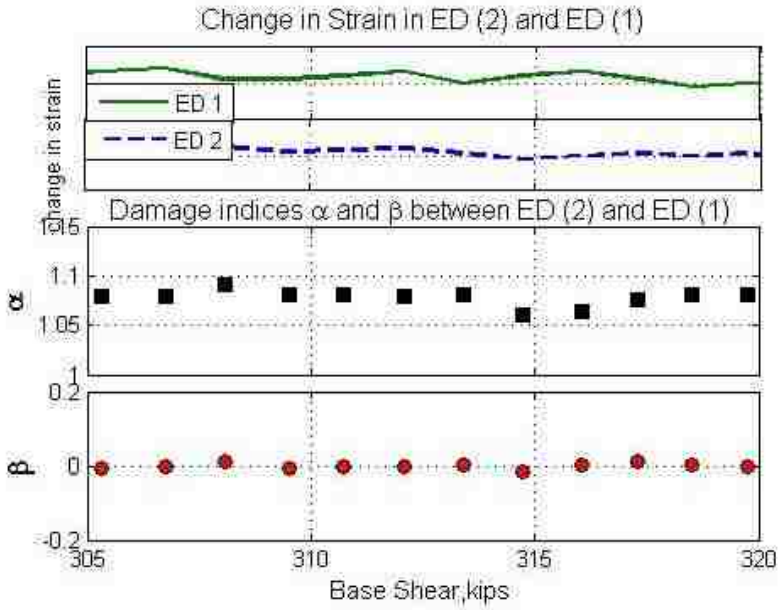

Figure B.2.9: Concrete cover spalling not detected by 1st story damage index ED2/ED1

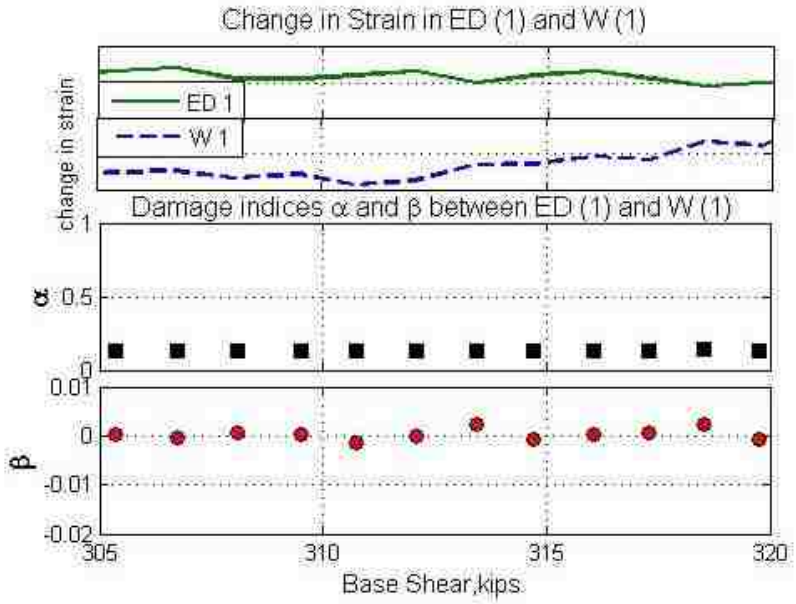

Figure B.2.10: Concrete cover spalling not detected by 1st story damage index W1/ED1

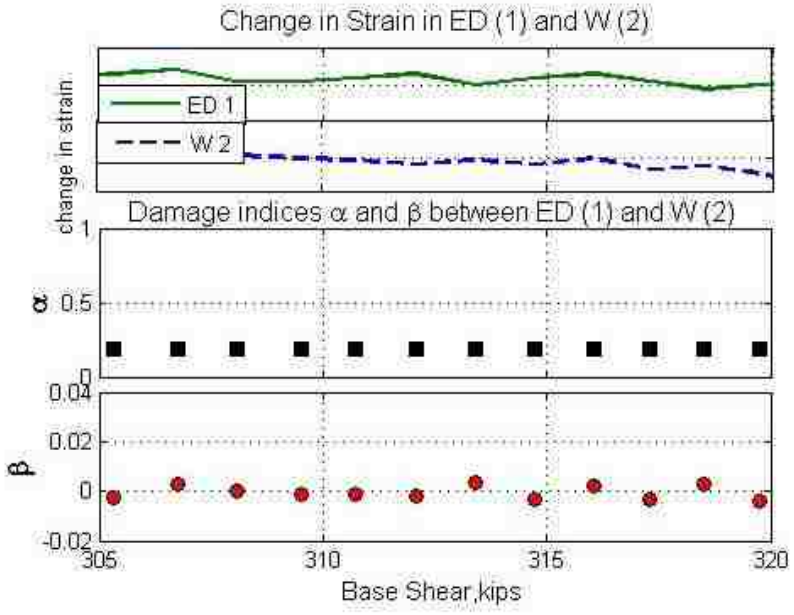

Figure B.2.11: Concrete cover spalling not detected by 1st story damage index W2/ED1

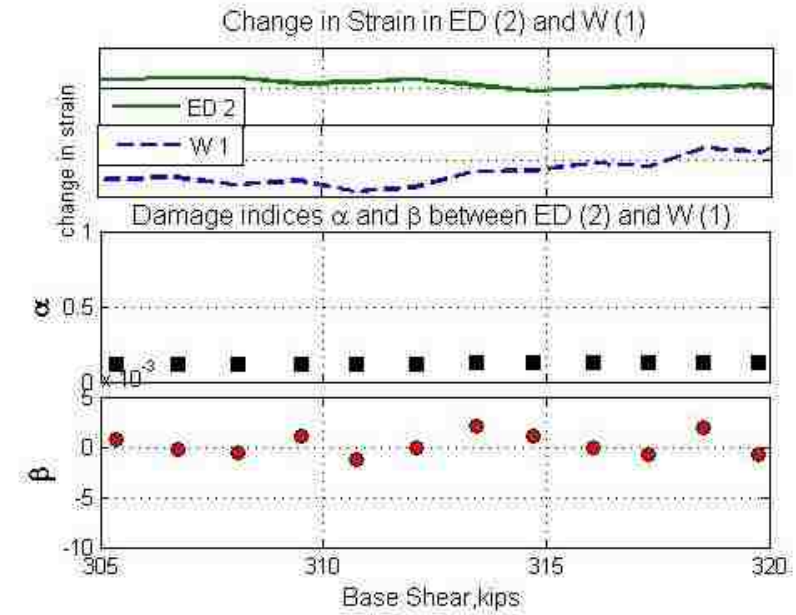

Figure B.2.12: Concrete cover spalling not detected by 1st story damage index W1/ED2

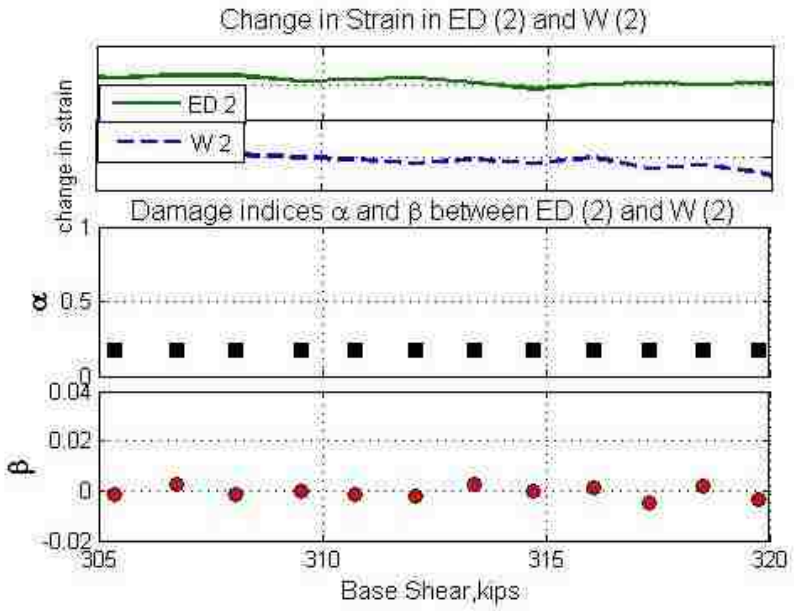

Figure B.2.13: Concrete cover spalling not detected by 1st story damage index W2/ED2

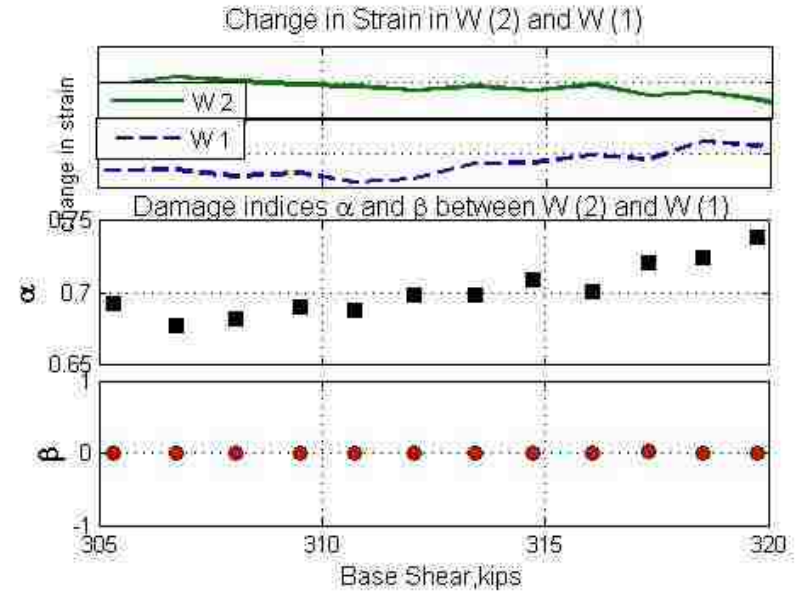

Figure B.2.14: Concrete cover spalling not detected by 1st story damage index W1/W2

Appendix B.3: Additional Damage Index Plots for Concrete Core Crushing using 1st Story Sensors in DRAIN Model

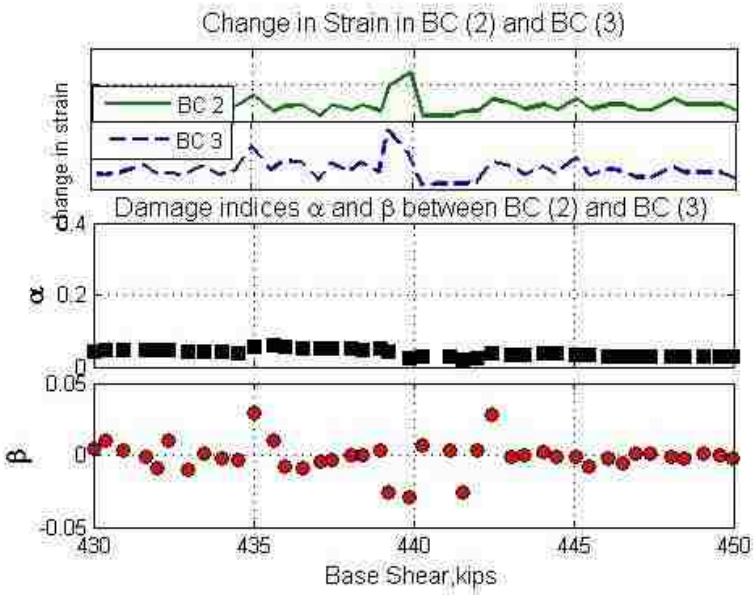

Figure B.3.1: Detection of concrete core crushing by 1st story damage index BC3/BC2

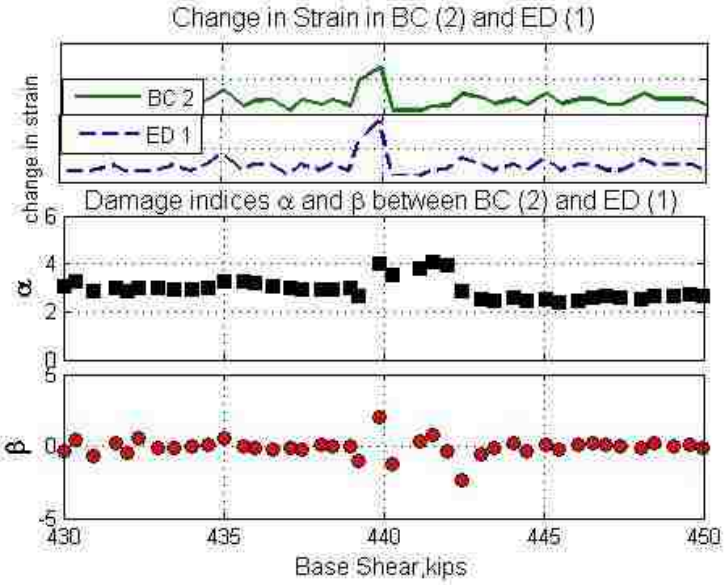

Figure B.3.2: Detection of concrete core crushing by 1st story damage index ED1/BC2

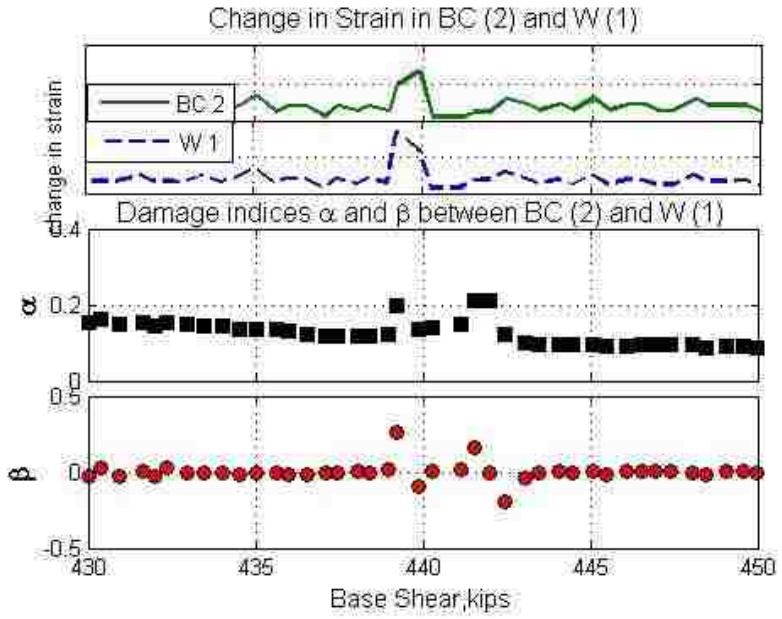

Figure B.3.3: Detection of concrete core crushing by 1st story damage index W1/BC2

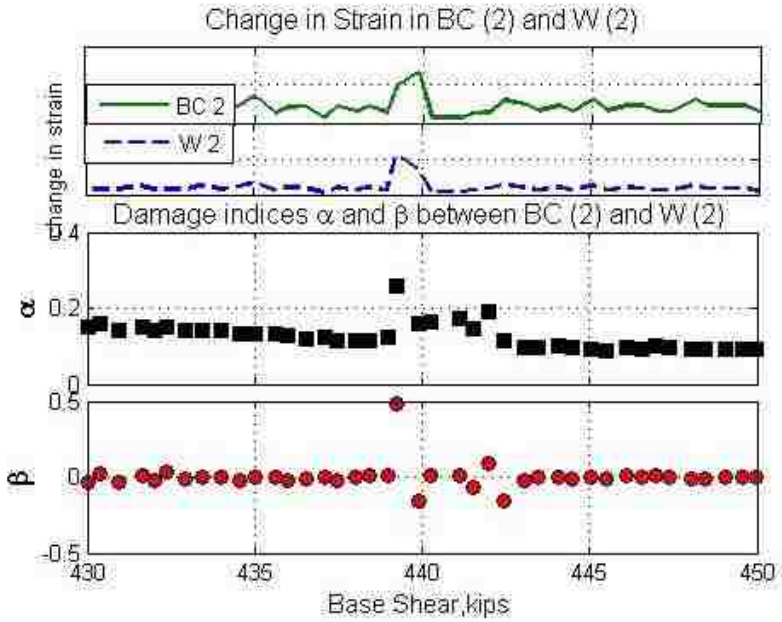

Figure B.3.4: Detection of concrete core crushing by 1st story damage index W2/BC2

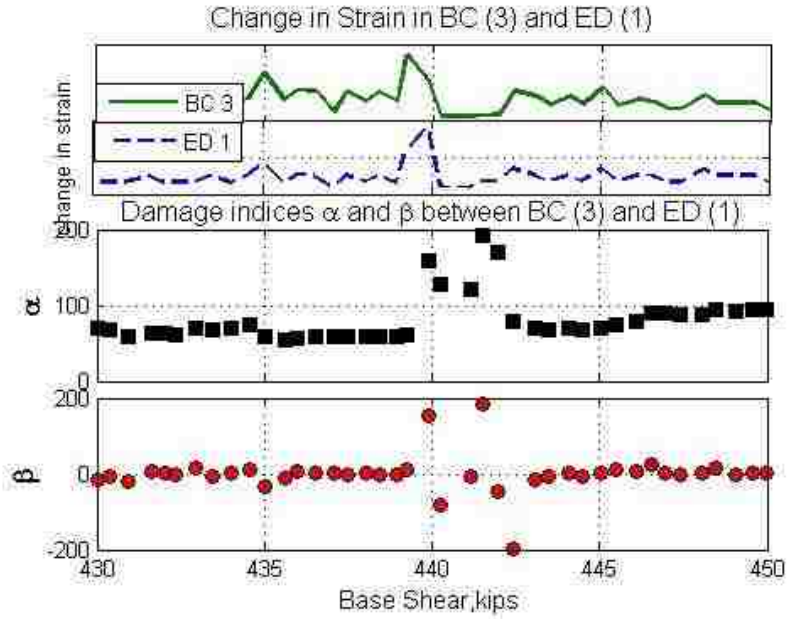

Figure B.3.5: Detection of concrete core crushing by 1st story damage index ED1/BC3

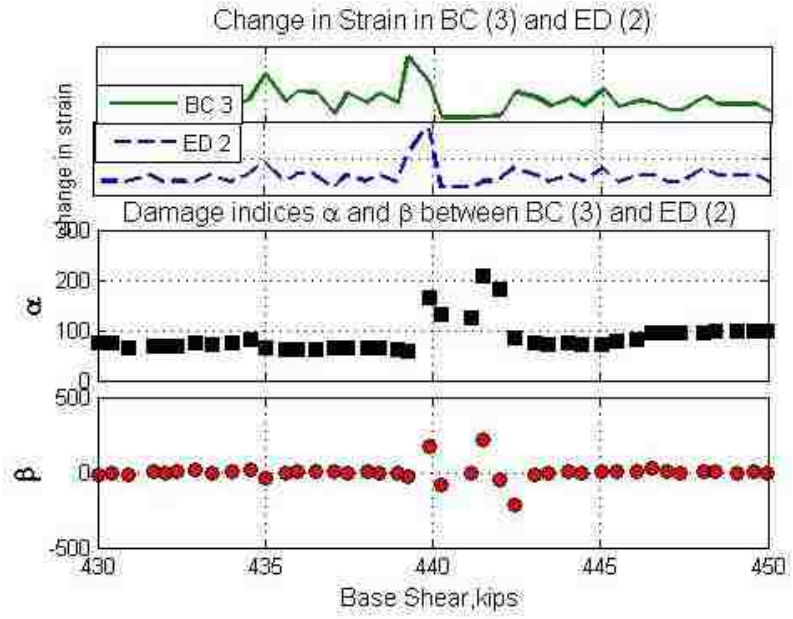

Figure B.3.6: Detection of concrete core crushing by 1st story damage index ED2/BC3

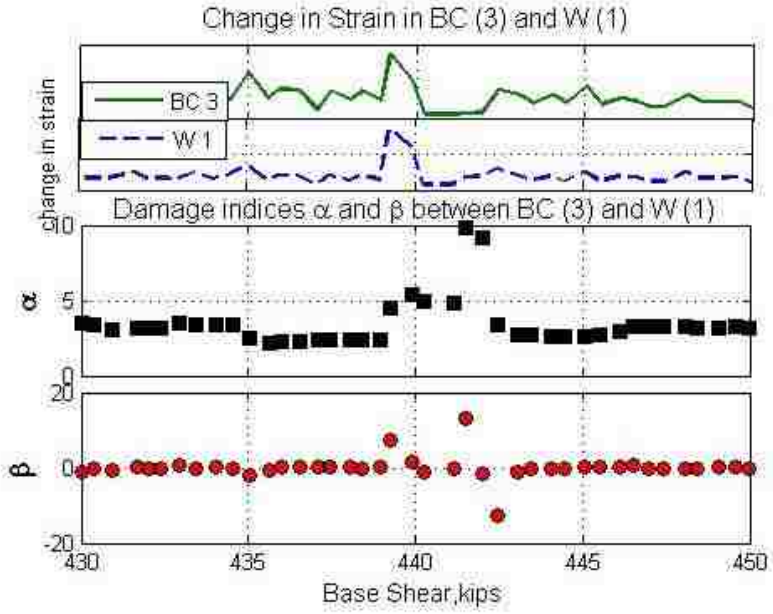

Figure B.3.7: Detection of concrete core crushing by 1st story damage index W1/BC3

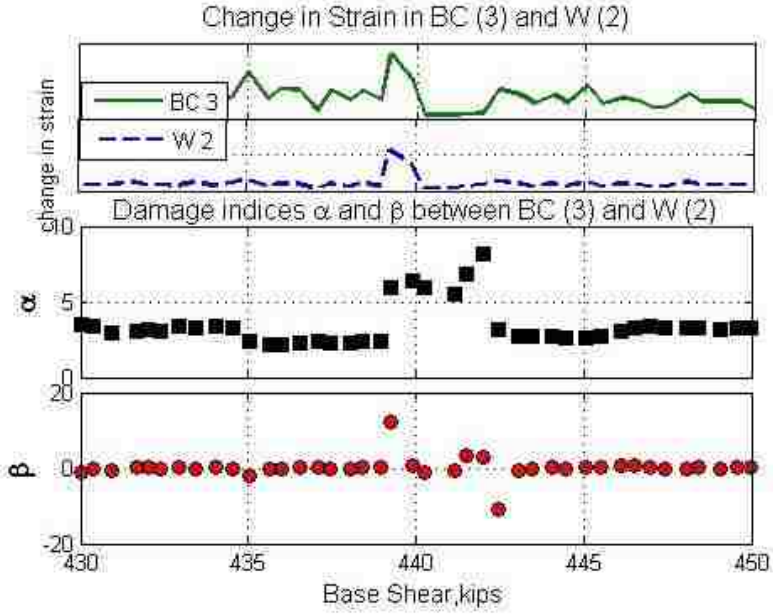

Figure B.3.8: Detection of concrete core crushing by 1st story damage index W2/BC3

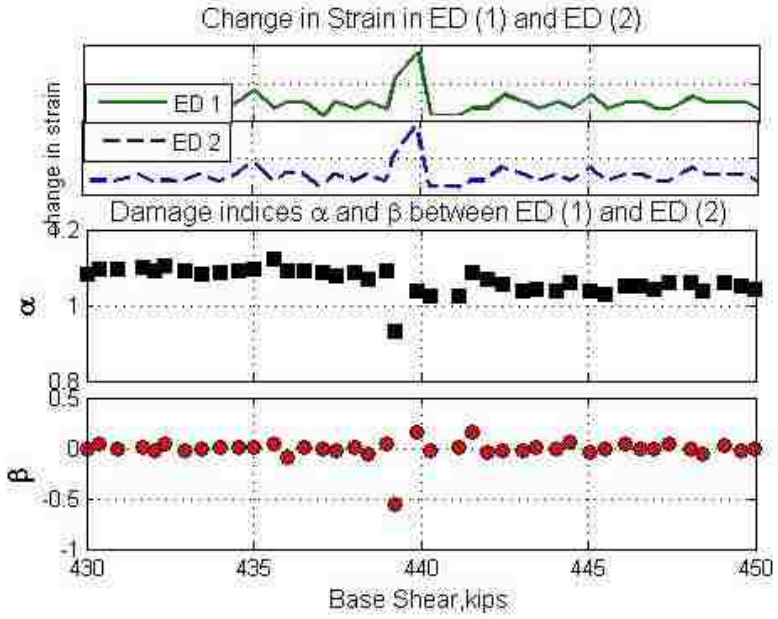

Figure B.3.9: Detection of concrete core crushing by 1st story damage index ED2/ED1

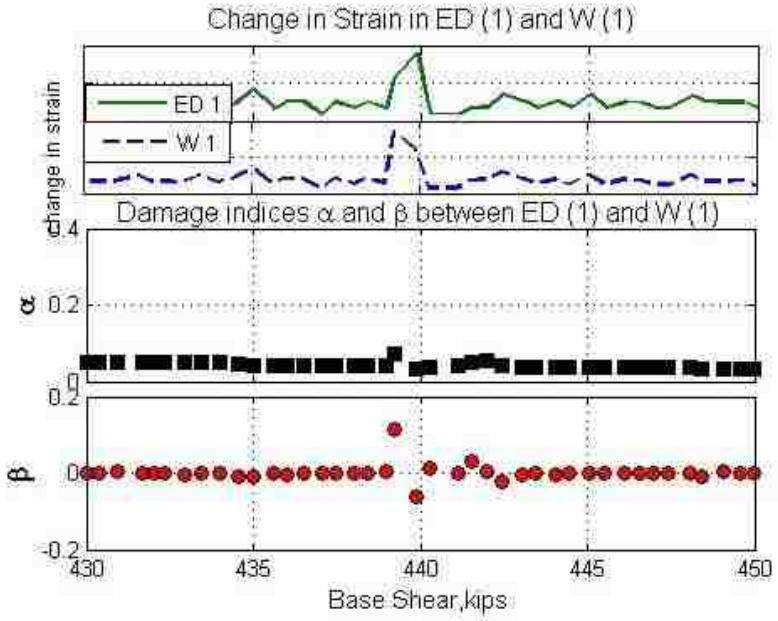

Figure B.3.10: Detection of concrete core crushing by 1st story damage index W1/ED1

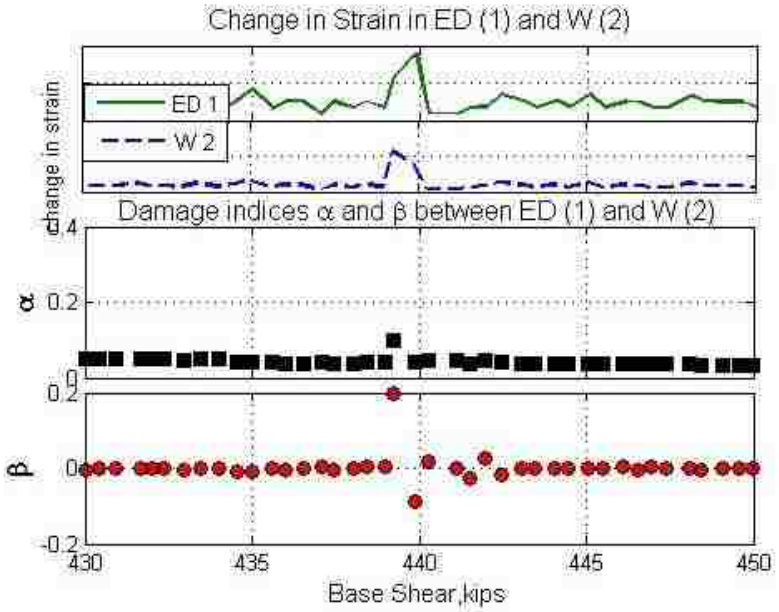

Figure B.3.11: Detection of concrete core crushing by 1st story damage index W2/ED1

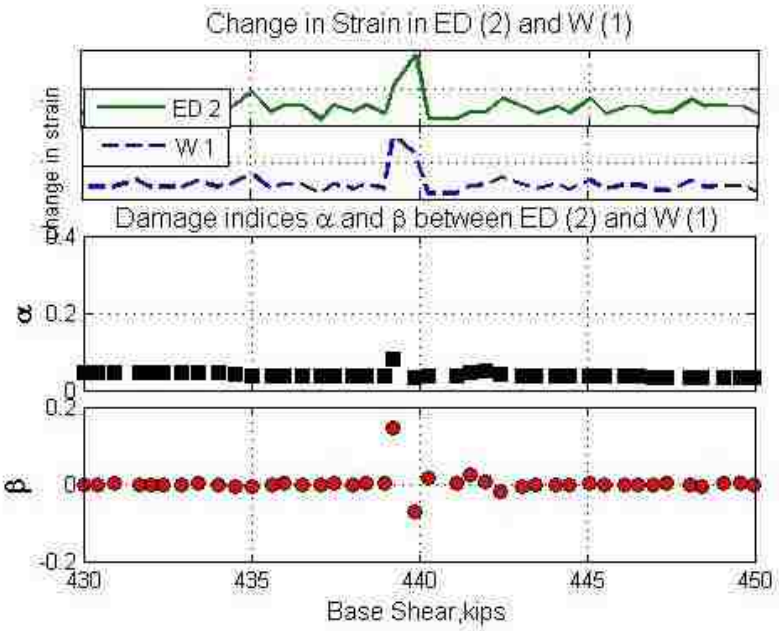

Figure B.3.12: Detection of concrete core crushing by 1st story damage index W1/ED2

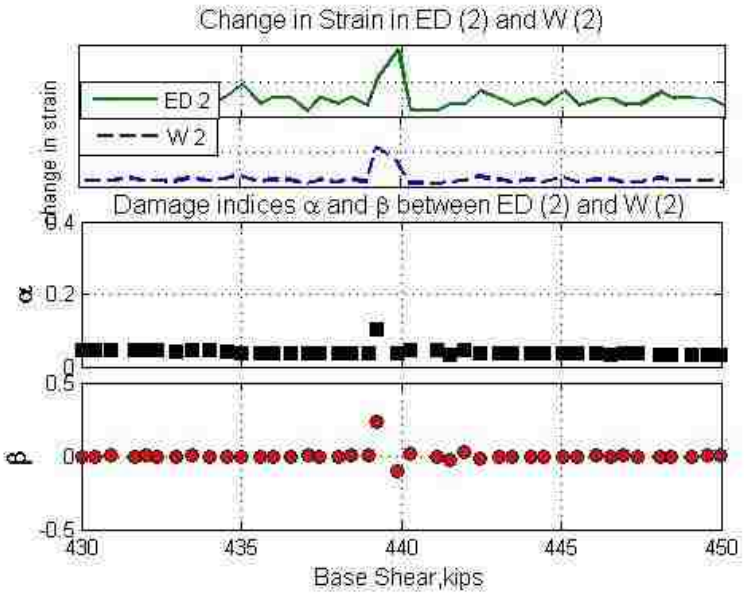

Figure B.3.13: Detection of concrete core crushing by 1st story damage index W2/ED2

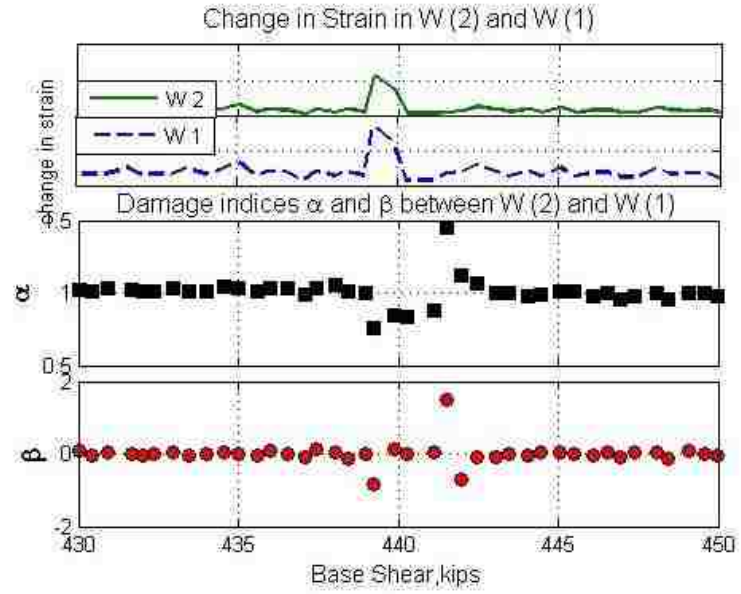

Figure B.3.14: Detection of concrete core crushing by 1st story damage index W1/W2

Appendix B.4: Additional Damage Index Plots for Steel Yielding and Concrete Cover Spalling using 2nd and 3rd Story Sensors in DRAIN Model

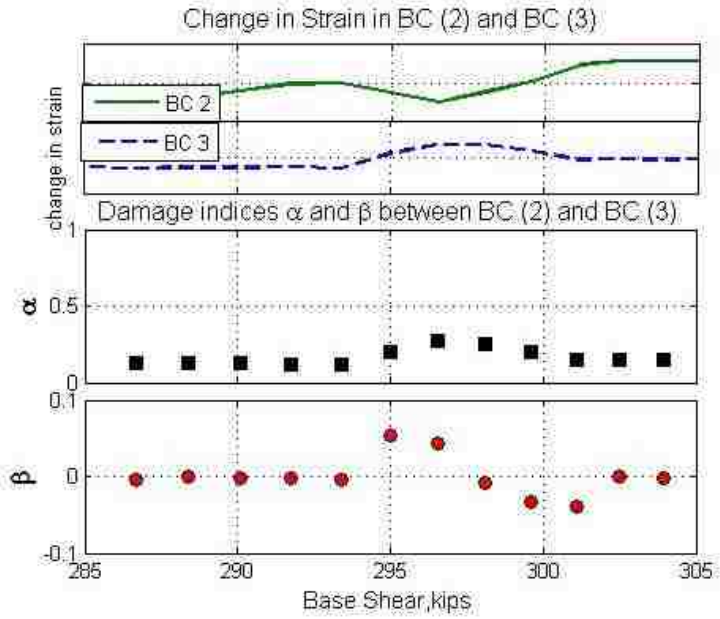

Figure B.4.1: Detection steel yielding and concrete cover spalling by 2nd story damage index BC3/BC2

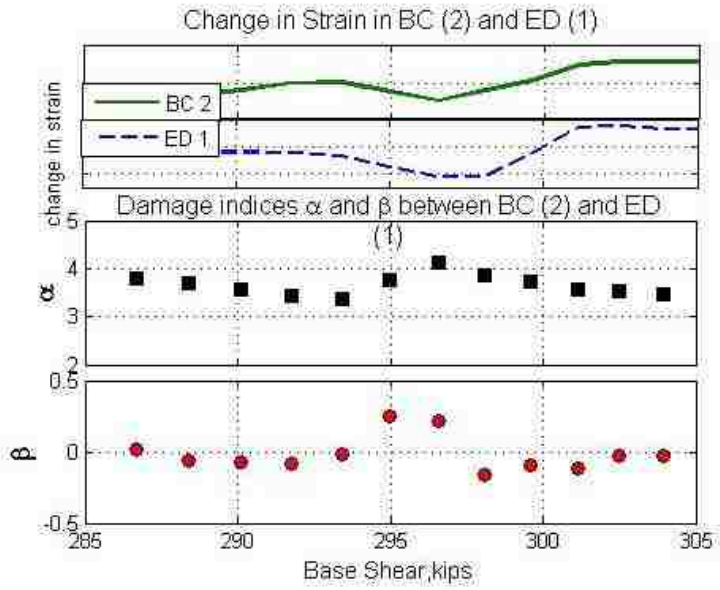

Figure B.4.2: Detection steel yielding and concrete cover spalling by 2nd story damage index ED1/BC2

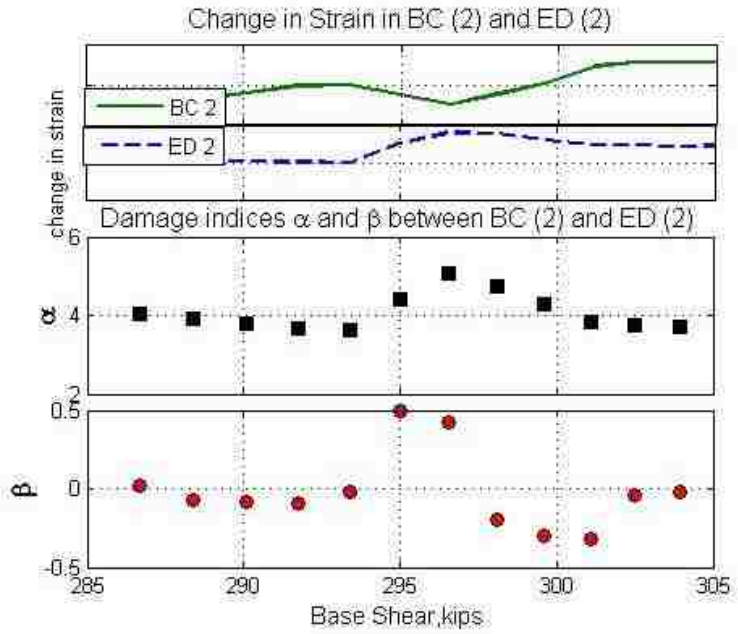

Figure B.4.3: Detection steel yielding and concrete cover spalling by 2nd story damage index ED2/BC2

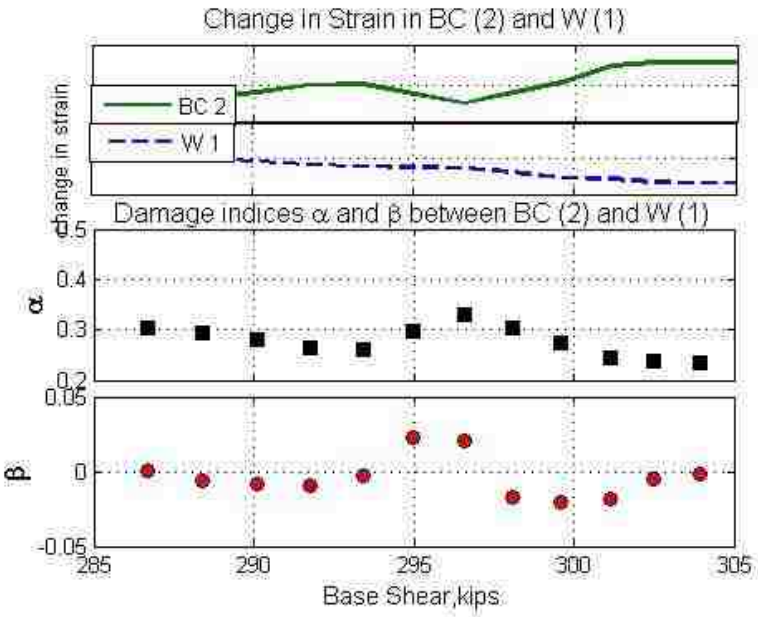

Figure B.4.4: Detection steel yielding and concrete cover spalling by 2nd story damage index W1/BC2

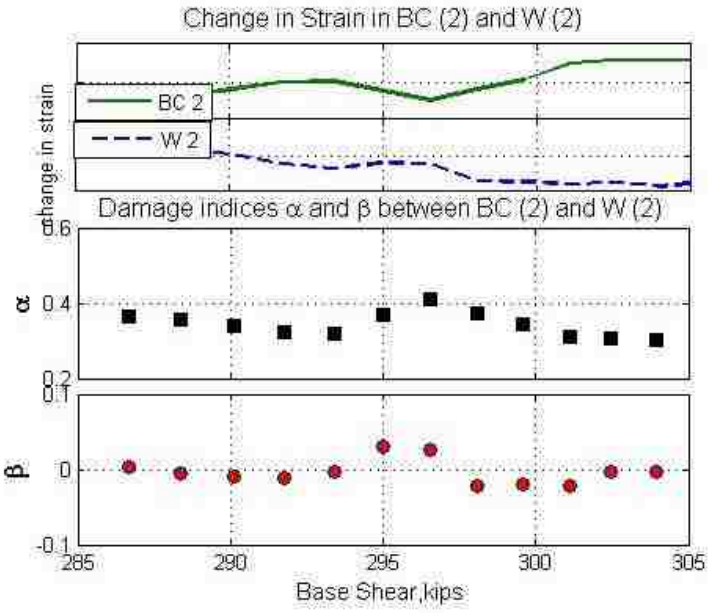

Figure B.4.5: Detection steel yielding and concrete cover spalling by 2nd story damage index W2/BC2

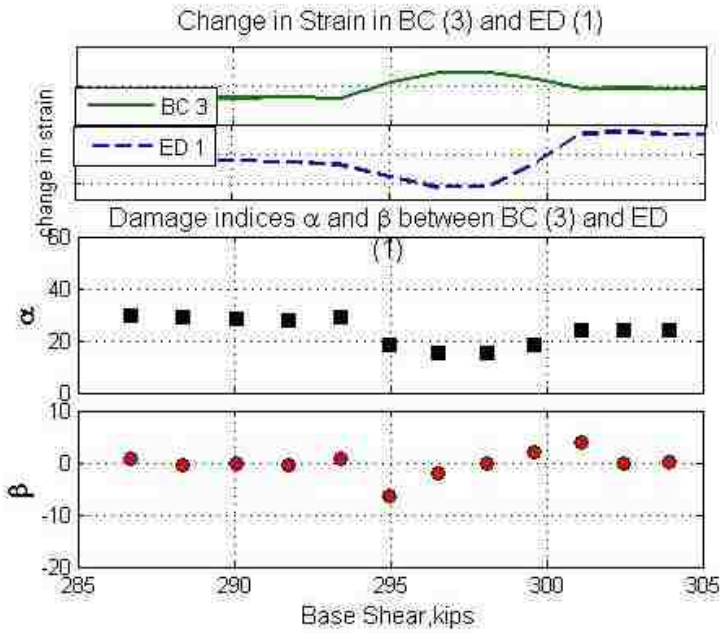

Figure B.4.6: Detection steel yielding and concrete cover spalling by 2nd story damage index ED1/BC3

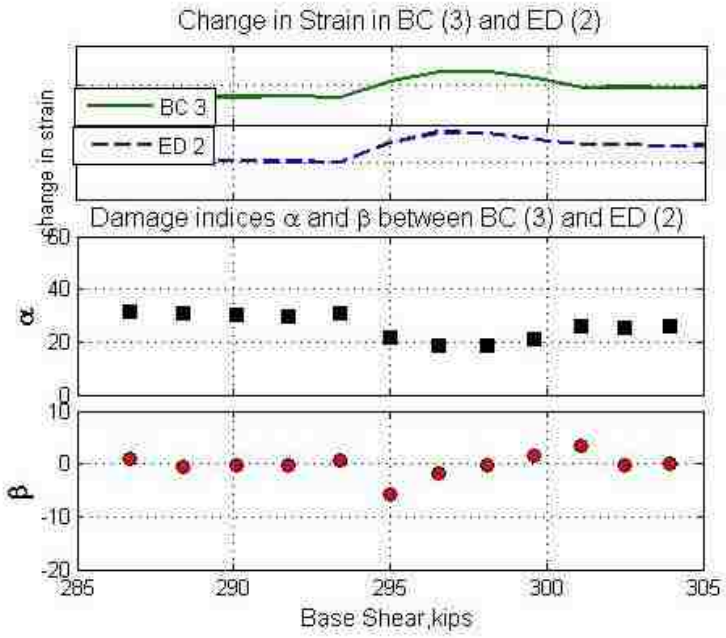

Figure B.4.7: Detection steel yielding and concrete cover spalling by 2nd story damage index ED2/BC3

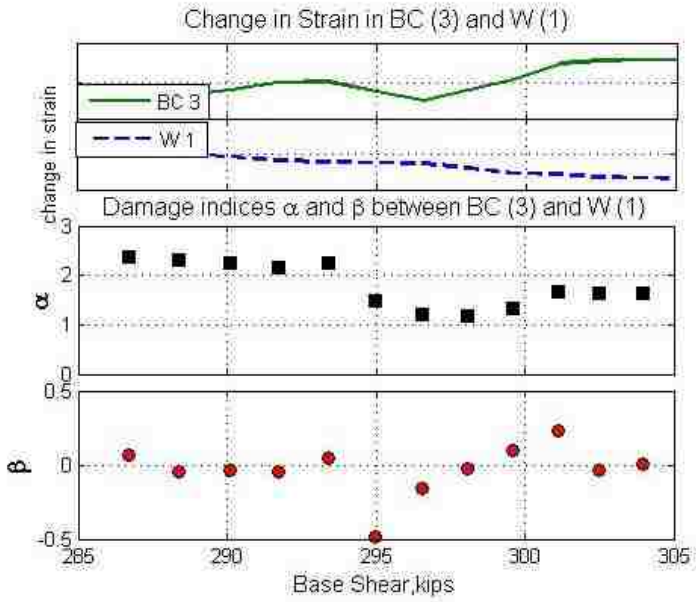

Figure B.4.8: Detection steel yielding and concrete cover spalling by 2nd story damage index W1/BC3

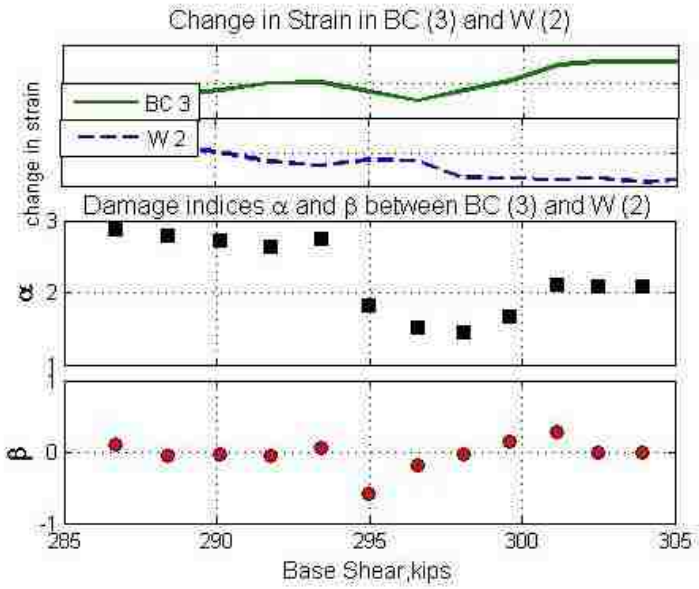

Figure B.4.9: Detection steel yielding and concrete cover spalling by 2nd story damage index W2/BC3

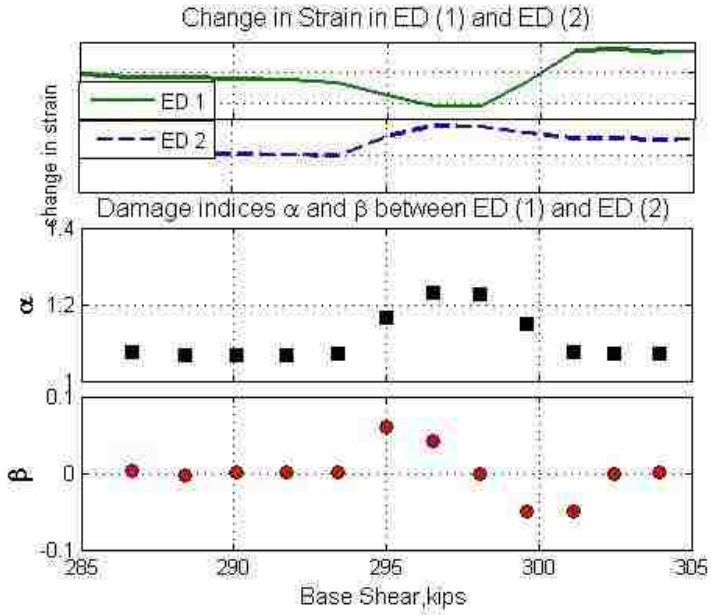

Figure B.4.10: Detection steel yielding and concrete cover spalling by 2nd story damage index ED2/ED1

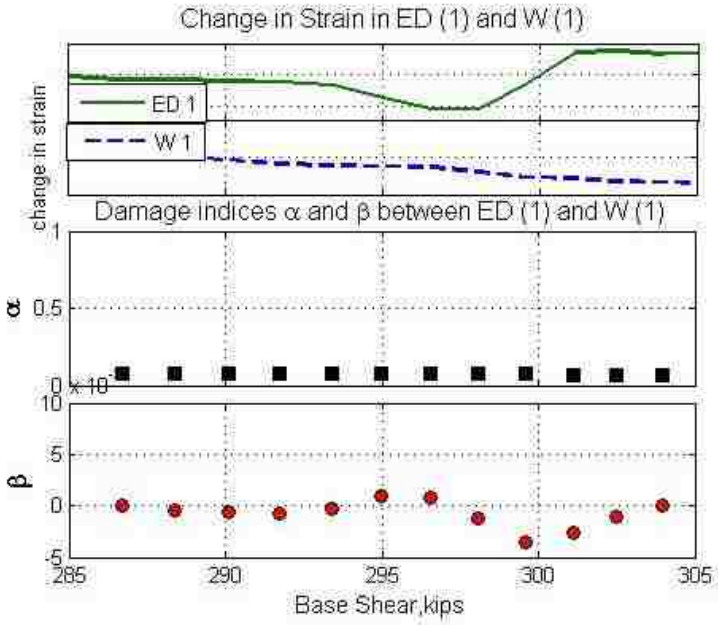

Figure B.4.11: Detection steel yielding and concrete cover spalling by 2nd story damage index W1/ED1

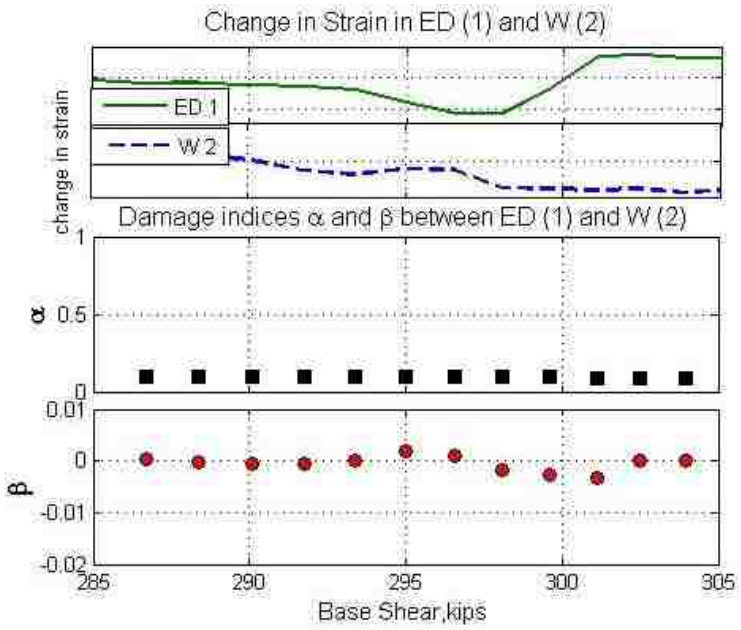

Figure B.4.12: Detection steel yielding and concrete cover spalling by 2nd story damage index W2/ED1

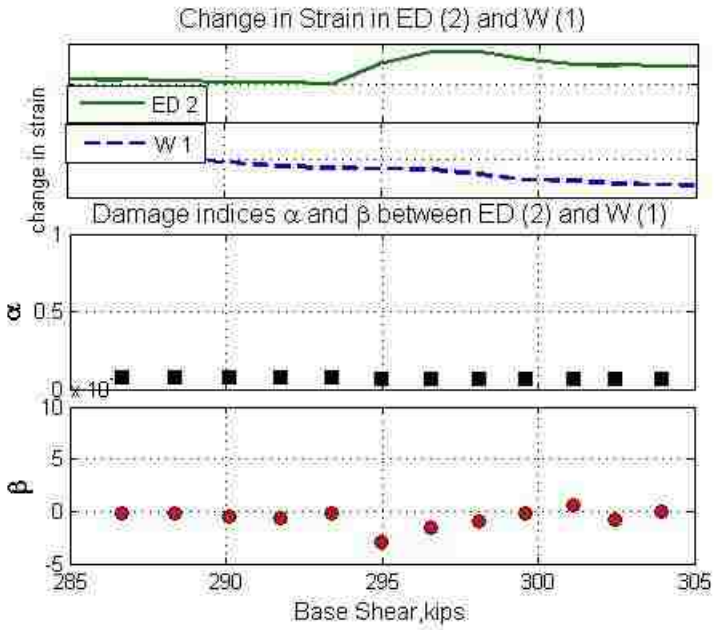

Figure B.4.13: Detection steel yielding and concrete cover spalling by 2nd story damage index W1/ED2

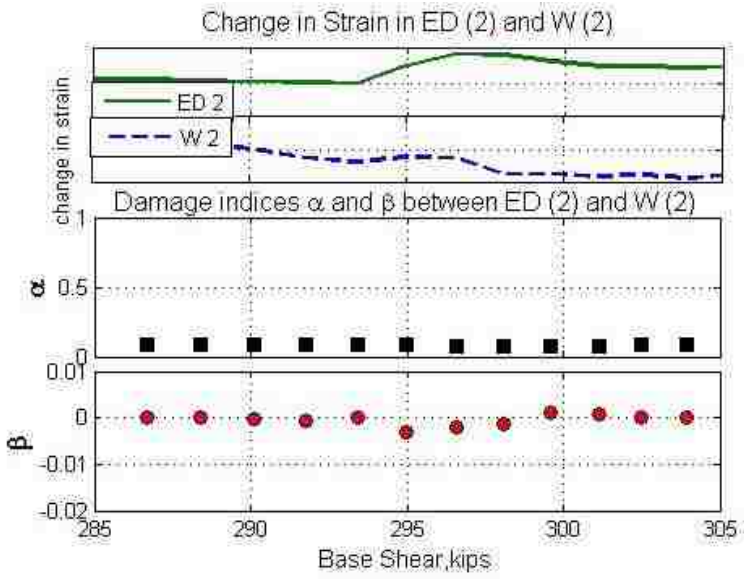

Figure B.4.14: Detection steel yielding and concrete cover spalling by 2nd story damage index W2/ED2

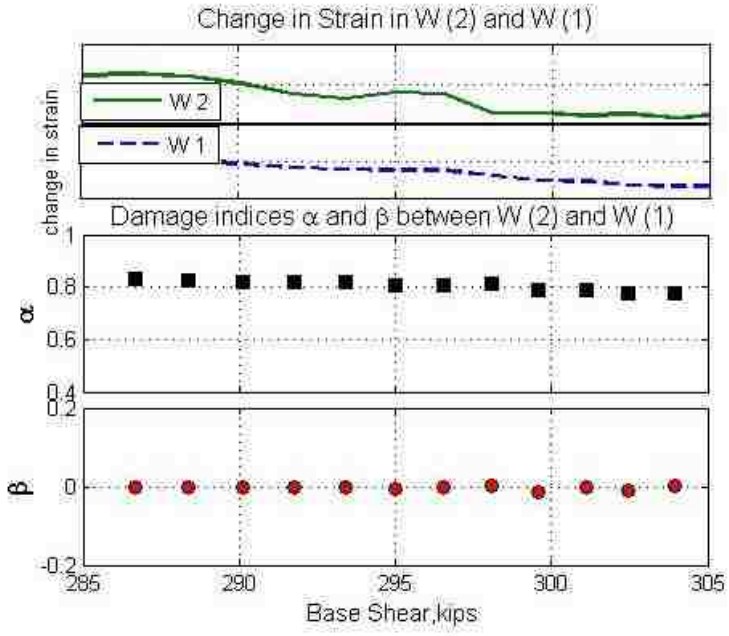

Figure B.4.15: Detection steel yielding and concrete cover spalling by 2nd story damage index W1/W2

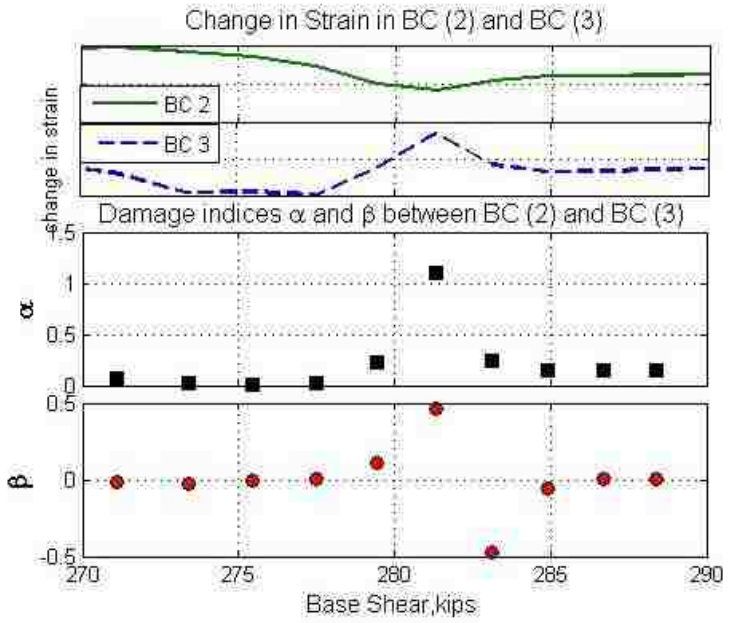

Figure B.4.16: Detection steel yielding and concrete cover spalling by 3rd story damage index BC3/BC2

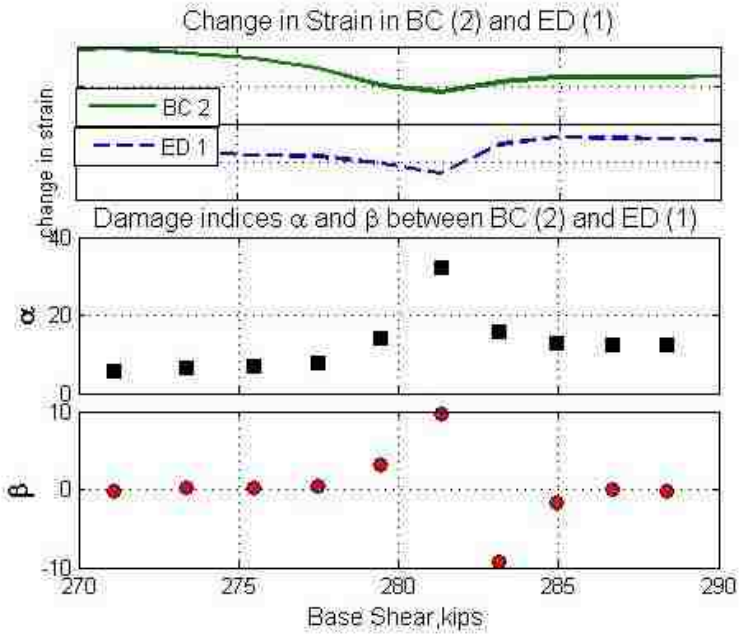

Figure B.4.17: Detection steel yielding and concrete cover spalling by 3rd story damage index ED1/BC2

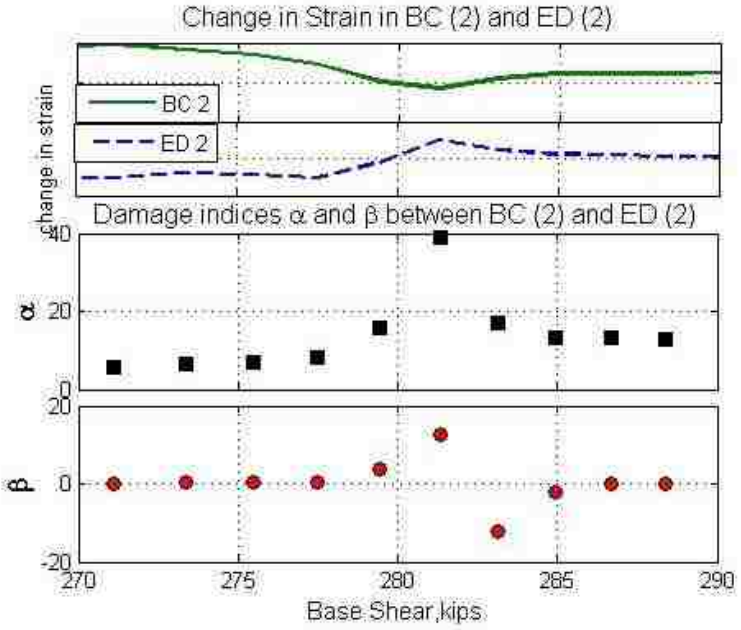

Figure B.4.19: Detection steel yielding and concrete cover spalling by 3rd story damage index ED2/BC2

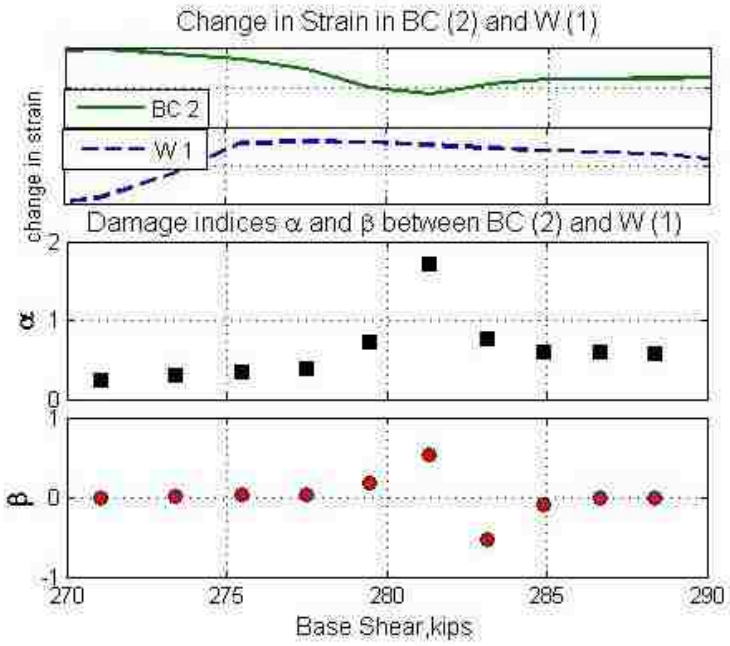

Figure B.4.18: Detection steel yielding and concrete cover spalling by 3rd story damage index W1/BC2

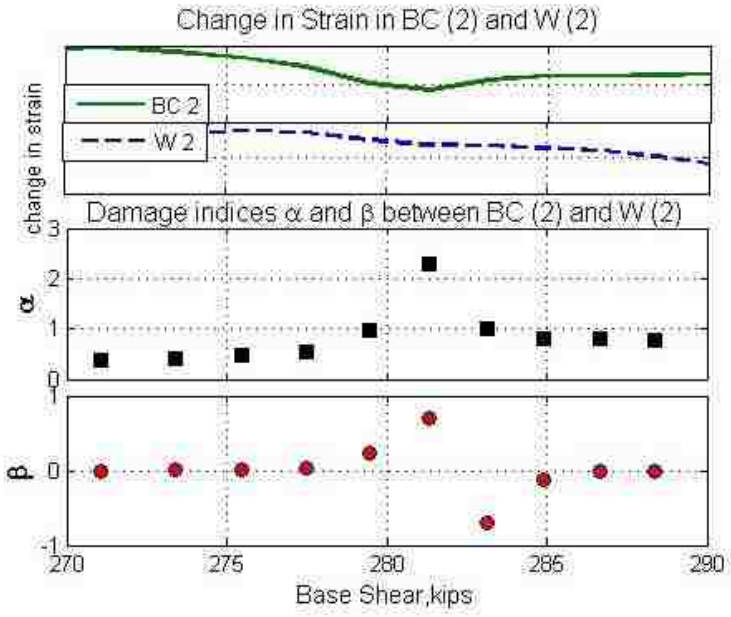

Figure B.4.20 Detection steel yielding and concrete cover spalling by 3rd story damage index W2/BC2

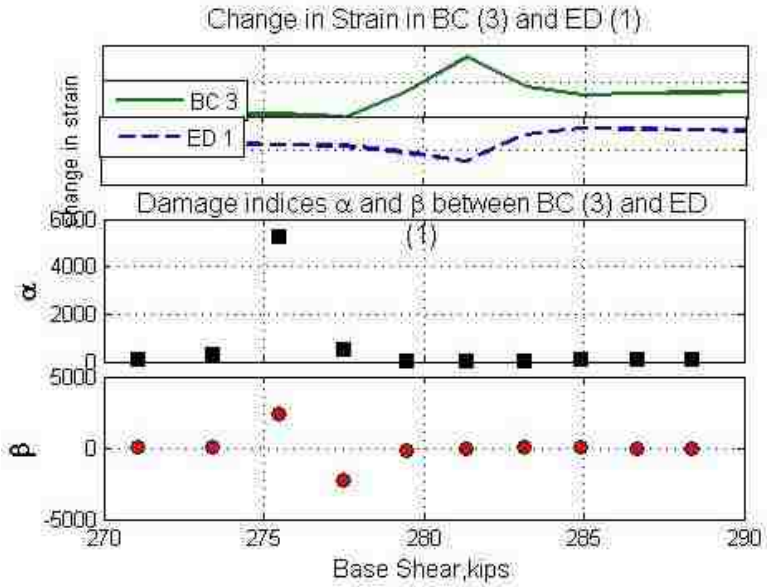

Figure B.4.21: Detection steel yielding and concrete cover spalling by 3rd story damage index ED1/BC3

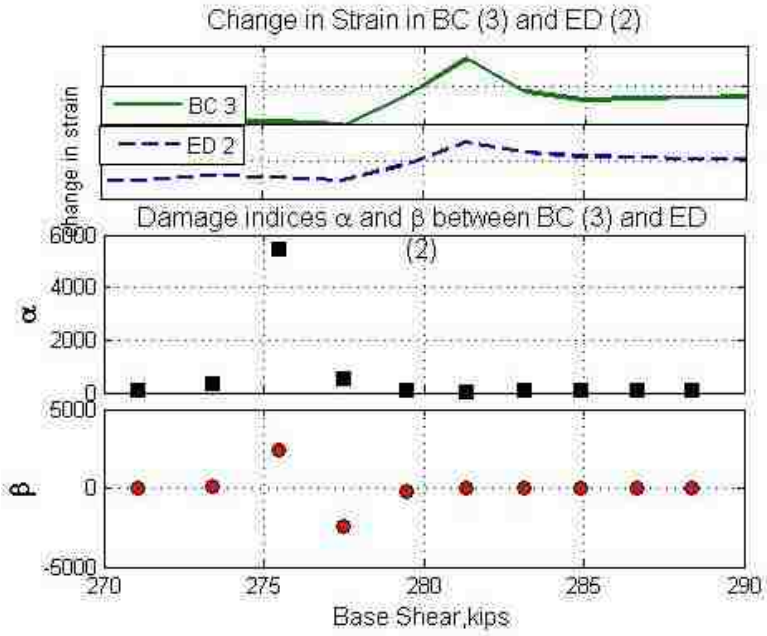

Figure B.4.22: Detection steel yielding and concrete cover spalling by 3rd story damage index ED2/BC3

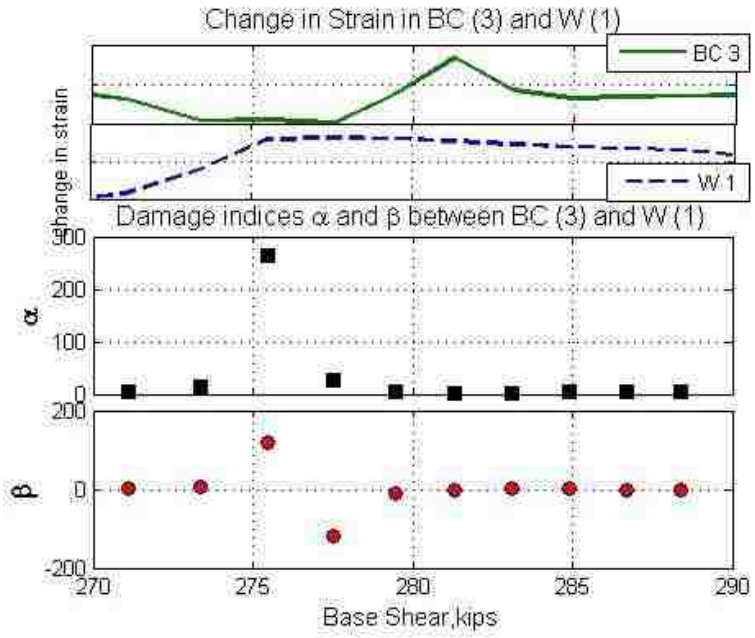

Figure B.4.23: Detection steel yielding and concrete cover spalling by 3rd story damage index W1/BC3

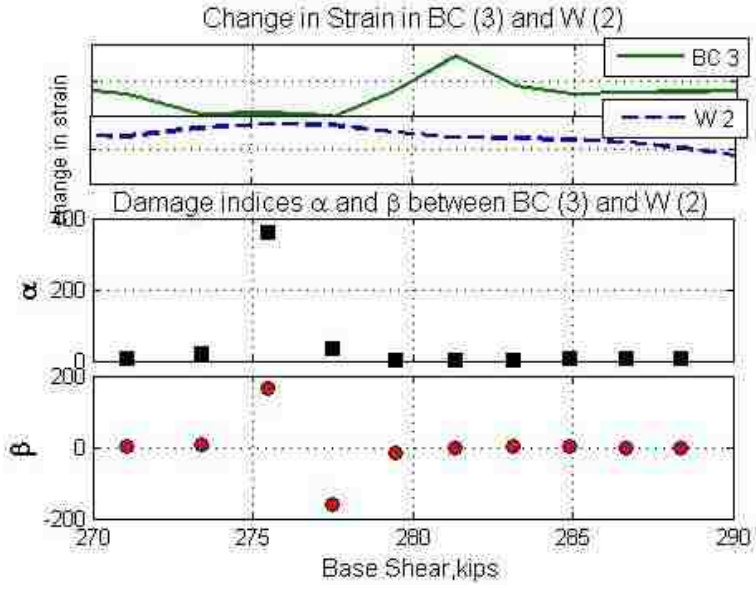

Figure B.4.24: Detection steel yielding and concrete cover spalling by 3rd story damage index W2/BC3

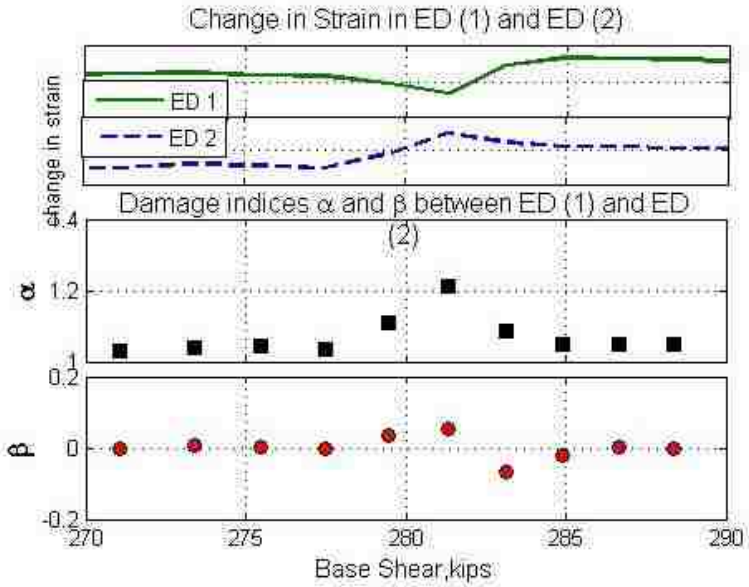

Figure B.4.25: Detection steel yielding and concrete cover spalling by 3rd story damage index ED2/ED1

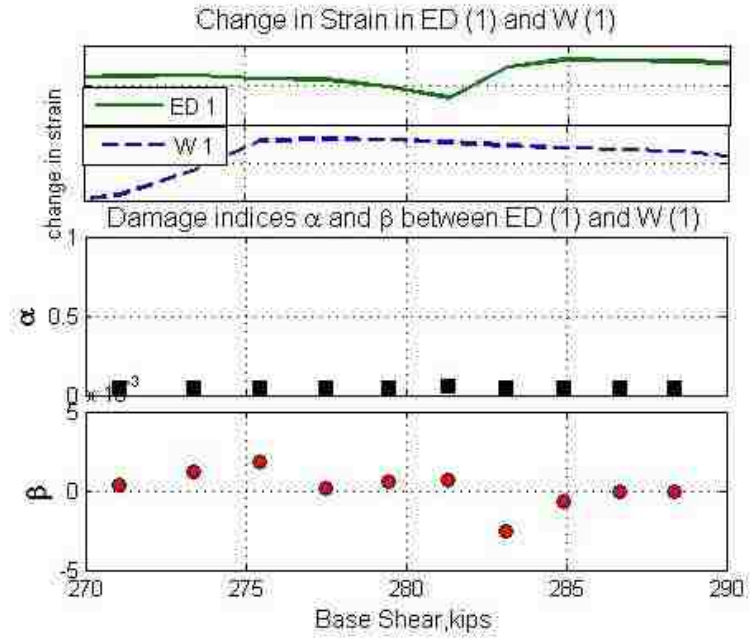

Figure B.4.26: Detection steel yielding and concrete cover spalling by 3rd story damage index W1/ED1

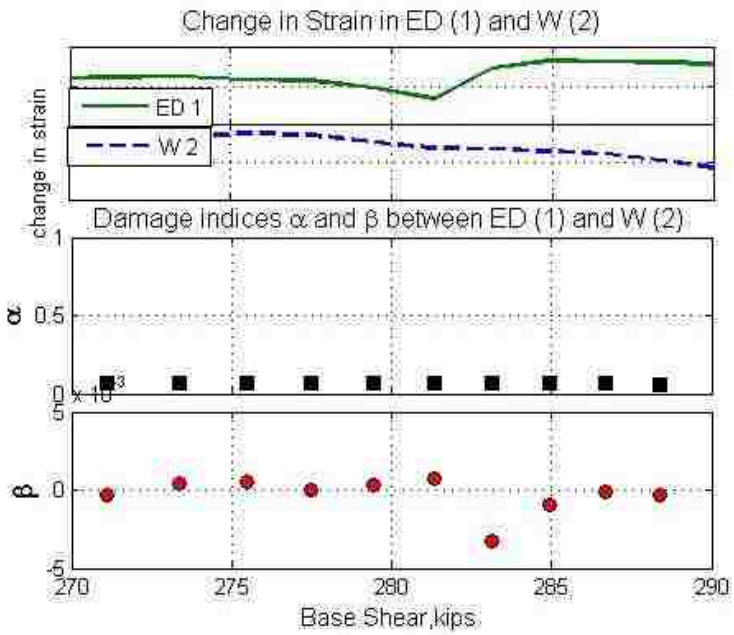

Figure B.4.27: Detection steel yielding and concrete cover spalling by 3rd story damage index W2/ED1

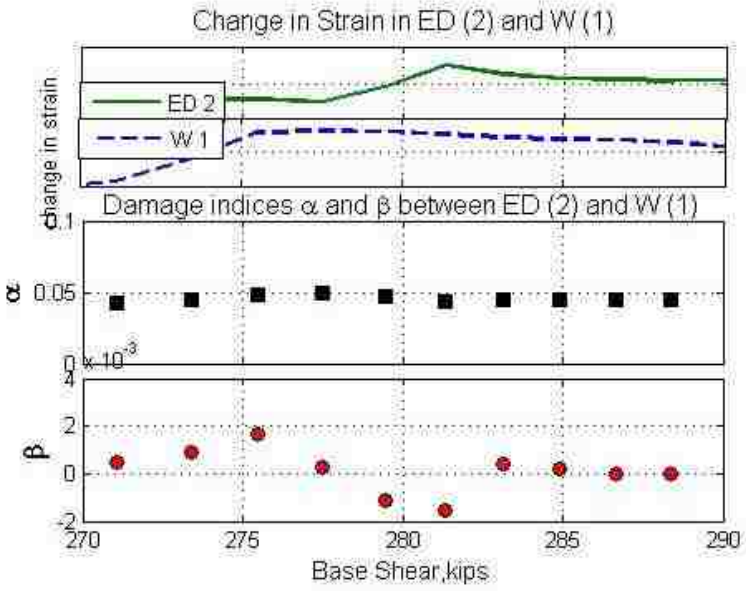

Figure B.4.28: Detection steel yielding and concrete cover spalling by 3rd story damage index W1/ED2

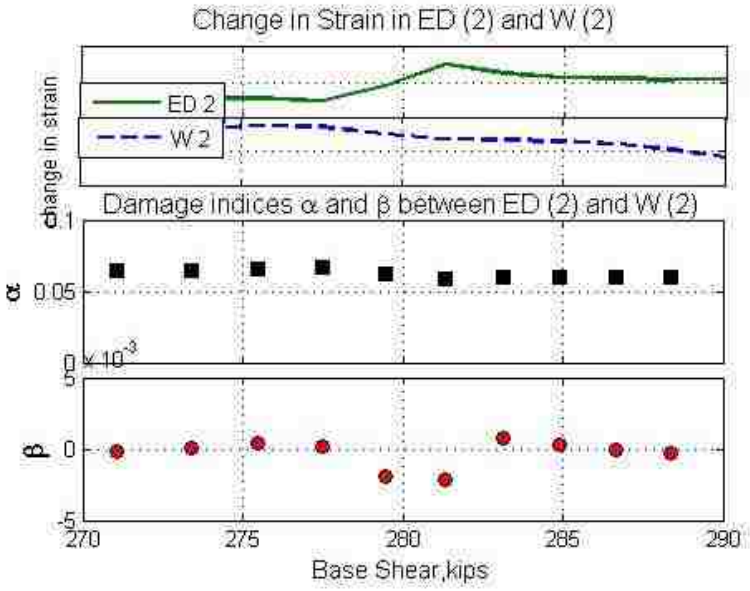

Figure B.4.29: Detection steel yielding and concrete cover spalling by 3rd story damage index W2/ED2

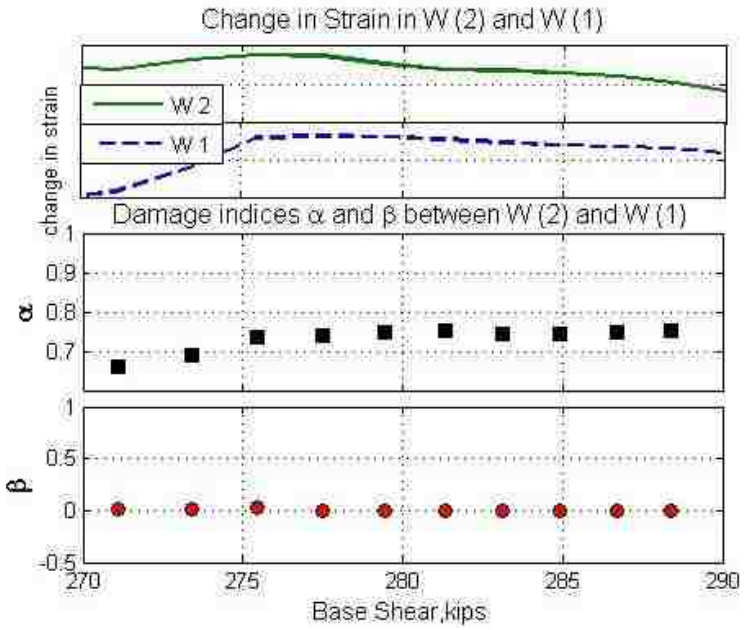

Figure B.4.30: Detection steel yielding and concrete cover spalling by 3rd story damage index W1/W2

Appendix B.5: Additional Damage Index Plots for Concrete Core Crushing using 2nd and 3rd Story Sensors in DRAIN Model

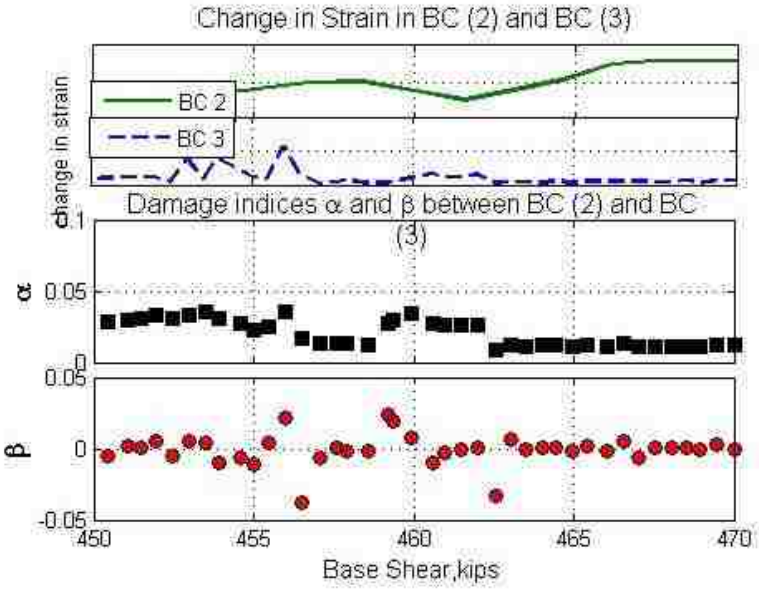

Figure B.5.1: Detection of concrete core crushing by 2nd story damage index BC3/BC2

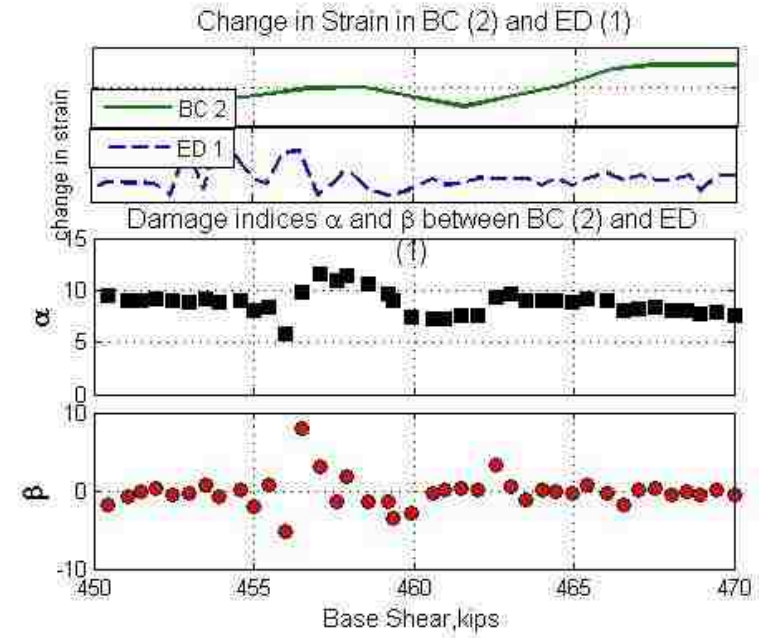

Figure B.5.2: Detection of concrete core crushing by 2nd story damage index ED1/BC2

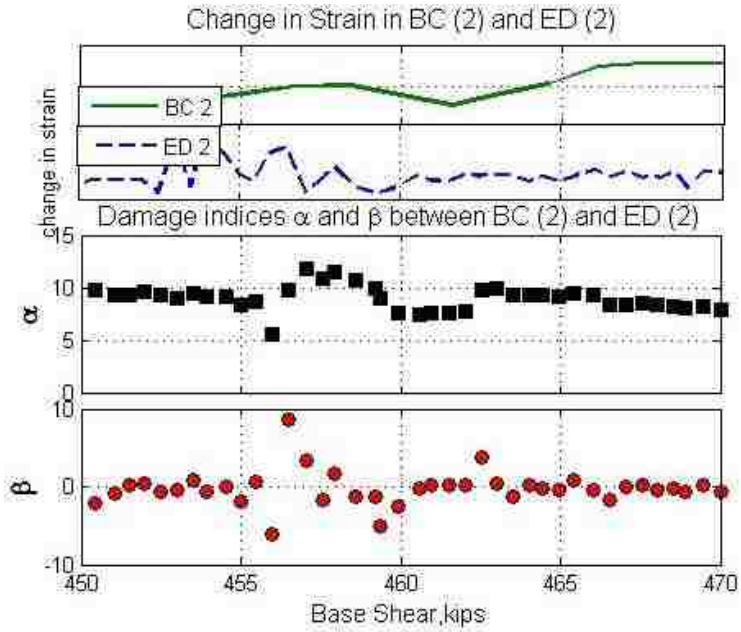

Figure B.5.3: Detection of concrete core crushing by 2nd story damage index ED2/BC2

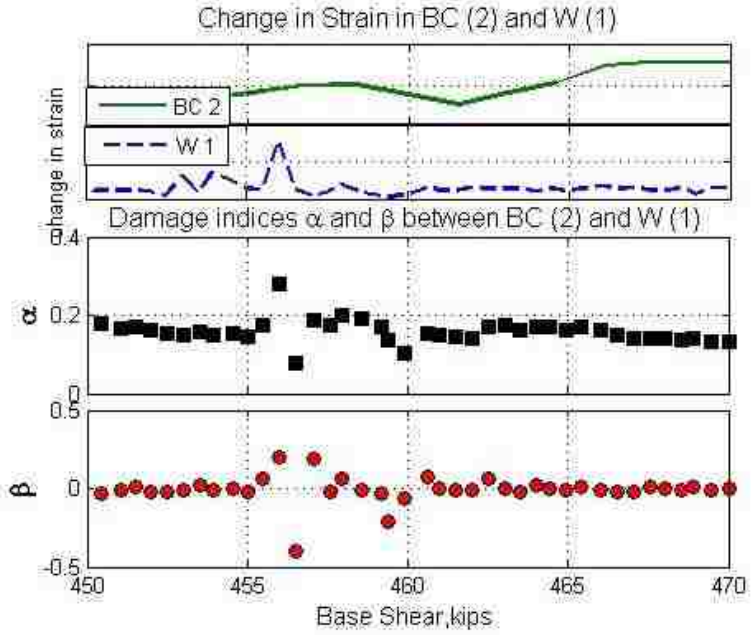

Figure B.5.4: Detection of concrete core crushing by 2nd story damage index W1/BC2

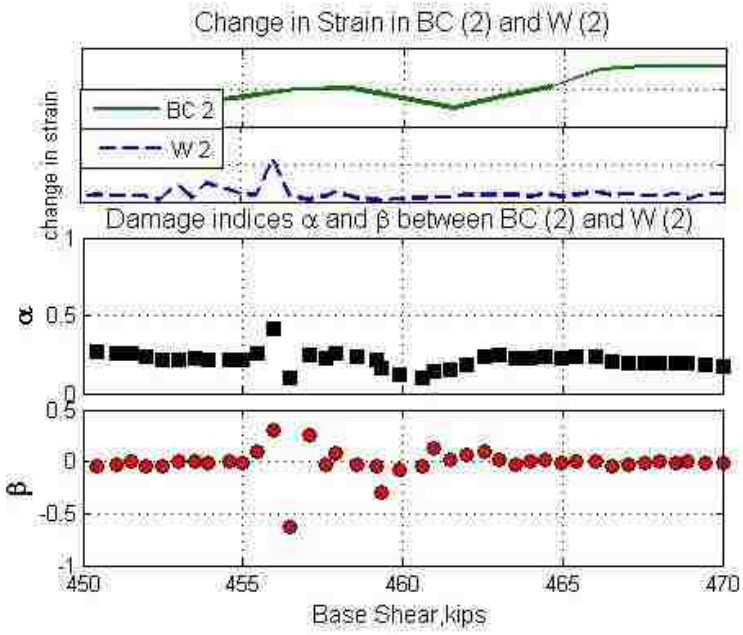

Figure B.5.5: Detection of concrete core crushing by 2nd story damage index W2/BC2

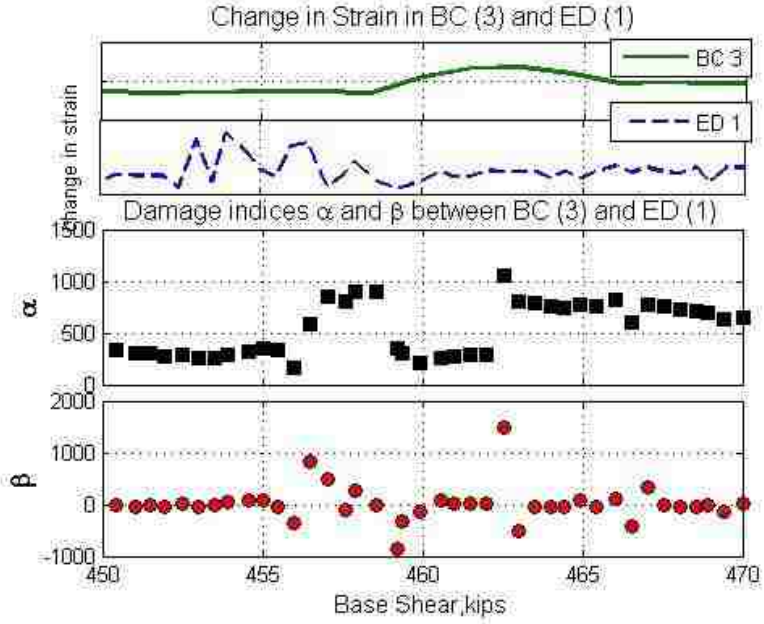

Figure B.5.6: Detection of concrete core crushing by 2nd story damage index ED1/BC3

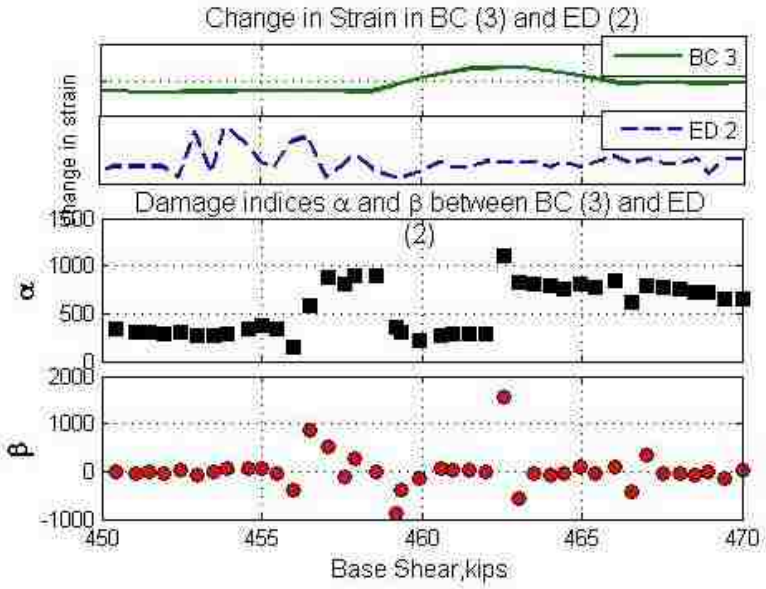

Figure B.5.7: Detection of concrete core crushing by 2nd story damage index ED2/BC3

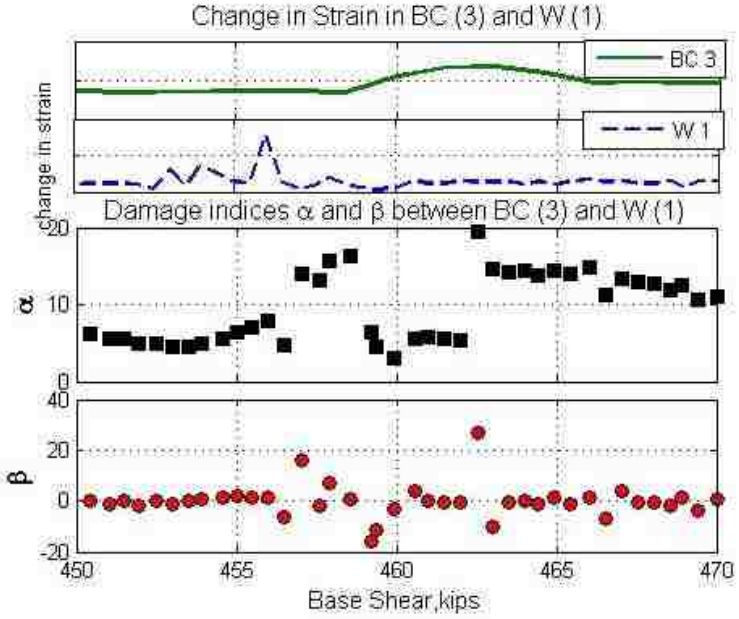

Figure B.5.8: Detection of concrete core crushing by 2nd story damage index W1/BC3

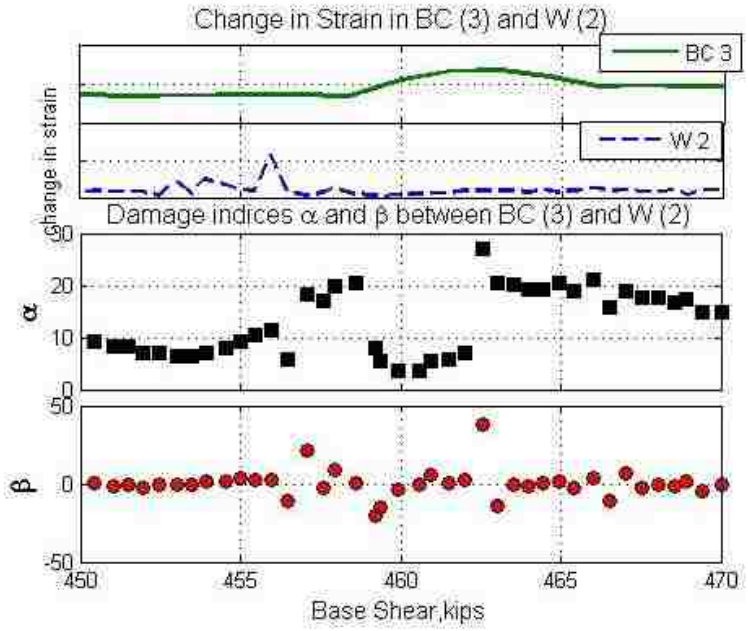

Figure B.5.9: Detection of concrete core crushing by 2nd story damage index W2/BC3

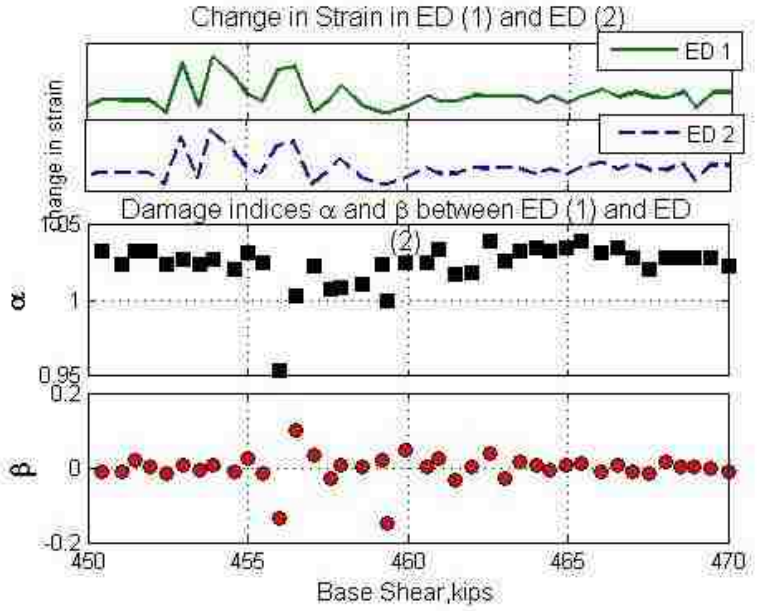

Figure B.5.10: Detection of concrete core crushing by 2nd story damage index ED2/ED1

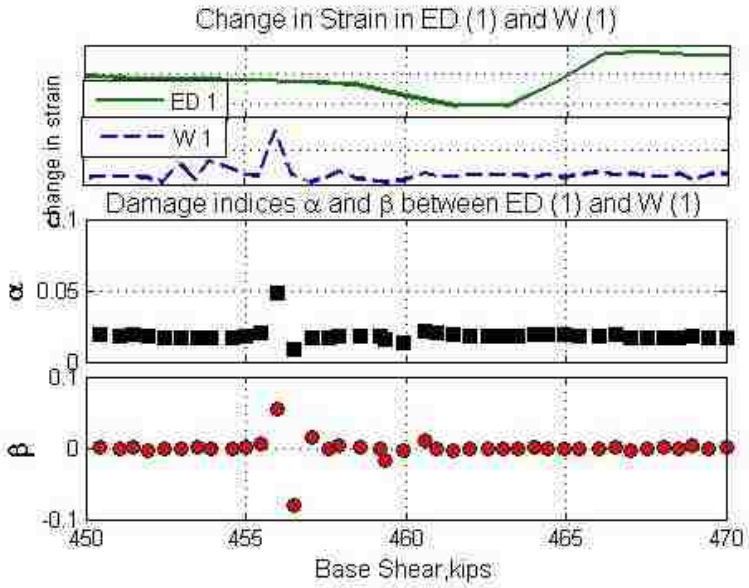

Figure B.5.11: Detection of concrete core crushing by 2nd story damage index W1/ED1

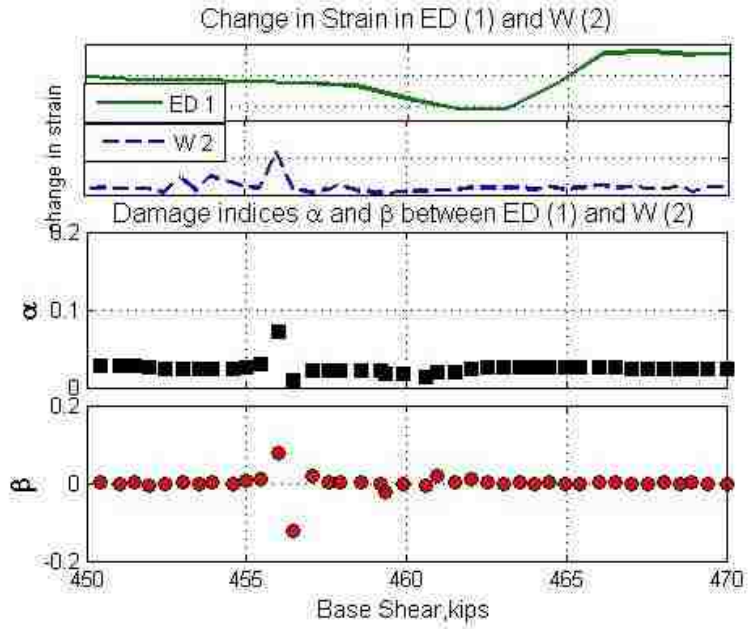

Figure B.5.12: Detection of concrete core crushing by 2nd story damage index W2/ED1

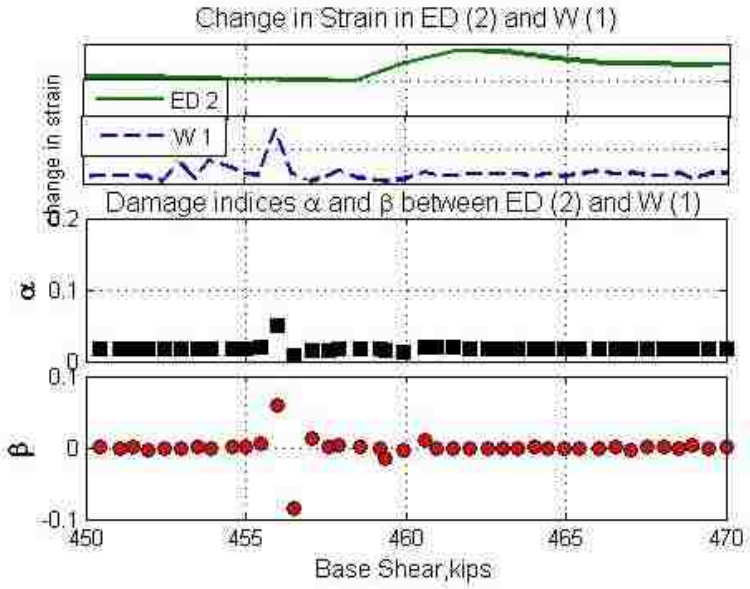

Figure B.5.13: Detection of concrete core crushing by 2nd story damage index W1/ED2

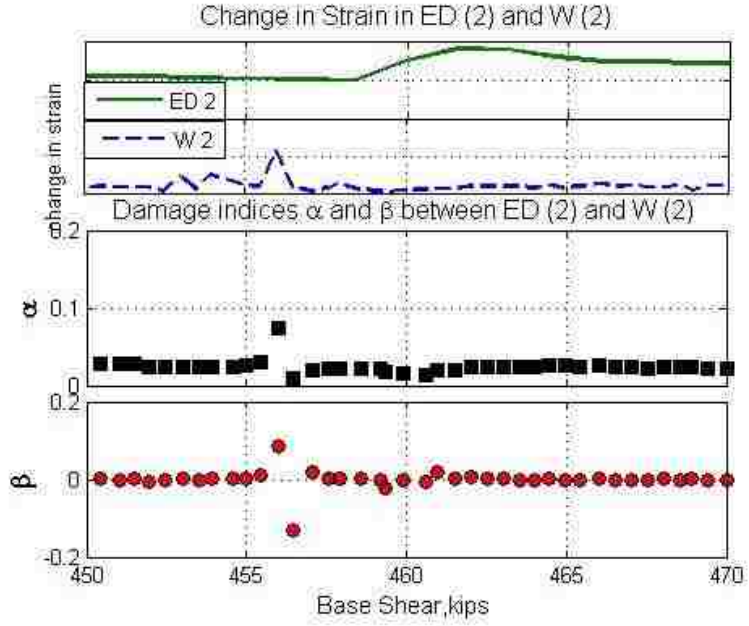

Figure B.5.14: Detection of concrete core crushing by 2nd story damage index W2/ED2

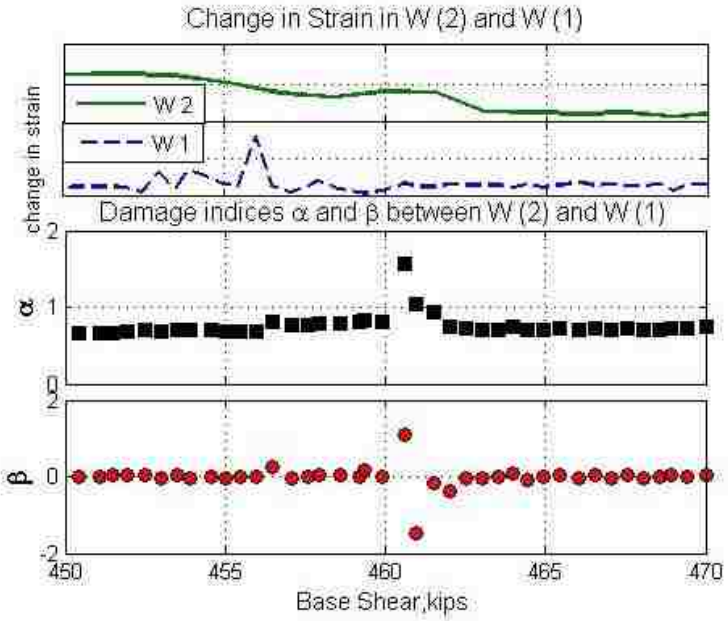

Figure B.5.15 Detection of concrete core crushing by 2nd story damage index W1/W2

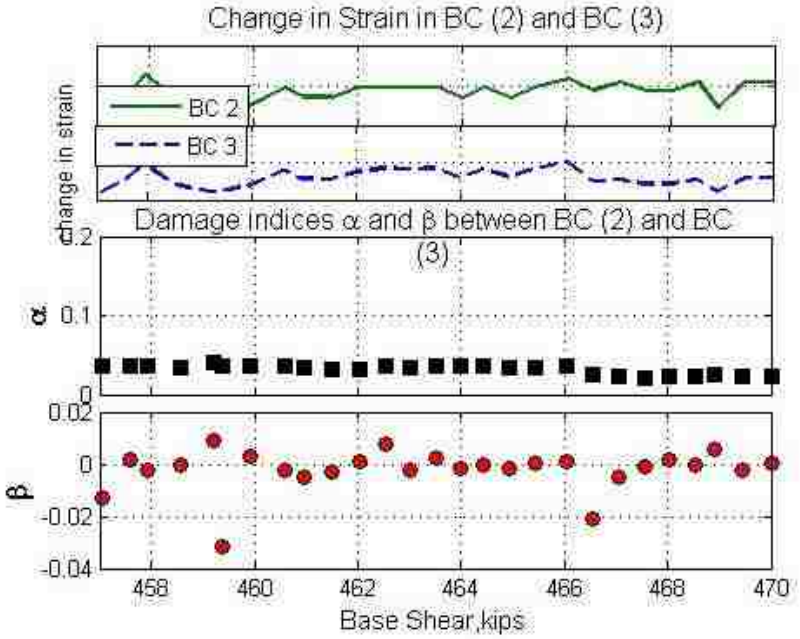

Figure B.5.16: Detection of concrete core crushing by 3rd story damage index BC3/BC2

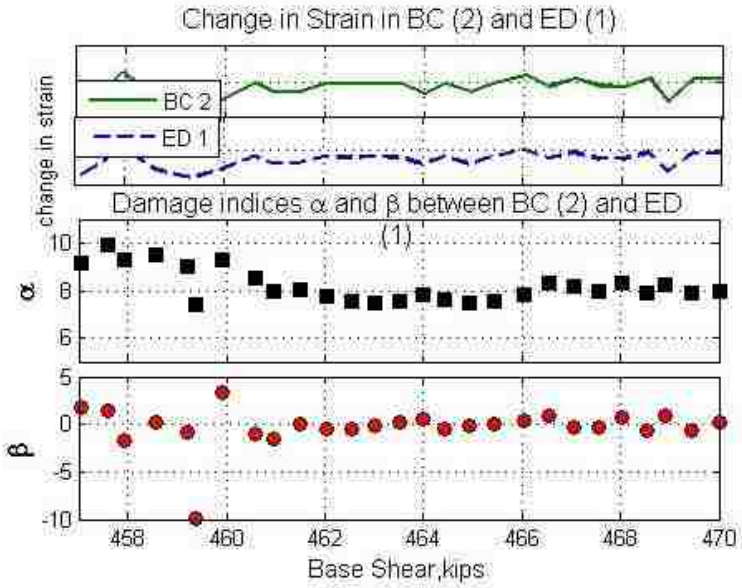

Figure B.5.17: Detection of concrete core crushing by 3rd story damage index ED1/BC2

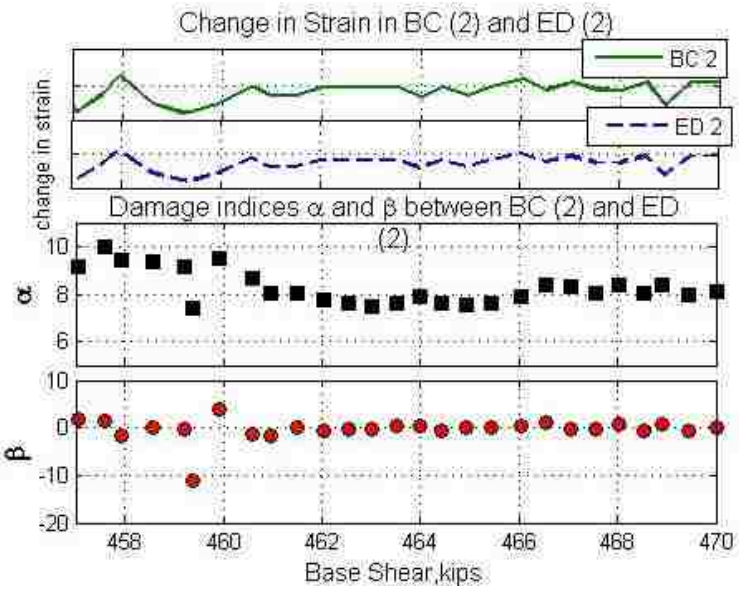

Figure B.5.18: Detection of concrete core crushing by 3rd story damage index ED2/BC2

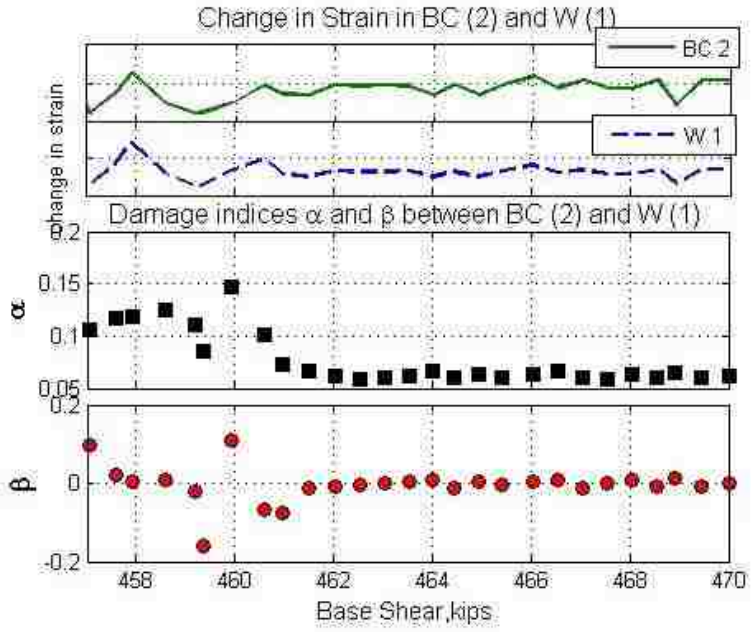

Figure B.5.19: Detection of concrete core crushing by 3rd story damage index W1/BC2

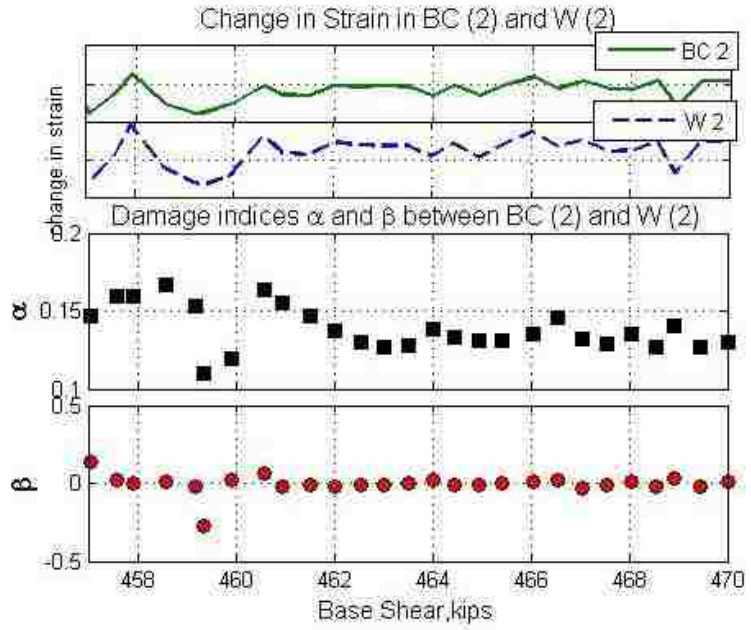

Figure B.5.20 Detection of concrete core crushing by 3rd story damage index W2/BC2

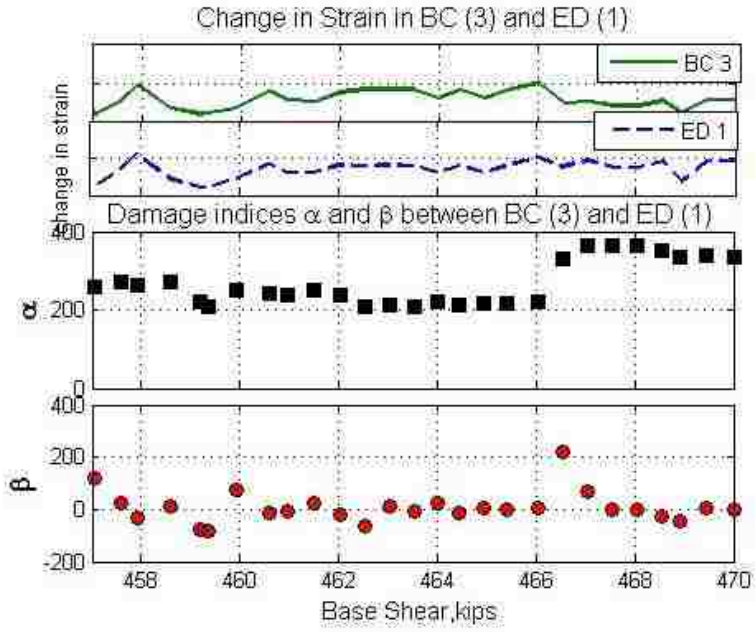

Figure B.5.21: Detection of concrete core crushing by 3rd story damage index ED1/BC3

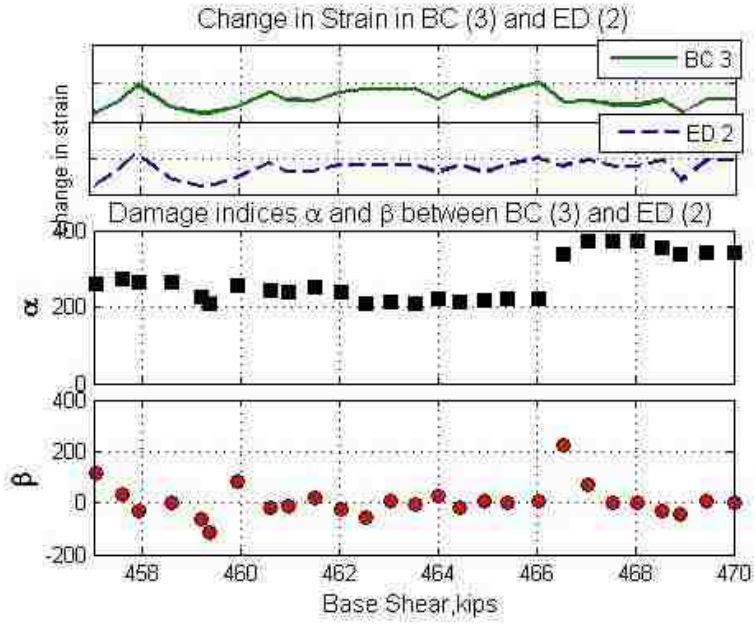

Figure B.5.22: Detection of concrete core crushing by 3rd story damage index ED2/BC3

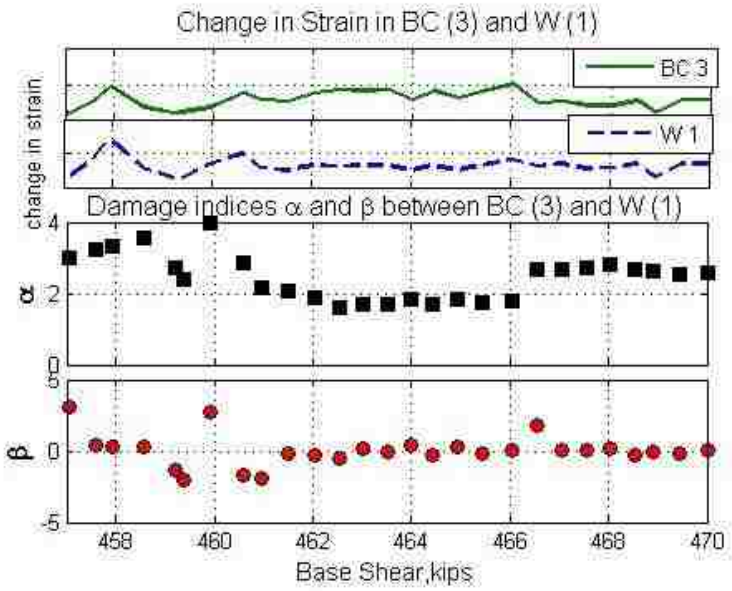

Figure B.5.23: Detection of concrete core crushing by 3rd story damage index W1/BC3

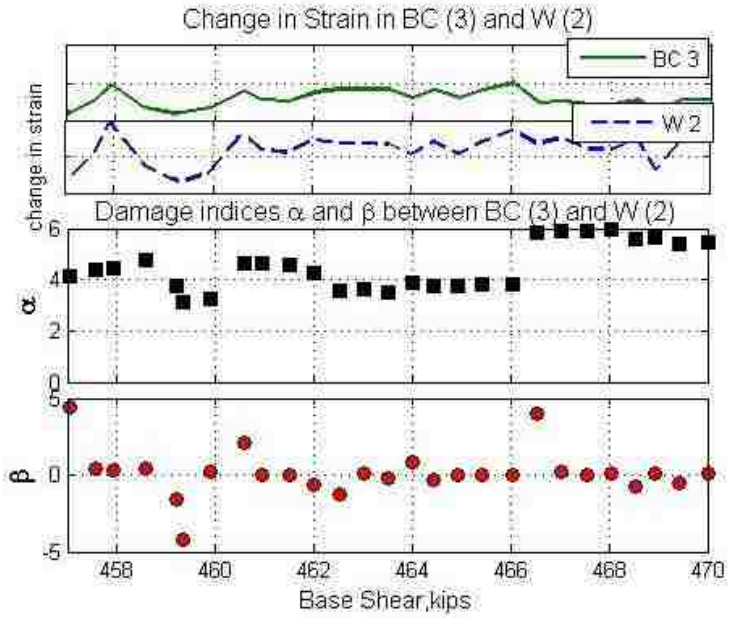

Figure B.5.24: Detection of concrete core crushing by 3rd story damage index W2/BC3

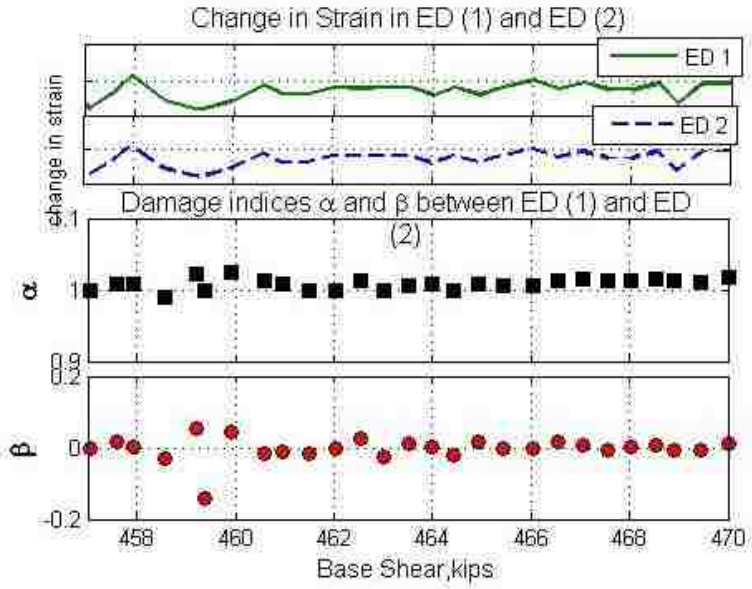

Figure B.5.25: Detection of concrete core crushing by 3rd story damage index ED2/ED1

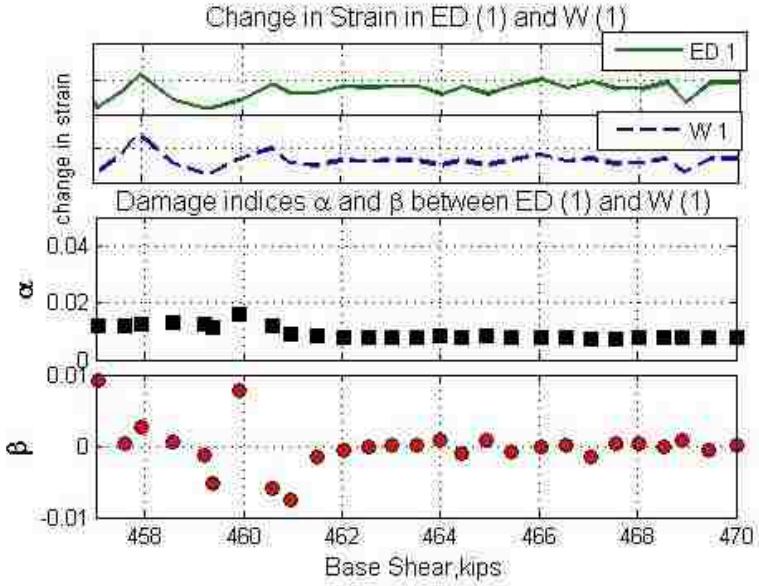

Figure B.5.26: Detection of concrete core crushing by 3rd story damage index W1/ED1

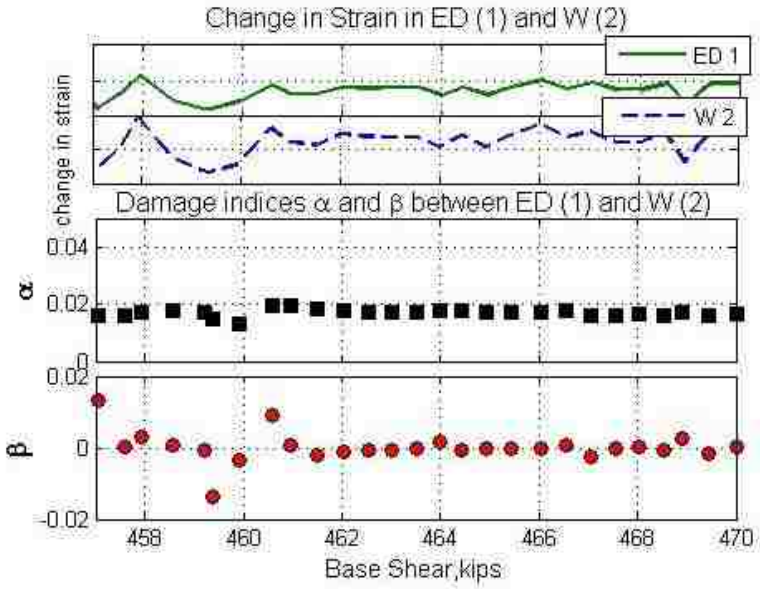

Figure B.5.27: Detection of concrete core crushing by 3rd story damage index W2/ED1

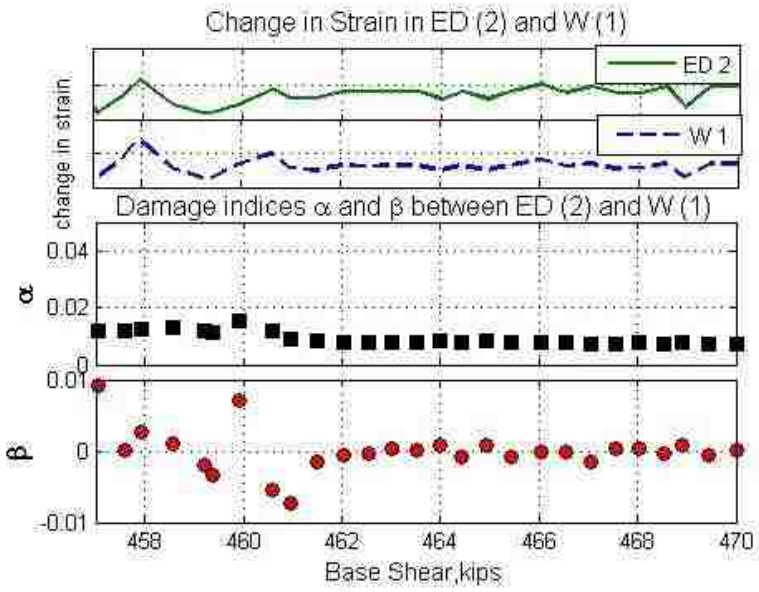

Figure B.5.28: Detection of concrete core crushing by 3rd story damage index W1/ED2

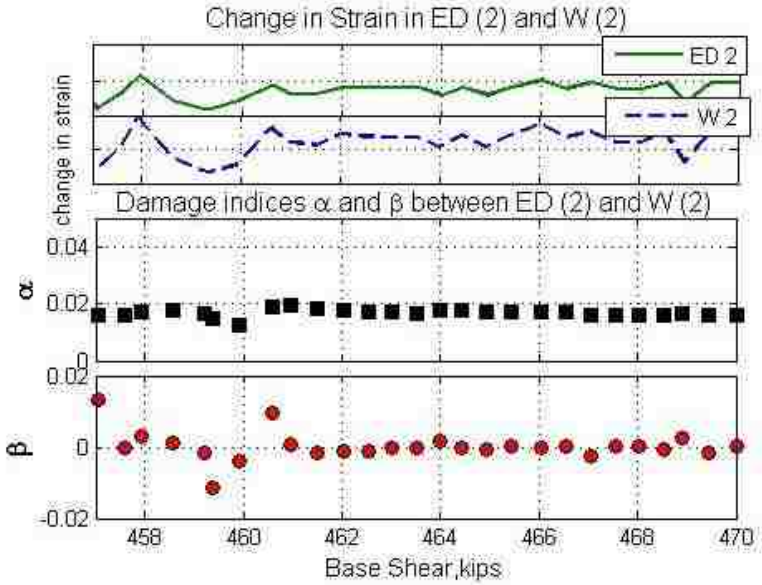

Figure B.5.29: Detection of concrete core crushing by 3rd story damage index W2/ED2

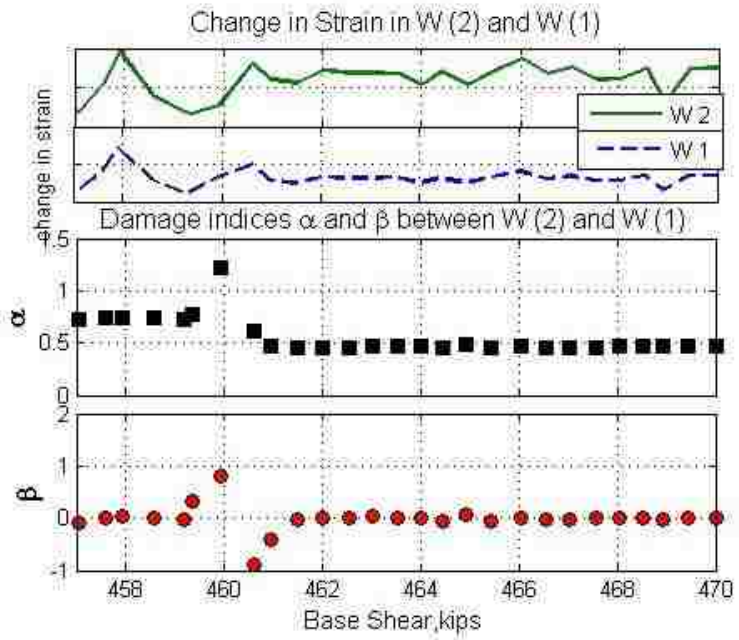

Figure B.5.30: Detection of concrete core crushing by 3rd story damage index W1/W2

Appendix C.1: Additional Damage Index Plots for Detection in ABAQUS Model

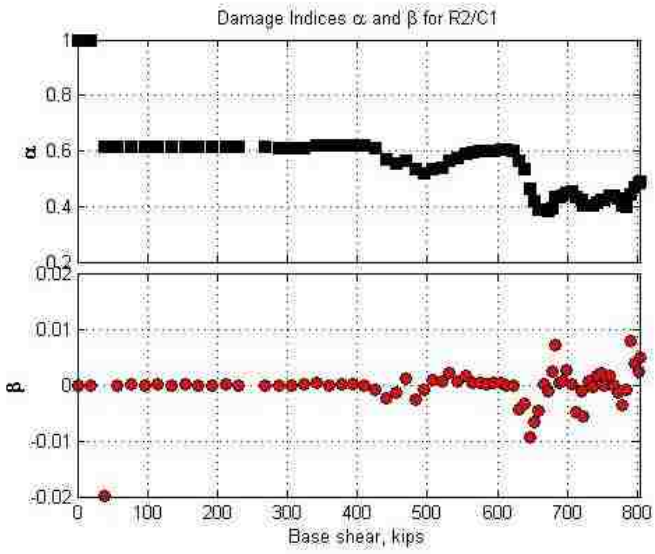

Figure C.1.1: Detection of concrete cover spalling and rebar yielding by damage index R2/C1

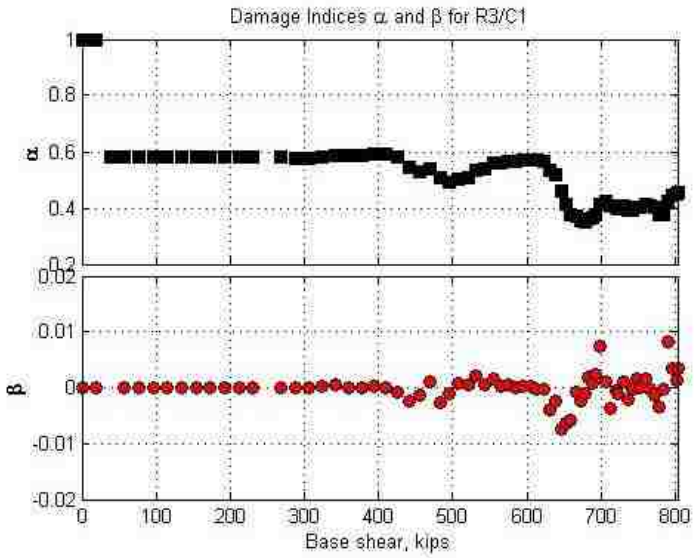

Figure C.1.2: Detection of concrete cover spalling and rebar yielding by damage index R3/C1

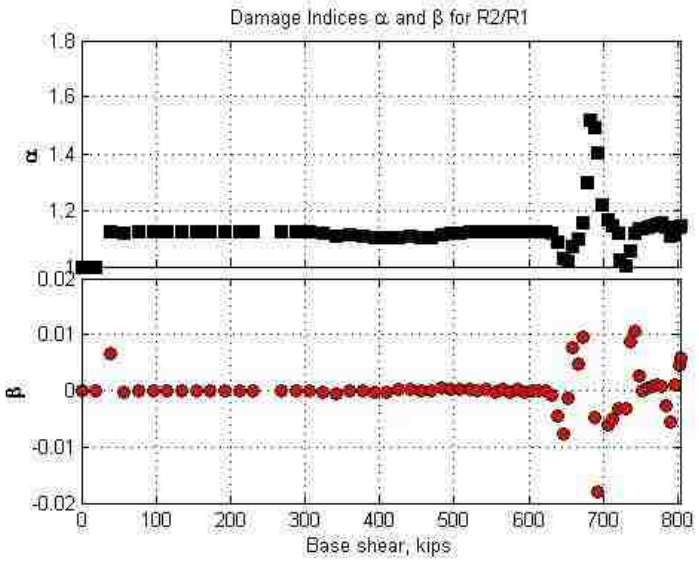

Figure C.1.3: Detection of concrete cover spalling and rebar yielding by damage index R2/R1

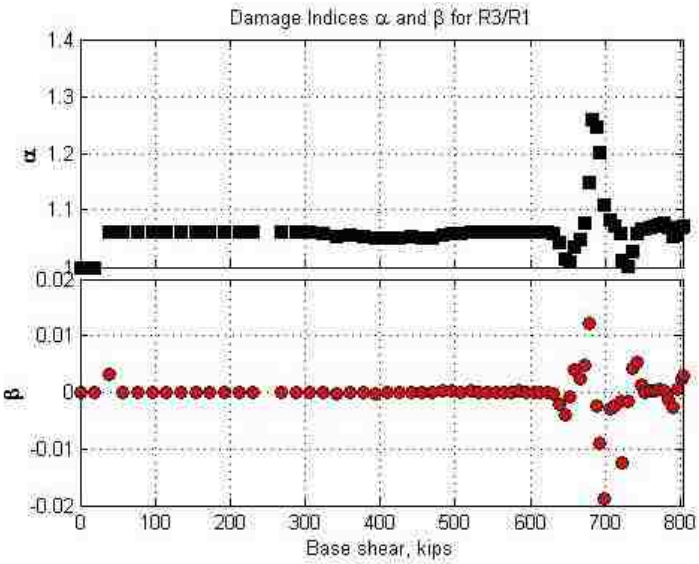

Figure C.1.4: Detection of concrete cover spalling and rebar yielding by damage index R3/R1

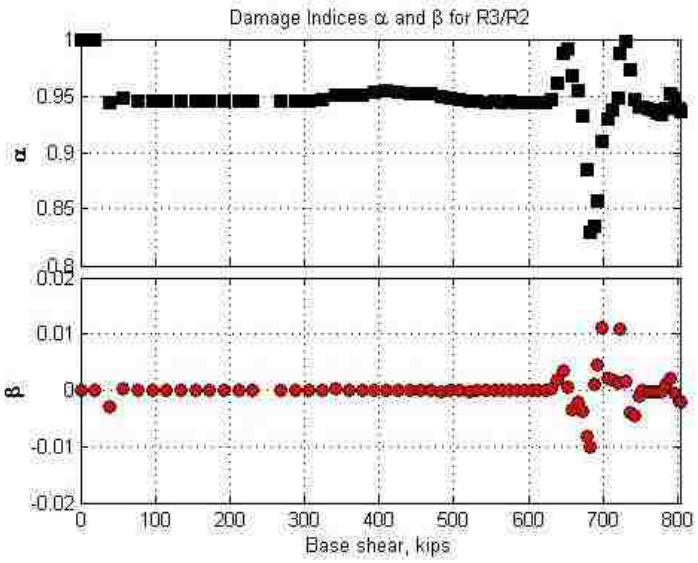

Figure C.1.5: Detection of concrete cover spalling and rebar yielding by damage index R3/R2

Appendix C.2: Additional Damage Index Plots for Yielding of Rebar in ABAQUS Model

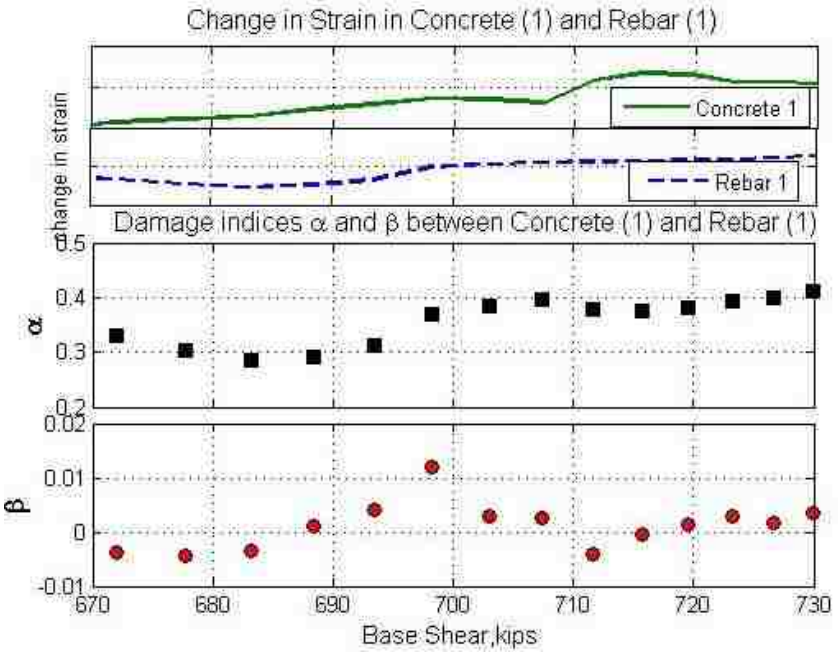

Figure C.2.1: Detection of rebar yielding by damage indices R1/C

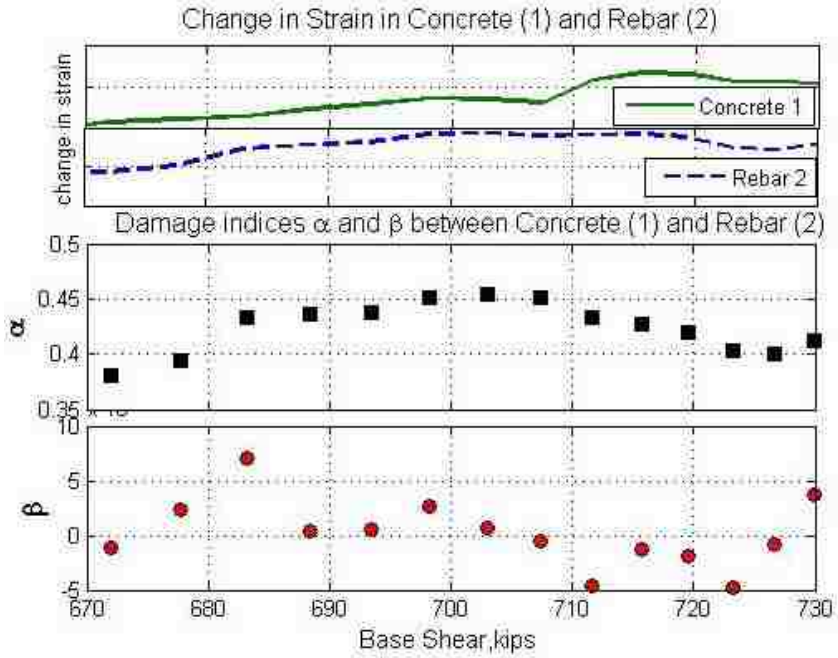

Figure C.2.2: Detection of rebar yielding by damage indices R2/C1

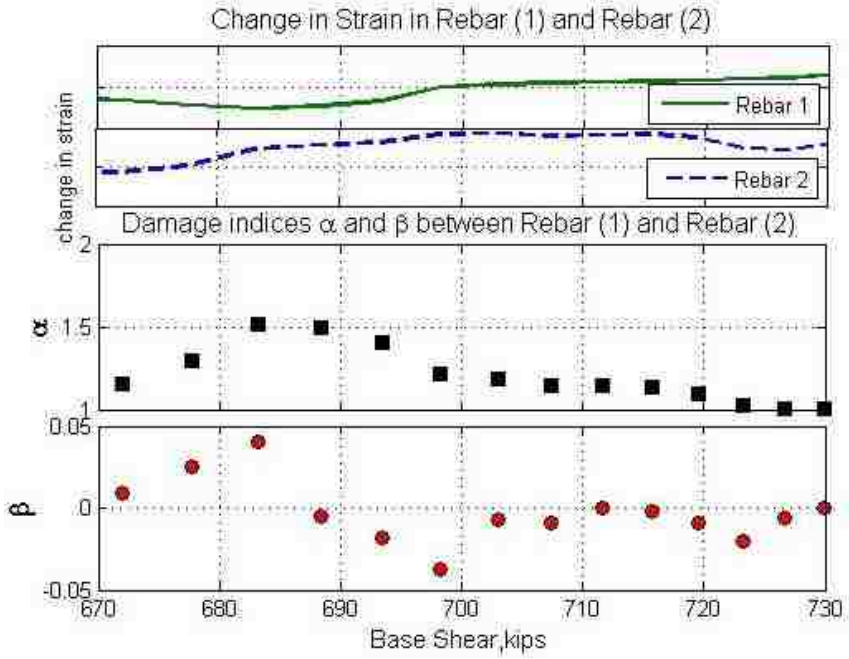

Figure C.2.3: Detection of rebar yielding by damage indices R2/R1

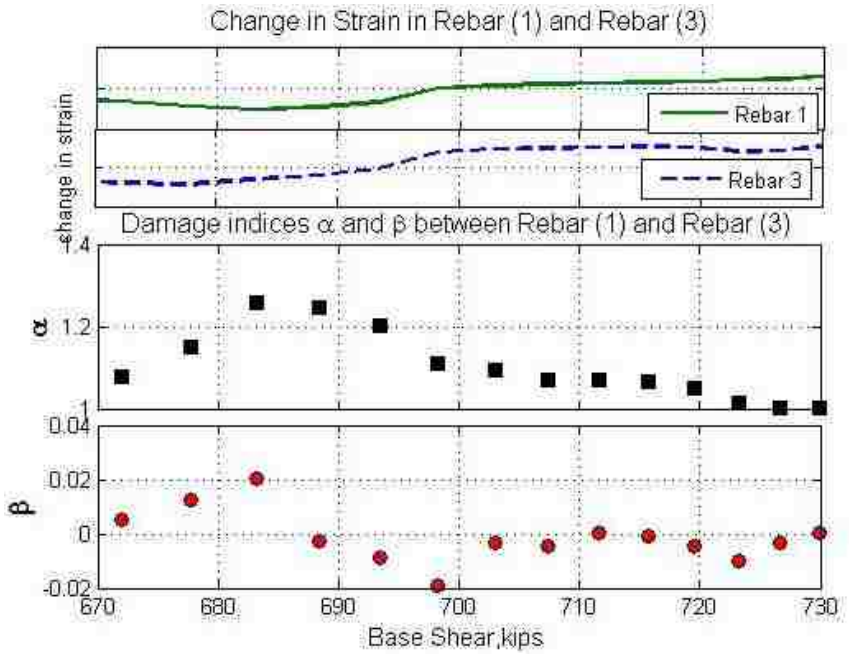

Figure C.2.4: Detection of rebar yielding by damage indices R3/R1

Appendix C.3: Additional Damage Index Plots for Concrete Cover Spalling in ABAQUS Model

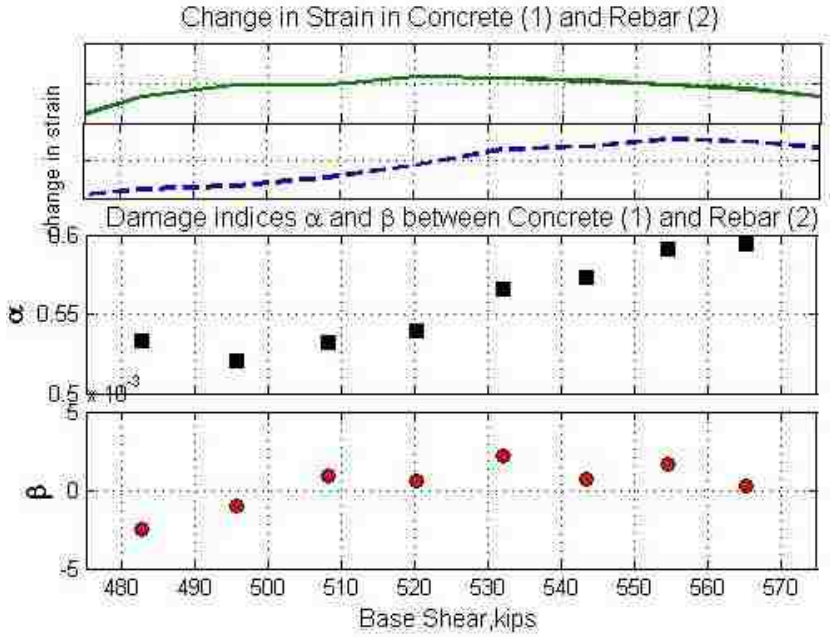

Figure C.3.1: Detection of concrete cover spalling by damage indices R2/C1

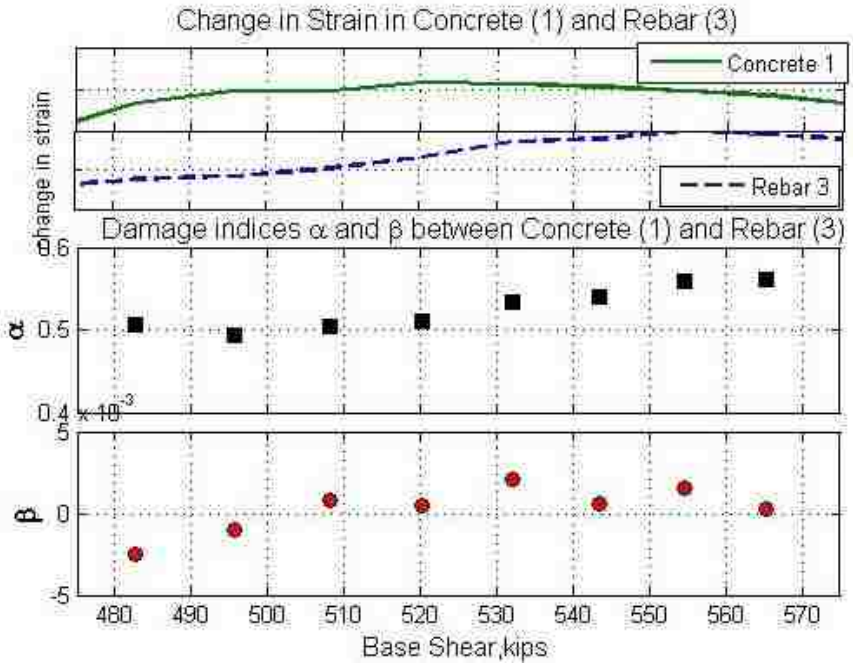

Figure C.3.20.1: Detection of concrete cover spalling by damage indices R3/C1

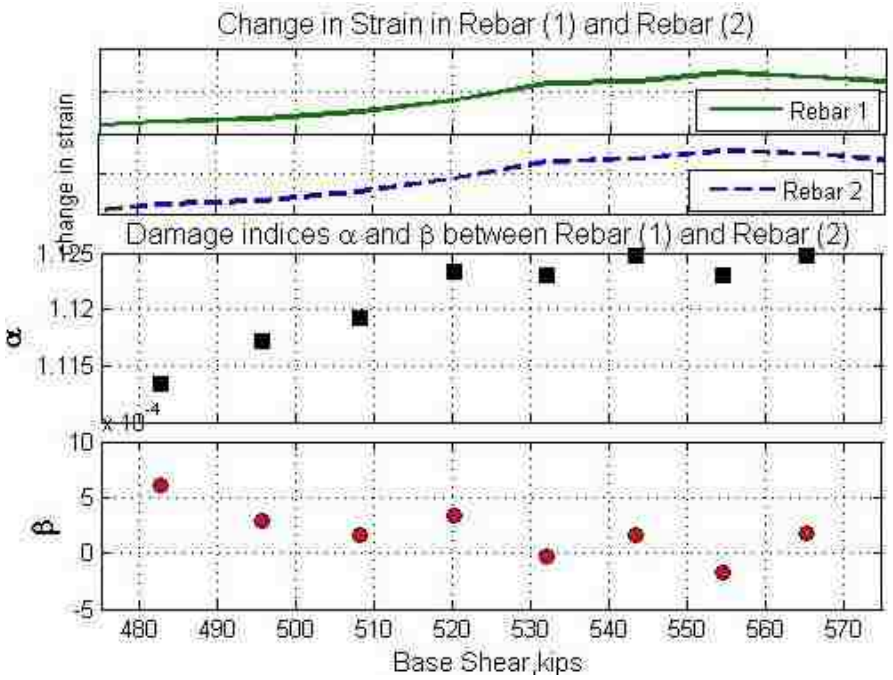

Figure C.3.3: Detection of concrete cover spalling by damage indices R2/R1

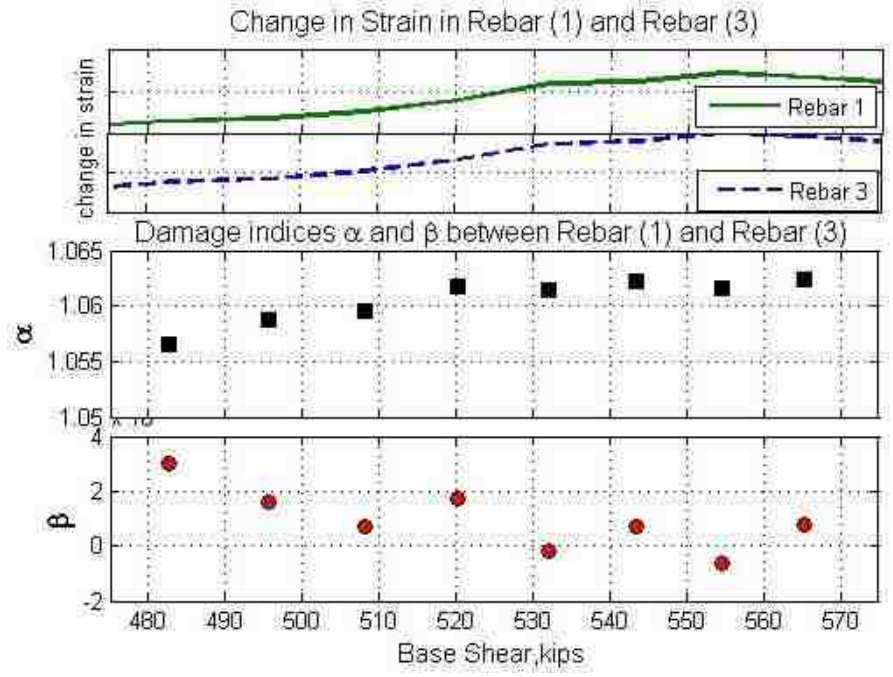

Figure C.3.4: Detection of concrete cover spalling by damage indices R3/R1

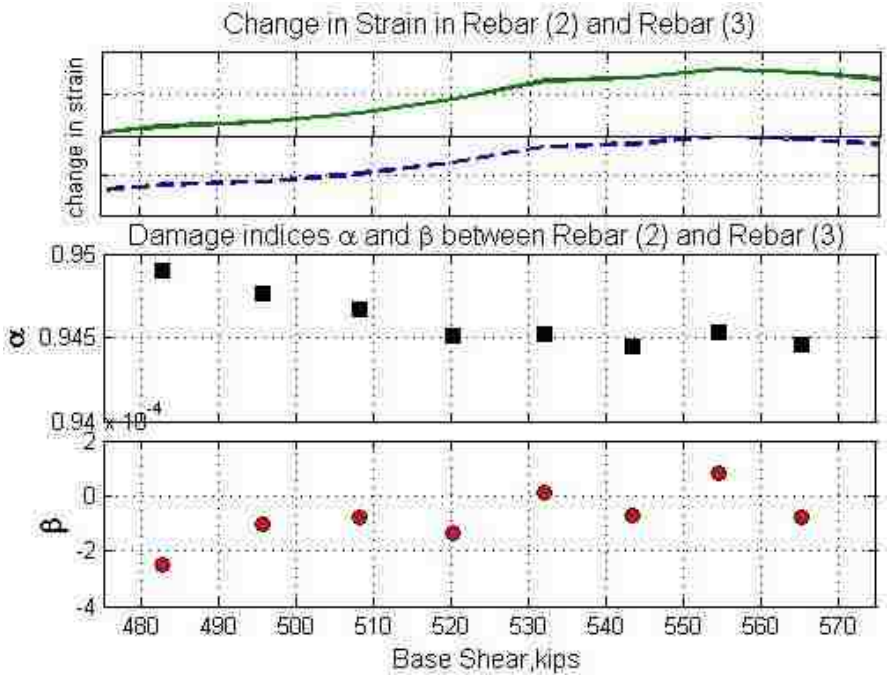

Figure C.3.5: Detection of concrete cover spalling by damage indices R3/R2

Vita

Kristen Ann Peterson, daughter of Kenneth and Anna Peterson, was born on December 29, 1990 in Framingham, Massachusetts. She earned her Bachelor of Science in Civil Engineering in May 2012 from Lehigh University in Bethlehem, Pennsylvania. Directly after graduation, Kristen stayed at Lehigh University to pursue her Master of Science in Structural Engineering as a President's Scholar. She will receive her M.S. in Structural Engineering in September 2013.